Georg M. Ausweger

Influences of Water Level Changes on the Behaviour of a Slow Moving Landslide - In-situ Measurements, Model Tests and Numerical Analyses

DOCTORAL THESIS

to achieve the university degree of

Doktor der technischen Wissenschaften

submitted to

Graz University of Technology

Supervisor

Ao.Univ.-Prof. Dipl.-Ing. Dr.techn. Helmut F. Schweiger, M.Sc.
Institute of Soil Mechanics and Foundation Engineering, Graz University of Technology

izr. prof. dr. Janko Logar, univ. dipl. inž. grad.
Faculty of Civil and Geodetic Engineering, University of Ljubljana

Graz, December 2017

AFFIDAVIT

I declare that I have authored this thesis independently, that I have not used other than the declared sources/resources, and that I have explicitly indicated all material which has been quoted either literally or by content from the sources used. The text document uploaded to TUGRAZonline is identical to the present doctoral thesis.

Date

Signature

Acknowledgements

This dissertation would not have been possible without the continuous support and advice of Ao.Univ.-Prof. Dipl.-Ing. Dr.techn. Helmut F. Schweiger. I thank Helmut for giving me the opportunity to join his research group and for his extensive help at all stages of this work. I greatly enjoyed working in the Computational Geotechnics Group at Graz University of Technology. I am thankful to Helmut for sharing his knowledge about soil mechanics and giving me the opportunity to attend many interesting conferences and workshops, which were very informative for me.

I am grateful to Prof. Janko Logar of University of Ljubljana for reviewing this thesis.

I would also like to thank Univ.-Prof. Dipl.-Ing. Dr.techn. Roman Marte, Head of the Institute of Soil Mechanics and Foundation Engineering who motivated me to start with my dissertation and continuously supported me with finishing this work. Thank you Roman for all personal and professional discussions.

A special thanks to all my colleagues at the Institute of Soil Mechanics and Foundation Engineering in Graz for the pleasant years and the fruitful discussions. In particular, I would like to thank Franz Tschuchnigg, Patrick Pichler, Michael Havinga, Matthias Rebhan, Pouya Sedighi, Laurin Hauser, Christopher Krammer and the colleagues from the laboratory.

I gratefully acknowledge Dr.techn. Helfried Breymann and Dr.techn. Robert Hofmann for many fruitful discussions on my thesis and geotechnical engineering. I would also like to thank Dipl.-Ing. Stephan Seiwald and Dipl.-Ing. Bernhard Reithofer (Salzburg AG) for providing me with the data, without which this thesis would not have been possible.

The financial support by the Austrian Society of Geomechanics (ÖGG) is gratefully acknowledged.

I am deeply thankful to my parents, who have enabled my education and motivated and supported me all these years.

Last but not least, I would like to thank Christiane for her understanding, patience and support these past years. Thanks also to my two sons Jakob and Lukas, who often welcomed me at home with a broad grin after a working day.

Graz, December 2017 Georg M. Ausweger

Kurzfassung

Einflüsse von Wasserspiegelschwankungen auf das Verhalten einer langsamen Massenbewegung – In situ-Messungen, Modellversuche und numerische Berechnungen

Langsame Massenbewegungen stellen eine Gefahr für die Umwelt dar und können Schäden an Infrastrukturbauten verursachen. In dieser Arbeit wird der Einfluss von Wasserspiegeländerungen in einem Speicherbecken, Kriecheffekten und Umwelteinflüssen (Regen und Evaporation) auf das Verhalten einer realen Massenbewegung untersucht. Die Verschiebungs- und Porenwasserdruckmessungen bei der untersuchten Massenbewegung im Bereich des Speicherbeckens eines Pumpspeicherkraftwerkes haben interessante Ergebnisse gezeigt. Erstens, treten am Böschungsfuß signifikante Porenwasserüberdrücke auf und deren Größe ist vom Speicherbetrieb abhängig. Zweitens, die Verschiebungsraten am Böschungsfuß korrelieren mit dem Speicherbetrieb.

Diese Arbeit diskutiert auf Basis von theoretischen Grundlagen und In situ-Messungen mögliche Gründe für die gemessenen Porenwasserüberdrücke am Böschungsfuß. Hierfür wurde das Verhalten des Bodens in einem quasi-gesättigten Zustand und während eines schnellen Absenkens untersucht. Die Ergebnisse eines Modellversuchs und vergleichende numerische Berechnungen zeigten, dass im quasi-gesättigten Boden zufolge externer Wasserspiegelschwankungen Porenwasserüberdrucke entstehen. Numerische Untersuchungen zeigten allerdings, dass Porenwasserüberdrücke aufgrund schneller Absenkvorgänge auch im gesättigten Zustand entstehen können, wenn der betrachtete Bereich nahe an einer Böschung ist. Die Größe der Porenwasserüberdrücke ist von der Absenkgeschwindigkeit, der Durchlässigkeit und der Steifigkeit des Bodens und des Wassers abhängig. 2D FE-Berechnungen der Fallstudie zeigten, dass die Berücksichtigung eines quasi-gesättigten Zustandes für die Rückrechnung der gemessenen Porenwasserdrücke nicht zwingend notwendig ist.

Der quantitative Anteil verschiedener Einflussfaktoren (Wasserspiegeländerungen, Umwelt und Kriechen) an den totalen Verschiebungen wird im Zuge dieser Arbeit ebenfalls bestimmt. Rückrechnungen der Verschiebungen mit dem Soft Soil Creep Modell zeigen, dass die Wasserspiegelschwankungen den wesentlichen Einflussfaktor für die Verschiebungen darstellen. Allerdings führen auch Kriecheffekte und Niederschlagsereignisse zu Verschiebungen. Außerdem werden Effekte, welche zu veränderten Verschiebungsraten führen, untersucht.

Eine numerische Untersuchung hinsichtlich des Einflusses der Wasserspiegelschwankungen auf die Sicherheitszahl der Massenbewegung und Empfehlungen für Stabilisierungsmaßnahmen schließen diese Arbeit ab.

Abstract

Influences of Water Level Changes on the Behaviour of a Slow Moving Landslide – In-situ Measurements, Model Tests and Numerical Analyses

Slow moving landslides pose a risk to the environment and may cause severe damage to infrastructures. In this thesis, the influences of water level changes in a water storage basin, creep effects and environmental factors (precipitation and evaporation) on the behaviour of a real slow moving landslide are investigated. Displacement measurements and pore water pressure recordings at the investigated landslide next to a storage basin of a pumped-storage power plant showed interesting measurement results. Firstly, significant excess pore water pressures are present at the slope toe and the magnitude of the excess pore water pressures depends on the storage operation. Secondly, the movement rates at the slope toe correlate with the velocity and the height of the water level changes.

Presenting a theoretical background and the measurements, this thesis discusses possible reasons for the excess pore water pressures at the slope toe. For this, the soil behaviour in a quasi-saturated stage and during rapid drawdowns is studied. Results of a model test and comparative finite element analyses showed that excess pore water pressures develop in quasi-saturated soils due to external fluctuating water levels. However, according to numerical studies, excess pore water pressures due to rapid drawdowns might also occur under saturated conditions, if the considered area is next to a slope. The magnitude of the excess pore water pressures is significantly influenced by the drawdown rate, the soil permeability, stiffness of the soil skeleton and bulk modulus of the pore water. Numerical studies with a 2D FE-model of the case study showed that a quasi-saturated stage is not necessarily required for the back-calculation of the measured pore water pressures at the slope toe.

The quantitative contribution of the various influencing factors (water level changes, environment and creep) on the total slope displacements are also determined in this thesis. Back-calculations of the slope movements with the Soft Soil Creep model showed that the storage operation is the main influencing factor for the displacements. However, creep effects and precipitation also lead to displacements. Furthermore, factors leading to variations in displacement rates, are investigated.

A numerical study concerning the influence of the water level changes on the safety factor of the slow moving landslide and recommendations for possible stabilization measures complete this thesis.

Table of contents

List of symbols

The symbols used in this thesis are listed in alphabetic order. Additional explanation is provided in the text at first appearance. Units are not included in this list.

Capital letters

A	Skempton's pore pressure coefficient
A^*	Skempton's pore pressure coefficient for triaxial compression stress path
B	Skempton's pore pressure coefficient
B^{oed}	Skempton's pore pressure coefficient under oedometer conditions
C_0	fitting parameter
C_{air}	air compressibility
C_{fluid}	pore fluid compressibility
C_m	compressibility of porous medium (soil skeleton)
C_s	compressibility of particles
C_{water}	pore water compressibility
E	Young's modulus
E_0	small strain stiffness in HSS model at actual stress
E_{50}	secant stiffness in standard drained triaxial test in HS model and HSS model at actual stress
$E_{50,ref}$	secant stiffness in standard drained triaxial test in HS model and HSS model at reference stress
E_{oed}	actual stiffness for primary oedometer loading
$E_{oed,ref}$	tangent stiffness for primary oedometer loading in HS model and HSS model at reference stress
E_{ur}	stiffness for un- and reloading in HS model and HSS model at actual stress
$E_{ur,ref}$	stiffness for un- and reloading in HS model and HSS model at reference stress
G	shear modulus
G_0	small strain stiffness shear modulus in HSS model at actual stress
$G_{0,ref}$	small strain stiffness shear modulus in HSS model at reference stress
G_b	fitting parameter
G_{ur}	tangential shear modulus for un- and reloading in HS model and HSS model
G_s	secant shear modulus in HS model and HSS model
G_t	tangent shear modulus in HS model and HSS model
I	fitting parameter
K'	bulk modulus of the soil skeleton / isotropic compression modulus
K_0	lateral earth pressure coefficient at rest

K_0^{nc}	lateral earth pressure coefficient at rest for normally consolidated conditions
K_{fluid}	bulk modulus of the pore fluid
K_w	bulk modulus of the pore water
L_d	length of daylight
M	ellipse parameter for SSC model
N	number of days per month
PE	potential evaporation
PI	plasticity index
R	drawdown rate
S	degree of saturation
S_{ref}	reference degree of saturation
$S_{(pwater=0)}$	reference degree of saturation at a pore water pressure $p_{water} = 0$ kPa
$S_{qs,min}$	minimum degree of saturation in a quasi-saturated stage
S_{sat}	maximum degree of saturation
T	surface tension of water-air interface
T_a	mean monthly temperature
V	volume
V_a	volume of free air
V_{da}	volume of dissolved air
V_s	volume of soil particles
V_w	volume of water

Small letters

a_t	fitting parameter
c'	effective cohesion
e	void ratio
g_a, g_l, g_n	Van Genuchten parameters
h	Henry's parameter
k	hydraulic permeability
k_{qs}	quasi-saturated permeability
$k_{qs,min}$	minimum quasi-saturated permeability
k_{rel}	relative permeability
k_{sat}	saturated permeability
k_x	saturated permeability in horizontal direction
k_y	saturated permeability in vertical direction
m	power for stress-level dependency of stiffness in HS model and HSS model
n	porosity
$\bar{n}$	fitting parameter
$\hat{n}$	fitting parameter
p'	effective mean stress

p_{air}	pore air pressure
$p_{air,ref}$	reference pore air pressure
p_{atm}	atmospheric air pressure
$p_{calculated}$	calculated pore water pressure
p_{eq}'	equivalent isotropic stress in SSC model
p_{excess}	excess pore water pressure
p_{fluid}	pore fluid pressure
$p_{hydrostatic}$	hydrostatic pore water pressure
$p_{measured}$	measured pore water pressure
p_p'	isotropic pre-consolidation stress in SSC model
p_{p0}'	initial isotropic pre-consolidation stress in SSC model
p_{ref}	reference stress for stiffness in HS model and HSS model
p_{vapour}	vapour pressure
p_{water}	pore water pressure
$p_{water,ref}$	reference pore water pressure
q	deviatoric stress
q_f	ultimate deviatoric stress in HS model and HSS model
r_{air}	radius of air bubbles
s	suction
t	time
t_c	temperature
u	displacements
v	velocity
w	water content

Greek letters

α	Biot's coefficient
Δh	change in water level height
Δp	change in total mean stress
$\Delta p_{hydrostatic}$	change in hydrostatic pore water pressure
Δp_{water}	change in pore water pressure
Δq	change in deviatoric stress
$\Delta \sigma$	change in stress
$\Delta \sigma_1$	change in total major principal stress
$\Delta \sigma_3$	change in total minor principal stress
$\Delta \sigma^{total}$	change in total stress
ε_1	major principal strain
ε_2	intermediate principal strain
ε_3	minor principal strain
ε_{vol}	volumetric strains
ε_{vol}^{c}	volumetric creep strains
$\dot{\varepsilon}_{vol}^{c}$	volumetric creep strain rate
ε_{yy}	strain in y-direction

γ	unit weight of soil
$\gamma_{0.7}$	shear strain parameter for small strain stiffness in HSS model
γ_{sat}	bulk unit weight of soil below ground water table
γ_{unsat}	bulk unit weight of soil above ground water table
γ_w	unit weight of water
φ'	effective friction angle
φ_{res}'	effective residual friction angle
κ^*	modified swelling index for SSC model
λ^*	modified compression index for SSC model
μ^*	modified creep index for SSC model
ν'	Poisson’s ratio
ν'_{ur}	Poisson’s ratio for un- and reloading
ρ_{dry}	dry density of soil
ρ_f	fluid density
$\rho_{Proctor}$	proctor density
ρ_s	particle density
σ	stress / total stress
$\bar{\sigma}$	in-situ confining pressure
σ_1	total major principal stress
σ_3	total minor principal stress
σ'	effective stress
σ_1'	effective major principal stress
σ_2'	effective intermediate principal stress
σ_3'	effective minor principal stress
σ_{cons}'	consolidation stress
σ_h	total horizontal stress
σ_v	total vertical stress
σ_h'	effective horizontal stress
σ_v'	effective vertical stress
σ_{yy}'	effective normal stress in y-direction
σ_{zz}	total normal stress in z-direction
τ	shear stress / time parameter in SSC model (1.0 day)
ψ	matric potential
ψ'	dilatancy angle

Abbreviations

APH	absolute pressure height
CSS	current stress state surface in SSC model
EPWP	excess pore water pressure
EXT	extensometer
FE	finite element
FEA	finite element analysis
FoS	factor of safety

HS	Hardening Soil model
HSS	Hardening Soil Small model
INC	inclinometer
masl	meter above sea level
NCS	normal consolidation state surface in SSC model
OCR	isotropic overconsolidation ratio
PPG	pore water pressure gauge
SSC	Soft Soil Creep model
WL	water level changes
WRC	water retention curve

1 Introduction

1.1 Motivation

In alpine regions and other mountainous regions, many areas are affected by slow moving landslides (e.g. Puzrin & Sterba 2006, Puzrin & Schmid 2012, Engl 2013, Marte & Ausweger 2014, Schwager 2013, Hofmann & Sausgruber 2017). Slow moving landslides are characterized by small movement rates, ranging from several mm / year to dm / years but progressive deformations. The magnitude of the movement rates often depends on external influences. The volume of slow moving landslides can be up to several million m^3. In the case of such large volumes, a stabilization of the landslide, reducing the movement rates to zero, is hardly possible from a technical perspective. Furthermore, in most cases, impossible from an economical perspective.

In many cases, these slow moving landslides pose a risk to human life and may cause severe damage to infrastructures. As a complete stabilization is usually not possible due to the large volume of the landslide, at least a reduction of the movement rates by suitable measures is intended, in order to reduce potential risk and damage. For the best design of such suitable remediation measures, the behaviour of the landslide, i.e. its causes, triggers and mechanisms, must be understood in detail. Otherwise, stabilization measures may create no improvements, and may actually lead to a change to the worse.

To ensure a good understanding of the landslide mechanism, a comprehensive monitoring of the landslide is advisable. Important insights concerning the movement behaviour can be derived from the monitoring results and from comparisons of various measurement quantities. Moreover, leaving the measurement equipment in place after the application of remediation measures enable an evaluation of their impact. Furthermore, the many heterogeneities, especially of material parameters and deformation behaviour, that characterize large landslides make modelling of the landslide very difficult and monitoring is unavoidable in order to perform analytical and numerical investigations that result in satisfactory and realistic results. Numerical analyses may help to obtain an improved understanding of the landslide behaviour as the application of numerical methods offers numerous advantages. Depending on the numerical method used, different mechanisms leading to movements can be studied in detail, failure probabilities can be determined, inverse parameter identifications are possible or the affected areas in case of a sudden failure can be determined.

In this thesis, the behaviour of a slow moving landslide next to a water storage basin is studied by means of the finite element method and comprehensive analyses of in-situ measurement data. In the case of such slow moving landslides next to water basins, the possible risk of its sudden failure is usually significant due to the destructive flood wave it would cause. Furthermore, the water level changes in the basin (or river) might have an influence on the movement behaviour of the landslide (e.g. Engl 2013, Pinyol et al. 2012, Hendry et al. 2014).

The slow moving landslide presented in this thesis was detected in an adjacent slope during extension works for a later presented water storage basin of a pumped-storage power plant (the case study). Consequently, measurement devices (inclinometer, geodetic measurement points and pore water pressure gauges) were installed. This measurement system was extended in subsequent years. After several years of monitoring, important knowledge about the interaction of the storage operation and the movement behaviour of the landslide could be gained. The water level in the basin is changed up to three times a day with a maximum difference in height of approximately 7 m. The measurements of the pore water pressure gauges at the slope toe showed excess pore water pressures of up to approximately 40 kPa with regard to the water level in the water storage basin. An analysis of measurement values indicated that fast and high water level changes in the basin lead to high excess pore water pressures at the slope toe. Furthermore, it could be worked out that periods with many water level changes coincide with periods of high movement rates at the slope toe. It was especially noted that a fast water level lowering after a longer period with a high water level leads to an acceleration of the landslide deformations. Due to these observations, questions were raised that cannot be answered only on the basis of measurements. These questions, presented in the following, form the basis for this thesis. Firstly, the reasons for the excess pore water pressures linked to the storage operation should be discussed. Secondly, the influence of the water level changes on the velocity of the landslide movement are to be clarified. Thirdly, any possible further factors influencing the movement behaviour are to be determined. Finally, based on the insights from the previous tasks, possible remediation measures are developed. All questions are studied by means of the finite element method in combination with interpretation of available measurement data.

The sign convention in this thesis is according to classical soil mechanics. Compression is marked by a positive sign, whereas tension is marked by a negative sign.

1.2 Outline of thesis

The thesis is divided into two major parts. In the first part (chapter 2 to chapter 4) the theoretical background for the subsequent investigations of the slow moving landslide is explained. The second part (chapter 5 and chapter 6), deals with the specific case study where the aforementioned questions are answered.

Chapter 2 deals thoroughly with the behaviour of quasi-saturated soils. It has to be pointed out that the focus is on the influences of the quasi-saturation on the hydraulic behaviour rather than on the mechanical behaviour. Quasi-saturated soils are characterized as soils with a continuous water phase and a discontinuous air phase, which occurs in the form of small air bubbles or air pockets. Any air in the pore water significantly increases the compressibility of the pore water. It is known that this effect leads to excess pore water pressures in the subsoil when the water level is changed above the ground surface (e.g. Stelzer et al. 2014). This circumstance shows that the quasi-saturation might be one reason for the excess pore water pressures measured at the slope toe and linked to the storage operation. Therefore, this special type of saturation is investigated in chapter 2. This is done on a theoretical level and with the aid of a model test. Finally, a preliminary study, inspired by the case study is performed.

Chapter 3 summarizes the main effects of a rapid drawdown. This mechanism is defined as a fast water level change with regard to the soil permeability in the area of an inclined ground surface. Such rapid drawdowns also lead to excess pore water pressures (e.g. Berilgen 2006, Pinyol et al. 2008) and occur in the storage basin of the case study on a daily basis. Therefore, this mechanism might also be the reason for the measured excess pore water pressures. The general soil behaviour during a rapid drawdown is studied by means of finite element analyses on a simple slope model. In those analyses, the permeability conditions and the drawdown velocity are varied. Furthermore, a quasi-saturated stage and a saturated stage are simulated. The influence of various factors on the development of the excess pore water pressures is studied. Finally, the change in the factor of safety of the slope due to the drawdown is analysed.

Chapter 4 briefly presents three possible constitutive models that could be used to model the lacustrine fine sediments, found beneath the water storage basin investigated in the case study. Then the preferred constitutive model for the case study (Soft Soil Creep model) is applied in the simulation of a biaxial test with partial drainage conditions. In the test, a recurring load is applied similar to the real site conditions (fluctuating water levels, precipitation). Based on this preliminary study, the general behaviour of the Soft Soil Creep model under this applied loading is investigated.

In chapter 5, the specific site (water storage basin with slow moving landslide) is presented. Based on laboratory tests and back-calculations, the input parameters for the constitutive models presented in chapter 4 are determined. Furthermore, selected measurement results are presented for a better understanding of the mechanisms leading to the slope movements.

In chapter 6, the numerical analyses concerning the pore water pressures and the movement behaviour of the landslide are presented. First, the finite element model and the simulation procedure are introduced. Afterwards, the measured excess pore water pressures are back-calculated to determine whether they only occur due to the rapid drawdowns during the storage operation or also due to a quasi-saturated stage of the subsoil. Furthermore, the displacements of the slow moving landslide are back-calculated, considering the water level changes, environmental factors (precipitation and evaporation) and creep effects. By considering each factor in a separate calculation phase, its contribution to the total displacements is determined. Based on the knowledge of which factor has the major influence on the slope displacements, possible remediation measures are discussed. In the course of the back-calculation of the displacements, the influence of the constitutive model used for the lacustrine fine sediments on the movement behaviour is also discussed. Furthermore, possible reasons for increased displacement rates are presented, applying the Soft Soil Creep model for the lacustrine fine sediments at the slope toe. Finally, the factor of safety of the slope for various states is calculated.

The conclusions of this thesis and recommendations for further investigations are summarized in chapter 7. References are provided in chapter 8.

2 Quasi-saturated soils

In classical soil mechanics, soils below the ground water table are considered as a two-phase medium. All pores are filled with water and the pore water is assumed to be incompressible, at least for practical purposes. However, if a small amount of air is present in the pore water, the compressibility of the pore fluid and the soil permeability are significantly influenced. Such soils are termed quasi-saturated soils (Faybishenko 1995). This chapter discusses the influences of small entrapped air bubbles in the soil on the soil's hydro-mechanical behaviour. Furthermore, possibilities for modelling the behaviour of quasi-saturated soils are presented based on a comprehensive literature review and in a theoretical context. The theoretical considerations are verified by experiments performed in the laboratory. Finally, the pore water pressure measurements beneath a water storage basin are back-calculated with a simple axisymmetric finite element model by considering a quasi-saturated state of the soil.

2.1 Definition

Through the past decades, various authors (e.g. Peck 1969, Fredlund 1976, Faybishenko 1995, Bicalho 1999, Köhler 2000, Voughan 2003, Boutonnier 2007, Sakaguchi 2005, Stelzer et al. 2014) discussed the behaviour of entrapped air bubbles in soils and their influences on soil behaviour. Faybishenko (1995) introduced a new term, quasi-saturated soils, to describe soils beneath the groundwater table containing entrapped air bubbles. Quasi-saturated soils are not fully saturated due to the entrapped air. However, the air phase is discontinuous and therefore the quasi-saturated stage differs significantly from the conventional unsaturated (partially saturated) stage.

Köhler & Montenegro (2005), Tarantino (2010) and Boutonnier (2010) presented a similar distinction between the stages of saturation. Köhler & Montenegro (2005) and Boutonnier (2010) basically distinguish four stages of saturation. In case of full saturation no air is present in the pore water. With decreasing pore water pressure small air bubbles may be entrapped in the pore water. At the transition from pore water pressure to suction, pores filled with air develop. At the air entry value the conventional unsaturated stage with a continuous water phase and a continuous air phase is reached. In contrast to the definition according to Faybishenko (1995), Köhler & Montenegro (2005) and Boutonnier (2010) extent the quasi-saturated stage also into the suction range. Figure 1 shows the different stages of saturation in combination with a qualitative water retention curve (WRC). Figure 2 shows the different stages in a section of a soil column.

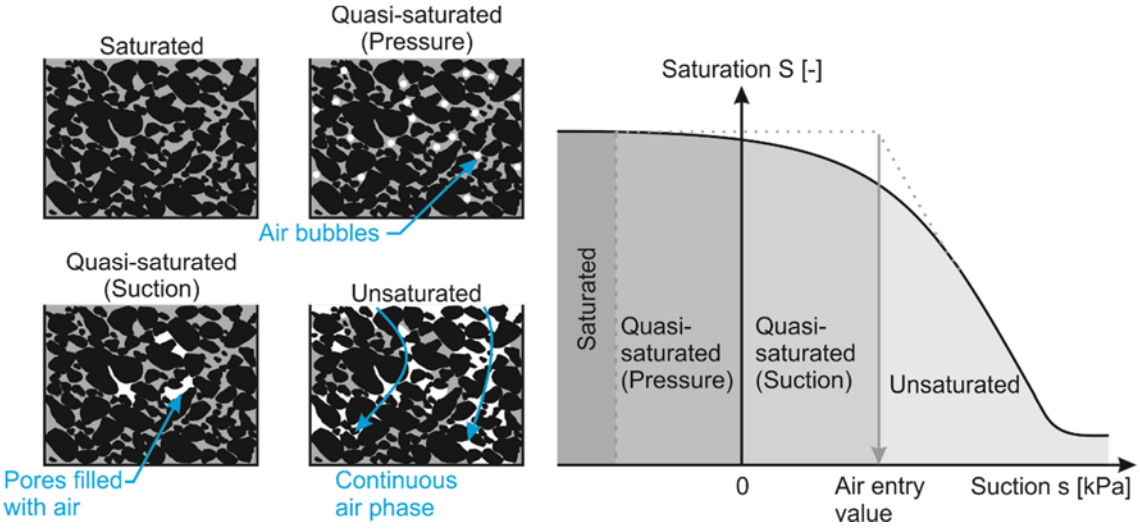

Fig. 1: Stages of saturation and qualitative water retention curve (after Boutonnier 2010)

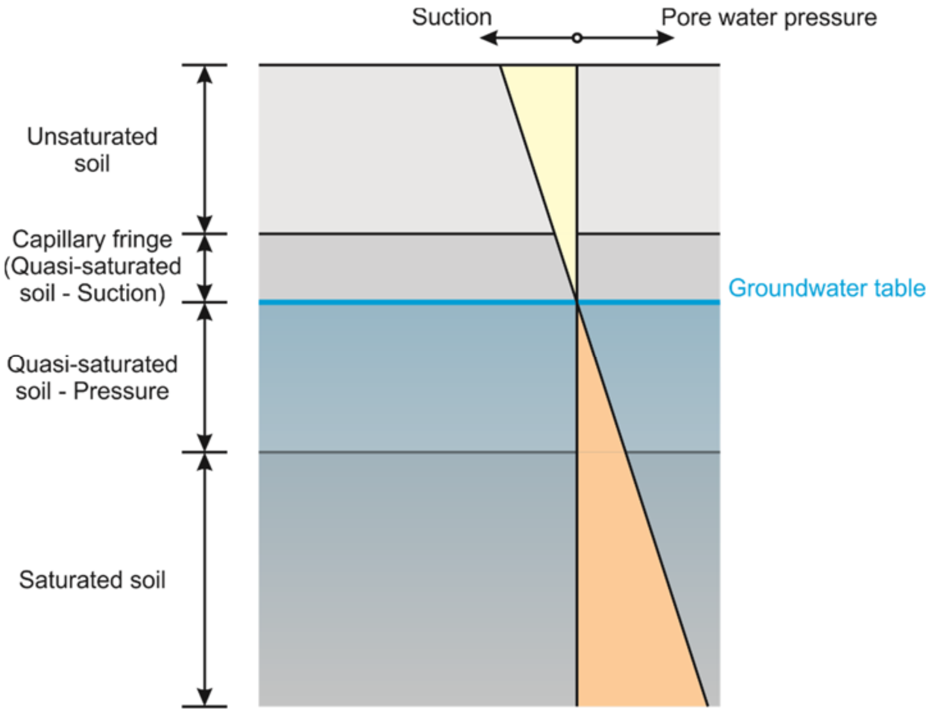

Fig. 2: Stages of saturation in a section of a soil column (after Köhler & Montenegro 2005)

According to Boutonnier (2010) and Bicalho (1999) the transition from unsaturated to quasi-saturated stage is typically at a degree of saturation between 80% and 90%. Wheeler (1986) defines this same transition at approximately 85%. This range usually corresponds to the optimum water content of compacted soils. Boutonnier (2010) also showed the stages of saturation in a proctor diagram (see Figure 3).

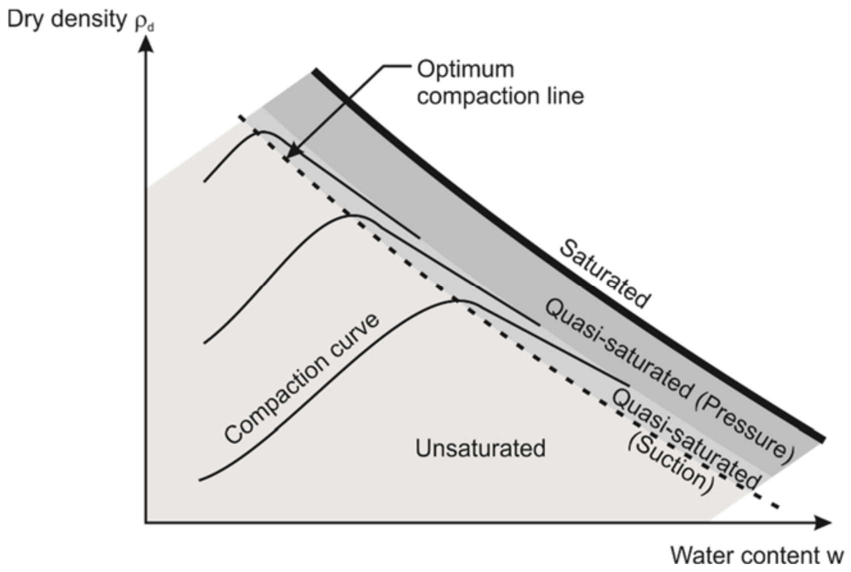

Fig. 3: Proctor diagram with stages of saturation (after Boutonnier 2010)

Reasons for the entrapment of air bubbles might be (Faybishenko 1995, Vaughan 2003)

- Fluctuating ground water tables
- Impoundment of dams and embankments
- Infiltration of water into the subsoil and pumping of water out of the soil

This thesis focuses mainly on quasi-saturated soils in the positive pore water pressure range as the later presented pore pressure measurements are exclusively in areas beneath the ground water table.

The entrapped air bubbles influence the hydraulic behaviour significantly. First, the compressibility of the pore fluid (water-air mixture) is increased. Second, the soil permeability is decreased. These effects of entrapped air bubbles are discussed in the following.

2.2 Bulk modulus of pore fluid

Schuurmann (1966), Fredlund (1976) and Boutonnier (2007, 2010) presented in their works the fundamental physical laws to determine the compressibility of a water-air mixture. Schuurmann (1966) summarized the different formulations known at that time for determining the pore fluid compressibility. In the formulation of Schuurmann (1966) the difference between pore water pressure and air pressure in the air bubbles is considered. Fredlund (1976) derived an equation to determine the pressure dependent density and compressibility of a water-air mixture. Furthermore, Fredlund (1976) emphasized the importance of the increased pore fluid compressibility for the pore pressure development in soils, especially in case of transient processes. Boutonnier (2007, 2010) presented a mathematical formulation to determine the compressibility of the pore fluid in a quasi-saturated stage in the positive pressure range. In the following pages, the derivation of the compressibility of a water-air mixture is shown. The following theory is only valid for the quasi-saturated stage in the positive pressure range, i.e. the air phase has to be present in the form of small entrapped air bubbles.

Generally, the isothermal compressibility of a fluid is defined as (Schuurmann 1966, Fredlund et al. 2012)

$$C_{fluid} = -\frac{1}{V} \cdot \frac{dV}{dp_{fluid}} \tag{1}$$

C_{fluid} is the compressibility of the fluid, V is the Volume and dV is the volume change with respect to a pore fluid pressure change dp_{fluid}.

Assuming a constant atmospheric air pressure p_{atm}, the compressibility of air C_{air} is inversely proportional to the absolute air pressure, which is the sum of the air pressure p_{air} and the atmospheric air pressure p_{atm} (Fredlund et al. 2012).

$$C_{air} = \frac{1}{p_{air}+p_{atm}} \tag{2}$$

Pure water can be assumed as nearly incompressible. Figure 4 shows measurement results of the compressibility of pure water from Dorsey (1940).

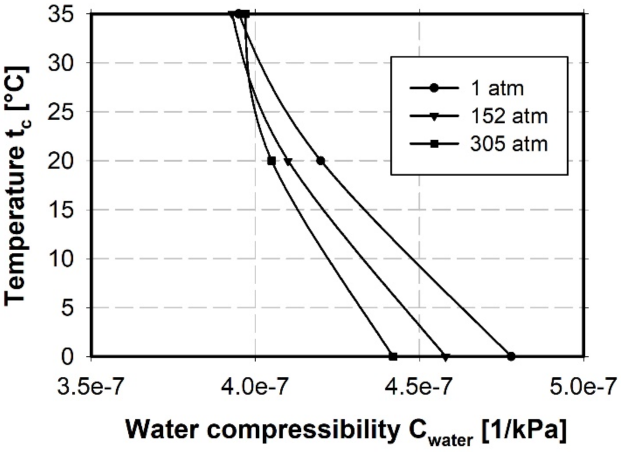

Fig. 4: Water compressibility (after Fredlund et al. 2012)

The compressibility of the water-air mixture can be derived from the compressibility of the individual constituents water and air, considering their proportion of the total volume (Fredlund 1976). In Figure 5 the volumetric composition of a quasi-saturated soil is shown.

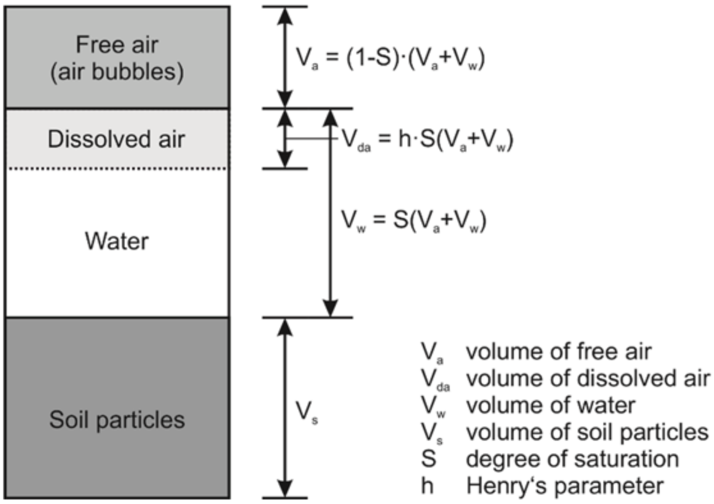

Fig. 5: Volumetric composition of a quasi-saturated soil (after Fredlund et al. 2012)

In the pore fluid, air occurs in the form of small entrapped air bubbles (free air) and dissolved air. For the derivation of the pore fluid compressibility, the free air and the dissolved air are treated as one volume. According to Equation 1 the volume change of the pore fluid with respect to a pore fluid pressure change has to be determined in order to derive the pore fluid compressibility. Considering the volumetric composition in Figure 5, the compressibility of a water-air mixture can be written as

$$C_{fluid} = -\frac{1}{V_w+V_a} \cdot \left(\frac{d(V_w - V_{da})}{dp_{water}} + \frac{d(V_a+V_{da})}{dp_{water}} \right) \tag{3}$$

V_w and V_a are the water volume and the air volume, respectively. According to Henry's law, the volume of the dissolved air in water V_{da} can be calculated with

$$V_{da} = h \cdot V_w \tag{4}$$

h is Henry's parameter and can be assumed for the relevant pore pressure range as h = 0.02 (Schuurman 1966).

In Equation 3 the pore water pressure p_{water} is assumed as the reference pressure, similar to the derivation of Fredlund (1976). According to Fredlund et al. (2012), Equation 3 can be rearranged to obtain

$$C_{fluid} = S \cdot C_{water} + (1 - S + h \cdot S) \cdot C_{air} \tag{5}$$

To obtain Equation 5 from Equation 3 it is assumed that the air pressure in the air bubble p_{air} is equal to the pore water pressure p_{water}, i.e. the suction s between water phase and air phase and the vapour pressure p_{vapour} are neglected. The acting pressures at the transition from air phase to water phase are summarized in Figure 6.

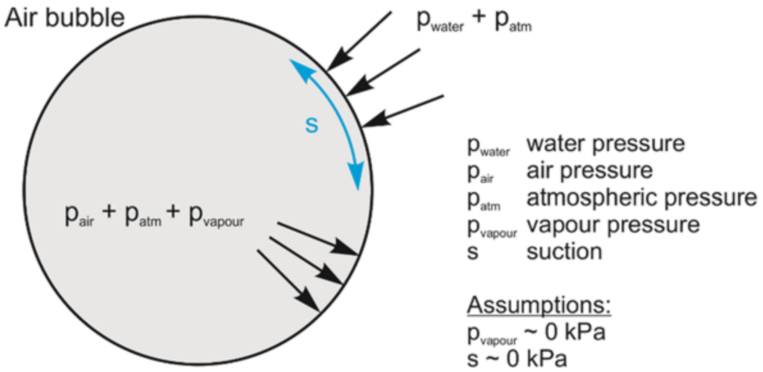

Fig. 6: Acting pressures at air bubble

According to Boutonnier (2007), the vapour pressure is $p_{vapour} \sim 2.3$ kPa and therefore negligible. Schuurman (1966) considered suction s in his derivation. In order to account for suction, the average radius of the air bubbles r_{air} has to be known. This complicates the determination of the pore fluid compressibility significantly. However, assuming that the diameter of the air bubbles is approximately equal to the diameter of the macro pores of the soil ($r_{air} \sim$ 5-30µm) and that the surface tension of the water-air interface is $T_s \sim 70$ mN/m, the suction s is calculated to be between 5 and 20 kPa (Boutonnier 2007). This is still in a negligible range if the pore water pressure p_{water} is not too small. Vaughan (2003) thoroughly discussed the decreasing influence of the suction s with increasing pore water pressure. Based on a simple calculation model, Vaughan (2003) showed that the maximum suction s is less than 30 kPa for a clayey silt at a degree of saturation S = 95%.

In Equation 5 the degree of saturation S is constant. However, assuming that air is an ideal gas, then according to Boyle's law, the product of total air pressure $p_{air} + p_{atm}$ and air volume V_a is constant, i.e. an increase in air pressure p_{air} leads to a decrease in air volume V_a.

$$(p_{air} + p_{atm}) \cdot V_a = \text{const.} \tag{6}$$

A change in the air volume leads simultaneously to a change in the degree of saturation. Furthermore, the changed water volume results in a changed volume of dissolved air according to Henry's law (see Equation 4). The latter mechanism also influences the degree of saturation . In addition to the pressure dependent air compressibility, the changing degree of saturation also leads to a pressure dependent pore fluid compressibility $C_{fluid} = f(p_{water})$.

Based on Boyle’s law and Henry’s law, the degree of saturation can be derived as a function of pore water pressure S = f(p_{water}). Applying Boyle’s law leads to

$$\frac{d}{dp_{air}} \cdot [(p_{air} + p_{atm}) \cdot (V_a + V_{da})] = 0 \tag{7}$$

In Equation 7, the free air and the dissolved air are treated as one volume $V_a + V_{da}$. Furthermore, the volumetric relationship from Figure 5 is considered in order to solve Equation 7.

$$V_a = \frac{(1-S)}{S} \cdot V_w \tag{8}$$

$$V_{da} = h \cdot V_w \tag{9}$$

Rearranging Equation 7 and considering Equation 8 and 9 leads to

$$\frac{1}{p_{air}+p_{atm}} dp_{air} = \frac{1}{S \cdot [1+S \cdot (h-1)]} dS \tag{10}$$

Integration of Equation 10 yields

$$\int \frac{1}{p_{air}+p_{atm}} dp_{air} = \int \frac{1}{S \cdot [1+S \cdot (h-1)]} dS \tag{11}$$

$$\ln(p_{air} + p_{atm}) = \ln\left(\frac{S}{1+S \cdot (h-1)}\right) + C$$

Substituting $p_{air} = p_{air,ref}$ and S = S_{ref} gives the integration constant C.

$$C = \ln\left[\frac{(p_{air,ref}+p_{atm}) \cdot \left(1+S_{ref} \cdot (h-1)\right)}{S_{ref}}\right] \tag{12}$$

Substituting Equation 12 in Equation 11 and solving for the degree of saturation *S* yields

$$S = \frac{1}{1-h+\frac{p_{air,ref}+p_{atm}}{p_{air}+p_{atm}} \cdot \frac{1+S_{ref} \cdot (h-1)}{S_{ref}}} \tag{13}$$

Assuming that S_{ref} is the degree of saturation at a pore air pressure $p_{air,ref} = 0$ kPa and considering $p_{air} = p_{water}$ according to the aforementioned assumptions, Equation 13 changes to

$$S_{(p_{water})} = \frac{1}{1-h+\frac{p_{atm}}{p_{water}+p_{atm}}\cdot\frac{1+S_{(pwater=0)}\cdot(h-1)}{S_{(pwater=0)}}} \tag{14}$$

The atmospheric pressure can be assumed as a constant with $p_{atm} = 100$ kPa.

Substituting Equation 14 in Equation 5 finally leads to a pressure dependent pore fluid compressibility $C_{fluid} = f(p_{water})$.

$$C_{fluid(p_{water})} = S_{(p_{water})} \cdot 4.1 \cdot 10^{-7} + \cdots \tag{15}$$

$$\cdots \left(1 - S_{(p_{water})} + h \cdot S_{(p_{water})}\right) \cdot \frac{1}{p_{water}+p_{atm}}$$

In Equation 15, the compressibility of pure water is $C_{water} \sim 4.1 \cdot 10^{-7}\,\mathrm{kPa}^{-1}$ according to Figure 4. Air compressibility is calculated according to Equation 2, considering $p_{air} = p_{water}$.

Equation 14 corresponds to the derivation of Boutonnier (2010). Other formulations for the relationship between degree of saturation S and pore water pressure p_{water} are available in literature (e.g. Bicalho et al. 2000, Montenegro et al. 2005). These formulations are similar, but differ in underlying assumptions. Bicalho et al. (2000) considered a difference between air pressure p_{air} and pore water pressure p_{water}.

$$p_{water} = \frac{[1+S_{ref}\cdot(h-1)]\cdot(p_{air,ref}+p_{atm})}{1+S\cdot(h-1)} - \cdots \tag{16}$$

$$\cdots \left(p_{air,ref} - p_{water,ref}\right) \cdot \left(\frac{1-S_{ref}}{1-S}\right)^{1/3}$$

Montenegro et al. (2005) derived the following formulation

$$S_{(p_{water})} = S_{ref} + \frac{p_{water}}{p_{air,ref}+p_{atm}+p_{water}} \cdot \left[1 + S_{ref} \cdot (h-1)\right] \tag{17}$$

Figure 7 shows a comparison of the presented formulations for calculating the pressure dependent degree of saturation. Furthermore the influence of the parameters $S_{(pwater=0)}$ and h on the pore fluid compressibility, considering Equation 14 and 15, is shown. According to Figure 7 a, the difference between the different relationships between pore water pressures and degree of saturation for quasi-saturated soils do not differ significantly.

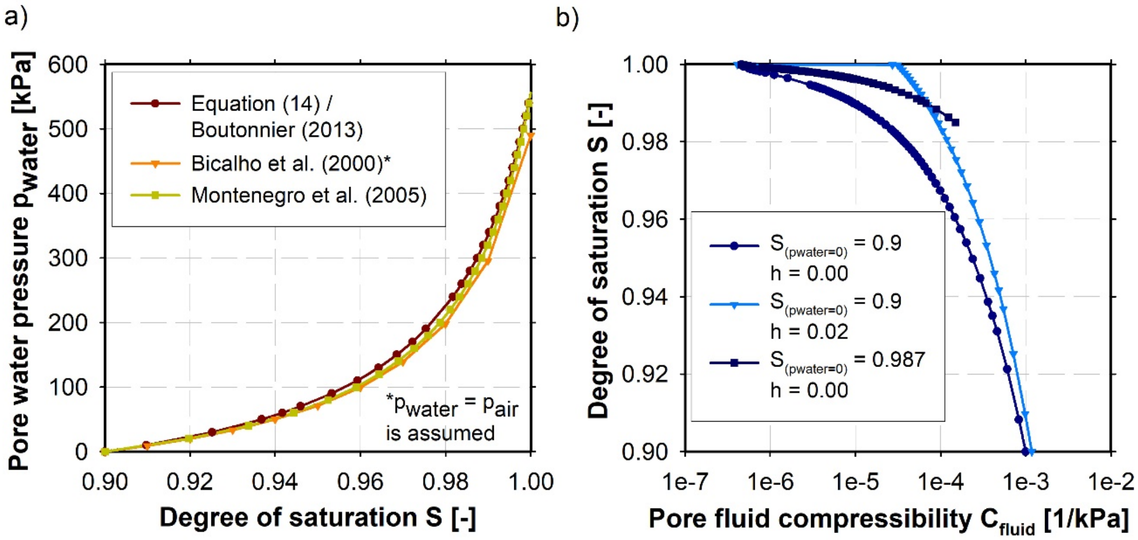

Fig. 7:a) Comparison of different formulations for S-p_{water}-curve ($S_{(pwater=0)} = 0.9$ & h = 0.02) and b) Influence of $S_{(pwater=0)}$ and h on pore fluid compressibility C_{fluid}

Figure 7 b shows the large influence of a small amount of entrapped air bubbles on the pore fluid compressibility. Various researchers (e.g. Black & Lee 1973, Fredlund 1976, Stelzer et al. 2014) already discussed this significant influence. A smaller reference degree of saturation $S_{(pwater=0)}$ leads to a faster increase of the pore fluid compressibility C_{fluid}. Assuming Henry's parameter h = 0.02 leads to a generally higher pore fluid compressibility C_{fluid} because of the additional compressibility due to the dissolving air into the water. Black & Lee (1973) and Li et al. (2001) showed, that a long time might be necessary to dissolve the entire air into the water. Time effects are not considered in the derivation of Equation 14, i.e. Henry's parameter should be assumed to h = 0.0 if not enough time for the dissolution process is available (Boutonnier 2010).

Based on Skempton's pore pressure coefficients (Skempton 1954) the significance of the increased pore fluid compressibility on the pore pressure development in soils can be clearly shown. Therefore, Skempton's pore pressure coefficients are summarized briefly in chapter 2.4.

2.3 Soil permeability in quasi-saturated stage

Numerous researcher (e.g. van Genuchten 1980) have extensively studied the permeability of water and air in unsaturated soils. In recent years, the permeability of quasi-saturated soils has also been investigated in laboratory tests (e.g. Faybishenko 1995, Sakaguchi et al. 2005, Bicalho et al. 2005, Marinas et al. 2013).

Similar to the formulation of van Genuchten (1980) for unsaturated soils, the decrease of quasi-saturated permeability k_{qs} with increasing air content (1-S) can be described by a power law with fitting parameters based on laboratory tests. Faybishenko (1995) developed a formulation (Equation 18), which was also used by other researchers (e.g. Sakaguchi et al. 2005, Marinas et al. 2013), to describe the quasi-saturated permeability.

$$k_{qs} = k_{qs,min} + \left(k_{sat} - k_{qs,min}\right) \cdot \left(1 - \frac{1-S}{S_{sat}-S_{qs,min}}\right)^{\bar{n}} \quad (18)$$

The quasi-saturated permeability k_{qs} depends on the saturated permeability k_{sat} and the minimum quasi-saturated permeability $k_{qs,min}$, which corresponds to the minimum degree of saturation in a quasi-saturated stage $S_{qs,min}$. S is the degree of saturation and S_{sat} is the maximum degree of saturation (usually $S_{sat} = 1.0$). $\bar{n}$ is a fitting parameter.

Bicalho et al. (2005) derived a similar formulation as Equation 18 to describe the quasi-saturated permeability.

Marinas et al. (2013) summarized the results of many laboratory tests on the quasi-saturated permeability and typical fitting functions as shown for example in Equation 18. The results are shown in Figure 8. The soil permeability decreases significantly with increasing air content, especially for fine grained soils. Faybishenko (1995) and Bicalho et al. (2005) performed tests at very high degrees of saturation (S = 90-100%) and confirmed the results, shown in Figure 8, for these high degrees of saturation. The range for the relative permeability of coarse grained soils shown in Figure 8 fits well with other formulations for the relative permeability of unsaturated soils, such as the cubic law $k_{rel} = S^3$ (Pinyol 2008).

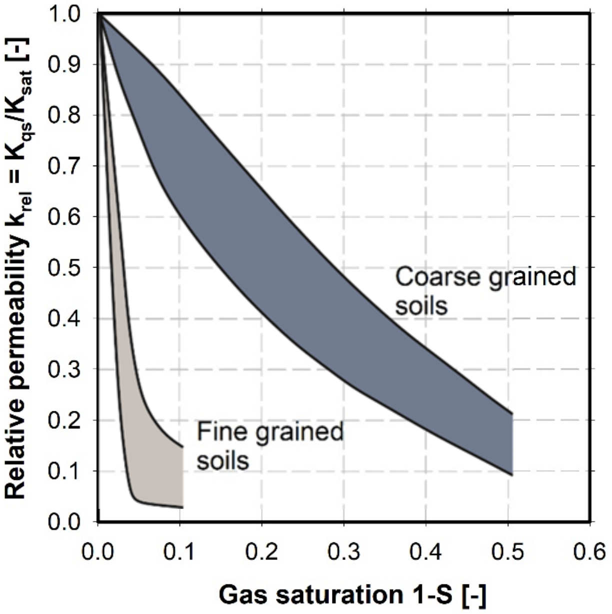

Fig. 8: Relative permeability for quasi-saturated soils (after Marinas et al. 2013)

2.4 Skempton's pore pressure coefficients considering quasi-saturated conditions

Assuming undrained behaviour, the generation of excess pore water pressure due to changes in total stresses can be studied by means of Skempton's pore pressure coefficients. According to Skempton (1954), the change in pore water pressure Δp_{water} can be calculated for triaxial compression stress paths with

$$\Delta p_{water} = B \cdot [\Delta\sigma_3 + A^* \cdot (\Delta\sigma_1 - \Delta\sigma_3)] \tag{19}$$

Equation 19 can be rearranged for general stress paths into the following form

$$\Delta p_{water} = B \cdot \left[\Delta p + \frac{3A-1}{3} \cdot \Delta q\right] \tag{20}$$

where A and B are Skempton's pore pressure coefficients. Δp is the change in total mean stress and Δq is the change in deviatoric stress. Assuming incompressible particles (Biot's coefficient $\alpha = 1$), Skempton's B-coefficient can be calculated as

$$B = \frac{1}{1+n \cdot \frac{K'}{K_w}} \tag{21}$$

Equation 21 shows that the B-coefficient depends mainly on the ratio between bulk modulus of the soil skeleton K' and the bulk modulus of the pore water K_w. The bulk modulus of the pore water is the reciprocal of the pore water compressibility C_{water}. n is the porosity. Assuming a stage of full saturation, the B-coefficient is approximately 1.0, as the bulk modulus of pure water $K_w \sim 2.4 \cdot 10^6$ kPa is significantly higher than the bulk modulus of the soil skeleton K'. Experimental data (Black & Lee 1973) show that the value of B-coefficient decreases rapidly with the degree of saturation due to the reduced bulk modulus of the water-air mixture in the pores $K_{fluid} = 1/C_{fluid}$ (see Figure 9).

According to Equation 20, the change in pore water pressure results from a change in total mean stress Δp and deviatoric stress Δq. The influence of changes in deviatoric stress on the pore water pressure depends strongly on the A-coefficient. The A-coefficient varies with stresses and strains (Skempton 1954) and depends, therefore, also on the compressibility of the different constituents (soil particles, water and air). The A-coefficient has to be determined in laboratory tests (undrained triaxial test) and is a result of the constitutive model used in numerical analyses. According to Skempton (1954), $A = 1/3$ if linear-elastic material is assumed. Consequently, under the aforementioned conditions, the excess pore water pressure depends only on the change in total mean stress Δp (see Equation 20). In case of an undrained oedometric loading the change in pore water pressure also depends only on the change in total mean stress independent of the A-coefficient, as this loading type results in no change of deviatoric stress. As can be seen from Equation 20, in this case only the B-coefficient is needed to determine the change in pore water pressure Δp_{water}.

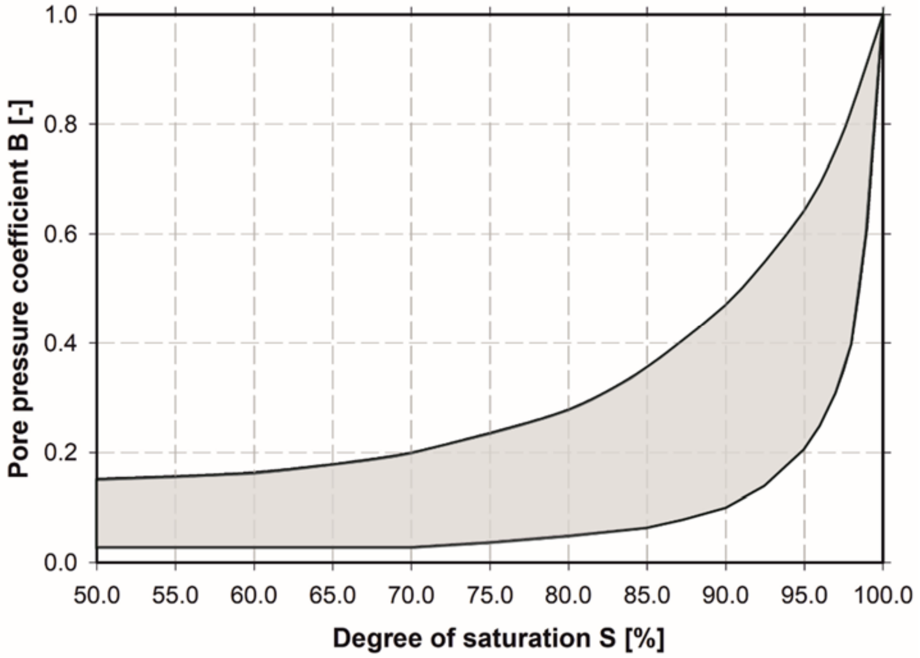

Fig. 9: Possible range for B-coefficient depending on degree of saturation for different soil types (after Black & Lee 1973)

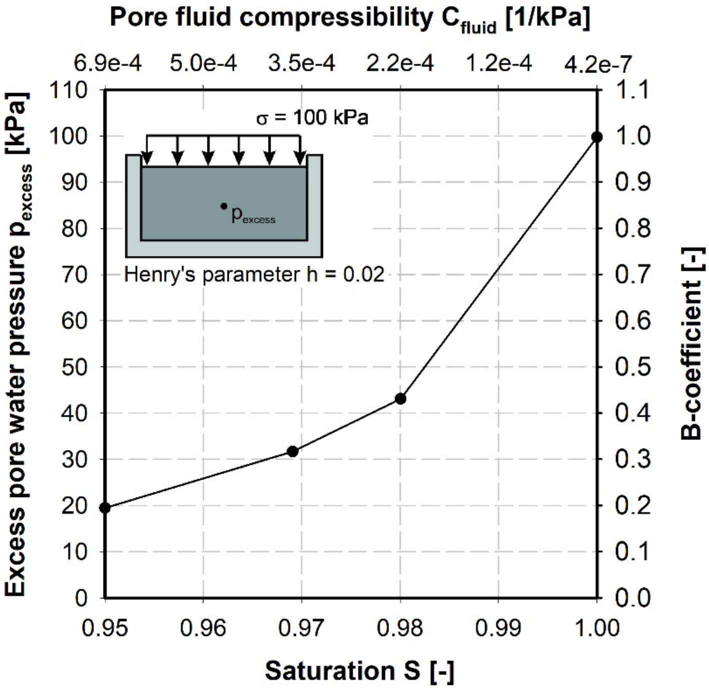

Fig. 10: Excess pore water pressure due to undrained oedometric loading as a function of degree of saturation

When considering Equations 14 and 15 for the determination of the B-coefficient, the significant influence of the degree of saturation on the excess pore water pressure development can be shown exemplarily with an undrained oedometric loading. Figure 10 shows the theoretical results of an oedometer test due to different degrees of saturation. To calculate the B-coefficient, a linear-elastic constitutive model was assumed with a Young's modulus $E = 20{,}000$ kPa, Poisson's ratio $\nu = 0.3$ and porosity $n = 0.3$. Starting with a degree of saturation $S = 1.0$, the excess pore water pressure immediately after a loading of $\sigma = 100$ kPa is equal to $p_{excess} = 100$ kPa. The B-coefficient is not exactly 1.0 (see Equation 21) due to the small pore fluid compressibility $C_{fluid} \sim 4.1 \cdot 10^{-7}\,\text{kPa}^{-1}$. With increasing air content, the pore fluid compressibility is increasing and the B-coefficient is decreasing. The increasing pore fluid compressibility leads to decreasing excess pore water pressures i.e. the additional load is transferred to both, the pore fluid and the soil skeleton. As shown in Figure 10, even an air content of 5% is enough to reduce the excess pore water pressure by 80% to $p_{excess} \sim 20$ kPa.

The increased pore fluid compressibility influences the pore water pressure not only in the case of a mechanical loading but also in the case of a hydraulic loading. This can be shown with a simple 1D-model, numerically and analytically. For example, the water level above a 10 m high soil column is increased from 1.0 to 6.0 m above ground level (see Figure 11). For the sake of simplicity, again a linear-elastic constitutive model is used. The material parameters are E = 20,000 kPa and Poisson's ratio $\nu = 0.3$. Undrained conditions are considered for the water level increase.

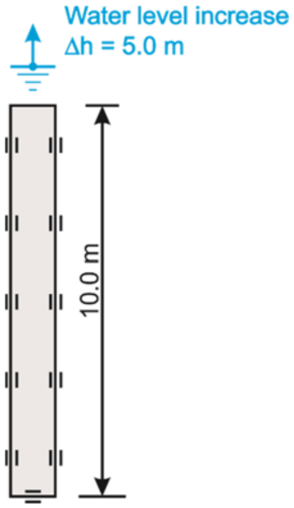

Fig. 11: 1D-model to determine excess pore water pressure due to a water level increase

The total vertical stress at the ground surface $\Delta\sigma^{total}$ is increased due to the water level change Δh.

$$\Delta\sigma^{total} = \Delta h \cdot \gamma_w = 5.0 \cdot 10.0 = 50.0\ kPa \tag{22}$$

According to Skempton's theory (Skempton 1954), the change of pore water pressure due to a change of total stresses for a 1D-loading can be determined with Skempton's B-coefficient. In a first step a nearly incompressible pore fluid is assumed and therefore B ~ 1.0. The change of total stress $\Delta\sigma^{total}$ in the soil column leads to a pore water pressure change Δp_{water} in the entire soil column.

$$\Delta p_{water} = B^{oed} \cdot \Delta\sigma^{total} = 1.0 \cdot 50.0 = 50.0\ kPa \tag{23}$$

The excess pore water pressure p_{excess} is the difference between pore water pressure p_{water} and hydrostatic pore water pressure $p_{hydrostatic}$. Assuming hydrostatic pore water conditions were in place before the water level increase and assuming undrained loading conditions, the excess pore water pressure p_{excess} is constant with depth.

$$p_{excess} = \Delta p_{water} - \Delta p_{hydrostatic} \tag{24}$$

$$p_{excess} = 50.0 - 50.0 = 0\ kPa$$

Equation 24 confirms the general assumption, that water level changes above the horizontal ground surface lead to no excess pore water pressures. However, in a second step, 5% air content is assumed, and the B-coefficient decreases down to $B^{oed} = 0.195$ (see Figure 10). In this case the pore water pressure change due to a water level increase of h = 5.0 m is

$$\Delta p_{water} = B^{oed} \cdot \Delta\sigma^{total} = 0.195 \cdot 50.0 = 9.75\ kPa \tag{25}$$

Furthermore the excess pore water pressure is

$$p_{excess} = \Delta p_{water} - \Delta p_{hydrostatic} \tag{26}$$

$$p_{excess} = 9.75 - 50.0 = -40.25\ kPa$$

As shown by Equation 26, a water level increase above the ground surface of a quasi-saturated soil leads to negative excess pore water pressures. The magnitude of the excess pore water pressure depends on the degree of saturation, and as a consequence, on the derived B-coefficient. In this simple example a constant B-coefficient is assumed. However, as shown by Equation 15, the pore fluid compressibility increases with pore water pressure. Therefore, the B-coefficient also would increase with depth and the excess pore water pressure p_{excess} would no longer be a constant.

Stelzer et al. (2014) conducted similar studies and concluded that the excess pore water pressure in case of a hydraulic loading can be calculated with

$$p_{ecxess} = (B^{oed} - 1) \cdot \Delta\sigma^{total} \tag{27}$$

Equation 27 results in the same calculated excess pore water pressure as Equation 26.

Figure 12 shows the results of an undrained FEA of a water level increase, according to the model in Figure 11. The calculated total stresses and pore water pressures are consistent with the analytical solution and confirm that water level changes above a horizontal ground surface may lead to excess pore water pressures in case of quasi-saturated soils.

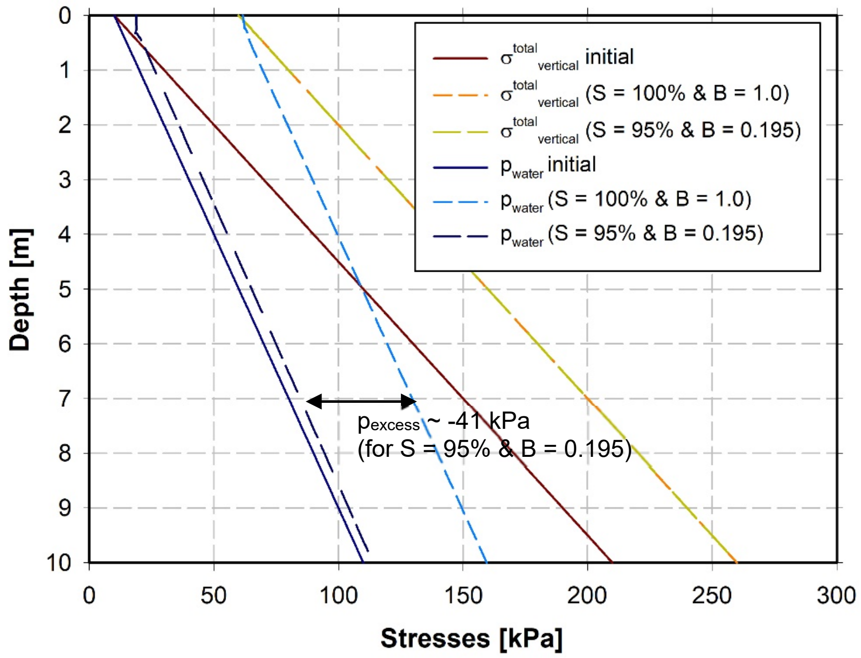

Fig. 12: FEA results of undrained water level increase

2.5 Modelling quasi-saturated soils

In the field of soil mechanics, poroelasticity deals with the flow of the pore fluid and the deformation of porous material under (nearly) saturated conditions. An increasing amount of air leads to a continuous air phase (see chapter 2.1). Accordingly, the pore air pressure differs from the pore water pressure and is equal to the atmospheric pressure. The behaviour of the pore fluid and the porous medium in this stage of saturation are the main objective of unsaturated soil mechanics.

Poroelasticity was first presented by Terzaghi (1925). For practical reasons, Terzaghi (1925) neglected the compressibility of the pore fluid and the soil particles. Biot (1941) considered these compressibilities in his general theory of consolidation and showed that Terzaghi's theory is a special case of his own theory. Since then, a lot of effort has been put into the development of a generally accepted theory of linear poroelasticity (e.g. Wang 2000, Verruijt 2015).

Starting in the 1930's, large efforts have been made in the last decades to investigate the behaviour of unsaturated soils. Based on Darcy's law and continuity equation, Richards (1931) derived a differential equation to describe the flow in an unsaturated porous medium. Richards (1931) already considered a change of the moisture content with respect to the capillary potential (suction) in the porous medium. However, the coupling of the flow problem with equations of equilibrium and a constitutive model for the soil material is not considered in Richards equation. Further developments led to fully coupled formulations for unsaturated soils. To avoid additional state variables accounting for the gas phase under unsaturated conditions, a relationship between degree of saturation and pore water pressure, referred to as water retention curve (WRC), is often considered. This approach enables the application of Biot's theory of consolidation for unsaturated soils, considering additional terms (Montenegro 2016). Additionally to hydro-mechanical coupling, thermal and chemical effects are often considered. During the course of recent formulation developments, the flow of air and water in the soil are coupled with high-quality constitutive models considering expansive behaviour, microstructural effects, rate effects and much more.

Stelzer et al. (2014) showed clearly that the modelling of quasi-saturated soils can be based on both classical consolidation theory and unsaturated soil mechanics. Based on consolidation theory, the compressibility of the pore fluid is reduced according to the amount of air in the pore fluid. In the case of linear poroelasticity, the soil behaviour is assumed to be linear-elastic. In contrast to that, according to unsaturated soil mechanics, it is possible to consider the effect of air bubbles in the pore fluid by adapting the water retention curve (WRC) in the range of quasi-saturation ($S \sim 85\text{-}100\%$), i.e. a degree of saturation smaller than one is also possible for positive pore fluid pressures. However, in this case the used compressibility of the pore fluid in the continuity equation is equivalent to the compressibility of pure water and therefore, a constant value.

In the past, researchers applied different approaches to model quasi-saturated soils. For instance Wheeler (1986) presented a theoretical model to describe the hydro-mechanical behaviour and failure definition of quasi-saturated soils. However, Wheeler (1986) investigated exclusively the behaviour of "gassy soils" with air bubbles considerable larger than the soil particles. He stressed the significant difference between the behaviour of quasi-saturated soils with air bubbles smaller than the voids and soils with air bubbles larger than the soil particles. Boutonnier (2010) presented continuity equations for the four different stages of saturation based on mass conservation and Darcy's law. Furthermore, the Cam Clay model is applied as constitutive model in the formulation of Boutonnier (2010). For the quasi-saturated stage in the suction regime a WRC is considered. However, for the quasi-saturated stage in the positive pressure regime, classical consolidation theory with an increased pore fluid compressibility is applied by Boutonnier (2010). However, in the formulation according to Boutonnier (2010) the pore fluid compressibility depends on the pore water pressure. Lai et al. (2015) developed a rigorous theoretical framework, which allows a description of coupled problems in poromechanics, considering all stages of saturation simultaneously.

As the focus of this thesis is on the behaviour of a slow moving landslide in combination with water level changes in a water storage basin, the modelling of quasi-saturated soils is not investigated in detail here as this has already been done by others, e.g. by Lai et al. (2015). The aim of this thesis is to obtain a simple and practically applicable formulation of the behaviour of quasi-saturated soils. Such an approach was also chosen by Stelzer et al. (2014) (see also Montenegro et al. 2015, Montenegro 2016). In the following, the consideration of the quasi-saturated stage is briefly discussed in the frameworks of poroelasticity and unsaturated soil mechanics (with a WRC). The following discussions are again limited to the quasi-saturated stage in the positive pressure regime.

Based on Song (1990), Galavi (2010) showed that the continuity equation for unsaturated soils considering Darcy's law and incompressible grains (Biot's coefficient $\alpha = 1.0$) is obtained as

$$S \cdot \frac{\partial \varepsilon_{vol}}{\partial t} - n \cdot \left(S \cdot C_{fluid} - \frac{\partial S}{\partial p_{fluid}} \right) \cdot \frac{\partial p_{fluid}}{\partial t} + \cdots \tag{28}$$

$$\cdots + \nabla^T \cdot \frac{k}{\rho_f \cdot g} \cdot \nabla \cdot p_{fluid} = 0$$

Equation 28 is very similar to the continuity equation according to poroelasticity. However, the main difference between linear poroelasticity and unsaturated soil mechanics can be found in the storage term of the continuity equation (Equation 28). Linear poroelasticity (assuming incompressible grains) considers a storage potential due to changes in the porosity because of changes in effective stresses $\partial \varepsilon_{vol}/\partial t$ and changes in the pore fluid density $n \cdot S \cdot C_{fluid} \cdot \partial p_{fluid}/\partial t$. The degree of saturation is assumed in poroelasticity as $S = 1.0$. Consequently, the term $\partial S/\partial p_{fluid} \cdot \partial p_{fluid}/\partial t$ in Equation 28 is neglected. Therefore, in the case of linear poroelasticity, the quasi-saturated stage can be considered by an increased pore fluid compressibility C_{fluid} as discussed in chapter 2.2.

In addition to the aforementioned storage potentials, a change in the degree of saturation $\partial S/\partial p_{fluid} \cdot \partial p_{fluid}/\partial t$ (water retention curve) is considered in the storage term of unsaturated soils, as shown in Equation 28. In the formulation according to unsaturated soil mechanics, the influence of quasi-saturation is considered with the WRC instead of an increased pore fluid compressibility. For this purpose, the WRC is extended to the positive pore water pressure range as shown in Equation 14. In the case of unsaturated soil mechanics, the pore fluid compressibility is constant and equal to the compressibility of pure water. Therefore, the WRC is especially helpful for transient analyses because it removes the need for assumptions of an average pore fluid compressibility. Furthermore, the use of the finite element software PLAXIS 2D 2016 (Brinkgreve et al. 2016) allows the implementation of a user defined WRC (also for the positive pore water pressure range). Therefore, additional implementation work can be avoided (Stelzer et al. 2014, Montenegro 2016). Due to these reasons, in the following, the consideration of a WRC for the quasi-saturated stage is preferred, as compared to an increased pore fluid compressibility, as shown in Equation 28.

2.6 Model test for quasi-saturated soils

In the previous chapters, the characteristics of quasi-saturated soils and their consideration within theoretical approaches have been discussed. In this chapter, the pore water pressure development in quasi-saturated soils is investigated by means of an experimental model test (Widmoser 2016). Subsequently, the test results are back-calculated with PLAXIS 2D 2016, considering a quasi-saturated stage of the soil. The main objective of these model tests is the qualitative illustration of the pore water pressure development in quasi-saturated soils rather than the determination of quantitative results. Similar tests were also performed at the Bundesanstalt für Wasserbau, Germany (Montenegro 2005, Ewers 2016).

2.6.1 Model test setup

The model test was developed to simulate water level changes with different velocities above the ground surface of a quasi-saturated soil column. Figure 13 and Figure 14 show a sketch and pictures of the model test.

The test consists of a steel cylinder with a height of 50 cm and a diameter of 35 cm, a lifting device to change the water level and measurement equipment. The steel cylinder is filled with 35 cm of quasi-saturated soil and 15 cm of water. At the top, the steel cylinder is closed in a waterproof manner with a Plexiglas cap. Two connections are mounted at the cap for the saturation of the soil and for the connection to the lifting device, as well as acting as vent valves. At the bottom of the steel cylinder, 5 outlets are mounted to enable a water flow through the soil sample from the top to the bottom. To simulate the water level changes, a tube filled with water and connected to the steel cylinder is mounted on a lifting device. By lifting and lowering the spindle of the lifting device at varying velocities, the water pressure at the ground surface can be changed with different velocities. The pore water pressure is measured at four different depths: three measurement planes are situated within the soil, and one is situated within the water for reference measurements. HBM Digibar II are used as pore water pressure gauges. They are connected to the steel cylinder by water filled tubes.

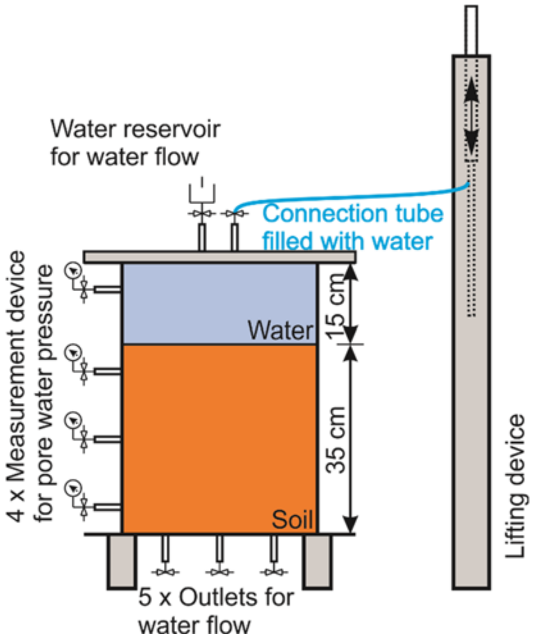

Fig. 13: Drawing of test setup for quasi-saturated soils (after Widmoser 2016)

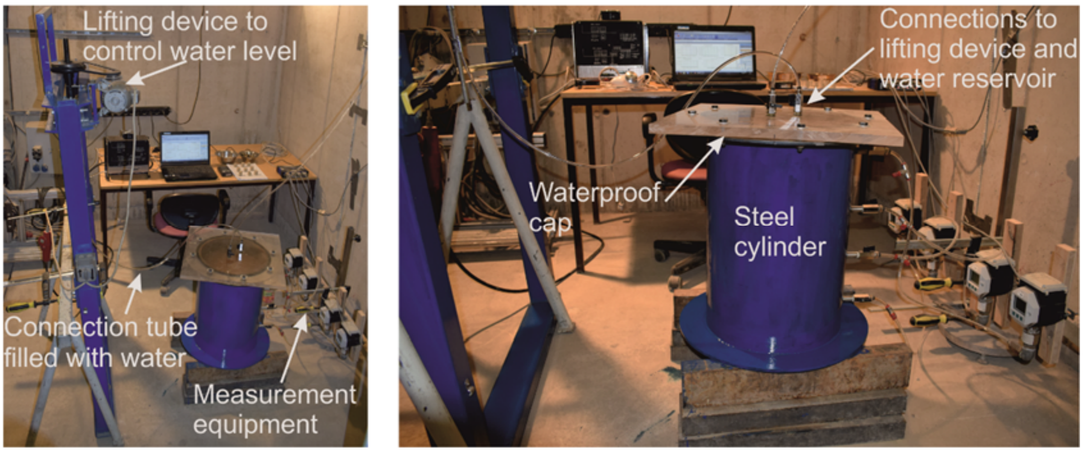

Fig. 14: Picture of test setup for quasi-saturated soils

2.6.2 Test materials

Two different materials are used for the model test – a sandy, clayey silt and a sand. These materials are similar to the typical material found at the site of the later presented slow moving landslide. Furthermore, the two materials cover a wide range of soil permeability, which is interesting from the experimental perspective. Figure 15 shows the grain size distribution of the materials used.

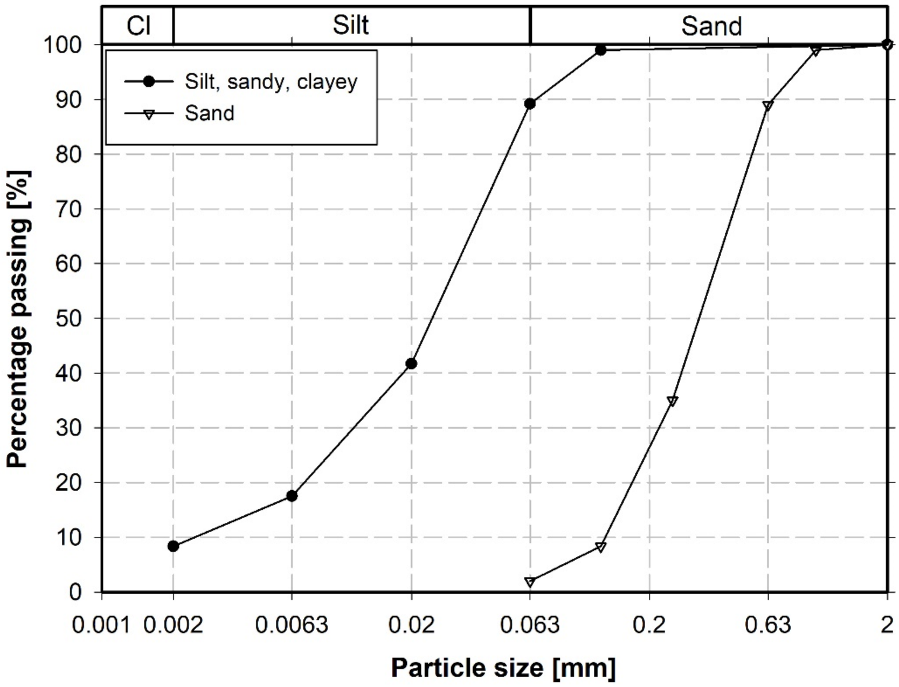

Fig. 15: Grain size distribution of test material

The particle density of the silt is $\rho_{s,Silt} = 2.71$ g/cm³. The stiffness and the permeability of the silt were determined by laboratory tests, which were conducted with the same soil density as in the model test ($\rho_{dry,Silt} = 1.55$ g/cm³). The oedometer stiffness of the silt is approximately $E_{oed} \sim 20{,}000$ kPa under conditions (stress state and density), similar to the model test. The permeability was tested in a permeability cell. The cell pressure was 50 kPa and the pressure head difference was 37 kPa. After a test period of 5 days, a constant value for the permeability of $k_{Silt} = 1.2 \cdot 10^{-7}$ m/sec was reached.

For the sand, the same material parameters as for the silt were determined. The particle density is $\rho_{s,Sand} = 2.72$ g/cm³. The parameters (stiffness and permeability) were tested again under the same conditions as in the model test ($\rho_{dry,Sand} = 1.65$ g/cm³). The oedometer stiffness is approximately $E_{oed} \sim 40{,}000$ kPa. The saturated permeability of the sand was determined to be $k_{Sand} = 1.15 \cdot 10^{-5}$ m/sec.

The following table shows a summary of the material parameters determined in the laboratory.

Tab. 1: Material parameters from laboratory tests for model test

Parameter	Unit	Silt, sandy, clayey	Sand
ρ_s	g/cm³	2.71	2.72
ρ_{dry}	g/cm³	1.55[1]	1.65
E_{oed}	kPa	20,000	40,000
k_{sat}	m/sec	$1.2 \cdot 10^{-7}$	$1.15 \cdot 10^{-5}$

[1] corresponds to Proctor density $\rho_{proctor}$

2.6.3 Test procedure

The soil body was installed in layers in the steel cylinder with a dry density as shown in Table 1, which corresponds approximately to the dry Proctor density of the material (silt). The water content during the installation was slightly higher than the optimum water content (from the Proctor test) in case of the silt (w = 26% and S = 94%). The sand was installed with a water content of w = 20% (S = 79%). The compaction was performed manually as shown in Figure 16.

Fig. 16: Tools for material compaction

After the installation of the soil material, the steel cylinder was closed in a waterproof manner with the Plexiglas cap and the remaining space in the cylinder was filled with tap water through one of the connections. Then the steel cylinder was connected with the water reservoir, which was installed 3.0 m above the steel cylinder. Simultaneously, the outlets at the bottom of the steel cylinder were opened. This led to a water flow through the soil from the top to the bottom to entrap as much air bubbles as possible in the pore water (Faybishenko 1995). The water inflow and the water outflow were continuously measured to record the increase in water content in the soil body. When the inflow and the outflow reached an approximately constant value, the connection to the water reservoir and the outlets were closed. Afterwards, the steel cylinder was connected with a tube filled with water to the lifting device. Before the start of the tests, the water level was kept at a constant level to reach an equilibrium state (hydrostatic) in the measured pore water pressures.

Once a hydrostatic pore water pressure distribution was reached in the steel cylinder, the tests were started. To change the water level, the water filled tube which was connected to the steel cylinder was mounted at the spindle of the lifting device and the spindle was moved upwards and downwards with a predetermined velocity. The maximum change in height was approximately 10 cm. The tests were conducted with different velocities and different patterns of water level changes. The velocities were varied in the ranges of $v_{Silt} = 2{,}000\text{-}50{,}000 \cdot k_{Silt}$ and $v_{Sand} = 30\text{-}400 \cdot k_{Sand}$ for the silt and the sand, respectively. The following water level changes were simulated

- Up – Down
- Down – Up
- Up – Consolidation
- Down – Consolidation
- Combinations of the aforementioned

Once the tests were completed, soil samples were taken from the steel cylinder to determine the density and the degree of saturation post-test. This was done because during the compaction process (pre-test) it was recognized that water was squeezed out of the soil. Furthermore, the compaction of the last layers proved extremely difficult. Thus, it has to be assumed that the soil density is not equal to the predetermined density. For the sampling, small brass cylinders with a known inside volume and mass were manufactured. These small cylinders were pushed into the soil and carved out (with the sample within) with great care. The parameters (density and degree of saturation) were subsequently determined from the weighing of the cylinder and the sample. This procedure worked very well for the silt. Although the silt was installed in the steel cylinder with a degree of saturation $S = 94\%$, the samples taken after the tests showed a degree of saturation of only $S = 90\%$. This shows that during the compaction process a considerable amount of water was squeezed out of the soil. The dry density was similar to the one before the tests ($\rho_{dry,Silt} = 1.55$ g/cm^3). However, for the sand, the scattering of the results was too high due to problems during the sampling. Therefore, no reproducible values from the samples could be determined for the sand. Based on the measurement of the inflow and the outflow during the saturation phase, the degree of saturation of the sand should have been higher than 90%.

2.6.4 Test results

In the following, the evaluation of the tests is always carried out in the same manner: the diagrams show the pressure head above the top of the soil body, as measured by the four pore water pressure gauges. Figure 17 shows the definition of each plotted pore water pressure label in the graph and an example for the evaluation of a test with a decreasing water level and a subsequent consolidation phase. A hydrostatic pore water pressure distribution in the steel cylinder is achieved when the pore water pressure gauges show the same values. Values higher than the water level indicate positive excess pore water pressures, whereas values below the water level mean a negative excess pore water pressure.

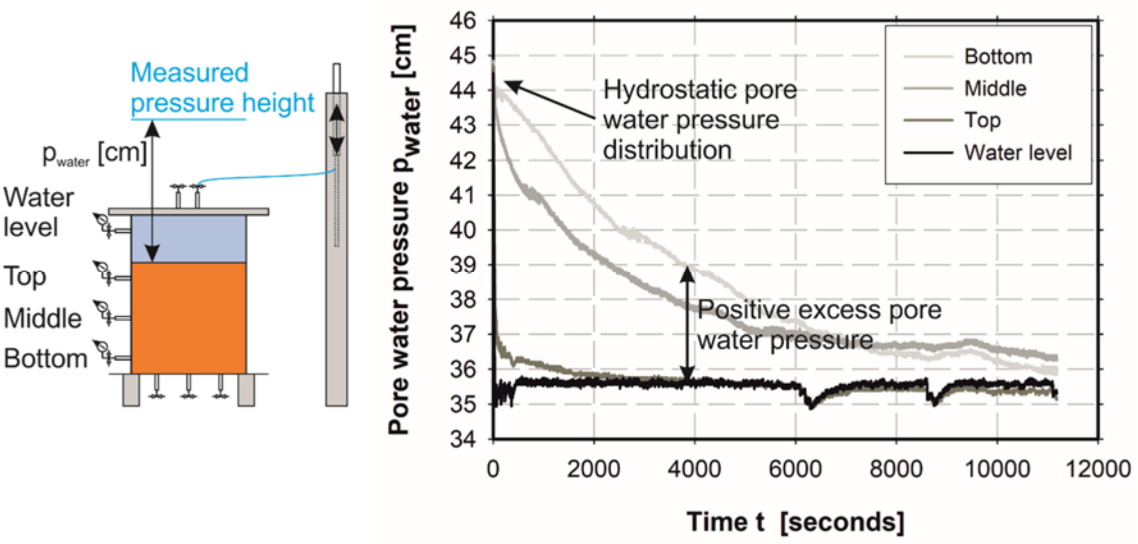

Fig. 17: Example for test evaluation

Figure 18 and Figure 19 present the results for two tests with silt. During these tests the water level was decreased and increased three (four) times. The tests were conducted with different velocities for the water level change ($v \sim 2{,}400 \cdot k_{Silt}$ and $v \sim 28{,}000 \cdot k_{Silt}$). The graphs show a clear difference between the measured pressure heights in the soil body and the water pressure above the soil body, i.e. positive and negative excess pore water pressures are produced due to the quasi-saturated stage. These test results confirm the theoretical considerations in chapter 2.4, where the development of excess pore water pressures due to water level changes above the ground surface of quasi-saturated soils was discussed. The magnitude of the excess pore water pressures depends strongly on the velocity of the water level changes, e.g. the excess pore water pressure in the middle of the soil layer is larger for fast ($v \sim 28{,}000 \cdot k_{Silt}$) changes (Figure 19) than for the slow ($v \sim 2{,}400 \cdot k_{Silt}$) water level changes (Figure 18).

Furthermore, the excess pore water pressure increases with depth throughout the soil column, i.e. the pore water pressure gauge “Bottom” shows the highest excess pore water pressures. With an increasing number of water level changes, the mean value of the pressure heights decreases towards a constant level. When this level is reached, the absolute magnitude of the excess pore water pressure no longer changes (see Figure 18).

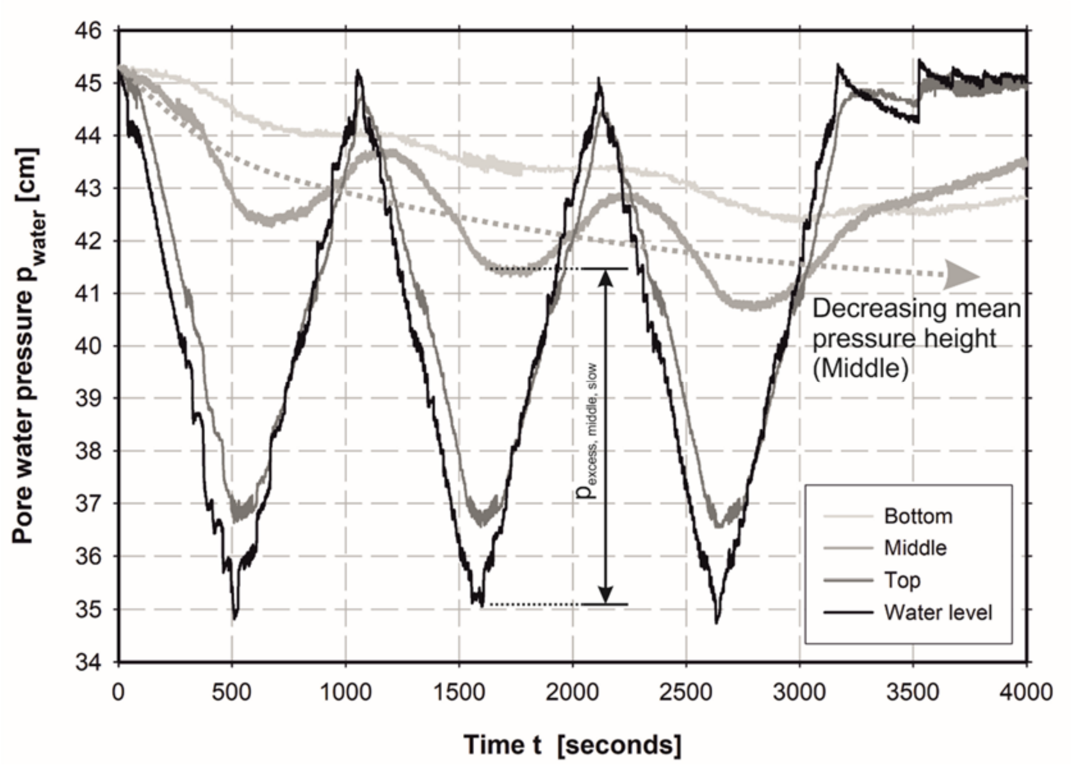

Fig. 18: Test results for silt: three cycles of water level decrease and increase ($v \sim 2{,}400 \cdot k_{Silt}$)

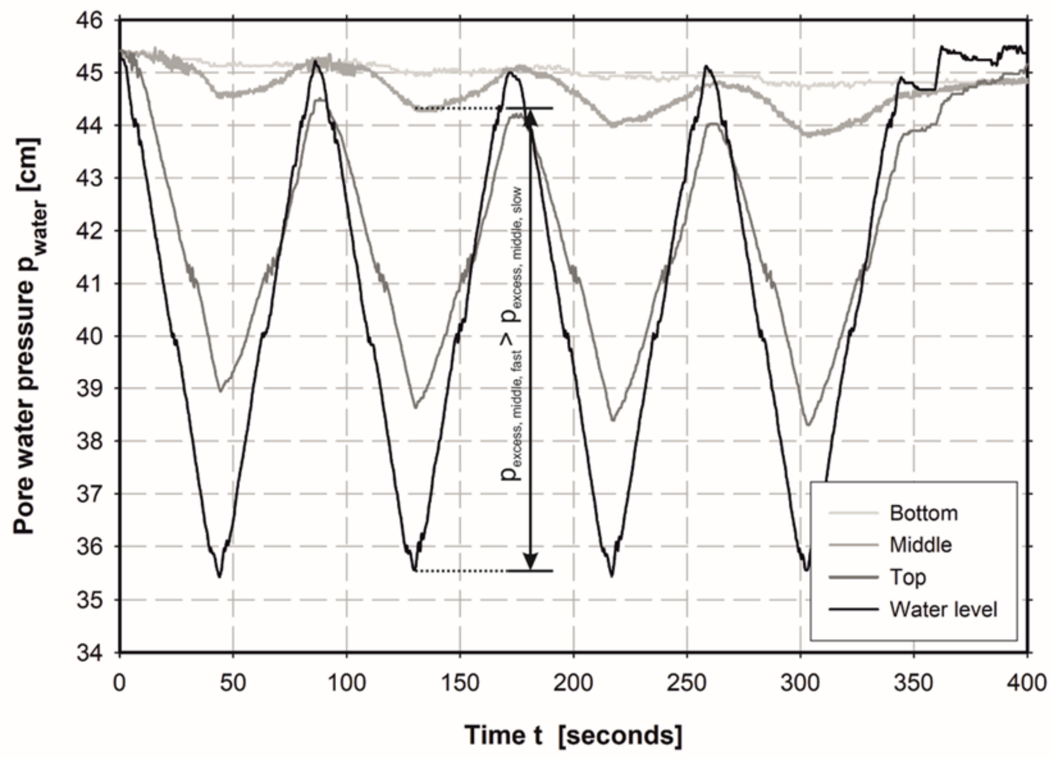

Fig. 19: Test results for silt: four cycles of water level decrease and increase ($v \sim 28{,}000 \cdot k_{Silt}$)

The results for a test with a decreasing water level and a subsequent consolidation phase with the silt are visualized in Figure 20. The high velocity of the water level change ($v \sim 35{,}000 \cdot k_{Silt}$) leads to significant excess pore water pressures, which dissipate during the consolidation phase. As water flow is only permitted in the upwards direction in this test, consolidation is finished much faster in the upper part than in the lower part of the soil column.

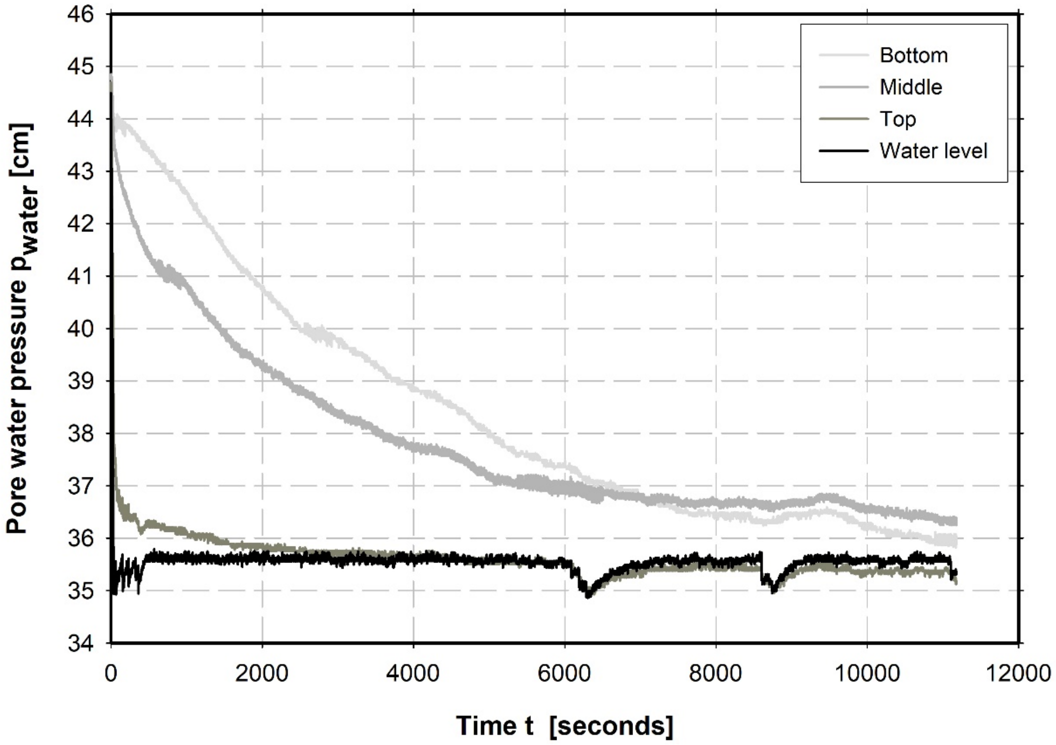

Fig. 20: Test results for silt: water level lowering and subsequent consolidation phase ($v \sim 35{,}000 \cdot k_{Silt}$)

Similar tests as shown above (Figure 18 to Figure 20) were also conducted with the sandy material (Figure 21 to Figure 23). The absolute velocity of the water level changes was similar, regardless of the used material (silt or sand). However, the ratio between velocity of water level change *v* and soil permeability *k* is completely different for silt and sand ($v = 2{,}400 \cdot k_{Silt} \sim 30 \cdot k_{Sand}$). In the case of the silt (Figure 18), this velocity leads to significant excess pore water pressures, whereas no excess pore water pressures are observed during the model test with sand (Figure 21). This comparison shows that the magnitude of excess pore water pressures does not depend solely on the absolute value of the velocity of the water level changes but on the ratio between water level change velocity and soil permeability. A high velocity ($v \sim 370 \cdot k_{Sand}$) also leads to small excess pore water pressures in model tests with the sandy material (see Figure 22 and Figure 23).

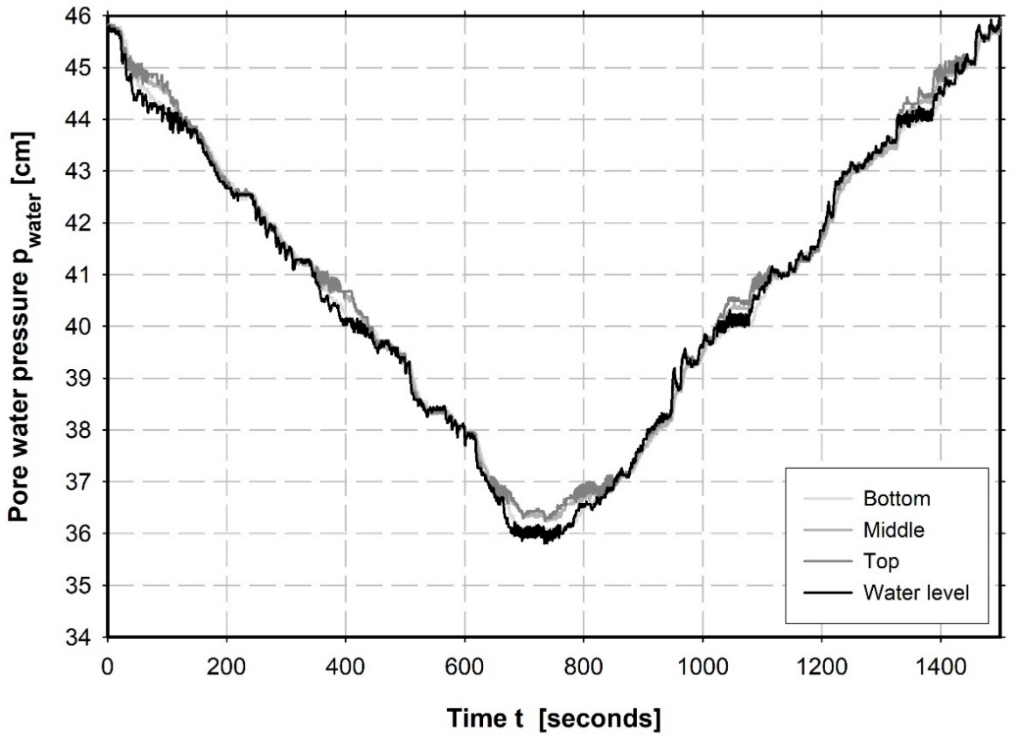

Fig. 21: Test results for sand: water level decrease and increase (v ~ 30·k_{Sand})

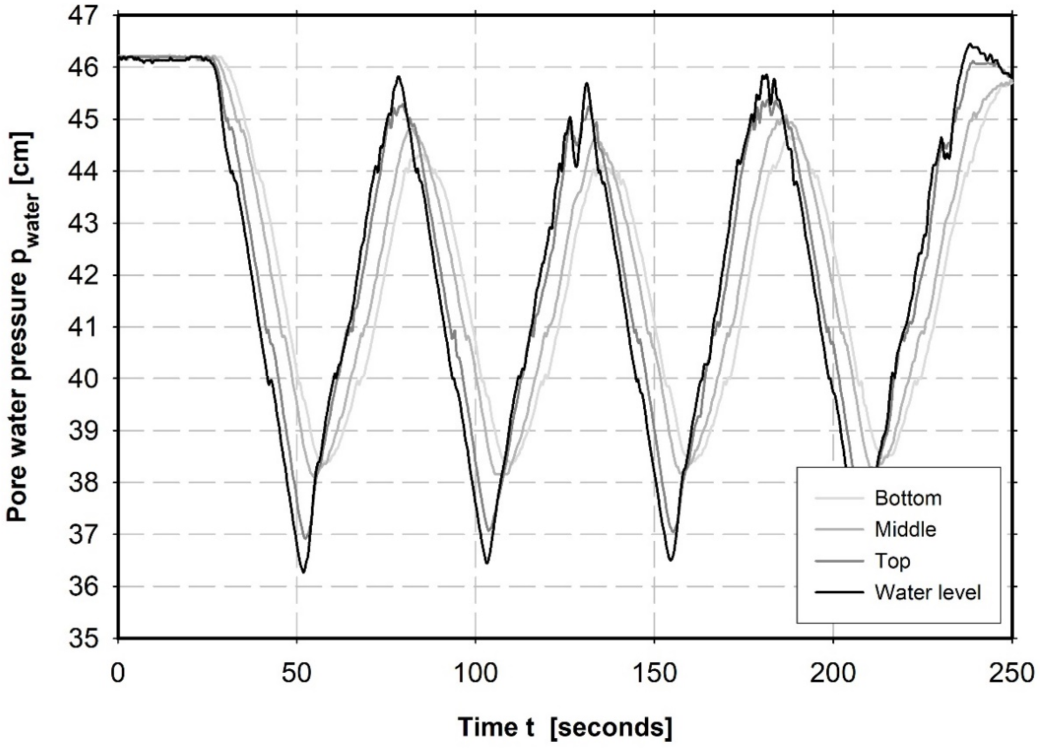

Fig. 22: Test results for sand: four cycles of water level decrease and increase (v ~ 370·k_{Sand})

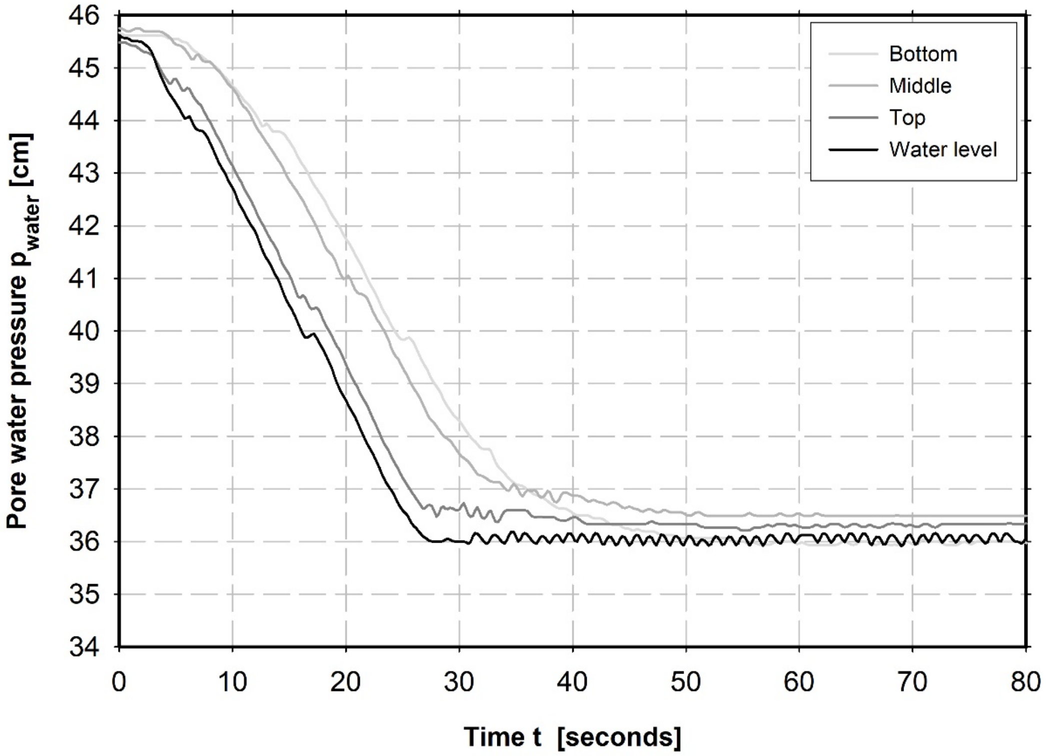

Fig. 23: Test results for sand: water level lowering and subsequent consolidation phase (v ~ 370·k_{Sand})

2.6.5 Back-calculation of test results

Numerical back-calculations (finite element analyses) of the model test are presented in this chapter. The main objective of these finite element analyses is the validation of the theoretical considerations in chapter 2.5. As the stress increments are small, a simple Mohr-Coulomb model is used as constitutive model. Due to the small pore water pressure increments in the model test, a constant pore fluid compressibility, corresponding to the measured degree of saturation, could have been used for the calculations. However, in the presented analyses a water retention curve (WRC) for the quasi-saturated stage was used to test the PLAXIS 2D 2016 feature that allows the input of a user-defined WRC (Stelzer et al. 2014). The material parameters used for the calculations are summarized in Table 2. The unit weight γ, the void ratio n and the stiffness of the soil E_{oed} were determined in laboratory tests. Strength parameters were assumed as they have no influence on the investigated pore water pressures. The reduced quasi-saturated permeability k_{qs} was calculated with the cubic law (Equation 29), based on the saturated permeability k_{sat} and the degree of saturation S.

$$k_{qs} = S^3 \cdot k_{sat} \tag{29}$$

Tab. 2: Material parameters for back-calculation of model test

Parameter	**Unit**	**Silt, sandy, clayey**	**Sand**
Model		Mohr-Coulomb	Mohr-Coulomb
γ_{unsat}	kN/m³	18.6	19.3
γ_{sat}	kN/m³	19.8	20.2
E_{oed}	kPa	20,000	40,000
ν	-	0.3	0.3
c'	kPa	5	0
φ'	°	20	37
ψ'	°	0	0
n	-	0.43	0.41
k_{qs}	m/sec	$8.8 \cdot 10^{-8}$	$1.0 \cdot 10^{-5}$
$S_{(pwater=0)}$	%	90	95

The reference degree of saturation of the silt was assumed according to the results of the sampling after the model test (described in chapter 2.6.3). For the sand, all procedures (measurement of inflow and outflow during saturation, sampling after model test) lead to inaccurate results. Therefore, the degree of saturation for the sand was back-calculated based on one model test (fast water level increase with subsequent consolidation phase). This back-calculation resulted in a degree of saturation of S = 95% which was used for all comparative numerical analyses.

The calculations were performed with an axisymmetric model as a fully coupled flow-deformation analysis. At the top of the model the transient hydraulic boundary conditions were simulated according to the model test.

Figure 24 and Figure 25 show exemplarily the comparison of measurement results and numerical results for tests with silt. For this comparison, the absolute pore water pressure is plotted instead of the pressure height above the top of the soil column. In general, the numerical results correlate well with the experimental results. However, small discrepancies are visible, especially for the pore water pressures at the bottom of the soil column. As a higher degree of compaction at the bottom of the soil column and the effects of small strains both influence the soil stiffness at the bottom, this changed stiffness might provide a possible explanation for the differences between measurement and calculation results. However, it has to be mentioned that the magnitude of these differences is almost within the accuracy of the measurement devices, indicating that these differences are likely to negligible.

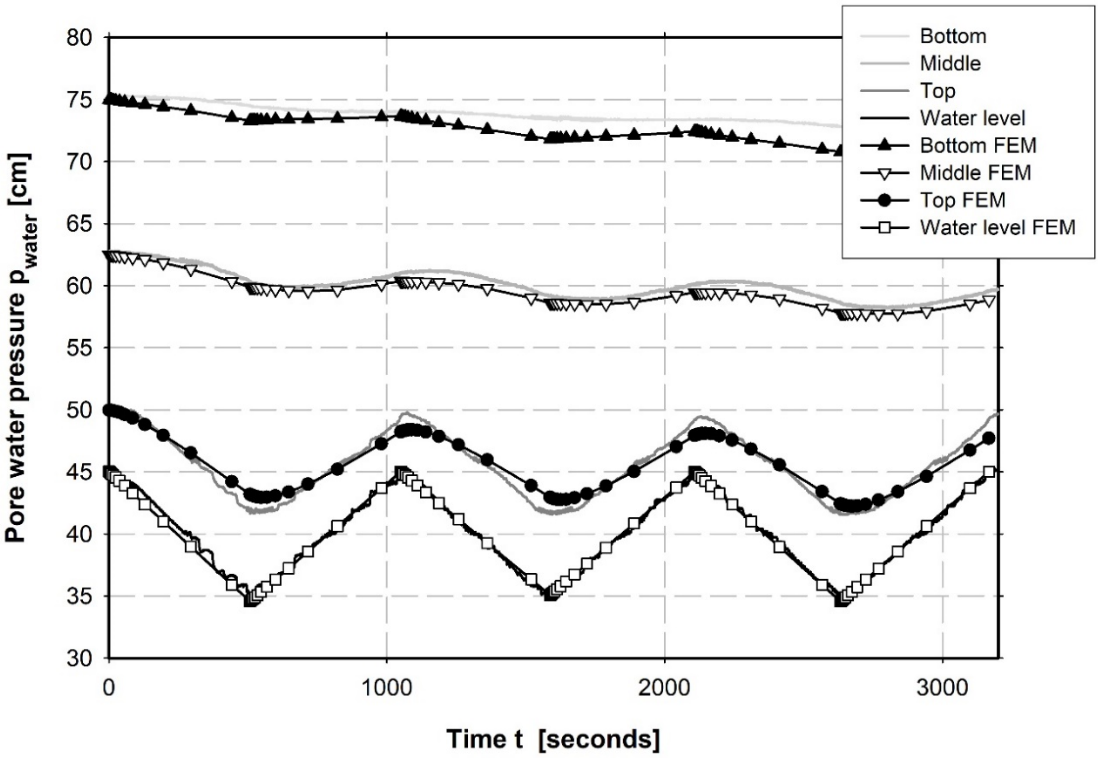

Fig. 24: Comparison of measurements and numerical results for silt: three cycles of water level decrease and increase (v ~ 2,400·k_{Silt})

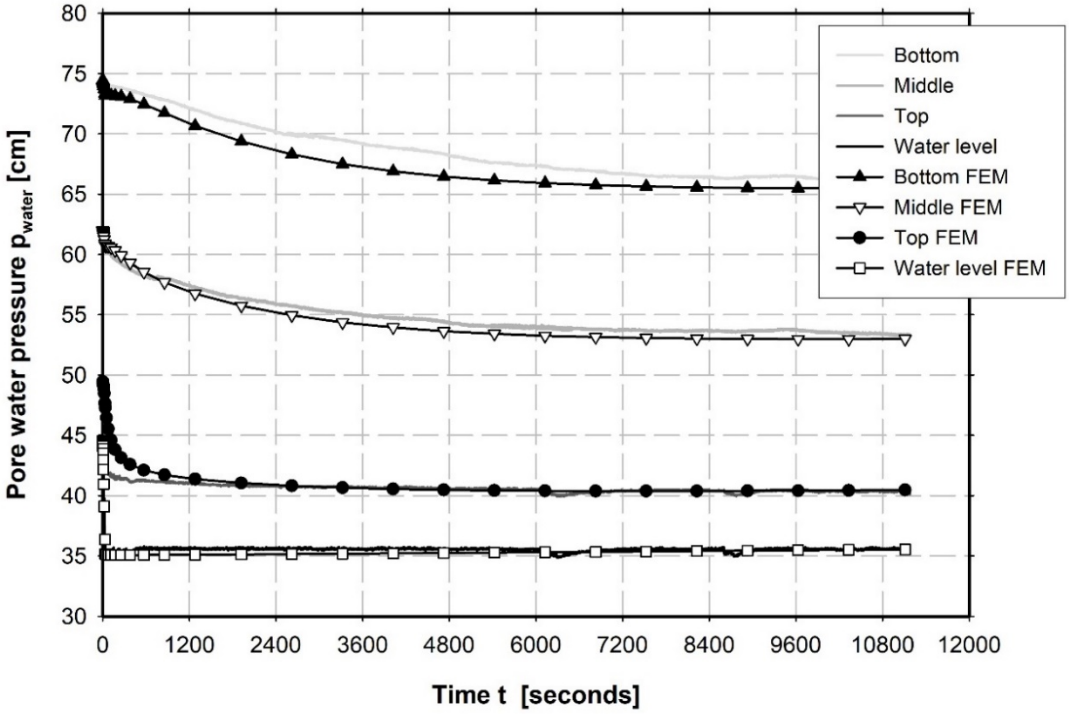

Fig. 25: Comparison of measurements and numerical results for silt: water level lowering and subsequent consolidation phase (v ~ 35,000·k_{Silt})

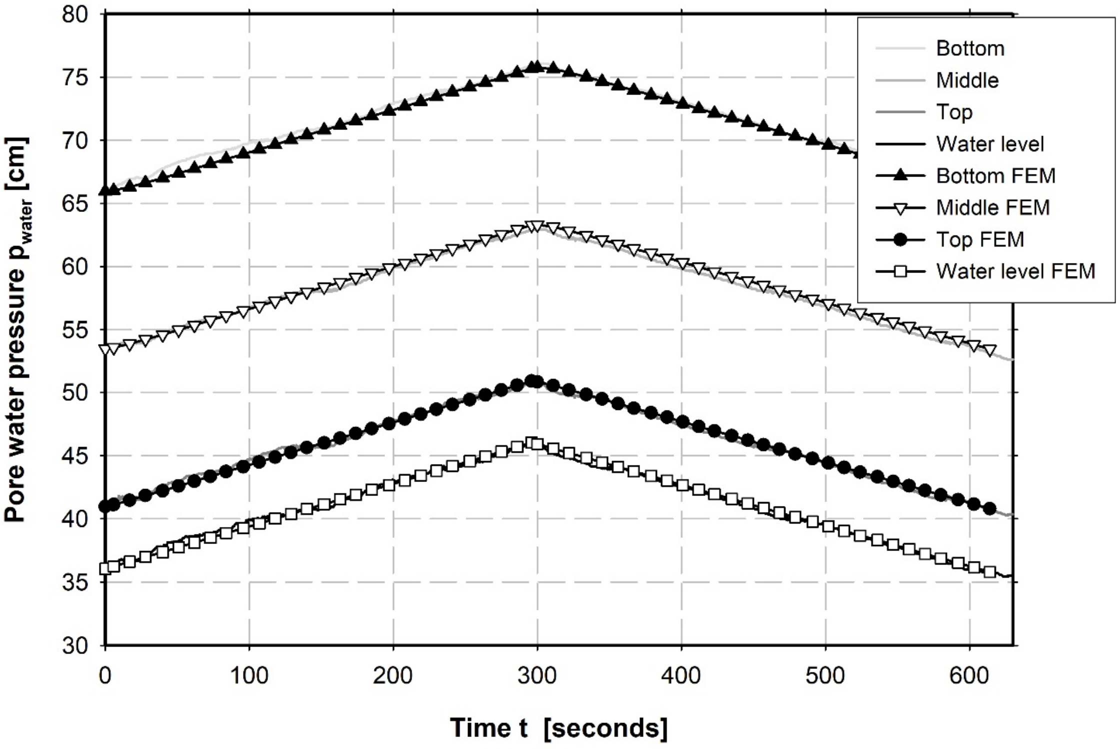

Fig. 26: Comparison of measurements and numerical results for sand: water level increase and decrease ($v \sim 30 \cdot k_{Sand}$)

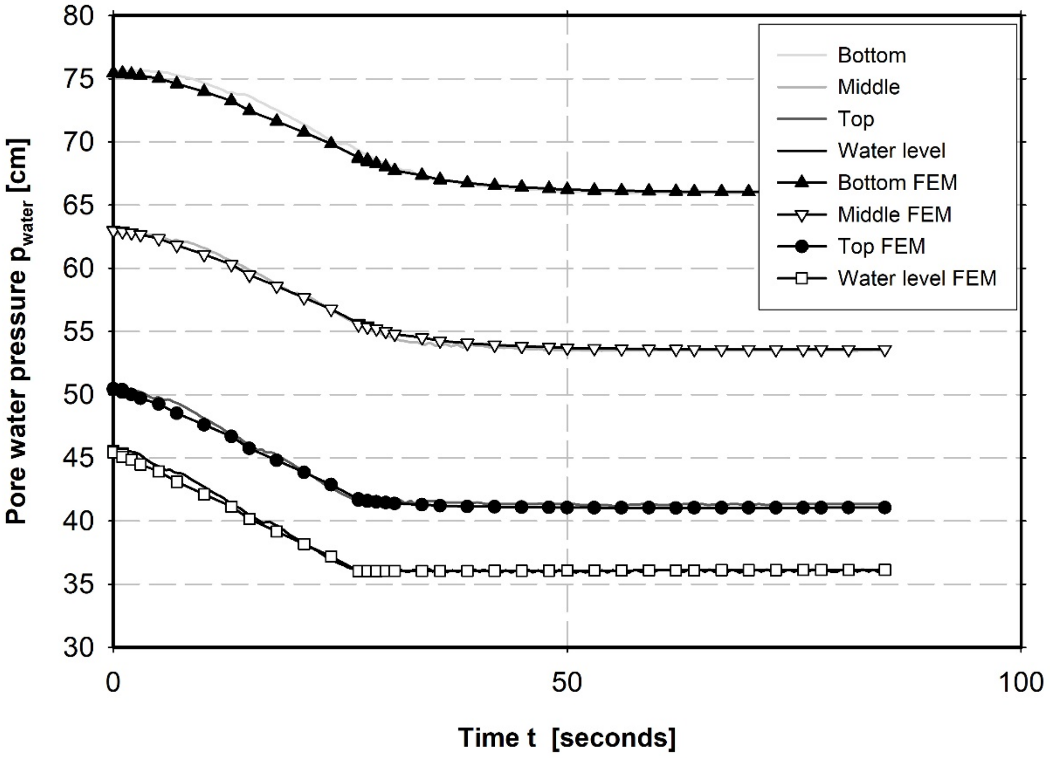

Fig. 27: Comparison of measurements and numerical results for sand: water level lowering and subsequent consolidation phase ($v \sim 370 \cdot k_{Sand}$)

The graphs in Figure 26 and Figure 27 show a comparison of measurement results and numerical results for the model tests with sand. As the graphs show, the calculated results are almost identical to the measurement results.

Assuming undrained conditions during the water level lowering in the model test with silt, Skempton's B-coefficient can be used to analytically determine the excess pore water pressure. According to Equation 15, Equation 21 and Equation 27, the pore fluid compressibility C_{fluid}, the B-coefficient and the excess pore water pressure p_{excess} can be calculated. The required material parameters are summarized in Table 2.

$$\begin{aligned} C_{fluid(p_{water})} &= 0.9 \cdot 4.1 \cdot 10^{-7} + \cdots \\ \cdots (1 - 0.9 + 0.02 \cdot 0.9) \cdot \frac{1}{0+100} &= 1.18 \cdot 10^{-3}\ 1/kPa \end{aligned} \tag{30}$$

$$B^{oed} = \frac{1}{1+0.43 \cdot 20{,}000 \cdot 1.18 \cdot 10^{-3}} = 0.09 \tag{31}$$

The change in total stresses due to a water level lowering of -10 cm is $\Delta\sigma^{total} = -\,0.1 \cdot 10 = -\,1$ kPa. The excess pore water pressure p_{excess} is obtained with

$$p_{ecxess} = (0.09 - 1) \cdot -1 = 0.91kPa = 9.1cm \tag{32}$$

Comparing the results for the excess pore water pressure in Equation 32 with the measurement results from the test with silt (shown in Figure 28), a good agreement with the pore pressure measurement at the bottom of the soil column can be recognized ($p_{excess} = 8.8$ cm). This shows that an almost undrained condition prevails at the bottom of the soil column during a fast water level lowering ($v \sim 35{,}000 \cdot k_{Silt}$).

To show the influence of the degree of saturation and the soil skeleton stiffness on the pore water pressures, these parameters were varied in the numerical back-calculation for the silt while the other parameters were not changed. Figure 29 and Figure 30 show the resulting pore water pressure at the bottom of the soil column for varying degrees of saturation and for a varying stiffness of the soil skeleton, respectively. The influence of the considered parameters is significant. The correct determination of these parameters is, therefore, crucial for the correct calculation of the pore water pressures in quasi-saturated soils.

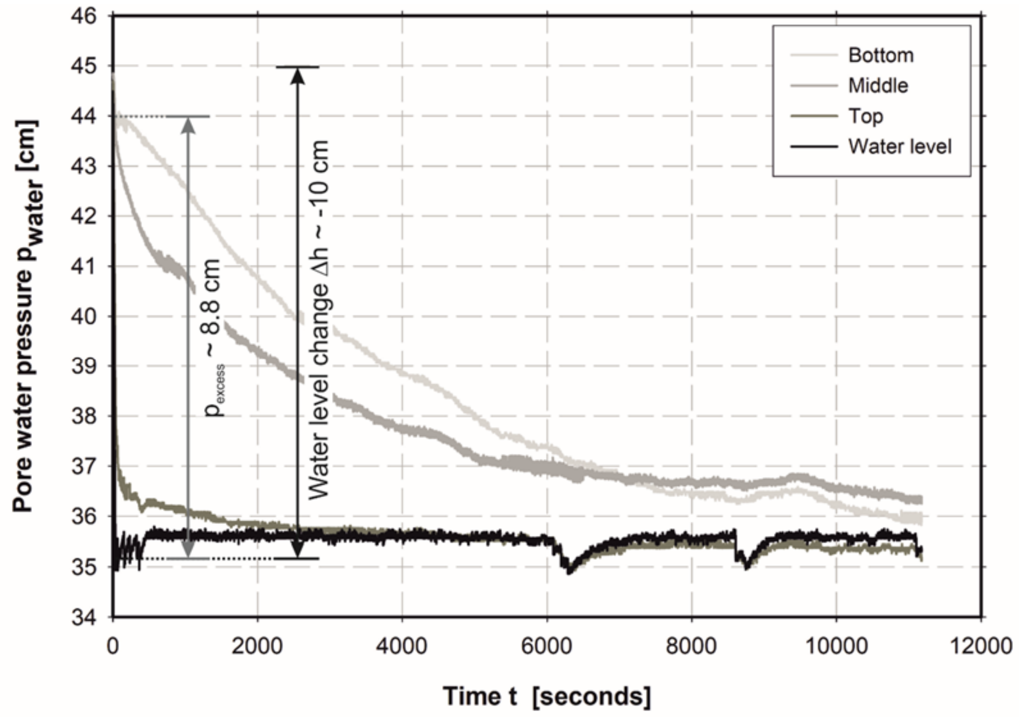

Fig. 28: Test results for silt: excess pore water pressure after water level lowering (v ~ 35,000·k_{Silt})

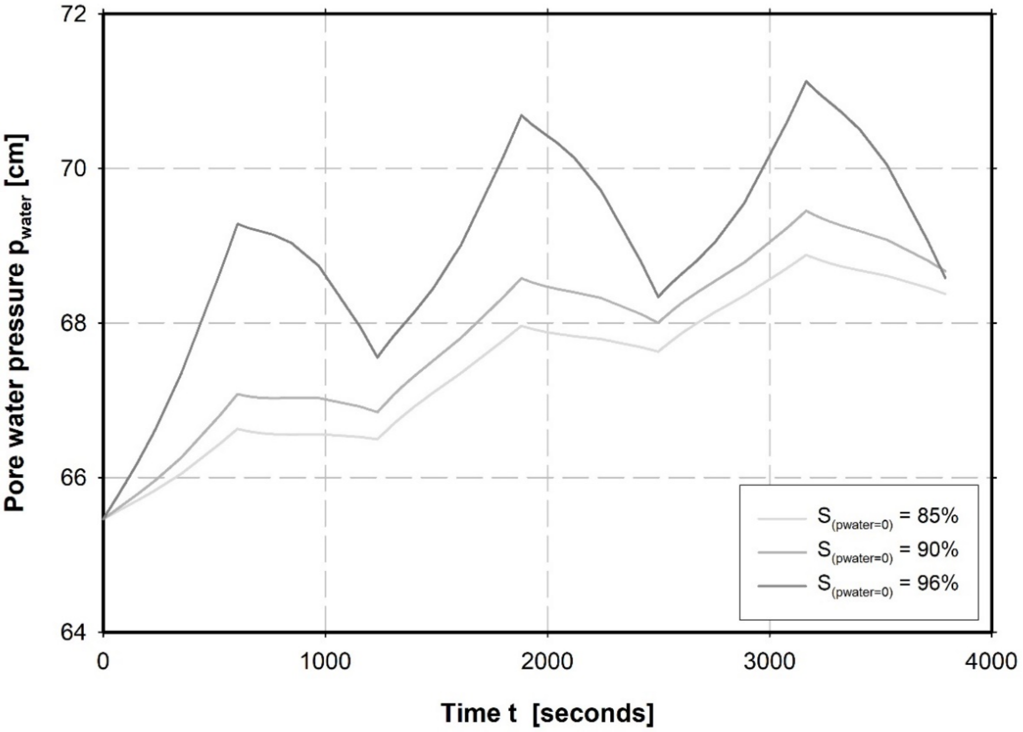

Fig. 29: Three cycles of water level increase and decrease (v ~ 2,400·k_{Silt}): influence of the reference degree of saturation $S_{(pwater=0)}$

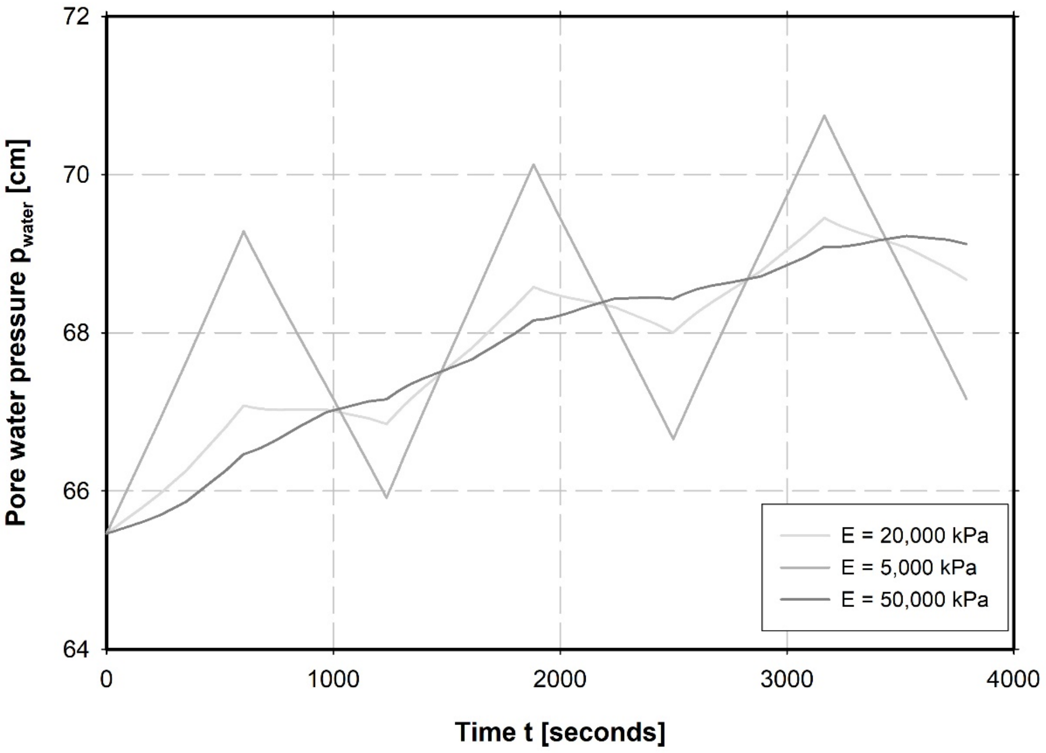

Fig. 30: Three cycles of water level increase and decrease ($v \sim 2{,}400 \cdot k_{Silt}$): influence of the soil skeleton stiffness *E*

2.6.6 Summary of model tests

The conducted model tests confirm that there is a development of excess pore water pressures in the case of a water level change above the ground surface of a quasi-saturated soil. The magnitude of the excess pore water pressures strongly depends on the ratio between the velocity of the water level change and the soil permeability. Furthermore, the significant influence of the soil skeleton stiffness and the reference degree of saturation has been discussed in the course of a parameter study.

The comparative numerical analyses with a user-defined WRC for the quasi-saturated stage show similar results as the model tests. Therefore, it can be assumed that the theoretically derived relationship between the degree of saturation and pore water pressure for the quasi-saturated stage in the positive pressure regime is validated, at least for the determination of the pore water pressures under this saturation condition.

Considering the primary question of this thesis, regarding the influence of water level changes on the movement behaviour of a landslide, the following interesting conclusion can be drawn from these model tests. When comparing the excess pore water pressures developed during a water level increase and a water level lowering, the latter leads to positive excess pore water pressures whereas the former leads to negative excess pore water pressures (see Figure 31). In the context of effective stresses in the subsoil, the worst situation is, therefore, a high water level over a long period, followed by a fast water level lowering. In this case the excess pore water pressures reach a maximum which leads to minimum effective stresses and furthermore to a low factor of safety for the slope.

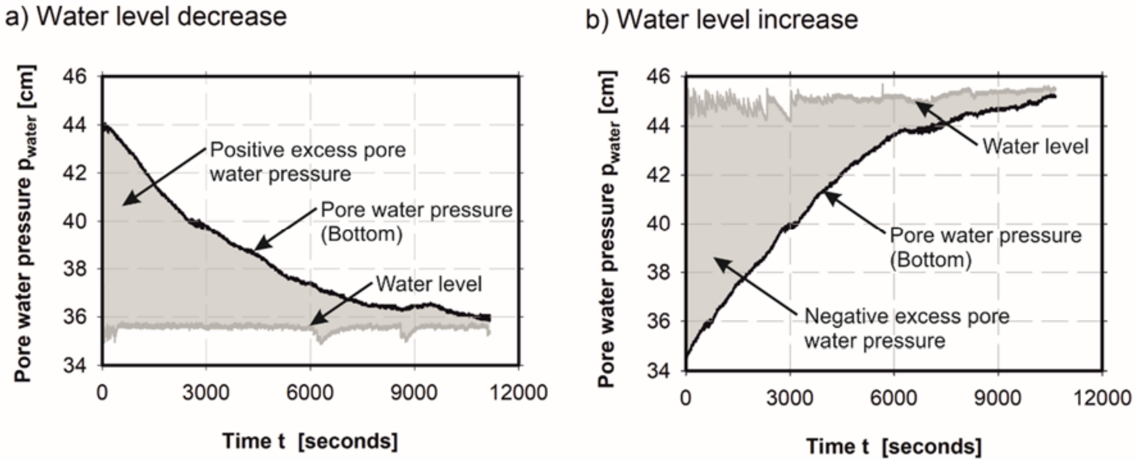

Fig. 31: Comparison of excess pore water pressure due to a) water level lowering and b) water level increase

To investigate the influence of waves on the seepage in the subsoil, Ewers (2016) conducted model tests similar to the one described in this chapter. Ewers (2016) also showed the significant influence of the quasi-saturated stage on the development of excess pore water pressures due to fluctuating water levels. Furthermore, a good agreement between the performed numerical calculations and model tests is also shown in Ewers (2016).

2.7 Preliminary study – excess pore water pressures beneath a water storage basin

2.7.1 Introduction

As discussed in chapter 1, it was observed that the fluctuating water levels in the water storage basin of the case study lead to excess pore water pressures in the subsoil. The quasi-saturated stage could be one possible reason for these observations. Therefore, the investigations described thus far in chapter 2, concerning the quasi-saturated stage of soils, were performed. A preliminary numerical study concerning quasi-saturated soils is presented in this chapter. This study should show whether the measured excess pore pressures in the particular basin of the case study can be back-calculated qualitatively with a simple axisymmetric model, considering a quasi-saturated stage for the subsoil.

2.7.2 Numerical model and material parameters

Figure 32 shows the numerical model for the preliminary study. The height of the model is 30 m, comprising two soil materials. The upper 20 m consists of silty sand. The material for the lower 10 m is sandy clayey silt. The lateral boundaries and the lower boundary were assumed to be impermeable. The hydraulic boundary condition at the top is the changing water level (pore water pressure) according to the water level-time curve in Figure 32. This water level corresponds to the real storage operation of the considered basin in September 2014. A fully coupled flow-deformation analysis was performed. The calculated pore water pressures were evaluated at 20 m and 30 m depths. These depths correspond approximately to the installation depths of the pore water pressure gauges in the field.

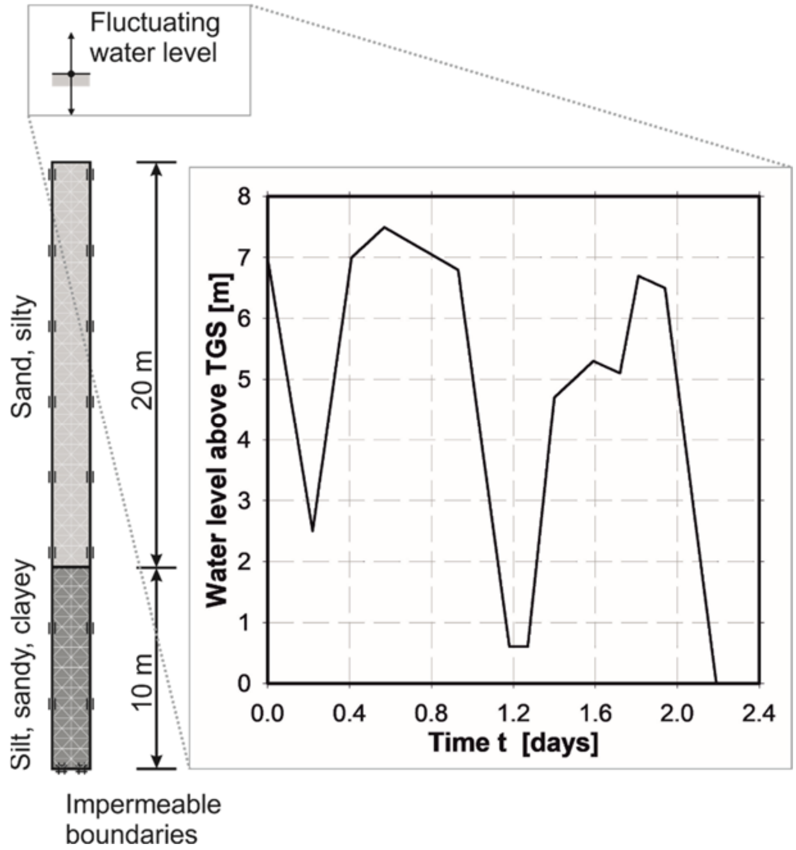

Fig. 32: Finite element model for preliminary study – excess pore water pressures beneath a water storage basin (360 15-noded elements)

The Hardening Soil Small model (HSS model) (Schanz 1999, Benz 2007) was used as the constitutive model for both soil materials. First calculations showed that the incorporation of a stress dependent stiffness and the increased stiffness due to small strains are necessary for the back-calculation of the measured pore water pressures. The soil properties were determined from engineering judgement, following the laboratory test results of the material from the later presented site. As the qualitative pore pressure distribution in the soil column is the main issue of the current analysis, the same mechanical properties were used for both soil types;

only the assigned soil permeability is different. As already discussed in the previous chapters, the stiffness parameters have a significant influence on the pore water pressure development due to fluctuating water levels. However, the difference between the stiffness parameters for the silty sand and the sandy, clayey silt were not significant for the purpose of this preliminary study. Therefore, the assumption of averaged values seems reasonable. The material parameters are summarised in Table 3.

Tab. 3: Material parameters for the preliminary study – excess pore water pressures beneath a water storage basin

Parameter	**Unit**	**Sand, silty**	**Silt, sandy, clayey**
Model		Hardening Soil Small	Hardening Soil Small
γ_{unsat}	kN/m³	18.0	
γ_{sat}	kN/m³	20.0	
$E_{50,ref}$	kPa	25,000	
$E_{oed,ref}$	kPa	20,000	
$E_{ur,ref}$	kPa	60,000	
ν'_{ur}	-	0.2	
p_{ref}	kPa	100	
m	-	0.8	
φ'	°	35.0	
c'	kPa	1.0	
ψ'	°	0.0	
k_{sat}	m/sec	10^{-6}	10^{-8}
$G_{0,ref}$ / $\gamma_{0.7}$	kPa / -	$62{,}500 / 2 \cdot 10^{-4}$	

For the quasi-saturated stage, a user-defined WRC according to Equation 14 was considered in the FEA. The necessary parameters for the WRC were calibrated on the basis of the first water level lowering. To simplify this calibration, Henry's parameter was assumed with h = 0.0. This assumption is reasonable as the dissolution of air into water requires time (Boutonnier 2010), while the water level changes are very fast. Therefore, the water retention curve only depends on the reference degree of saturation $S_{(pwater=0)}$. Compared to the measured field data, a reference degree of saturation $S_{(\mathrm{pwater}=0)} = 0.987$ led to similar excess pore water pressures in the finite element analysis for the first water level lowering. The water retention curve used for this analysis is shown in Figure 33.

A parameter study showed that the influence of the relative permeability on the results is not very high in this case. This is due to the fact that the saturated permeability is already very small compared to the velocity of the water level changes. Therefore, the behaviour during the water level changes is similar to undrained behaviour. A further decrease in soil permeability would lead to no significant change in the calculated pore water pressures (except for the analysis of longer periods with a constant water level). Thus, and due to the lack of data concerning the relative permeability, the relative permeability was assumed as $k_{rel} = 1.0$.

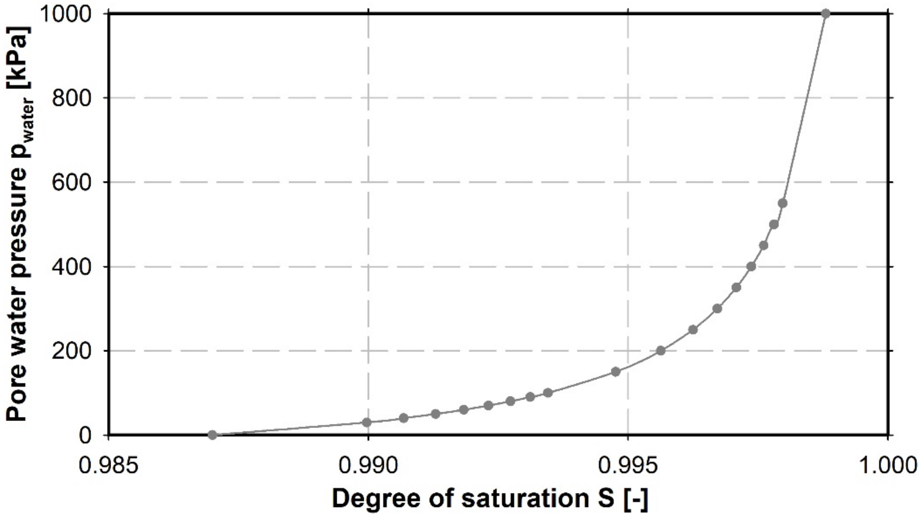

Fig. 33: Water retention curve for preliminary study – excess pore water pressure beneath water storage basin ($S_{(pwater=0)} = 98.7\%$ & h = 0.02)

2.7.3 Numerical results and comparison with measurement results

The field measurements show a mean excess pore water pressure of 0 kPa at a depth of 20 m. The average excess pore water pressure at 30 m depth is approximately 20 kPa, which was not considered in the preliminary study. A hydrostatic pore water pressure distribution was assumed in the initial phase. However, as shown in Figure 33, the degree of saturation depends on the absolute pore water pressure. Consequently, this simplification (assumed initial hydrostatic pore water pressures) leads to some errors in the numerical results. Therefore, the results of the measurements and the FEA can be only compared in a qualitative manner. For comparison purposes, the measurement results for 30 m depth were shifted to a mean excess pore water pressure of 0 kPa.

In Figure 34, the measured and the calculated excess pore water pressures are compared. The excess pore water pressures were determined according to the following equation.

$$p_{excess} = p_{measured/calculated} - p_{hydrostatic} \tag{33}$$

The FEA results show very similar excess pore water pressure developments as the field measurements. A decrease in the water level leads to positive excess pore water pressures and vice versa. Furthermore, fast and high water level changes (as from 0.0 to 0.4 days and from 1.0 to 1.4 days) lead to higher excess pore water pressures than slow water level changes. The characteristics of the pore water pressure development are also comparable with the main results from the model tests in chapter 2.6.

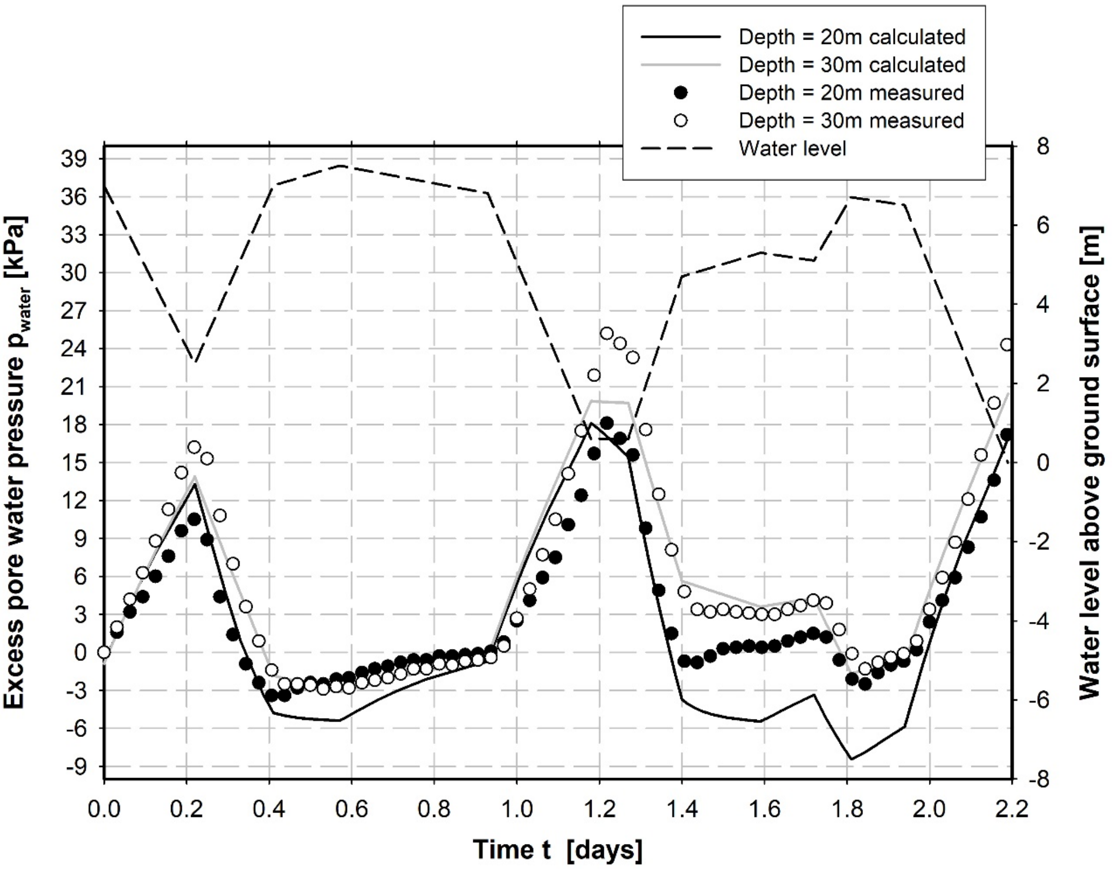

Fig. 34: Preliminary study: Comparison of field measurements and numerical results for excess pore water pressure

Considering the good consistency in results, presented in Figure 34, the quasi-saturated stage can be confirmed as a possible reason for the excess pore water pressures beneath the considered basin. This confirmation can be made in particular because a FEA using a saturated stage instead of a quasi-saturated stage would lead to no excess pore water pressures under the aforementioned conditions. However, it is to be noted that great simplifications concerning the geometry, the material parameters and the boundary conditions have been made. The influence of the slow moving landslide is completely neglected in the presented analyses. A back-calculation of the measured excess pore water pressures in order to determine their actual causes has to be done with a 2D finite element model which incorporates the real geometry, the correct boundary conditions and a more specific definition of the material parameters. This is presented in chapter 6.

2.8 Summary and conclusions quasi-saturated soils

In this chapter, a basic introduction to quasi-saturated soils has been presented and the behaviour of quasi-saturated soils in the positive pressure range has been discussed in detail. The significant influence of a small amount of entrapped air bubbles on the pore water pressure development in the subsoil has been shown on the basis of a literature review and theoretical considerations.

Based on already existing formulations, a theoretical water retention curve for the quasi-saturated stage has been derived by applying Boyle’s law and Henry’s law. Furthermore, a formulation for a pressure dependent compressibility of the air-water mixture has been presented.

The main reasons for the investigation of quasi-saturated soils were the field measurement results of installed pore water pressure gauges beneath a water storage basin, next to a slow moving landslide. These measurements showed excess pore water pressures in the subsoil, corresponding to the water level changes in the basin. Based on present literature, one hypothesis was that ground water level changes above the ground surface lead to excess pore water pressures in the subsoil and therefore the quasi-saturated stage might be the reason for the measured excess pore water pressure. To confirm this hypothesis, a model test and comprehensive numerical studies were performed.

The results of a model test simulating water level changes above a soil column has been discussed in this chapter. It has been proved that water level changes above the ground surface produce excess pore water pressures in the soil column. In addition to the degree of saturation and the stiffness of the soil skeleton, the ratio between soil permeability and velocity of the water level change has been identified as a crucial factor for the magnitude of the produced excess pore water pressures. Comparative FEA have been used to verify the theoretically derived relationship between pore water pressure and degree of saturation.

Finally, in the course of a preliminary study the results of a FEA incorporating the quasi-saturated stage have been compared qualitatively to selected field measurements and a good consistency has been identified. The quasi-saturated stage should therefore be considered in the following back-calculations of the pore pressure measurements by means of a high quality 2D finite element model to determine the actual reason for the excess pore water pressures beneath a water storage basin next to a slow moving landslide.

3 Rapid drawdown and slope stability – an overview

3.1 Introduction

In the previous chapter, the development of excess pore water pressures in the subsoil due to external water level changes was discussed from the point of view of quasi-saturated soil mechanics. However, the effects of rapid drawdowns in the area of slopes might also produce excess pore water pressures in the subsoil. Therefore, the mechanisms leading to the excess pore water pressures in the subsoil during drawdowns are discussed in this chapter.

The term rapid drawdown refers to a water level change in water storage basins, canals or similar geotechnical structures with inclined ground surfaces, i.e. slopes. The falling water level proceeds with high velocities compared to soil permeability (Berilgen 2007). Rapid drawdowns may occur due to changing river levels, water discharge in flood control reservoirs or operation of pumped-storage power plants. During the rapid drawdown, the stabilizing external water load on adjacent slopes and the hydraulic boundary condition at the slope surface are changed. As a result, the pore water pressures in the subsoil are also changed (Berilgen 2007, Pinyol et al. 2008). These effects can lead to excess pore water pressures and furthermore, to a decrease in the stability of slopes which may lead to a failure of slopes or dams.

In water storage basins of pumped-storage power plants in particular, the rapid drawdown scenario can present a critical loading condition for adjacent slopes. The ratio between drawdown rate and soil permeability is very high in such cases, as the operation of the pumped-storage power plant has to respond immediately to changes at the electricity market, involving fast water level changes. For slopes near the ultimate limit state under natural conditions, the developing excess pore water pressures at the slope toe may lead to slope movements, or in the worst case, to slope failure.

The slow moving landslide presented in this thesis is significantly influenced by the operation of the water storage basin which involves daily rapid drawdowns. Therefore, the essential characteristics of soil behaviour during rapid drawdowns are presented in this chapter as a basis for the subsequent back-calculations of this landslide. To discuss the soil behaviour during a rapid drawdown, a simple numerical study is presented in this chapter. The quasi-saturated stage (see chapter 2) is also considered in this study to show the influence of the ratio between soil skeleton stiffness and pore water compressibility on the development of excess pore water pressures during a rapid drawdown. In addition, the influence of the ratio between drawdown rate and soil permeability on the magnitude of the excess pore water pressures is discussed. The factor of safety is analysed for the different conditions to show the significant influence of the developing excess pore water pressures on the slope stability.

3.2 Preliminary study on soil behaviour under rapid drawdown conditions

The effect of a rapid drawdown on the pore water pressure distribution in a slope has been shown by Berilgen (2007) and Pinyol et al. (2008), using a simple slope geometry and a real slope. Berilgen (2007) discussed, based on a comprehensive numerical study, the influence of the drawdown rate *R*, the soil permeability *k* and the drawdown ratio *L/H* (see Figure 35) on the factor of safety (FoS) of the submerged slope. As can be seen in Figure 35, the results of Berilgen (2007) indicate that the two limiting cases of fully slow drawdown (drained conditions) and fully rapid drawdown (undrained conditions) does not reflect the real soil behaviour in most cases. Therefore, a fully coupled flow-deformation analysis is recommended to study the soil behaviour during a rapid drawdown.

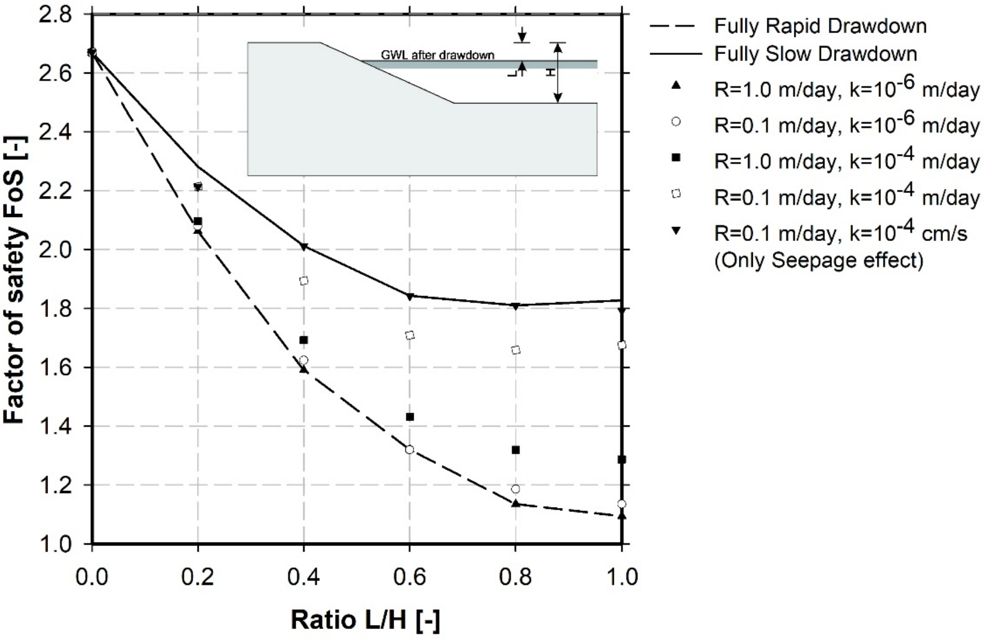

Fig. 35: Variation of FoS with drawdown ratio L/H for slope with 7.0 m height (after Berilgen 2007)

Stelzer et al. (2014) complemented the aforementioned studies by considering a quasi-saturated stage for the soil. For a better understanding of the following investigations concerning the mechanisms of the landslide next to a water storage basin, the influences of rapid drawdowns on the pore water pressures in the subsoil are discussed in this chapter based on a numerical study.

3.2.1 Numerical model and material parameters

The preliminary study is conducted on a simple slope geometry, as shown in Figure 36, with Plaxis 2D 2016 (Brinkgreve et al. 2016). The focus are on the influence of the ratio between drawdown rate and soil permeability as well as the soil-water stiffness ratio on the magnitude of the excess pore water pressures. Furthermore, the FoS after the drawdown is investigated. To study the influence of these factors, fully coupled flow-deformation analyses are necessary.

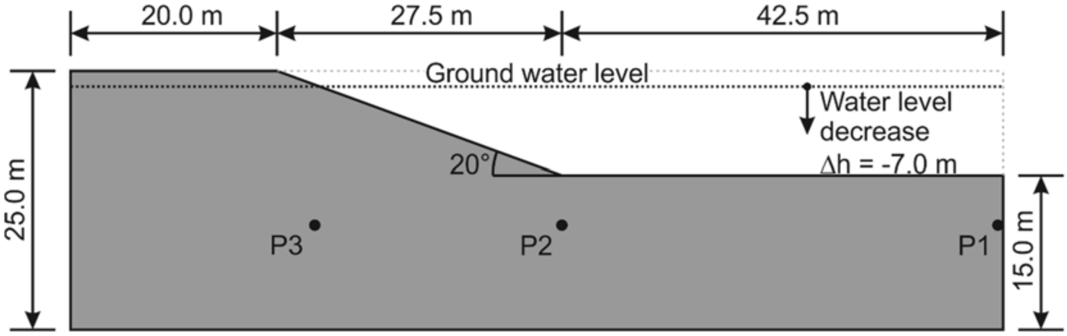

Fig. 36: FE-model for preliminary study – rapid drawdown (1,269 15-noded elements)

Employing a linear-elastic, perfectly plastic constitutive model (Mohr-Coulomb model) is considered sufficient for the purpose of this study. The Young's modulus of the soil is varied between 10,000 kPa and 100,000 kPa. On the one hand, the chosen stiffness moduli cover the entire range of stiffness parameters for a fine grained soil, ranging from primary loading stiffness up to small strain stiffness. On the other hand, this range reflects the primary loading stiffness for a relatively wide range of soil materials. Additionally, the soil permeability, the drawdown rate and the bulk modulus of the pore water are varied to show their influence. The bulk modulus of the pore water is assumed with $K_w = 2.4 \cdot 10^6$ kPa, which is valid for pure water and with $K_w = 10{,}000$ kPa and $K_w = 24{,}000$ kPa. This latter values are each an average value based on Henry's parameter $h = 0.00$ and $h = 0.02$, respectively, considering a reference degree of saturation of $S_{(pwater=0)} = 97\%$ and a mean pore water pressure of $p_{water} = 100$ kPa and $p_{water} = 200$ kPa, respectively. As shown in chapter 2, the bulk modulus of the pore water K_w depends strongly on the pore water pressure and is not a constant value. However, for this preliminary study, a constant value is assumed for the sake of simplicity. The material parameters are summarized in Table 4.

In addition to a homogeneous slope, the pore pressure distribution during a drawdown event in case of a highly permeable slope ($k = 10^{-2}$ m/sec) on a subsoil with a low permeability ($k = 10^{-7}$ m/sec) is investigated as similar conditions are present at the slow moving landslide site (case presented later in chapter 5 and chapter 6).

The numerical analysis is composed of the following calculation phases. Starting with a horizontal ground surface, the initial stress state is defined with $\sigma'_v = \gamma \cdot h$ and $\sigma'_h = \sigma'_v \cdot K_0^{nc}$. Afterwards, an excavation under drained conditions is performed. The excavation phase is followed by a fully coupled flow-deformation analysis in which the ground water table is lowered with different drawdown rates (R_{high} = 7 m/8 h and R_{low} = 7 m/80 h). Finally, a safety analysis under drained conditions is performed to determine the FoS after the drawdown.

The pore water pressures during the drawdown are evaluated in the nodes (P1, P2 and P3), shown in Figure 36. Node P3 is used additionally to evaluate the pore water pressures due to a drawdown in a high permeable slope on a low permeable subsoil.

Tab. 4: Material parameters for preliminary study – rapid drawdown

Parameter	Unit	Value
Model		Linear-elastic
γ_{unsat}	kN/m^3	19.0
γ_{sat}	kN/m^3	20.0
E	kPa	10,000 25,000 100,000
ν'	-	0.3
K_0^{nc}	-	0.426
φ'	°	35
c'	kPa	5
n	-	0.33
k	m/sec	10^{-7} 10^{-4}
K_w	kPa	$2.4 \cdot 10^6$ 24,000 10,000

3.2.2 Soil behaviour during drawdown

Pinyol et al. (2008) described very clearly the characteristics of a drawdown scenario. The decreasing water level during a drawdown scenario leads to a change in total stresses and changed hydraulic boundary conditions at the ground surface. These changes result in new total stresses in the subsoil and a transient water flow.

In case of no coupling between volumetric and deviatoric behaviour, the change in pore water pressure Δp_{water} is equal to the change in total mean stress Δp in a saturated soil under undrained conditions. This can be shown by means of Skempton's pore pressure coefficients (see Equation 20). Under the previously mentioned conditions, Skempton's coefficients are $B = 1.0$ and $A = 1/3$ (Skempton 1954).

$$\Delta p_{water} = B \cdot \Delta p = 1.0 \cdot \Delta p \tag{34}$$

Undrained conditions during a rapid drawdown result from very high drawdown rates in combination with low soil permeability as was shown by Berilgen (2007) (compare Figure 35). However, in reality the produced pore water pressures due to the rapid drawdown also depend on the seepage occurring due to the changed hydraulic boundary conditions.

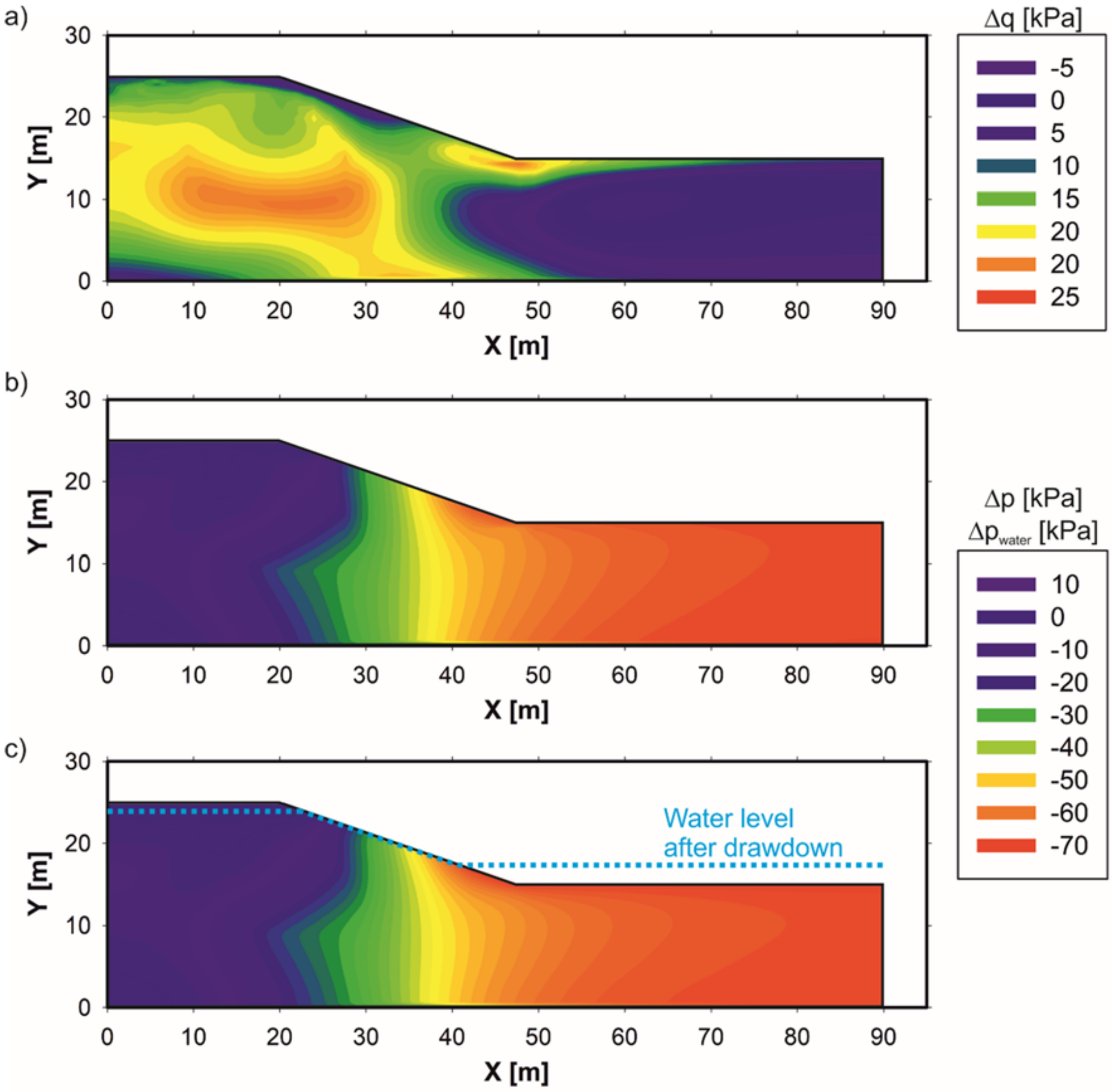

Fig. 37: Change in a) deviatoric stress, b) total mean stress and c) pore water pressure ($R_{high} = 7$ m/8 h and $k = 10^{-7}$ m/sec)

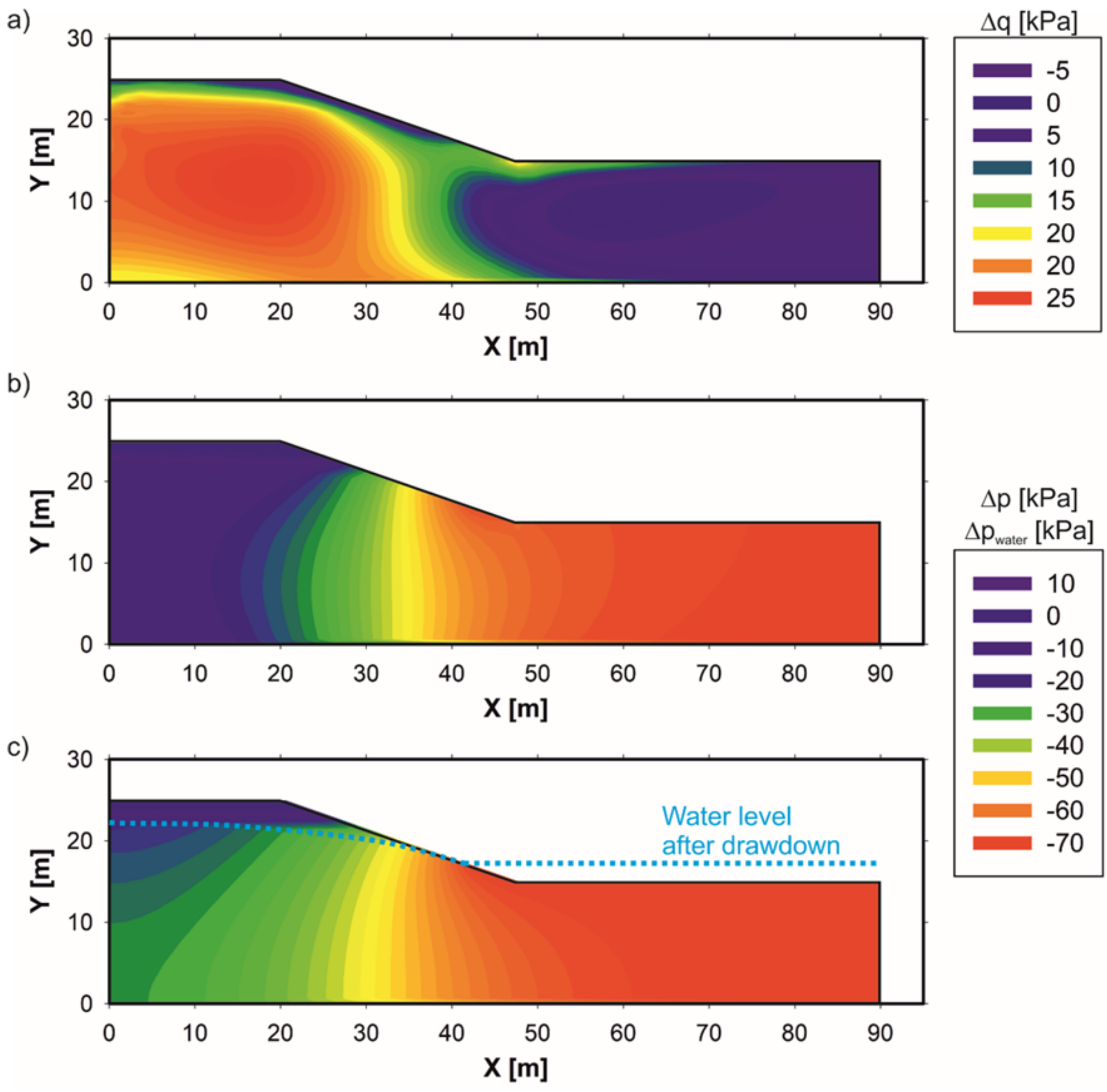

Fig. 38: Change in a) deviatoric stress, b) total mean stress and c) pore water pressure (R_{high} = 7 m/8 h and k = 10^{-4} m/sec)

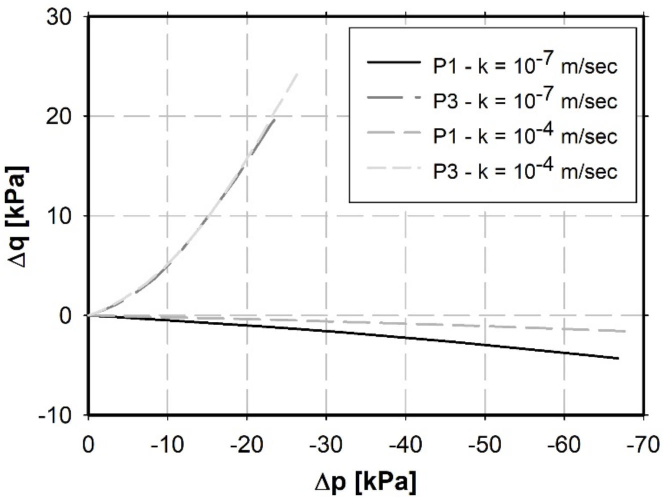

Fig. 39: Change in total stresses due to rapid drawdown in point P1 and P3 (pressure is positive)

Figure 37 and Figure 38 show the changes in total stresses and pore water pressures due to a rapid drawdown scenario on the model presented in Figure 36**Fig. 36**. The stiffness of the applied linear-elastic model (material parameters see Table 4) is E = 10,000 kPa. The permeability is k = 10^{-7} m/sec and k = 10^{-4} m/sec in Figure 37 and Figure 38, respectively. According to Figure 37, the change in pore water pressure Δp_{water} (Figure 37 c) is almost identical to the change in total mean stress (Figure 37 b) for a soil with a low permeability k = 10^{-7} m/sec. This shows that the soil behaviour under the given assumptions is almost undrained. In case of a high permeability k = 10^{-4} m/sec, however, the change in pore water pressure (Figure 38 c) differs significantly from the change in total mean stress (Figure 38 b). This result shows that the pore water distribution is also influenced by the occurring seepage.

In both cases (permeability k = 10^{-7} m/sec and k = 10^{-4} m/sec), the change in total mean stress and pore water pressure at the right boundary of the FE-model are about the same magnitude ($\Delta p_{water} = \Delta p = 70$ kPa). The hydrostatic pore water pressure change is also $\Delta p_{\text{hydrostatic}} = -\ 7.0\ \text{m} \cdot 10\ \text{kN/m}^3 = -\ 70$ kPa. Therefore, no excess pore water pressures are produced. This is due to the almost one-dimensional conditions in this area. Figure 39 confirms this one-dimensional situation as the change in the deviatoric stress Δq is negligible in node P1. In contrast, in node P3 the deviatoric stress changes significantly.

The pore water pressure changes in Figure 37 c and Figure 38 c can be also used as an indicator for excess pore water pressures, if a hydrostatic pore water distribution prevailed before the drawdown. Vertical contour lines show a hydrostatic pore water pressure after the drawdown event. However, contour lines turned to the right indicate a positive excess pore water pressure, whereas left-turned lines suggest negative excess pore water pressures. According to Figure 37 c, it is apparent that a drawdown leads to considerable excess pore water pressures at the slope toe in case of a low permeability soil. These excess pore water pressures are not noticeable to the same extent for the highly permeable soil (Figure 38 c). This shows already that the magnitude of the excess pore water pressure depends on the soil permeability in the case of a rapid drawdown. This is similar to the observations for external fluctuating water levels in case of quasi-saturated soils.

Figure 40 shows the development of pore water pressures in the nodes P1-P3 for a high and a low drawdown rate in combination with a low soil permeability (k = 10^{-7} m/sec) and saturated conditions. Furthermore, the hydrostatic pore water pressure after the drawdown event is indicated in Figure 40. The different behaviour in the evaluated nodes is obvious. In node P1 almost no excess pore water pressures are produced due to the one-dimensional situation and the fully saturated stage of the soil. In node P2, positive excess pore water pressures develop during the drawdown, whereas in node P3 negative excess pore water pressures develop. The general behaviour is similar for the high and the low drawdown rates, with the excess pore water pressures being slightly smaller in case of the low drawdown rate. Regardless, Figure 40 shows that, despite the low drawdown rate, excess pore water pressures are still produced in the subsoil. This is due to the low soil permeability.

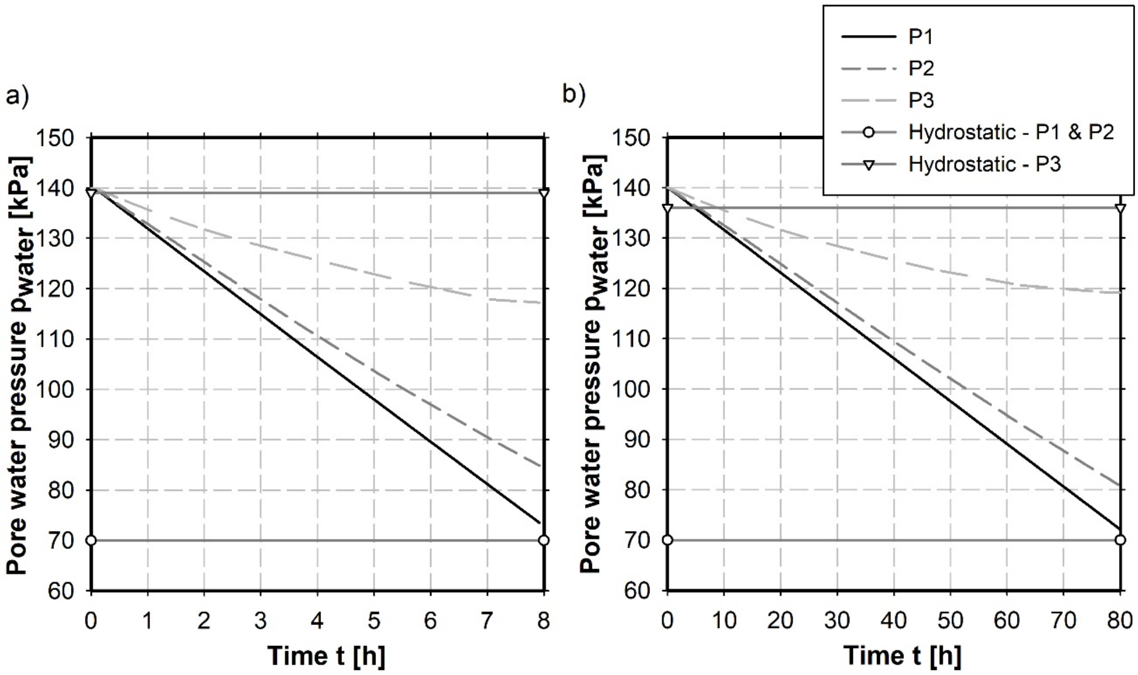

Fig. 40: Pore water pressures in P1-P3 for a) high drawdown rate (R_{high} = 7 m/8 h) and b) low drawdown rate (R_{low} = 7 m/80 h)

In addition to the excess pore water pressures occuring due to changes in the total mean stress, excess pore water pressures can result from a change in deviatoric stress in case of a coupling between volumetric and deviatoric behaviour, which is not considered with the linear-elastic constitutive model.

In the case of the slow moving landslide next to a water storage basin presented later, the material of the slope is highly permeable. Therefore, the water level in the (front section of the) slope may change with the water level in the basin. In contrast to the slope material, the subsoil is of low permeability. This scenario can be simplified as shown in Figure 41. In the following, the pore water pressure development during a rapid drawdown for this scenario is studied. The material for the slope and the subsoil was assumed according to Table 4 with a Young's modulus E = 10,000 kPa. The permeability of the slope is $k_{slope} = 10^{-2}$ m/sec. The permeability of the subsoil was assumed with $k_{subsoil} = 10^{-7}$ m/sec. A quasi-saturated stage is not considered in the analysis. After the rapid drawdown (R_{high} = 7 m/8 h) the water level is almost level across the entire model (see Figure 42). This is due to the high soil permeability in the slope. The modelled water level lowering produces excess pore water pressures in the subsoil as presented in Figure 42. The principles which lead to these excess pore water pressures are explained qualitatively in Figure 43. Similar numerical studies under 1D conditions were performed by Nitzsche (2016).

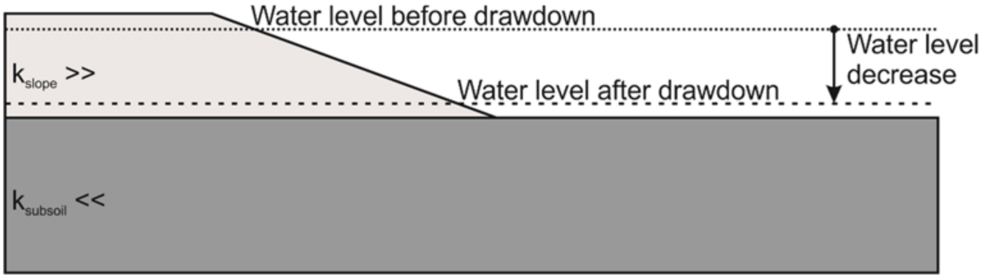

Fig. 41: Drawdown scenario at a highly permeable slope on low permeable subsoil

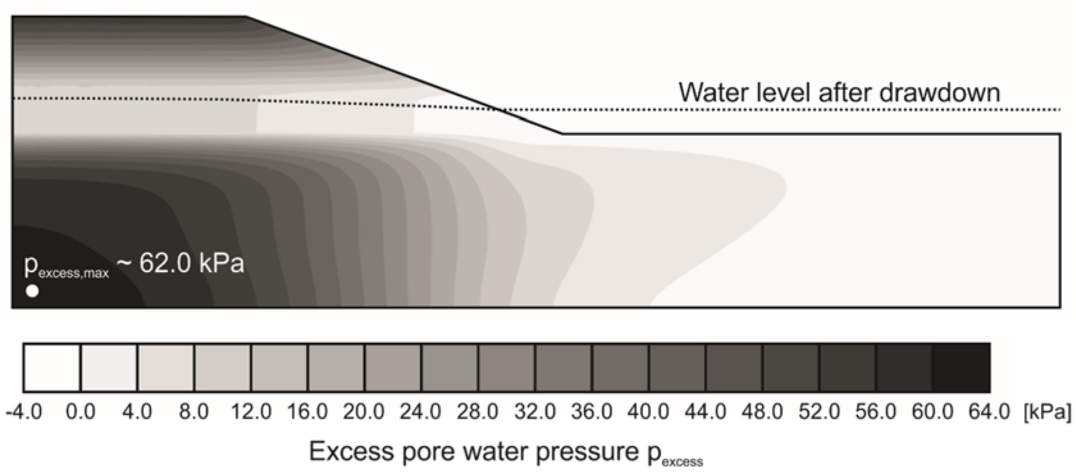

Fig. 42: Excess pore water pressure p_{excess} due to rapid drawdown (R_{high} = 7 m/8 h) at a highly permeable slope on low permeability subsoil

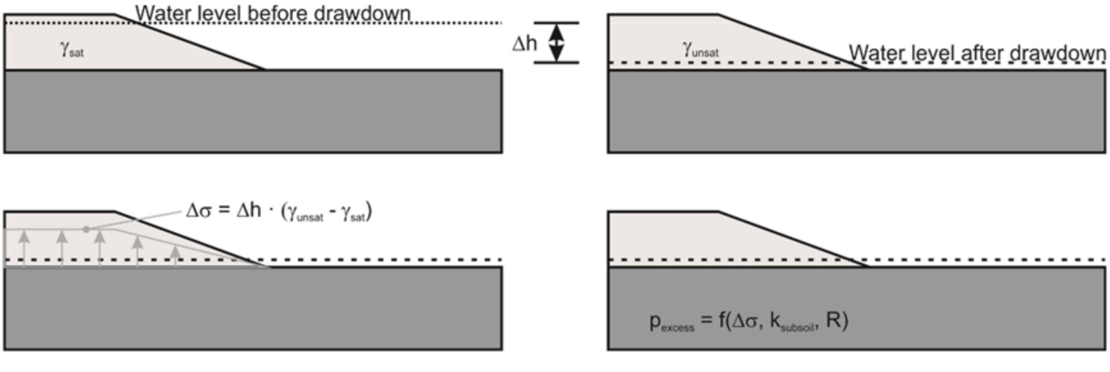

Fig. 43: Principles for excess pore water pressure generation beneath highly permeable slope

Due to the changed water level, the unit weight of the soil changes from saturated unit weight γ_{sat} to moist unit weight γ_{unsat} over the entire height of the water level decrease Δh. This changed unit weight leads to a decrease in total stresses $\Delta\sigma$ in the subsoil. Assuming fully undrained conditions in the subsoil due to the low soil permeability of the subsoil and the high drawdown rate above, these total stress changes result in a pore water pressure decrease of the same extent $\Delta p_{water} = \Delta\sigma$ according to Skempton (1954). However, this leads to excess pore water pressures in the subsoil, as the hydrostatic pore water pressure change is significantly higher $\Delta p_{hydrostatic} = \gamma_w \cdot \Delta h$. In the case of the presented numerical study, the maximum excess pore water pressure is $p_{excess,max} \sim 62.0$ kPa in the lower left corner. This maximum value corresponds approximately to the analytical undrained solution (see Equation 35).

$$p_{excess} = \Delta p_{water} - \Delta p_{hydrostatic}$$

$$p_{excess} = B \cdot (\gamma_{unsat} - \gamma_{sat}) \cdot \Delta h - \gamma_w \cdot \Delta h \tag{35}$$

$$p_{excess} = 1.0 \cdot (19 - 20) \cdot 7 - 10 \cdot (-7) = 63kPa$$

Assuming a highly permeable slope on a low permeability subsoil, the highest excess pore water pressures are produced beneath the slope. Excess pore water pressures also develop at the slope toe but not in the far right area of the model, where one-dimensional conditions prevail.

The previous presented studies show the general soil behaviour during rapid drawdowns based on a simple geometry and a simple constitutive model. In the following section, the factors, which influence the magnitude of the excess pore water pressures after a drawdown event are discussed.

3.2.3 Influence of soil skeleton stiffness and pore water bulk modulus on pore water pressures

Skempton (1954) showed the importance of the ratio between the soil skeleton stiffness and the bulk modulus of the pore water for the determination of the pore water pressures under undrained conditions. The numerical back-calculation of the performed model test confirmed this significant influence of the stiffness ratio (see chapter 2.6.5). Pinyol et al. (2008) investigated the influence of the soil stiffness on the pore water pressures during a rapid drawdown. Stelzer et al. (2014) and Montenegro (2016) emphasized the importance of the stiffness ratio E / K_w in the case of quasi-saturated soils based on numerical studies concerning water level changes above a soil column and in a building pit. In the following the influence of both, soil skeleton stiffness and bulk modulus of the pore water on the pore water pressures during a drawdown event is investigated. This is done with a numerical study, based on the geometrical model and the material parameters described in chapter 3.2.1. The soil permeability was assumed with $k = 10^{-7}$ m/sec for this parameter study. The applied drawdown rate is R = 7 m/8 h. The investigated stiffness ratios and the resulting B-coefficients (Skempton 1954) are shown in Table 5.

Tab. 5: Investigated combinations of soil skeleton stiffness *E* and bulk modulus of the pore water K_w

	K_w = 10,000 kPa	**K_w = 24,000 kPa**	**$K_w = 2.4 \cdot 10^6$ kPa**
E = 10,000 kPa	$E / K_w = 1.0$ $B = 0.75$	$E / K_w = 0.42$ $B = 0.88$	$E / K_w = 4.2 \cdot 10^{-3}$ $B = 1.00$*
E = 25,000 kPa	$E / K_w = 2.5$ $B = 0.55$	$E / K_w = 1.04$ $B = 0.74$	$E / K_w = 1.04 \cdot 10^{-2}$ $B = 1.00$*
E = 100,000 kPa	$E / K_w = 10.0$ $B = 0.23^{+}$	$E / K_w = 4.17$ $B = 0.42$	$E / K_w = 4.17 \cdot 10^{-2}$ $B = 0.99$

* due to numerical reasons in FEA assumed with B = 0.995

$^{+}$ resulted in a slope failure

Figure 44 shows the excess pore water pressures after the drawdown event for the nodes P1-P3, with values varying with the soil skeleton stiffness and the bulk modulus of the pore water. As already shown in chapter 3.2.2, the excess pore water pressures are positive in node P2 and negative in node P3. However, positive excess pore water pressures are also produced in node P1 if a quasi-saturated stage is considered although 1D conditions prevail. Such a behaviour has been already discussed in chapter 2 and cannot be observed in case of saturated conditions. In general, the magnitude of the excess pore water pressures is higher in node P2 than in node P1.

In case of a fully saturated soil (black dots in Figure 44), i.e. $K_w = 2.4 \cdot 10^6$ kPa, the influence of the soil stiffness on the magnitude of the excess pore water pressure is small in all evaluated nodes. As mentioned before, the excess pore pressures in node P1 are approximately zero due to the one-dimensional conditions in the corresponding area. In contrast to the fully saturated soil, the excess pore water pressure is influenced significantly by the soil stiffness and the bulk modulus of the pore water in the case of a quasi-saturated soil (white triangles and black squares). An increased soil stiffness leads to higher excess pore water pressures; whereas an increased bulk modulus of the pore water results in decreased excess pore water pressures. In this context, an increased pore water bulk modulus means a higher degree of saturation.

In case of a linear-elastic constitutive model, the change in pore water pressures results from the changes in total stresses and the modified hydraulic boundary conditions. In case of the low soil permeability and the high drawdown rate, the influence of the changed hydraulic boundary conditions can be neglected. The changed pore water pressures are mainly due to the changed total stresses initiated by the decreasing water pressure at the ground surface. Under these conditions, the increased excess pore water pressures in quasi-saturated soils develop due to the modified distribution of the total stress change between soil skeleton and pore water, as the stiffness of the soil and of the pore water are in a similar range. This can be also explained with Skempton's B-Coefficient, provided that the behaviour is fully undrained.

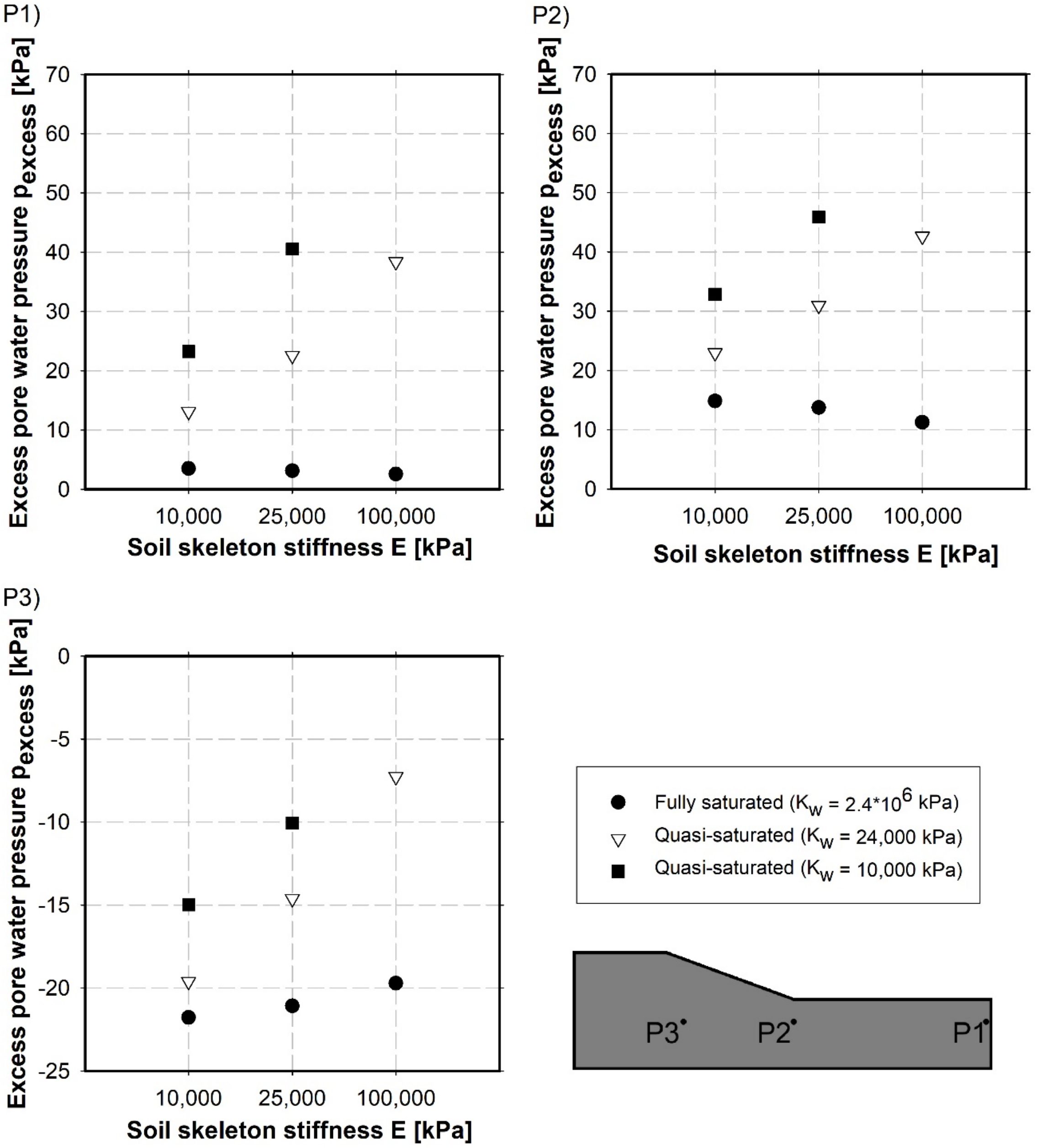

Fig. 44: Influence of soil skeleton stiffness and pore water bulk modulus on excess pore water pressures

Looking at node P1, the change in total mean stress is approximately the change in hydrostatic pore water pressure $\Delta p \sim -\Delta h \cdot \gamma_w$ due to the almost one-dimensional conditions. Assuming a soil skeleton stiffness E = 10,000 kPa and a bulk modulus of the pore water $K_w = 10{,}000$ kPa, Skempton's B-coefficient is $B = 0.75$ (see Table 5). In this case, the excess pore water pressure p_{excess} in the case of fully undrained behaviour is calculated according to Equation 27 in chapter 2.4 with

$$p_{ecxess} = (B^{oed} - 1) \cdot \Delta p \tag{36}$$

$$p_{ecxess} = (0.75 - 1) \cdot (-7 \cdot 10.0) = 17.5\ kPa$$

The calculated excess pore water pressure is similar to the numerical results, shown in Figure 44 (P1) ($p_{excess} = 23.2$ kPa). The higher value in the numerical calculation results from a small rotation of the principal stresses. Thus, the assumption of perfect one-dimensional conditions for the analytical solution is not completely met by the numerical results.

The 2D conditions in node P2 lead to higher excess pore water pressures in this area, compared to node P1.

The results for node P3 are interesting, as the absolute value of the excess pore water pressure decreases with an increasing soil stiffness and a decreasing bulk modulus of the pore water. This is contradictory to the earlier discussed results for node P1 and P2. Due to the water level lowering in front of the slope the total mean stress decreases and the deviatoric stress increases in the stress point next to node P3 (shown earlier in Figure 39). The decrease in pore water pressure is approximately equal to the decrease in total mean stress $\Delta p_{water} \sim \Delta p$ due to the low soil permeability, i.e. the pore water pressure also decreases due to the water level lowering. However, the water level in the slope itself does not change during the rapid drawdown. Therefore, the hydrostatic pore water pressure in node P3 is almost constant during the water level lowering. This combination of pore water pressure decrease and constant hydrostatic pore water pressure in the end leads to negative excess pore water pressures. However, in case of a quasi-saturated soil, the assumption of $\Delta p_{water} \sim \Delta p$ is not valid. The changes in total mean stress are only partially transferred to the pore water, i.e. the change in pore water pressure in quasi-saturated soils is smaller than for saturated soils. Therefore, the absolute value of the excess pore water pressure in node P3 also decreases in the case of quasi-saturation.

3.2.4 Influence of soil permeability and drawdown rate on pore water pressures

Previous studies (Berilgen 2006) showed the significant influence of the soil permeability and the drawdown rate on the pore water pressure development during a drawdown event. The influence of these factors is discussed in the current chapter based on a fully saturated soil ($K_w = 2.4 \cdot 10^6$ kPa) and a quasi-saturated soil ($K_w = 10{,}000$ kPa). For this parameter study, the soil skeleton stiffness is assumed with E = 10,000 kPa. Chapter 3.2.1 presents the numerical model and the material parameters. The following combinations of drawdown rate and soil permeability, presented in Table 6, are investigated.

Tab. 6: Investigated combinations of drawdown rate *R* and soil permeability *k*

	Low permeability **k = 10^{-7} m/sec**	**High permeability** **k = 10^{-4} m/sec**
Rapid drawdown rate **R = 7m / 8h**	R / k = $1.012 \cdot 10^{2}$	R / k = $1.012 \cdot 10^{-1}$
Slow drawdown rate **R = 7m / 80h**	R / k = $1.012 \cdot 10^{1}$	R / k = $1.012 \cdot 10^{-2}$

Recent literature (Berilgen 2007, Stelzer et al. 2014, Montenegro et al. 2015) showed that the ratio between drawdown rate and soil permeability is decisive for the magnitude of the excess pore water pressures. This was also confirmed by the model test for quasi-saturated soils in chapter 2.6. The magnitude of the excess pore water pressures is almost the same, irrespective which parameter (drawdown rate *R* or soil permeability *k*) is varied as long as the ratio *R* / *k* is the same.

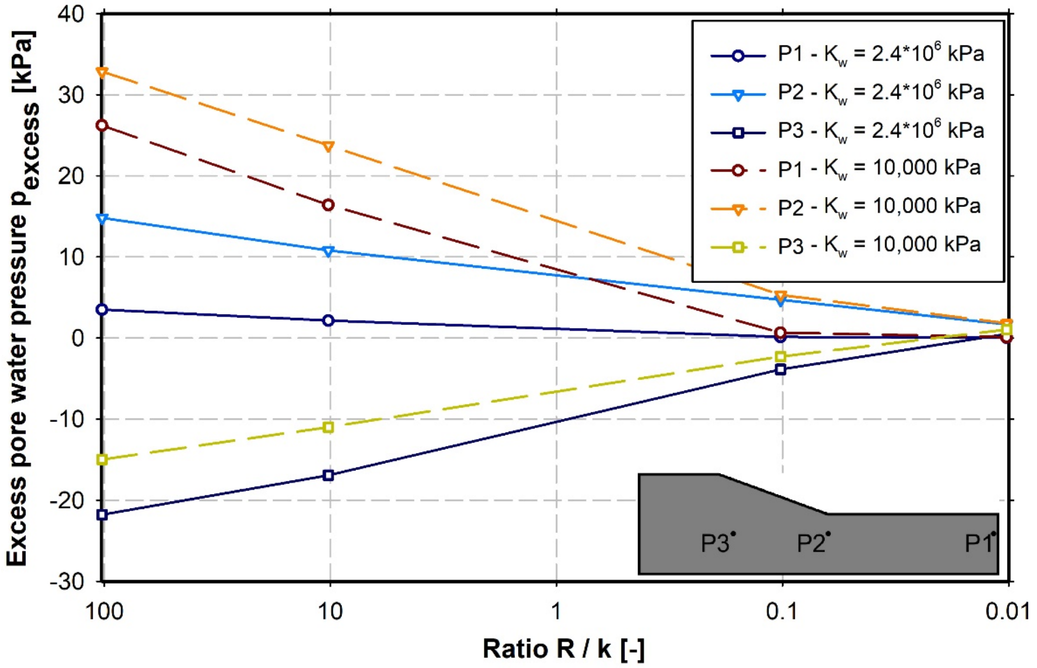

Fig. 45: Influence of ratio between drawdown rate *R* and soil permeability *k* on the magnitude of excess pore water pressures after drawdown event

Figure 45 presents the excess pore water pressures after the drawdown event. In general, the calculated results show the same behaviour as discussed in the previous chapters. After the drawdown, positive excess pore water pressures are present in the area of node P1 and P2. In case of node P3, negative excess pore water pressures are produced. The saturation stage has a significant influence on the magnitude of the excess pore water pressures. Furthermore, the parameter study in Figure 45 shows a clear increase of the absolute excess pore water pressure with increasing drawdown rate-permeability-ratio *R* / *k* for the fully saturated and the quasi-saturated soil. In case of a ratio R / k = $1.012 \cdot 10^{-2}$, almost no excess pore water pressures can be observed in the entire model, independent of the considered saturation stage. Therefore, an almost fully drained situation can be assumed under these circumstances. Additionally, the graphs in Figure 45 indicate a decreasing influence of quasi-saturation with a decreasing ratio R / k. For R / k < $1.012 \cdot 10^{-1}$ no significant differences between fully saturated and quasi-saturated soil are visible.

In summary, fast water level changes in low permeable soils lead to higher excess pore water pressures. A similar relationship between magnitude of pore water pressures and drawdown rate was observed in the model test for quasi-saturated soils and in the pore water pressure measurements from the water storage basin (see chapter 5.4).

3.2.5 Factor of safety after drawdown event

Finally, the influence of the aforementioned ratios (E / K_w and R / k) on the factor of safety (FoS) of the slope is discussed for this numerical study. The FoS is based on a numerical φ'-c'-reduction (Equation 37) used in the FEA.

$$FoS = \frac{tan\varphi'_{input}}{tan\varphi'_{reduced}} = \frac{c'_{input}}{c'_{reduced}} \tag{37}$$

The drawdown event was simulated by means of a fully coupled flow-deformation analysis. The following safety analysis can be performed either as a drained analysis or as an undrained analysis. In the former, the calculated pore water pressures are kept constant during the safety analysis, whereas the latter, leads to constant effective mean stresses. Neither of these methods leads to exactly the same pore water pressures and effective stresses as a fully coupled flow-deformation analysis with reduced strength parameters, corresponding to a FoS = 1.0. Furthermore, the FoS of the drained safety analysis does not coincide with the result from the undrained safety analysis (Blaickner 2017), i.e. both methods only represent an approximation to the true factor of safety.

The main aim of this chapter is the quantification of the influence of the previously studied parameters (stiffness, soil permeability, stage of saturation and drawdown rate) on the factor of safety of the investigated slope, i.e. the resulting FoS are compared to each other. Therefore, it is important that the FoS are determined using the same method (drained or undrained analysis). For the purpose of comparison, the analysis type is of minor interest.

However, the requirement for a constant effective mean stress during an undrained safety analysis is only valid for a fully saturated soil. In the case of a quasi-saturated soil, the effective mean stress also changes during an undrained safety analysis due to the reduced bulk modulus of the pore water, i.e. during the undrained safety analysis, the Mohr circle of a fully saturated soil only reduces its size, whereas the Mohr circle of a quasi-saturated soil reduces its size and shifts to the right. This is shown exemplarily in Figure 46 for a stress point on the sliding surface. The different behaviour of a saturated and a quasi-saturated soil during the undrained safety analysis additionally complicates the comparability of the calculated FoS. Furthermore, the drained safety analyses showed a more stable calculation behaviour than the undrained safety analyses. Thus, the following presented FoS are based on a drained analysis. It should be noted, however, that there might also be differences in the Mohr circle behaviour for a saturated and for a quasi-saturated soil in a drained analysis.

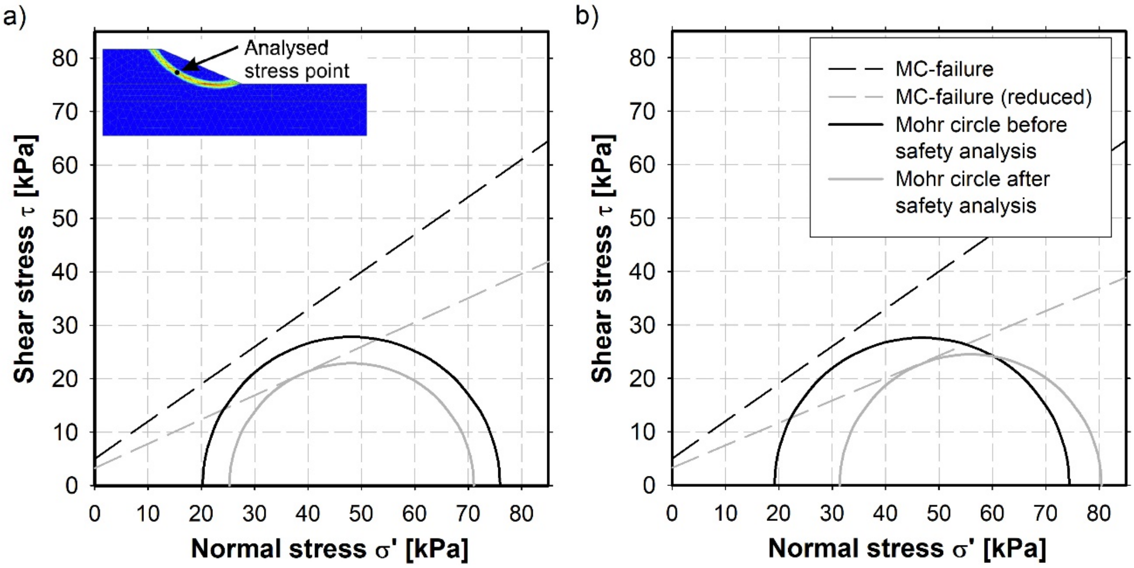

Fig. 46: Mohr circle before and after undrained safety analysis for a) fully saturated soil and b) quasi-saturated soil

Figure 47 presents an overview of the calculated FoS for various combinations of soil stiffness, saturation stage, soil permeability and drawdown rate. The fully saturated stage was again modelled by a pore water bulk modulus of $K_w = 2.4 \cdot 10^6$ kPa. For the quasi-saturated stage, $K_w = 10{,}000$ kPa was assumed. The soil stiffness was varied according to Table 4. All four ratios between drawdown rate and soil permeability R / k were considered for this study concerning the FoS. The strength parameters of the slope material are φ' = 35° and c' = 5 kPa. Considering these strength parameters, a factor of safety FoS = 2.6 (shown with the red line in Figure 47) was calculated for the submerged slope (initial condition).

After the drawdown event, the FoS is reduced to FoS ~ 2.15, considering a low ratio $R / k \sim 10^{-2}$. This already illustrates the significant influence of a drawdown event for the slope stability. Then various parameter combinations further reduce the FoS, as shown in Figure 47.

Interestingly, for low ratios between the drawdown rate and the soil permeability ($R / k \sim 10^{-2}$ and $R / k \sim 10^{-1}$), the FoS is hardly affected by the saturation stage.

However, the change of the drawdown rate from R_{low} = 7 m/80 h to R_{high} = 7 m/8 h in the case of a highly permeable soil ($k = 10^{-4}$ m/sec) reduces the factor of safety significantly from FoS ~ 2.1 to FoS ~ 1.7.

For the fully saturated soil (upper three lines in Figure 47), the factor of safety is almost unaffected by the soil stiffness *E*. This is different for the quasi-saturated soil at high ratios R / k. Due to the increasing excess pore water pressures with increasing soil stiffness (see Figure 44), the drawdown analyses with a high soil stiffness E = 100,000 kPa lead to slope failure. However, the calculations with lower values for the soil stiffness resulted in FoS ~ 1.0.

Furthermore, Figure 47 shows less influence of the ratio R / k on the FoS in case of a low permeability soil ($k = 10^{-7}$ m/sec) than for a highly permeable soil ($k = 10^{-4}$ m/sec).

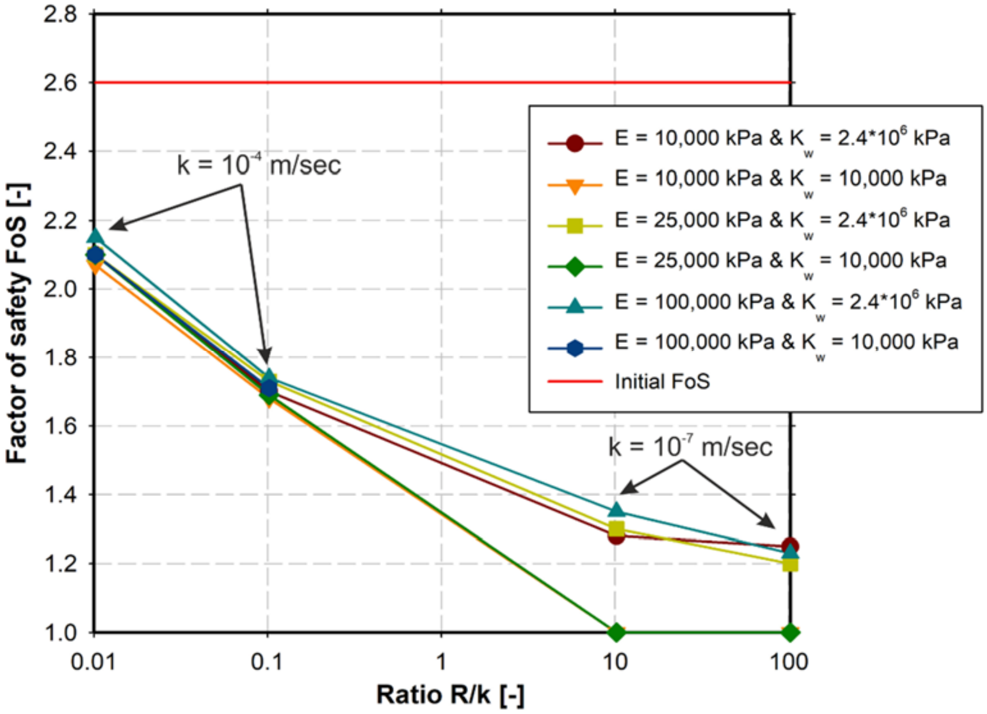

Fig. 47: Factor of safety (FoS) due to drawdown event, according to various parameter combinations

3.3 Summary and conclusions rapid drawdown

The numerical study presented here, concerning drawdown events in the area of dams and slopes confirmed that fast water level changes might lead to excess pore water pressures in the subsoil. This is true for both saturation stages (full saturation and quasi-saturation). In the case of a fully saturated soil, these excess pore water pressures occur mainly in the area of the slope and the slope toe. Under almost one-dimensional conditions, excess pore water pressures are only produced in a quasi-saturated soil. The development of excess pore water pressures under one-dimensional conditions in a quasi-saturated stage was confirmed by the investigations in chapter 2.

The magnitude of the excess pore water pressures in the subsoil depends primarily on the saturation stage beneath the ground water level (bulk modulus of the pore water). The ratio between drawdown rate and soil permeability also has a considerable influence on the pore water pressure development during drawdown events. However, if the soil permeability is high enough, the influences of the saturation stage and of the drawdown rate reduce significantly. In the case of quasi-saturation, the soil skeleton stiffness also influences the excess pore water pressures. The higher the soil skeleton stiffness, the higher the absolute excess pore water pressures. In contrast, the higher the bulk modulus of the pore water (degree of saturation), the lower the absolute excess pore water pressures. Consequently, this means that the influence of quasi-saturation is decreasing with depth, as the degree of saturation (pore water bulk modulus) is increasing with an increasing pore water pressure (see chapter 2.2).

Due to the produced excess pore water pressures, the factor of safety decreases considerably during a drawdown event. As the pore water pressure development is mainly influenced by the aforementioned parameters, the FoS also depends on them. Also for the FoS, the influence of soil skeleton stiffness, saturation stage and drawdown rate is reduced for high soil permeabilities.

According to chapter 2 and chapter 3, the measured excess pore water pressures beneath a water storage basin next to a slow moving landslide (the case presented later) are possible under the assumption of either saturation stages. However, whether the measured excess pore water pressure can be back-calculated without the quasi-saturated stage, and only on the basis of the effects of fast water level changes will depend on several factors, of which the primary two are explained here. Firstly, the location of the measurement device with regard to the slope is important. For example, if the conditions at the monitored area correspond to a one-dimensional behaviour, a back-calculation of the excess pore water pressures without quasi-saturation will be not possible. Secondly, the magnitude of the measured excess pore water pressures has a significant impact on which saturation stage can be considered. For example, if the soil permeability is too high or the drawdown rate is too small, excess pore water pressures in the measured extent will not occur under saturated conditions, even if the measurement devices are located at the slope toe.

The determination of the actual influence of the different parameters, especially of the saturation stage, on the pore water pressures beneath the investigated water storage basin is only possible with a 2D-finite element model, which models the real situation as realistically as possible. This model and the resulting analyses are presented in chapter 6.

4 Constitutive models for lacustrine fine sediments

4.1 Introduction

Slow moving landslides are characterized by small movement rates but progressive displacements. In many cases, the movement rates are not constant but change with time. These changes are due to external influences. The external influences can be seasonal, for example, varying precipitation rates, ground frost or water level changes in rivers at the slope toe of a landslide. Extreme natural events, such as earthquakes and heavy precipitation can be the triggers for an acceleration of the slow moving landslide and might result in a failure of the slope. In addition to natural influences, anthropogenic interventions (e.g. changes in the geometry of the slope, deforestation) might influence the movement rates. Furthermore, the movement behaviour of a landslide is often influenced by particular material characteristics, such as creep, strain softening or ageing phenomena.

One aim of numerical studies of slow moving landslides is to determine a valid back-calculation of the previous slope movements to gain a better understanding of the causes and triggers for the continuous movements. In a second stage, the numerical studies should help to predict the future behaviour of the slow moving landslide. In both cases, constitutive models, which are able to reproduce the effects of the aforementioned external influences and material characteristics on the landslide behaviour, are necessary. However, no available constitutive model incorporates all appropriate features to model the effect of each possible influencing factor. Therefore, the choice of a suitable constitutive model for each particular landslide is crucial. In making the choice of the most appropriate constitutive model, an important factor is the main objective of the numerical analysis. To appropriately model the movement behaviour, to determine the failure probability or model the post failure behaviour, a different constitutive model may be required.

For the following case study, the main objective of the numerical investigations is the determination of the influence of the fluctuating water levels in the water storage basin on the movement rate of the slow moving landslide. Furthermore, additional influencing factors should be identified where possible. In addition to the analysis on the movement behaviour, another objective of the following numerical study on the slow moving landslide is to determine the safety factor depending on the storage operation. Based on this problem definition, an appropriate constitutive model should be selected.

In general, the loading conditions for the investigated landslide with lacustrine fine sediments at the slope toe do not change significantly with time. The main reasons for changing stress states in the soil are the fluctuating water level at the slope toe and the changing infiltration at the ground surface due to the precipitation and evaporation. Therefore, the majority of the stress changes will occur in the unloading-reloading range. Thus, the applied constitutive models for the lacustrine fine sediments at the slope toe must be capable of producing increasing displacements, even though the magnitude of the loads does not change significantly. Creep phenomena can explain an increase of plastic strains, i.e. increasing displacements under the aforementioned conditions. Therefore, the Soft Soil Creep model (Vermeer & Neher 1999) is applied for the lacustrine fine sediments in the case study. The Soft Soil Creep model (SSC model) is an elasto-viscoplastic model that accounts for creep.

In addition, for comparison purposes, the Hardening Soil model (Schanz 1998, Schanz et al. 1999) and the Hardening Soil Small model (Benz 2007) are applied for the lacustrine fine sediments.

A short overview of the three applied constitutive models is presented in the following chapters. Special attention is given to the SSC models ability to simulate continuous displacements as they really occur in slow moving landslides. To demonstrate this, the behaviour of the SSC model during a cyclic loading is investigated in a preliminary study, where a recurring loading is applied to a biaxial test under partial drainage conditions.

4.2 Hardening Soil model and Hardening Soil Small model

The Hardening Soil model (HS model) and the Hardening Soil Small model (HSS model) are commonly known and have already been described several times in literature (e.g. Benz 2007, Tschuchnigg 2013, Brinkgreve et al. 2016). Therefore, only a very brief introduction is provided in this thesis. The HSS model is based on the HS model. In addition to the features of the HS model, the HSS model incorporates the effect of a high stiffness at small strains (small strain stiffness).

The HS model and the HSS model are double hardening models (compression and shear hardening) with a stress dependent stiffness. A different stiffness is used for stress paths in primary deviatoric loading (stiffness parameter E_{50}), in primary oedometric loading (stiffness parameter E_{oed}) and in the un- / reloading range (stiffness parameter E_{ur}). Furthermore, an increased stiffness is applied for small strains (stiffness parameter G_0 or E_0) in the case of the HSS model. The definition of the different stiffness parameters is shown in Figure 48. It should be noted, however, that the HS model only considers one un- / reloading stiffness during an un- / reloading stress path, i.e. the hysteresis loop shown in Figure 48 for the un- / reloading range (used in the HSS model) does not exist in the HS model. All stiffness parameters are stress dependent. Stress dependency is defined by the power m according to Equation 38 and Equation 39 for the primary loading and the oedometric loading, respectively (Brinkgreve et al. 2016). Equation 38 is also valid for the un- / reloading stiffness (replacing E_{50} with E_{ur}).

$$E_{50} = E_{50}^{ref} \cdot \left(\frac{c \cdot cos\varphi + \sigma'_3 \cdot sin\varphi}{c \cdot cos\varphi + p^{ref} \cdot sin\varphi}\right)^m \tag{38}$$

$$E_{oed} = E_{oed}^{ref} \cdot \left(\frac{c \cdot cos\varphi + \frac{\sigma'_3}{K_0^{nc}} \cdot sin\varphi}{c \cdot cos\varphi + p^{ref} \cdot sin\varphi}\right)^m \tag{39}$$

A hyperbolic stress-strain relationship is used in primary loading in a drained triaxial test (Figure 48). The failure criterion is formulated according to Mohr-Coulomb in the HS model and the HSS model.

The flow rule of the deviatoric yield surface is non-associated. However, for the cap yield surface (volumetric yield surface) an associated flow rule is used.

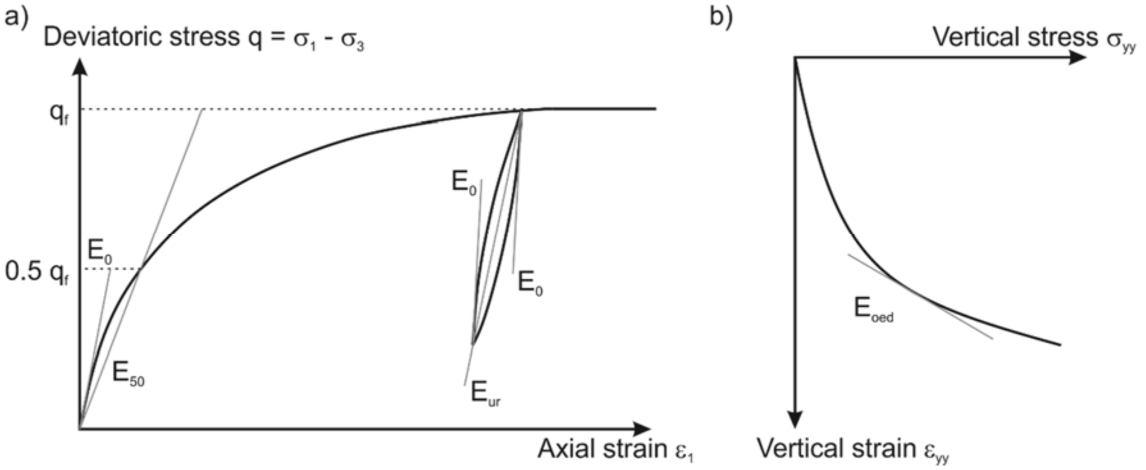

Fig. 48: Stiffness parameters of the HSS model in a a) standard drained triaxial test and b) oedometer test (after Brinkgreve et al. 2016)

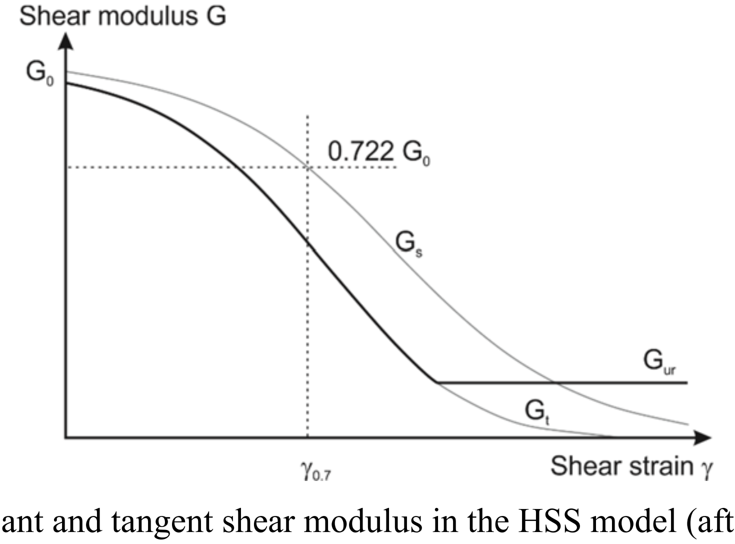

Fig. 49: Secant and tangent shear modulus in the HSS model (after Brinkgreve et al. 2016)

In the HSS model, the small strain stiffness decreases with increasing strain magnitude. The typical non-linear relationship between shear modulus and shear strain, as shown in Figure 49, is defined in the HSS model by the initial small strain stiffness shear modulus G_0 and the shear strain level $\gamma_{0.7}$, where the secant shear modulus G_s is decreased to about 70% of the initial shear modulus G_0. The lower threshold of the tangent shear modulus G_t is defined by the un- / reloading shear modulus G_{ur}.

4.3 Soft Soil Creep model

Thee SSC model has been also described in detail in literature (e.g. Vermeer & Neher 1999, Vermeer & Leoni 2005, Benz 2012). Therefore, only a short introduction is given in the context of this thesis. The SSC model is a 3D-model, which was developed as an extension of conventional 1D-creep models (Bjerrum 1967, Garlanger 1972, Butterfield 1979). To obtain the SSC model, a differential equation for 1D conditions was derived (Vermeer & Neher 1999). This derivation of the differential equation is based on the assumption that all inelastic strains are time dependent. Furthermore, an increasing pre-consolidation stress with accumulated creep strains is assumed (Vermeer & Neher 1999).

To extend the 1D-formulation to a three dimensional stress space, the equivalent isotropic stress p'_{eq} is introduced on the basis of the effective mean stress p' and the deviatoric stress q (Vermeer & Neher 1999).

$$p'_{eq} = p' + \frac{q^2}{M^2 \cdot p'} \tag{40}$$

The current stress state is situated on the ellipsoid associated to the equivalent isotropic stress p'_{eq}. However, the normally consolidated state is characterized by an ellipsoid associated to the pre-consolidation stress p'_p. According to the 1D-model, the pre-consolidation stress is increasing with accumulated volumetric creep strains ε^c_{vol} (Vermeer & Neher 1999), shown with Equation 41.

$$p'_p = p'_{p0} \cdot exp\left(\frac{\varepsilon^c_{vol}}{\lambda^* - \kappa^*}\right) \tag{41}$$

The definition of the ellipsoids representing the current stress state (CSS – p'_{eq}) and the normal consolidation state (NCS – p'_p) is according to the Soft Soil model (Brinkgreve et al. 2016). The parameter M defines the height of the ellipsoid and is described in Brinkgreve et al. (2016). The ellipsoids are shown in Figure 50.

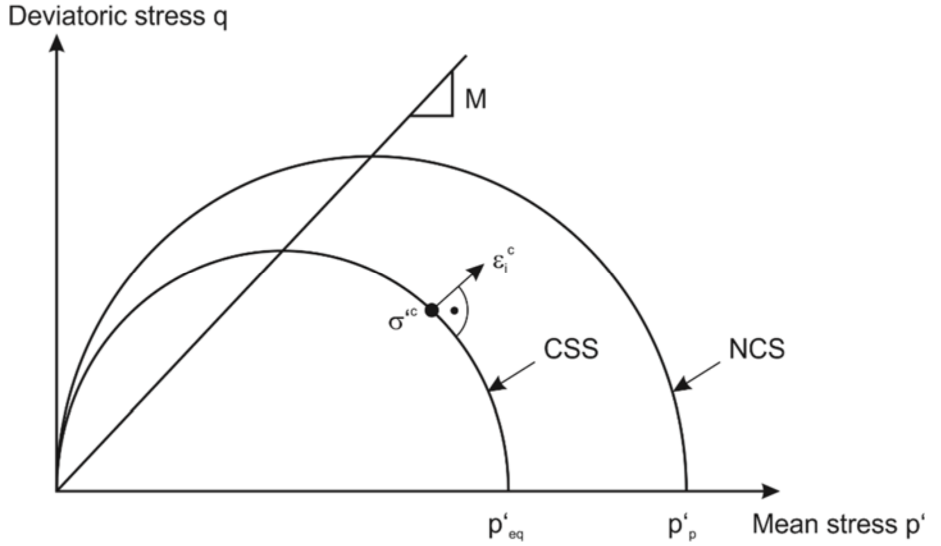

Fig. 50: State surfaces in the SSC model (after Vermeer & Leoni 2005, Brinkgreve et al. 2016)

In the case of the 3D-formulation (Vermeer & Neher 1999), the volumetric creep strain rate is calculated with

$$\dot{\varepsilon}_{vol}^{c} = \frac{\mu^*}{\tau}\left(\frac{p'_{eq}}{p'_p}\right)^{\frac{\lambda^*-\kappa^*}{\mu^*}} \tag{42}$$

As can be seen from Equation 42, the volumetric creep strain rate $\dot{\varepsilon}_{vol}^{c}$ depends on the ratio between the equivalent isotropic stress p'_{eq} and the pre-consolidation stress p'_p, which is also expressed by the overconsolidation ratio OCR = p'_p / p'_{eq}. In other words, the distance between the two ellipsoids (CSS and NCS) determines the magnitude of the creep rate (Vermeer & Leoni 2005).

For the definition of the entire strain rate vector, reference is made to Vermeer & Neher (1999).

The stiffness of the SSC model is defined by the modified compression index λ^* and the modified swelling index κ^*. These parameters can be obtained from an isotropic compression test with an isotropic unloading. The parameter definition is shown in Figure 51. The modified creep index μ^* is determined by plotting the volumetric strains over the logarithm of time.

Failure is formulated according to Mohr-Coulomb in the SSC model. Stress states at the Mohr-Coulomb failure surface lead to instantaneous plastic strains (Brinkgreve et al. 2016).

Generally, an associated flow rule is applied. However, the flow rule for stress states on the Mohr-Coulomb failure surface is non-associated.

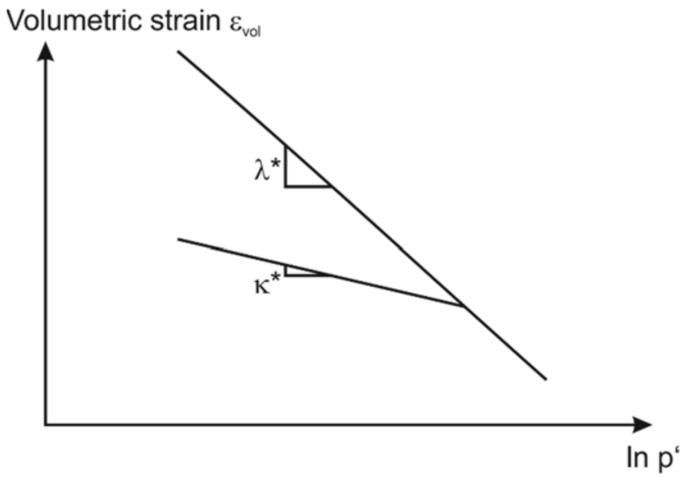

Fig. 51: Stiffness definition in the SSC model (after Brinkgreve et al. 2016)

4.4 Preliminary study on deformation behaviour in a biaxial test with un- / reloading cycles

In this study, the deformation behaviour due to a recurring loading under partially drained conditions was studied on a simple biaxial test. A changing vertical load simulates the recurring loading. The SSC model is applied as constitutive model for the biaxial test. The main focus of this numerical study is on the development of deformations with time (loading cycles). The aim is to clarify, whether the SSC model is able to simulate increasing displacements due to similar recurring loading patterns (as will be presented for the case study in chapter 6).

4.4.1 Numerical model and material parameters

The FE-model of the biaxial test is shown in Figure 52. The model dimensions are 0.25 x 1.0 m. Stiff plates (with a linear-elastic material) are considered at the top and the bottom of the soil specimen to obtain non-uniform stress states. Furthermore, a flow at the top boundary is possible. All other boundaries are impermeable. Plane strain conditions and model symmetry are assumed. After a drained, isotropic loading with $\sigma'_v = \sigma'_h = 100$ kPa is established, the vertical load is increased and decreased by $\Delta\sigma = 50$ kPa. Fifteen loading-unloading cycles are simulated in a fully coupled flow-deformation analysis. One loading-unloading cycle lasts 0.66 days. The change of the vertical load with time is shown in Figure 52.

The material parameters are chosen similar to the parameters presented for the lacustrine fine sediments in chapter 5.3. Table 7 summarizes the parameters for the SSC model.

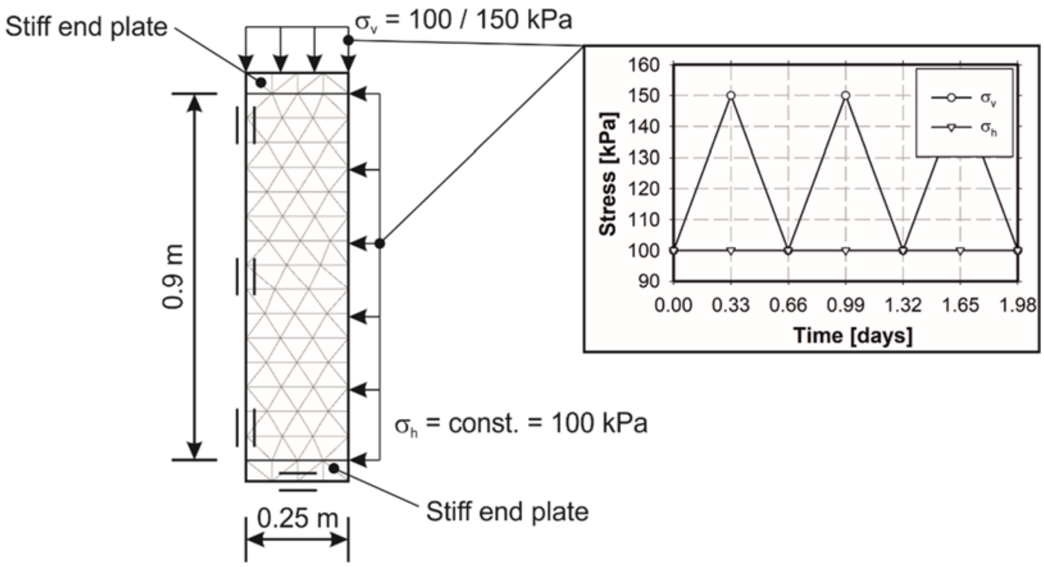

Fig. 52: Biaxial model for preliminary study – deformation behaviour in a biaxial test (120 15-noded elements)

Tab. 7: Material parameters for the preliminary study – deformation behaviour in a biaxial test: SSC model

Parameter	Unit	Soft Soil Creep
γ_{unsat}	kN/m³	19.0
γ_{sat}	kN/m³	20.0
λ^*	-	0.013
κ^*	-	$4.8 \cdot 10^{-3}$
μ^*	-	$0.6 \cdot 10^{-3}$
ν‘	-	0.15
φ‘	°	27.5
c‘	kPa	3.0
ψ‘	°	0.0
$k_x = k_y$	m/sec	10^{-7}

4.4.2 Deformation behaviour in biaxial test under recurring loading

To evaluate the deformation behaviour, the total displacements at the top of the soil specimen in the axis of symmetry are analysed. Figure 53 presents the results for the SSC model.

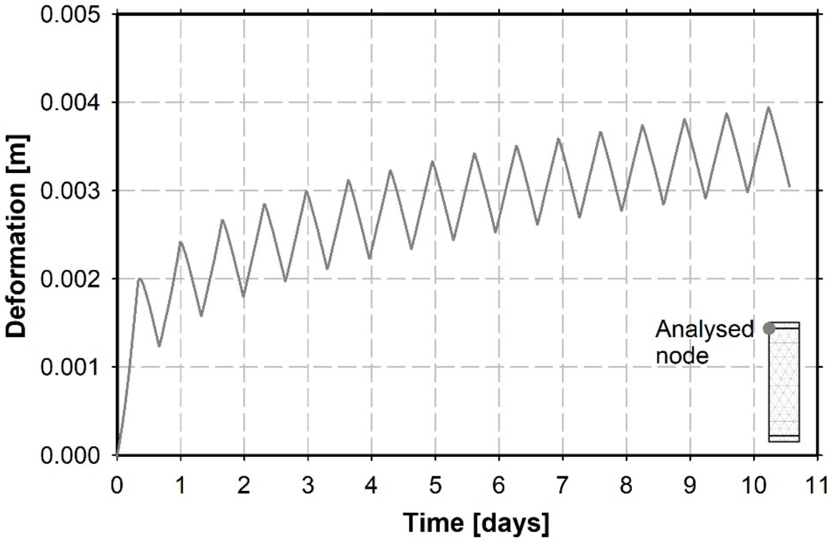

Fig. 53: Deformation behaviour in biaxial test

An evaluation of the numerical calculated pore water pressures showed that after approximately four days, the fluctuations of the pore water pressures due to the changing load show a constant upper and lower limit (see Figure 54). Consequently, after four days, additional plastic deformations due to dissipating excess pore water pressures can be neglected.

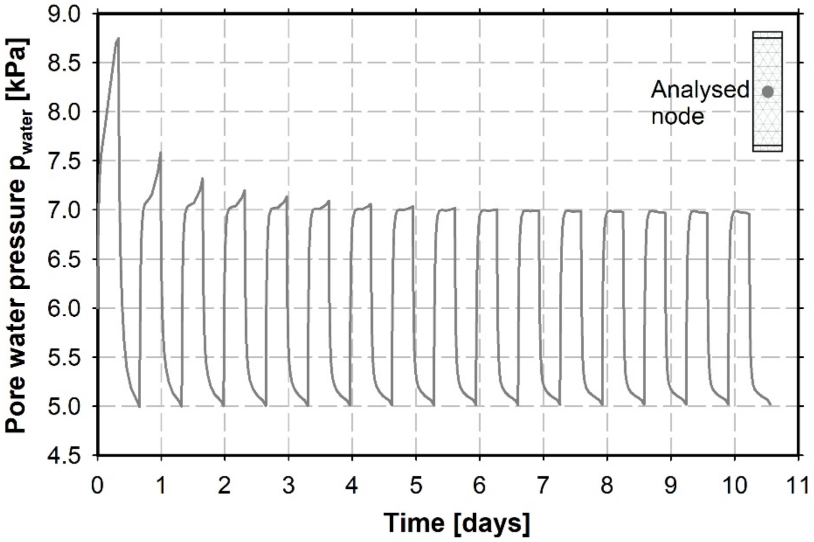

Fig. 54: Pore water pressures in biaxial test

The SSC model shows the expected behaviour. Plastic deformations occur with time due to the time-dependent formulation (creep). The amount of additional plastic strains per cycle is decreasing with increasing time, i.e. a decreasing displacement rate with time. This is due to the increasing pre-consolidation stress p'_p with creep strains ε_{vol}^{c} (Equation 41). This leads to an increase in the overconsolidation ratio and therefore, to a decrease in the creep rate (Equation 42). The increase in the pre-consolidation stress and the isotropic overconsolidation ratio for a randomly selected cycle (14th cycle) is shown in Figure 55.

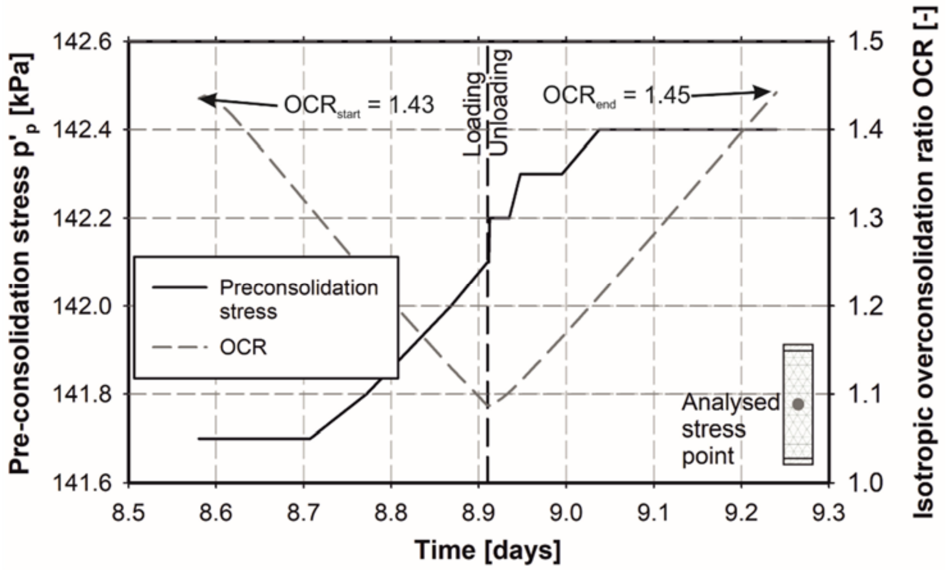

Fig. 55: Pre-consolidation stress and isotropic overconsolidation ratio during 14th cycle in biaxial test

The decreasing displacement rate results from the formulation of the constitutive model. For a validation of this behaviour based on the later presented measurements the observation period is too short. Therefore, the deformations of the lacustrine fine sediments and furthermore, of the slow moving landslide should be not simulated over multiple years with the SSC model. It is necessary, therefore, to determine the initial conditions (isotropic overconsolidation ratio) in such a way that the following calculations lead to almost constant displacement rates, at least for the period (max. one year in the following FEA) of the simulation.

While the SSC model is used for the case study, the deformations of the slow moving landslide are also back-calculated with the HS model and the HSS model for purposes of comparison.

5 Presentation of a slow moving landslide next to a water storage basin

5.1 Introduction

This chapter introduces the case study mentioned before. During extension works at a water storage basin for a pumped-storage power plant, slope movements at an adjacent slope were observed. This led to the installation of a comprehensive monitoring system comprising of inclinometers, extensometers, geodetic measurements and pore water pressure gauges. The installation of the monitoring system was accompanied by subsurface exploration (core drillings). The measurement devices have been installed for two reasons. First, to enable a continuous monitoring of the movement behaviour in order to detect unfavourable changes at an early stage, and second, to determine, in combination with numerical analyses, the triggers and mechanisms of the slow moving landslide. Based on the identified triggers and mechanisms, possible stabilization measures for the slow moving landslide are then investigated (which is not part of this thesis).

The theoretical background for the identification of the triggers and for the description of the major mechanisms leading to the continuous slope movements of this case study have been presented in the course of this thesis (chapter 2 to chapter 4). Based on the theoretical background, the following issues concerning the behaviour of a landslide adjacent to a water storage basin will be discussed in this and the following chapter.

- **Influence of water level changes in a water storage basin on the movement behaviour of a slow moving landslide**

  Field measurements revealed a relationship between the operation of the water storage basin and the movement rates of the landslide. Based on these observations, it is to be investigated how the water level changes in the storage basin influence the movement behaviour of the landslide. In this context, the connection between the water level changes and the measured excess pore water pressures is studied. Furthermore, the reason for the excess pore water pressures is determined. Finally, the influence of the water level changes on the factor of safety of the landslide is to be determined.

- **Further influences on slope movements**

  The influence of the precipitation and the creep behaviour of the lacustrine fine sediments on the slope movements is to be determined. By means of numerical studies, the quantitative influence of the different factors (water level changes, precipitation, creep) is to be determined.

- **Possible stabilization measures**

  The effect of selected stabilization measures for a reduction of the movement rate is discussed.

The presented issues are solved by combining the findings from field measurements with the insights from numerical analyses. Due to this combination the numerical model can be verified by field measurements. Subsequently, the system behaviour can be investigated by means of the numerical model. Furthermore, the influence of various factors can be determined by parametric studies.

In this chapter, after an introduction to the specific site, the results of the performed laboratory tests on samples of the lacustrine fine sediments are presented. Based on these results, the material parameters are determined for selected constitutive models, which will subsequently be used for the numerical analyses. Furthermore, selected results from the field measurements are presented in this chapter. Based on the field measurements, possible relationships between the water level changes in the storage basin and the movement rates of the slope are derived. The influence of the precipitation on the slope movements is investigated by comparing different measurement quantities. The effects of a possible creep behaviour of the lacustrine fine sediments are neglected in this chapter but it is investigated by means of numerical analyses in chapter 6. Possible reasons for the measured transient excess pore water pressures at the slope toe are also investigated in chapter 6 by means of numerical studies considering the effects of a quasi-saturated stage and of a rapid drawdown.

For the purpose of this thesis some minor simplifications have been made. Thus, a direct application of the outcomes from this thesis (chapter 5 and chapter 6) to the real project is not possible.

5.2 Site description

The pumped-storage power plant with the associated water storage basin is located in the Hohen Tauern, a region in the Central Eastern Alps. The dimensions of the water storage basin are roughly 400 x 100 m. The volume of the storage basin is roughly 300,000 m^3. Due to the operation of the power plant, the water level in the storage basin changes up to three times a day and the maximum change in water level is ~7.5 m. Figure 56 shows typical water level changes.

The length of the slow moving landslide is roughly 270 m. Movements were detected across a width of 220 m. The sliding surfaces were detected by inclinometer measurements between 20 and 40 m below ground surface in the lower part of the slope. Assuming the sliding surface becomes shallower in the upper part of the slope and that the average depth of the sliding surface is 20 m, the volume of the slow moving slope is estimated with 1.2 Mio. m^3. The inclination of the slope is 30° on average. Figure 57 shows a plan view and a side view of the storage basin and the slow moving landslide with a rough indication of the area with slope movements. The installed measurement devices are also indicated in Figure 57.

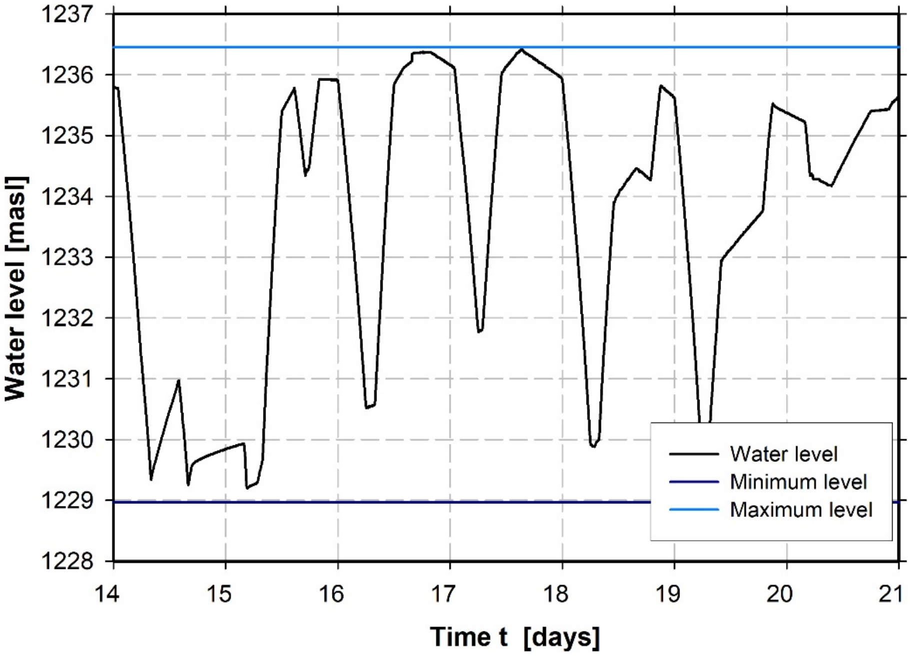

Fig. 56: Typical water level changes in the water storage basin

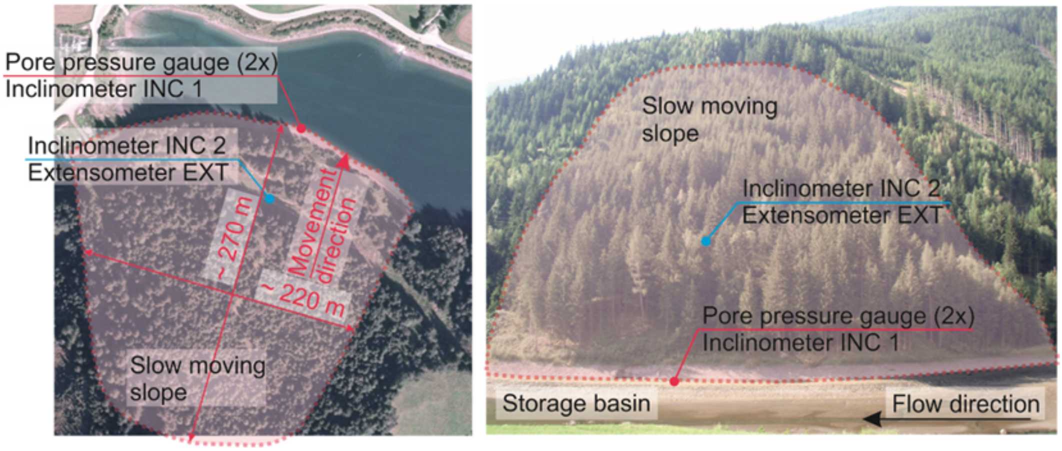

Fig. 57 Plan view and side view of water storage basin and slow moving slope

The subsurface explorations showed a sliding mass consisting mainly of weathered and sheared rock. Beneath the slope toe and beneath the water storage basin are fine laminated lacustrine fine sediments, consisting mainly silt. Figure 58 shows a schematic cross section of the slow moving landslide and the water storage basin with the relevant soil layers. This is the cross section used for the FEA. Figure 59 presents the observed range for the grain size distribution of the lacustrine fine sediments from varying depths. Furthermore, an image of a drill core with the fine layers of the fine sand is shown in Figure 59. The amount of fines is increasing with depth.

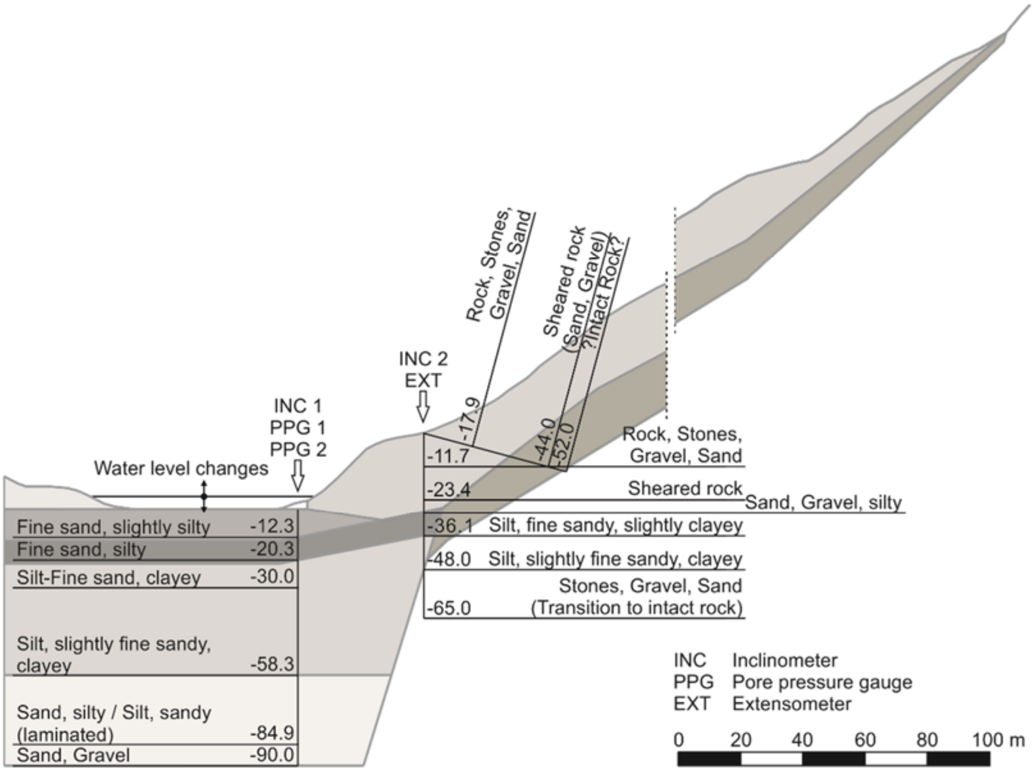

Fig. 58 Section of water storage basin and slow moving slope

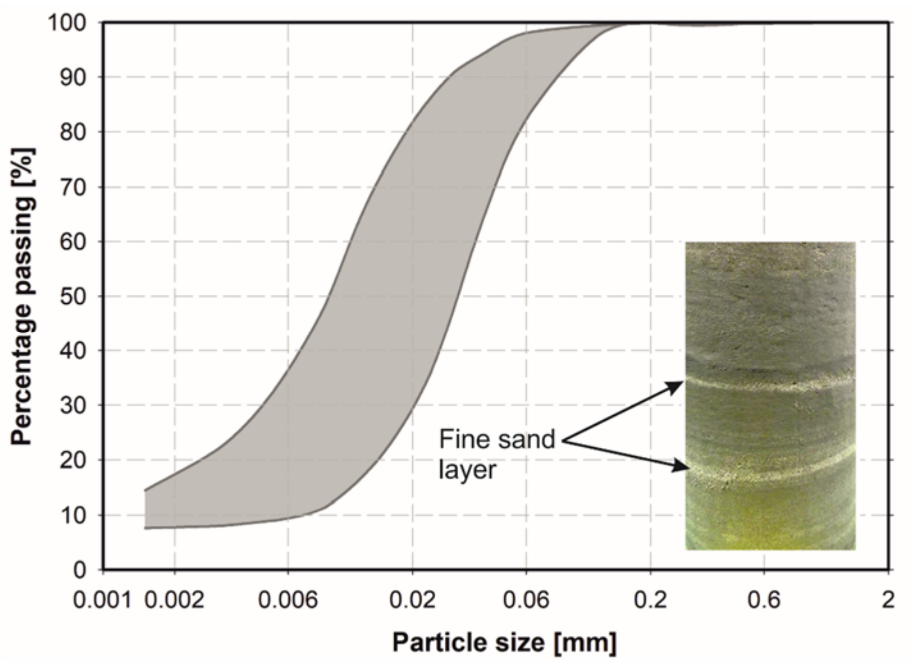

Fig. 59: Range of the grain size distribution of lacustrine fine sediments from varying depths

5.3 Laboratory tests and parameter definition

A subsurface exploration of this site was undertaken in 2014, from which several samples from drill cores were taken. The samples were only taken from the soil layers with lacustrine fine sediments (borehole INC 1 from -12.3 m to -58.3 m below ground surface) as the main sliding surfaces were detected in these layers. Furthermore, the sampling from the top layers with fine sand proved difficult. Laboratory tests were performed on these samples to determine permeability, soil stiffness and strength parameters. Furthermore, sieve analyses were performed to determine the grain size distribution in various depths (see Figure 59). Figure 60 shows the sample locations with their associated depths below the ground surface. Table 8 presents an overview of the laboratory tests used to determine the hydraulic and mechanical material parameters.

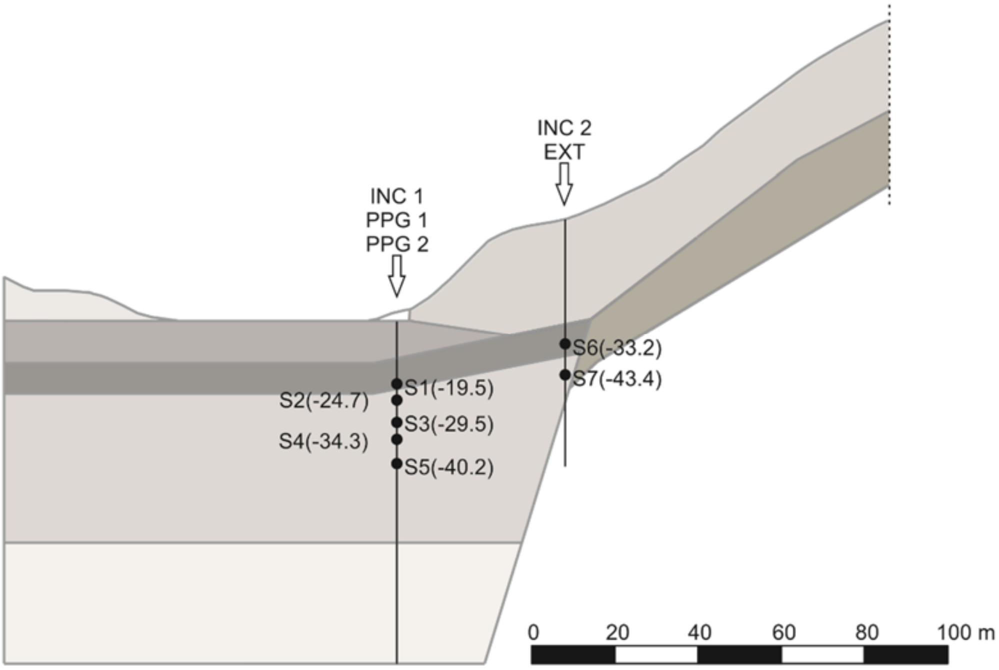

Fig. 60: Overview of samples from drill cores

In addition to laboratory tests for determining the hydraulic and mechanical parameters of the soil material, tests to determine the physical parameters (e.g. density, porosity, plasticity index) were performed, and their results are summarized here. The average particle density of the lacustrine fine sediments is $\rho_s = 2.80$ g/cm³. The average soil density was determined as $\rho_{dry} = 1.50$ g/cm³. Hence, the average porosity results as $n = 0.46$. The plasticity index of the lacustrine fine sediments was tested as PI = 2.5-11.5.

5.3.1 Soil permeability

The soil permeability of the lacustrine fine sediments was tested using triaxial permeability cells. The setup included a specimen height of 12 cm and a hydraulic gradient of 30. The soil permeability of sample S3 perpendicular to the fine soil layers was determined as $k = 7 \cdot 10^{-9}$ m/sec. The permeability test of sample S7 (situated in the silt layer) resulted in $k = 10^{-8}$ m/sec perpendicular to the soil layers. Both values were determined under saturated conditions.

Tab. 8: Laboratory tests performed on samples from drill cores

Borehole	Sample #	Depth	Laboratory test
INC 1	S1	-19.5	Direct shear test Undrained triaxial compression test
	S2	-24.7	Direct shear test
	S3	-29.5	Undrained triaxial compression test Oedometer test Permeability in a triaxial cell
	S4	-34.3	Oedometer test
	S5	-40.2	No laboratory tests performed
INC 2	S6	-33.2	Direct shear test
	S7	-43.4	Undrained triaxial test Oedometer test Permeability in a triaxial cell

In general, the exact determination of the soil permeability of fine laminated soils is difficult for the following two reasons. First, the soil permeability is significantly different for a flow perpendicular or parallel to the fine soil layers. Second, the theoretically calculated hydraulic gradient is only an average value as it changes between the low permeable and the high permeable layers (Scherzinger 1991). To consider the different permeability for different flow path directions with regard to the soil layers, the soil permeability parallel to the soil layers (in horizontal direction) was assumed to be a factor 10 higher than the soil permeability in vertical direction. The factor of 10 was determined by engineering judgement. However, the fact that the calculated permeability is only an average value due to the averaged hydraulic gradient does not matter for the following numerical studies, as the fine layers of the soil are not modelled explicitly, i.e. the numerical model also considers an averaged permeability. Furthermore, comprehensive laboratory tests on artificial specimen with a homogeneous structure and different soil layers showed that the permeability perpendicular to the soil layers is mainly influenced by the permeability of the lowest permeable layer (Daghighi 2016).

The permeability of the sliding mass was not determined in laboratory tests due to difficulties in sampling. Furthermore, as the joints and fractures in the sheared rock mainly influence the permeability of the sliding mass, the determination of its permeability based on single samples is not reliable. However, during the drilling works for bore hole INC 2 no groundwater level was detected in the sliding mass and a continuous air flow in the bore hole was observed. Both observations suggest a high permeability. Therefore, the saturated permeability of the sliding mass was estimated as $k = 10^{-3}$ m/sec for the FEA.

The permeability of the other soil layers was estimated based on the grain size distributions.

5.3.2 Stiffness parameters

Stiffness parameters were derived from oedometer tests. In addition, the results of undrained triaxial compression tests were used to verify the determined stiffness parameters.

The oedometer tests were performed as multiple stage loading tests with loading periods of 24 h on saturated samples. As shown in Table 8, oedometer tests were performed on three samples. All three of these samples were situated in the soil layer composed of higher amounts of silt and clay. However, the results from the three oedometer tests (Figure 61) showed significant differences. Sample S3 especially showed a considerably different behaviour. These differences might be due to problems during the sampling and the significant influence of the high deformations in the subsoil. Therefore, only averaged stiffness parameters could be determined.

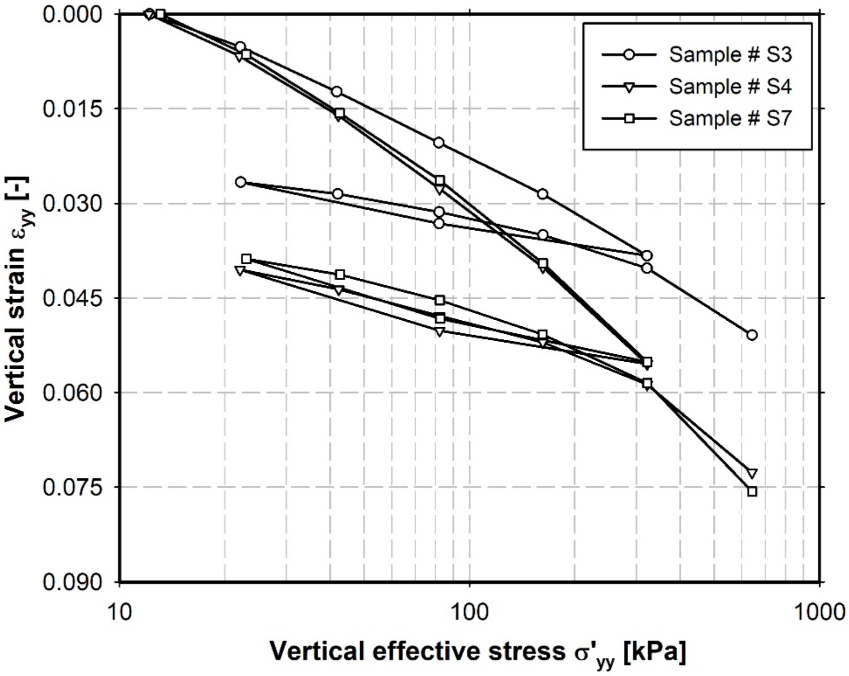

Fig. 61: Results from oedometer tests on sample S3, S4 and S7

The stiffness parameters for the SSC model are based on the results of the oedometer tests. However, a direct determination of the modified compression index λ^* and the modified swelling index κ^* from an oedometer test is not possible. In general, these parameters are determined from an isotropic compression test by plotting the volumetric strain over the logarithm of the effective mean stress. In accordance with this definition, for the determination of the modified compression index, a normally consolidated K_0-stress path during the oedometer test was assumed in order to determine the effective mean stress *p'* from the vertical effective stress σ'_{yy}. The earth pressure coefficient was calculated with $K_0 = 1 - \sin\varphi'$. The friction angle was assumed as $\varphi' = 35°$. This yields to the effective mean stress during primary loading

$$p' = \frac{\sigma'_{yy} \cdot [1 + 2 \cdot (1 - \sin\varphi')]}{3} \tag{43}$$

The determination of the modified swelling index κ^* is more difficult, as no normal consolidated K_0-value can be assumed during the un- / reloading. Therefore, the modified swelling index was back-calculated by modelling the laboratory tests in PLAXIS 2D. Furthermore, common ratios λ^* / κ^* from literature (Vermeer & Neher 1999, Vermeer & Leoni 2005) were used to estimate the modified swelling index.

The modified creep index μ^* is obtained by plotting the volumetric strain over the logarithm of time. Due to small measurement inaccuracies during the oedometer test, this approach occasionally leads to a high scattering of the determined modified creep indices. Therefore, a similar approach, as presented by Havel (2004), was chosen. In this approach, the plot of volumetric strains over time was approximated by a function with an equation of the following form.

$$\varepsilon_{vol} = \mu^* \cdot ln(t) + \varepsilon_{vol,0} \tag{44}$$

The modified creep index μ^* can be derived directly from Equation 44.

Applying the described procedures for the determination of stiffness used in the SSC model, the stiffness parameters for the SSC model are determined as $\lambda^* = 0.013$, $\kappa^* = 4.8 \cdot 10^{-3}$ and $\mu^* = 0.6 \cdot 10^{-3}$. The ratio $\lambda^* / \kappa^* \sim 3$ falls outside the proposed range of $\lambda^* / \kappa^* = 5\text{-}10$ according to Vermeer & Neher 1999, but is at the lower limit of the proposed range according to Brinkgreve et al 2016 ($\lambda^* / \kappa^* = 2.5\text{-}7$). However, some oedometer tests showed an even higher swelling index, which is considerably higher than the commonly known values for similar soils. The ratio $\lambda^* / \mu^* \sim 22$ is within the proposed range ($\lambda^* / \mu^* = 15\text{-}25$) according to Vermeer & Neher (1999). Figure 62 shows typical time-strain curves from an oedometer test and compares the test result with the approximation according to Equation 44 in order to determine the modified creep index. However, especially during the first minutes of the test, the approximation of the time-strain curve with a function of a natural logarithm (see Equation 44) is sometimes unsatisfactory. The reason for this is the fast consolidation of the sandy, clayey silt (at this site) compared to a pure clay, for which this evaluation is usually applied (Head & Epps 2011). This first part of the time-strain curve should, therefore, be neglected for the determination of the modified creep index.

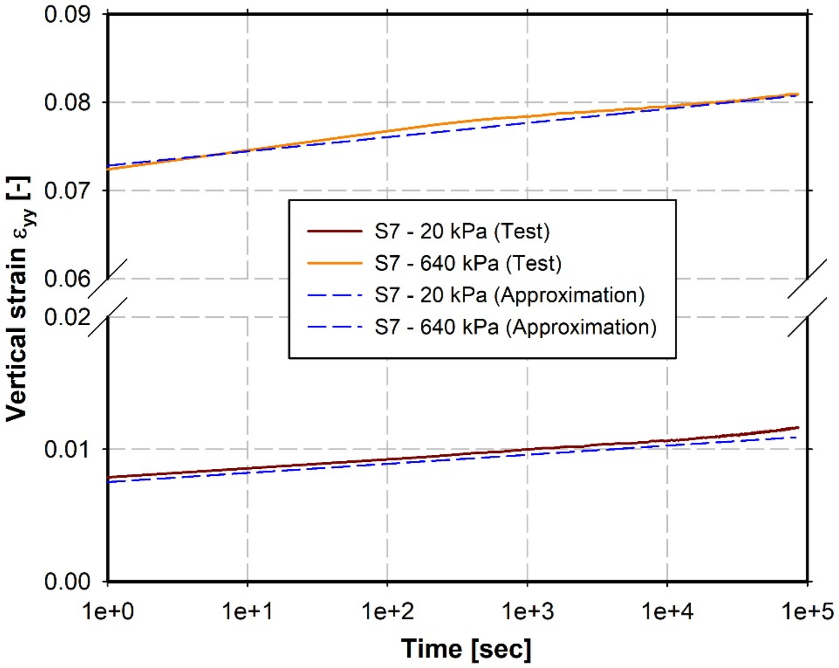

Fig. 62: Time-strain curve for selected load stages on sample S7

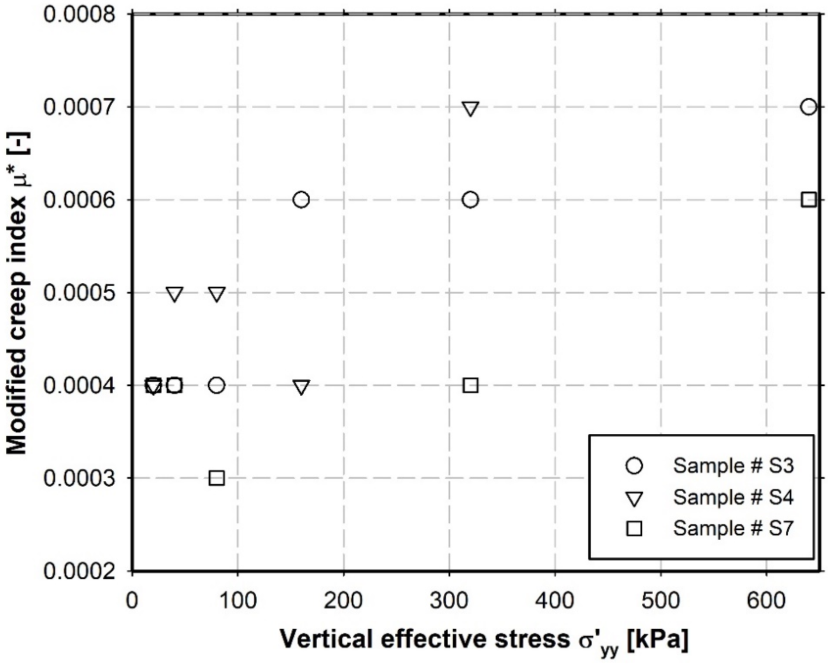

Fig. 63: Development of the modified creep index μ^* with increasing vertical effective stress in oedometer test

When the modified creep index is plotted over the vertical stress, usually a significant increase of the modified creep index at the transition from the overconsolidated state to the normally consolidated state is observed (Havel 2004). This high value is used as an input value for the SSC model as it represents the initial creep behaviour in a normally consolidated state. However, this significant increase of the modified creep index at a specific vertical effective stress was not observed in the analysed oedometer tests as shown in Figure 63. Instead, only a consistent small increase in the creep index could be recognized for the loading stage from $\sigma'_{yy} = 320$ kPa to $\sigma'_{yy} = 640$ kPa. This range for the vertical stress roughly corresponds to the theoretical overburden pressure at approximately 35 m depth. The samples for the oedometer tests were taken from depths between 29 m and 40 m. However, the sampling process, the progressive creep deformations in the subsoil and the loading history might also have an influence on the present overconsolidation. Nevertheless, the oedometer test results for the range of $\sigma'_{yy} = 320\text{-}640$ kPa were used to specify the modified creep index as $\mu^* = 0.0006$.

The reference oedometer stiffness $E_{oed,ref}$ at a vertical effective stress $\sigma'_{yy} = 100$ kPa for the HS model and the HSS model was determined directly from the stress-strain curve as shown in Figure 48 (chapter 4.2). According to this, the oedometer stiffness for the HS model and the HSS model was specified, based on the laboratory tests, as $E_{oed} = 7{,}000$ kPa. The primary loading stiffness E_{50} and the un- / reloading stiffness E_{ur} for both models were estimated based on the oedometer stiffness and the fitting of the results from numerical back-calculations to the results from undrained triaxial compression tests ($E_{50} = 12{,}000$ kPa & $E_{ur} = 36{,}000$ kPa). The parameter m, which defines the stress dependency of the stiffness was assumed as m = 1.0.

The small strain stiffness G_0 for the HSS model was derived from correlations in literature. Kim & Novak (1981) proposed the following correlation.

$$G_0 = C_0 \cdot \frac{(2.973-e)^2}{1+e} \cdot \bar{\sigma}^{\bar{n}} \qquad (45)$$

C_0 and $\bar{n}$ are correlation factors and were assumed according to Kim & Novak (1981) for a silt as $C_0 = 1200$ and $\bar{n} = 0.65$. The void ratio from the considered sample was determined in the laboratory as e = 0.81-0.92. $\bar{\sigma}$ is the in-situ confining pressure and was calculated by the overburden pressure and $K_0 = 1 - \sin\varphi'$.

Pestana & Salvati (2006) presented a correlation to determine the small strain stiffness of sands. Although the amount of sand is low, this correlation was also used for the lacustrine fine sediments.

$$G_0 = G_b \cdot 100 \cdot e^{-1.3} \cdot \left(\frac{p'}{100}\right)^{\hat{n}} \qquad (46)$$

G_b and $\hat{n}$ are again correlation factors and were assumed according to Pestana & Salvati (2006) as $G_b = 360$ and $\hat{n} = 0.5$. e is the void ratio and p' is the effective mean stress, which was calculated again under the assumption of a normal consolidated soil with $K_0 = 1 - \sin\varphi'$.

Benz (2007) (after Hardin & Black 1969) proposed the following correlation amongst others

$$G_0 = 33{,}000 \cdot \frac{(2.973-e)^2}{1+e} \cdot \left(\frac{p\prime}{100}\right)^{0.5} \tag{47}$$

These presented correlations (Equation 45 to 47) resulted in a wide scattering of calculated values for the small strain stiffness. Table 9 summarizes the lower and the upper limits of the reference small strain stiffness $G_0^{\sigma 3=100kPa}$ from the different correlations. As the oedometer tests of this soil also resulted in stiffness parameters at the lower limit, considering stiffness parameters for similar soils, it seemed reasonable to use the lower limit of the reference small strain stiffness $G_0^{\sigma 3=100kPa}$ = 45,000 kPa. The parameter $\gamma_{0.7}$ for defining the degradation of small strain stiffness with increasing shear strains in the HSS model was assumed as $\gamma_{0.7} = 2 \cdot 10^{-4}$ for the lacustrine fine sediments (e.g. according to Likitlersuang et al. 2013).

Tab. 9: Lower and upper limits of small strain stiffness of the lacustrine fine sediments based on published correlations

Correlation	Lower limit	Upper limit
Kim & Novak (1981)	50,000 kPa	56,000 kPa
Pestana & Salvati (2006)	44,000 kPa	48,000 kPa
Hardin & Black (1969)	80,000 kPa	87,000 kPa

Usually, slightly higher stiffness parameters are used with the HS model and the HSS model for the modelling of similar lacustrine fine sediments (Schweiger & Breymann 2005). However, the HS model and the HSS model have not yet been applied for soils from this specific location or for the analysis of a slow moving landslide in this area. Therefore, the low stiffness values presented above are also used for the following FEA.

To verify the determined parameters, selected laboratory tests (oedometer tests on sample S3 and S4 and an undrained triaxial compression test on sample S1) were back-calculated with PLAXIS 2D. The HS model, the HSS model and the SSC model were used for the back-calculation.

In the case of the oedometer tests, the numerical results are compared with the test results from sample S3 and S4. These two test results represent the upper and the lower limit of all odeometer test results. As can be seen in Figure 64, the numerical results are approximately between the two test result curves, but a better match between numerical and measured results can be observed for the stiffer sample

(S3). The three different constitutive models lead to almost the same results. The HSS model is slightly stiffer in the primary loading range, whereas the SSC model shows a stiffer behaviour in the un- / reloading path.

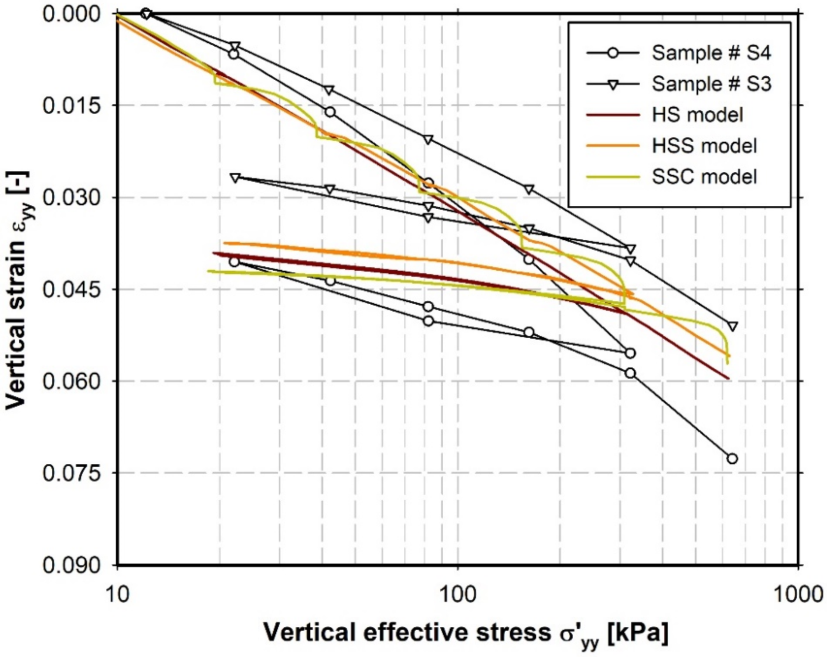

Fig. 64: Comparison of numerical results and test results of an oedometer test

In addition to the oedometer tests, the undrained triaxial compression test on sample S1 was back-calculated. The procedure for the back-calculation was as described in the following. First, a K_0-stress path with a maximum vertical stress approximately equal to the overburden pressure was modelled. Subsequently, an unloading stress path with a minimum vertical stress equal to zero was performed. In the next phase a drained, isotropic consolidation phase with three different stress levels ($\sigma'_{cons} = \sigma_1' = \sigma_3'$ = 100 kPa / 300 kPa / 500 kPa) was modelled and finally, the sample was sheared under undrained conditions until a vertical strain of $\varepsilon_1 = 1\%$ was reached. The total minor stress σ_3 was kept constant during the shear phase. In the case of the SSC model the K_0-stress path was performed within one day to reach an almost normally consolidated state. For all other calculation phases, the same time as taken in the laboratory test was used in the numerical model. The strain rate during all shear phases was approximately $\dot{\varepsilon}_1 \sim 0.083$ %/h. Figure 65 and Figure 66 present a comparison of the numerical results and the test results. The match between the results is good but there are some discrepancies. In general, the laboratory tests show a dilatant behaviour after reaching the Mohr-Coulomb failure line, which might be in some cases rather an issue of the test itself. However, this dilatant behaviour cannot be observed in the results of the numerical analyses. Comparing the p'-q-plots in Figure 65, it can be seen that a good match was achieved with all three constitutive models for the overconsolidated stress path (σ'_{cons} = 100 kPa). For the two stress paths with a higher consolidation stress (σ'_{cons} = 300 kPa / 500 kPa), the SSC model leads to almost the same stress path as the laboratory test, whereas the HS model and the HSS model produce too high pore water pressures.

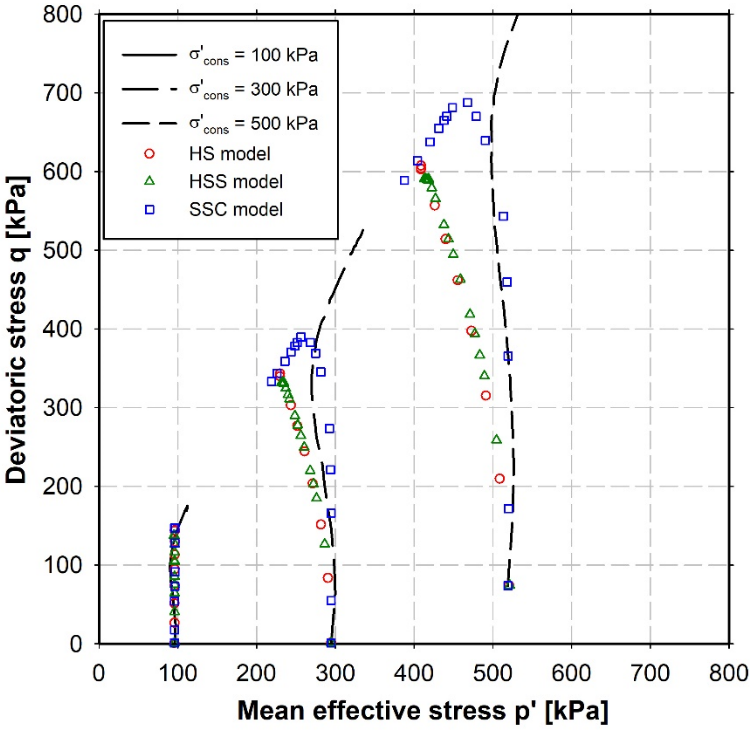

Fig. 65: Comparison of numerical results and test results of an undrained triaxial compression test: stress path in p'-q-plot

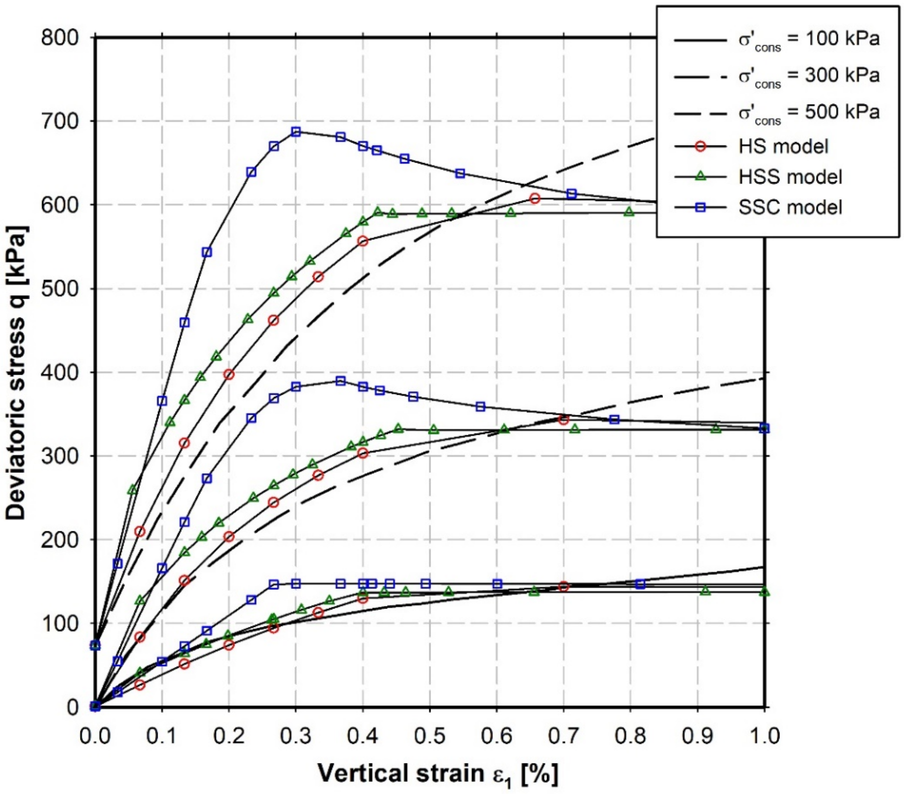

Fig. 66: Comparison of numerical results and test results of an undrained triaxial compression test: stress-strain-behaviour

Considering the stress-strain curve in Figure 66, a good agreement between the results of the HS model and the HSS model with the laboratory test can be observed for the pre-failure part ($\varepsilon_1 \sim 0.5$ %), while the behaviour of the SSC model is too stiff, at least for $\sigma'_{cons} = 300$ kPa and $\sigma'_{cons} = 500$ kPa.

Considering the presented back-calculations of performed laboratory tests, it can be stated that the determined input parameters for the constitutive models result in an acceptable match between numerical results and test results. The stiffness parameters specified in this chapter are therefore used for the following calculations concerning the behaviour of the slow moving landslide. For an overview over all input parameters for the different soil layers, reference is made to chapter 6.2.2.

5.3.3 Strength parameters

To determine the strength parameters, direct shear tests on disturbed samples (sample S1, S2 and S6) and undrained triaxial compression tests on undisturbed samples (sample S1, S3, S7) were performed. Unfortunately, the test results showed a wide scattering and the test type (direct shear test or undrained triaxial compression test) especially had a significant influence on the test results. An overview of the determined average values, depending on the test type is shown in Table 10**Tab. 10**.

Tab. 10: Minimal and maximal strength parameters from laboratory tests on lacustrine fine sediments

Test type	**Friction angle φ' (min – max)**	**Cohesion c' (min – max)**	**Residual friction angle φ'_{res} (min – max)**
Direct shear test	32.0° – 35.0°	16.2 – 22.9 kPa	26.7° – 32.7°
Undrained triaxial compression test	37.2° – 38.3°	0.7 – 4.0 kPa	-

Generally, the determination of the strength parameters in the case of slow moving landslide is challenging. A common method is the calibration of strength parameters on the basis of back-calculations. Initial simple calculations showed that even the strength parameters at the lower limit of the test results, for the lacustrine fine sediments, led to equilibrium and a high factor of safety for a slow moving landslide. Due to this finding, the strength parameters were assumed according to the lower limit of the test results, as $\varphi' = 27.5°$ and $c' = 3$ kPa. Furthermore, this assumption is preferred as it is a conservative approach with regard to the slope stability.

5.4 In-situ measurements

In-situ measurement systems were installed in two steps. Inclinometers, one pore pressure gauge at the toe of the slope and a geodetic measurement system were installed in 2007 and 2008 during the storage basin extension. In a second step in 2014, the existing measurement systems (pore pressure gauges and geodetic measurement system) were expanded and the damaged devices (inclinometers) were replaced. Additionally, four extensometers were installed, which produced no reliable results. The location of all relevant devices is shown in Figure 57. The geodetic measuring points are distributed over the entire slope to determine the spatial boundaries of the slow moving landslide.

The results of the relevant measurement systems are now presented.

5.4.1 Deformations

In 2007 / 2008, the slope was equipped with two inclinometers. One was installed at the toe of the slope (INC 1). The second inclinometer (INC 2) is situated approximately 50 m upslope inclinometer INC 1. In 2014, both inclinometers were replaced by new inclinometers as the first ones had been destroyed due to the slope movements. The inclinometers have been measured regularly since 2014. INC 1 and INC 2 were equipped with an inplace-inclinometer for 13 weeks and during that time, the deformations were recorded continuously.

Figure 67 shows the measured cumulative deformations since 2014 until 2016 in INC 1 and INC 2 for the A-direction, which corresponds roughly to the dip direction of the slope. Deformations in B-direction (strike direction) show similar curve shapes as the deformations in A-direction, but with smaller values. The black lines in Figure 67 represent the qualitative deformations of the old (replaced) inclinometers. INC 1 shows sliding surfaces from 11.0 to 30.0 m below ground surface, with a main sliding surface at 21.0 m. In INC 2, displacements occur mainly in the fine sediments beneath the sliding mass from 28.0 m to 48.0 m below ground surface with a main sliding surface at 36.0 m.

The progressive head displacements of inclinometers INC 1 and INC 2 are presented in Figure 68. The head displacements show two characteristics of particular importance for later comparison with the storage operation and the precipitation. Furthermore, these characteristics are important for the subsequent numerical analyses of the slow moving landslide. Firstly, in the period from September to November 2015 the displacement rate is significantly lower than in periods before and afterwards. In this period, almost no additional head displacements were measured. Secondly, every year from February to May, the measurements generally show a slightly decreased displacement rate.

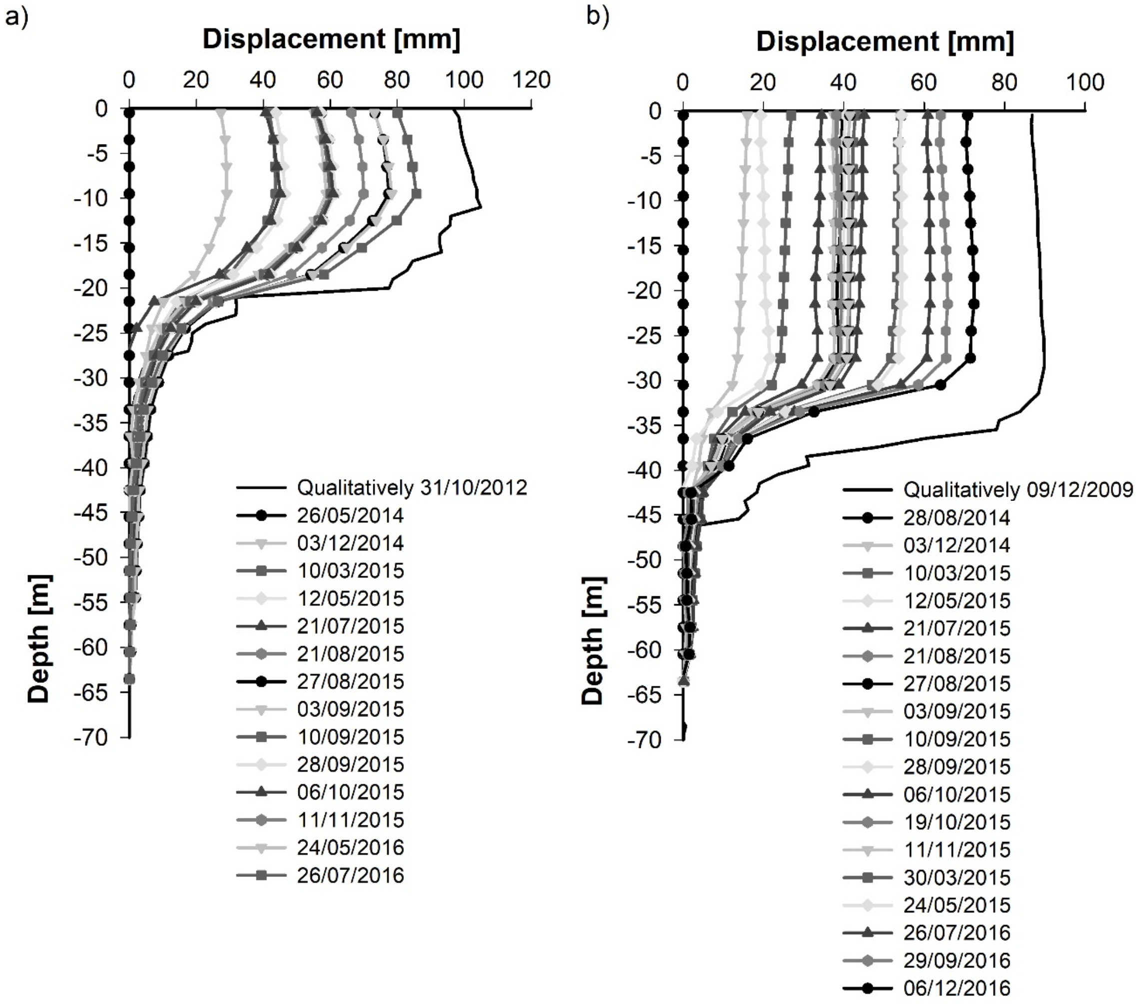

Fig. 67: Deformations in A-direction from 2014 until 2016 of a) INC 1 and b) INC 2

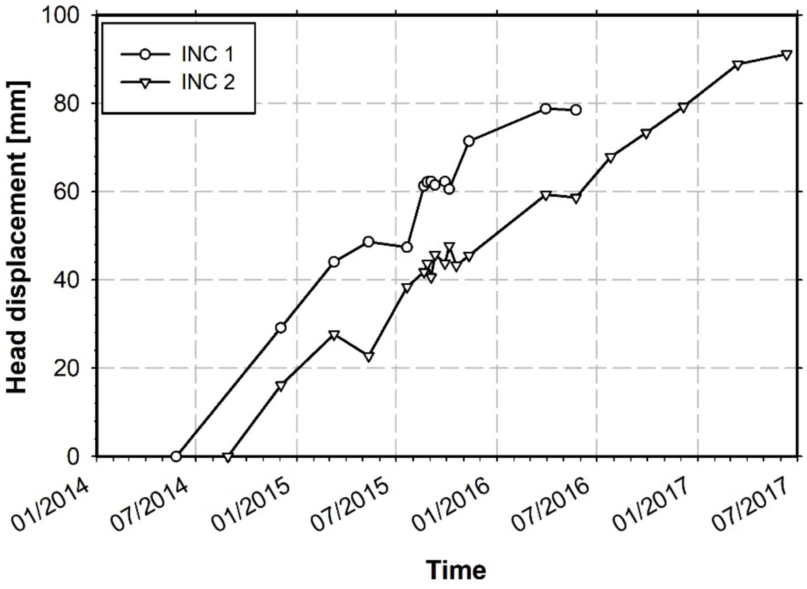

Fig. 68: Total head displacements of INC 1 and INC 2 from 2014 until 2017

To show the deformation characteristic of the entire slope, movement vectors from geodetic measurements are shown in Figure 69. The presented cross section is through inclinometers INC 1 and INC 2.

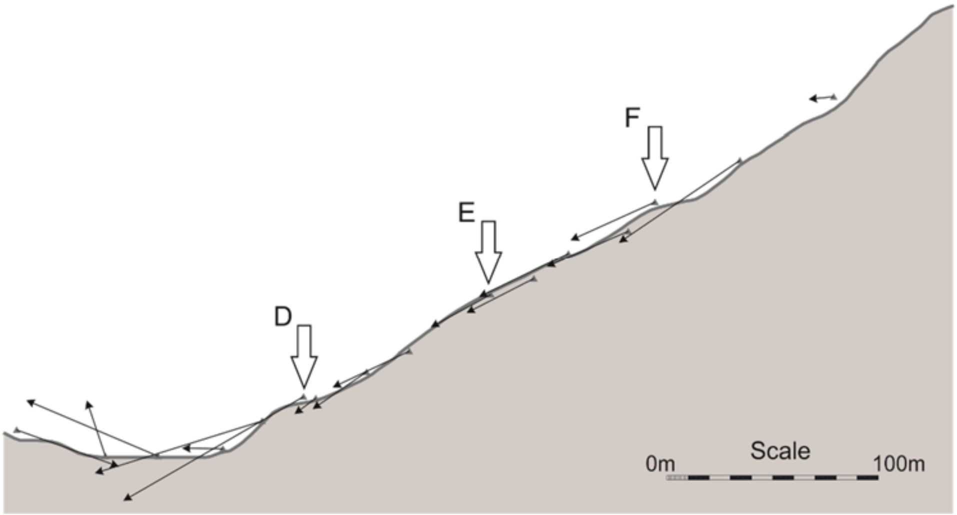

Fig. 69: Movement vectors from geodetic measurements

The selected geodetic measurement points to plot time-displacement curves, shown in Figure 70, are marked in Figure 69. The curves show a similar time-displacement behaviour as that displayed by the inclinometers. Similar to the head displacements of the inclinometers, the geodetic measurements seem to indicate an acceleration during the summer periods (July / August 2015 / 2016), as compared to the slowdowns during the spring period discussed above.

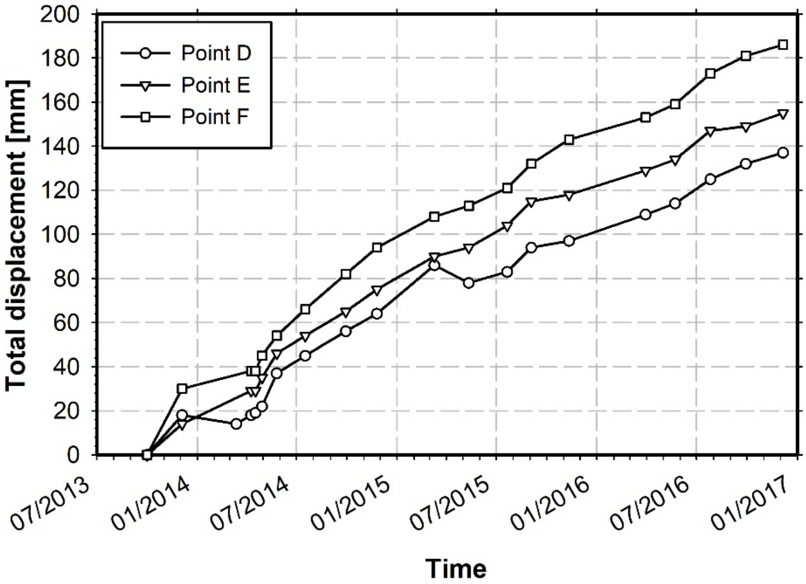

Fig. 70: Total displacements (vertical and horizontal direction) of selected geodetic measurement points from 2013 until 2017

In addition to the standard inclinometer measurements, INC 1 was equipped with an inplace-inclinometer from 14th July 2014 to 18th October 2014. The monitored section of the inclinometer was 11.0-31.0 m below ground surface. From 18th October 2014 to 16th November 2014, INC 2 was monitored with the inplace-inclinometer in a depth of 26.5-46.5 m below ground surface. Selected results of the inplace-inclinometers are presented in chapter 5.4.4 to discuss the influence of the storage operation on the movement rates of the landslide.

Based on the deformation measurements, it can be concluded that the average movement rate is approximately 40-50 mm/year (Figure 68 and Figure 70). The movement rate is almost the same for the entire slope, however, slightly higher rates are measured in the upper part of the slope (Figure 70). Moderate seasonal variations are also recognisable (Figure 68 and Figure 70).

5.4.2 Pore water pressure measurements

Two pore pressure gauges were installed at the slope toe, at a depth of 21.3 m (PPG 1) and 33.2 m (PPG 2). The pore water pressures are continuously monitored. The slope movements destroyed PPG 1 in July 2015.

In Figure 71, the absolute pressure heights of PPG 1 and PPG 2 are shown together with the water level in the storage basin, for a week with fast and high water level changes and for a week with less pronounced water level changes. Furthermore, the excess pore water pressures of PPG 1 and PPG 2 are plotted in the diagrams of Figure 71. The excess pore water pressure p_{excess} is defined as the difference between the measured pore water pressure and the hydrostatic pore water pressure according to the water level in the storage basin.

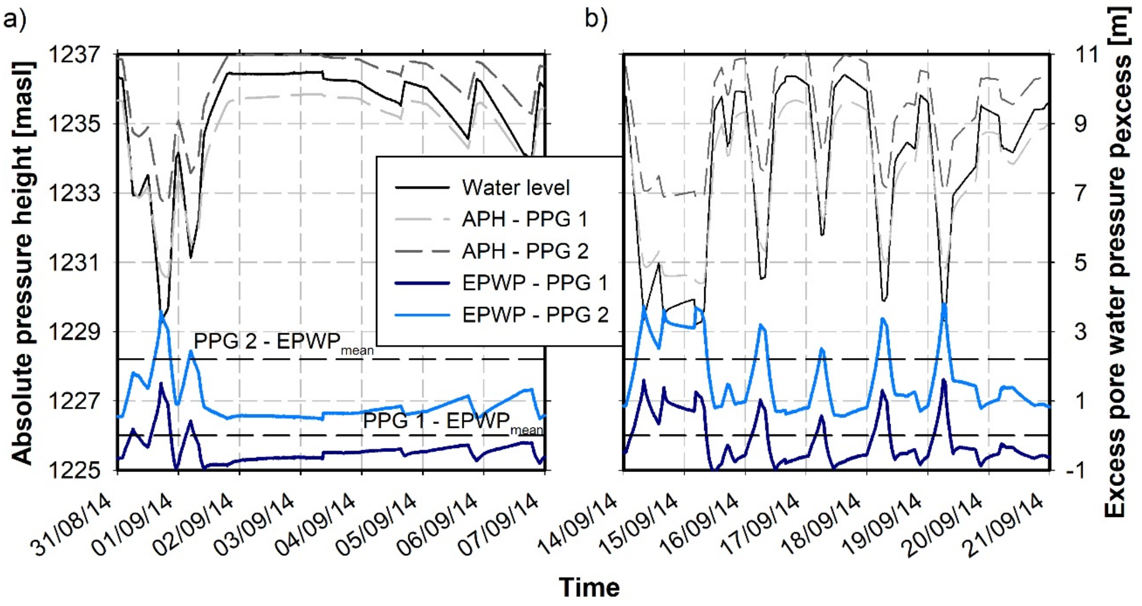

APH...Absolute pressure height EPWP...Excess pore water pressure PPG...Pore water pressure gauge

Fig. 71: Absolute pressure height and excess pore water pressure for a week with a) less pronounced and b) fast and high water level changes

The analysis of the measured pore water pressures in combination with the water level in the water storage basin (Figure 71) showed excess pore water pressures at the installation depth of the pore water pressure gauges. In general, the excess pore water pressures increase with decreasing water levels and vice versa. High and fast water level changes lead to higher excess pore water pressures than low and slow water level changes. In the case of a constant water level in the storage basin, the excess pore water pressures remain also almost constant (Figure 72), at least for the periods with constant water level which were monitored since 2014 (max. 38 days). The magnitudes of the excess pore water pressures during periods of constant water level in the storage basin are different at the two observed depths. When the water level is at its mean level (~1232-1233 masl), the excess pore water pressures are equal to their mean values, which are indicated in Figure 71. The mean values are based on the entire observation period from 2014 until 2017. The pore water pressure gauge PPG 1 shows a mean value of $p_{excess,mean} \sim 0$ m and the measurements of PPG 2 result in a mean value of $p_{excess,mean} \sim 2.2$ m. Figure 72 shows a long period (one month) with an almost constant water level in the storage basin. By this time, PPG 1 was no longer in operation. Therefore, only the results of PPG 2 are shown.

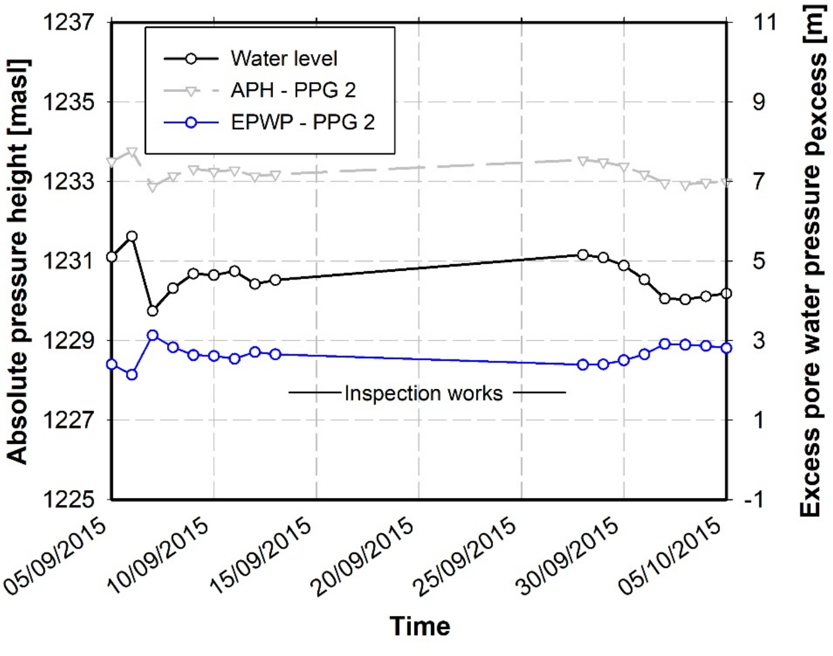

Fig. 72: Absolute pressure height and excess pore water pressure for a period without significant water level changes

The presented and discussed measurement data from the pore water pressure gauges indicate that the excess pore water pressures vary about a mean value, which is not equal to zero in the case of PPG 2. Furthermore, during a time with almost no water level changes (Figure 72), the excess pore water pressure at a depth of approximately 33 m (PPG 2) does not dissipate. Based on these observations, it can be assumed, in a first step, that the excess pore water pressures do not only result from the water level changes in the storage basin, at least at the depth of pore water pressure gauge PPG 2. One possible reason for pore water pressures higher than the hydrostatic pore water pressure (which would be not expected during long periods without water level changes) is the influence from other water levels with a higher potential. This could be a higher water level in the adjacent slope or another water level in the valley with a higher potential, which would be hydraulically connected to the monitored slope area. In addition, the high pore water pressures might result from an underconsolidated state (OCR<1) of the lacustrine fine sediments. Jagau (1990) and Scherzinger (1991) also observed excess pore water pressures in fine laminated lacustrine sediments, where the magnitude of the measured excess pore water pressures was in the same range as the one presented here. The dissipation of the excess pore water pressures in the laminated lacustrine fine sediments as presented in this thesis is hampered by the fine layers of silt and clay, which significantly reduce the permeability in the vertical direction. Additionally, a water flow in the horizontal, transverse direction of the valley is not likely due to the low permeability rock slopes, which enclose the sediments.

5.4.3 Precipitation characteristics

The precipitation data presented here (see Figure 73) was collected from a measurement station near to the site, approximately 4 km away. In general, the measurement data shows an increased precipitation from May to September every year. The increased precipitation during the summer period is more pronounced in the years 2008-2012 and 2016 than in the years 2013-2015.

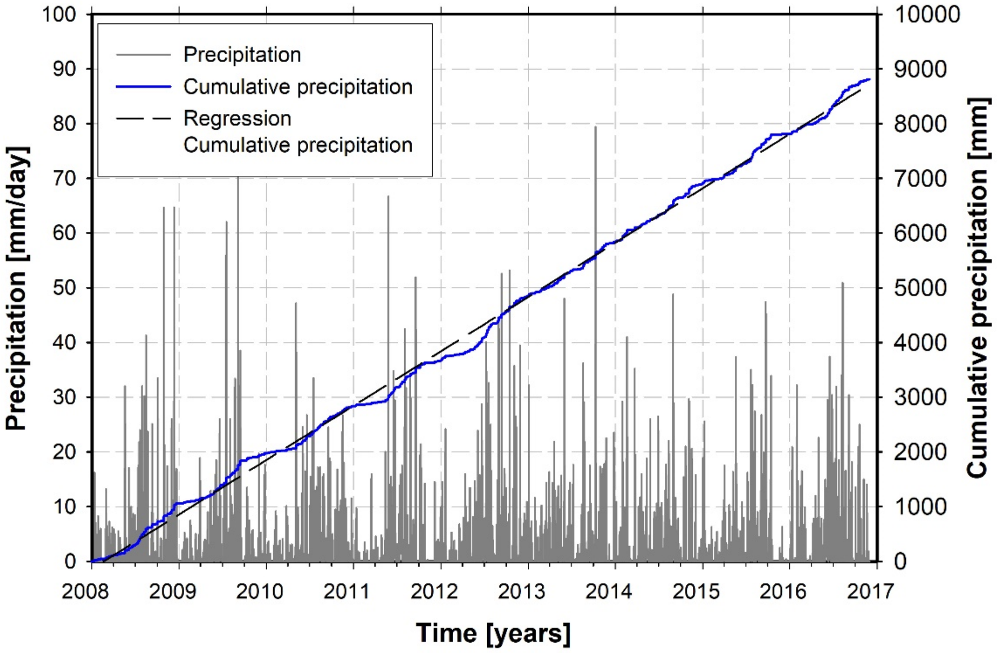

Fig. 73: Daily precipitation data from 2008 until 2017

5.4.4 Comparison of measurement results

In this chapter, the individual measurement types are compared with each other to identify possible interactions.

The interaction of storage operation and pore water pressures in the subsoil has already been discussed in chapter 5.4.2. Generally, the water level changes lead to excess pore water pressures in the subsoil. The magnitude of the excess pore water pressures depends on the velocity and height of the water level changes. These observations are consistent with the results from the preliminary studies in chapters 2.6, 2.7 and 3.2. According to the preliminary studies, the developing excess pore water pressures in the subsoil depend significantly on the velocity of the water level change in the case of a drawdown event. However, in addition to the velocity of the water level changes, the effects of quasi-saturation significantly influence the magnitude of the excess pore water pressures. The actual influence of the quasi-saturation on the development of the excess pore water pressures in this case study will be clarified in the following chapter (chapter 6.3), using numerical back-calculations.

As previously mentioned, both inclinometer casings were equipped with an inplace-inclinometer for a set period. The main objective of gathering the inplace-inclinometer measurements was to identify a possible connection between the storage operation (the excess pore water pressures) and the slope movements in the lower part of the slope. For this, the measured displacements of the inplace-inclinometer are compared with the water levels in the water storage basin.

Figure 74 exemplarily shows a comparison of the rotation of the inclinometer probe at 20 m depth (considered to be the main sliding surface) in the inclinometer casing INC 1 at the slope toe with the water level in the storage basin for one week. The rotation is defined as the displacements at the upper end of one inclinometer probe relative to the lower end (as shown in Figure 74). The 31st of August 2014 was selected as the reference date for the development of the rotation with time. A positive rotation means a displacement in the direction of the water storage basin. The measurement results presented in Figure 74 indicate an influence of the water level changes (and the resulting excess pore water pressures) on the deformations at the slope toe. During the period with fast and high water level changes (31/08/2014 – 02/09/2014), a significant amount of the week's displacements (rotation) occurred in this area, the main sliding surface. For the rest of the presented week, the increase of the displacements is small due to less (and small) water level changes. From time to time, the measurement results of the inplace-inclinometer show a decrease of the displacements, which means a movement backwards into the direction of the slope. These movements are mainly due to the elastic behaviour of the inclinometer casing and the surrounding material (grout and soil). Furthermore, the water flow in the inclinometer casing influences the measured rotations slightly.

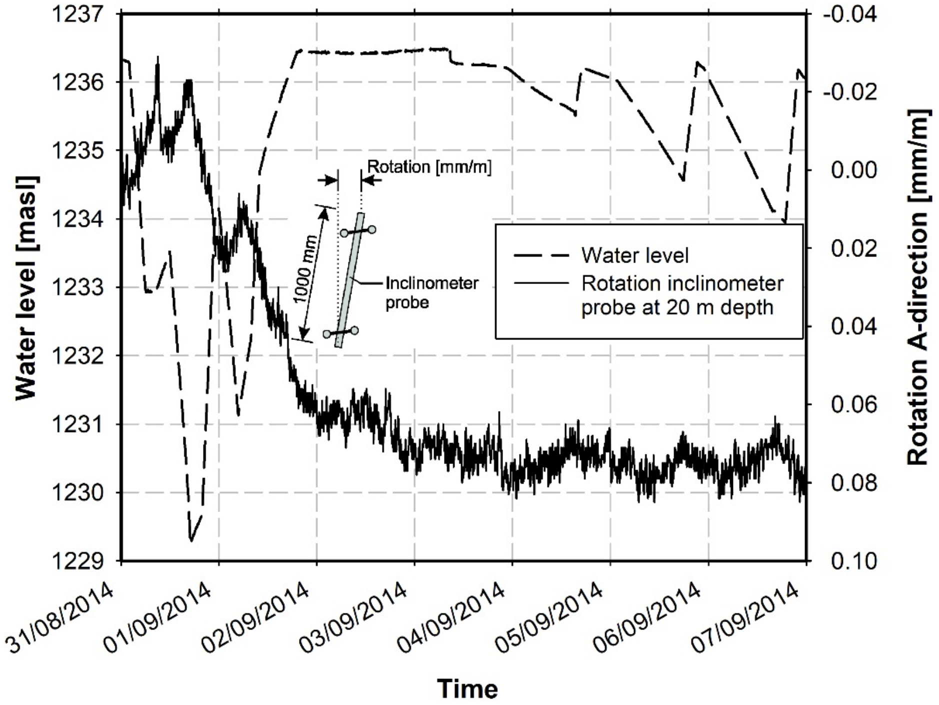

Fig. 74: Rotation of the inclinometer probe at 20 m depth (main sliding surface) in inclinometer INC 1 and water level in water storage basin

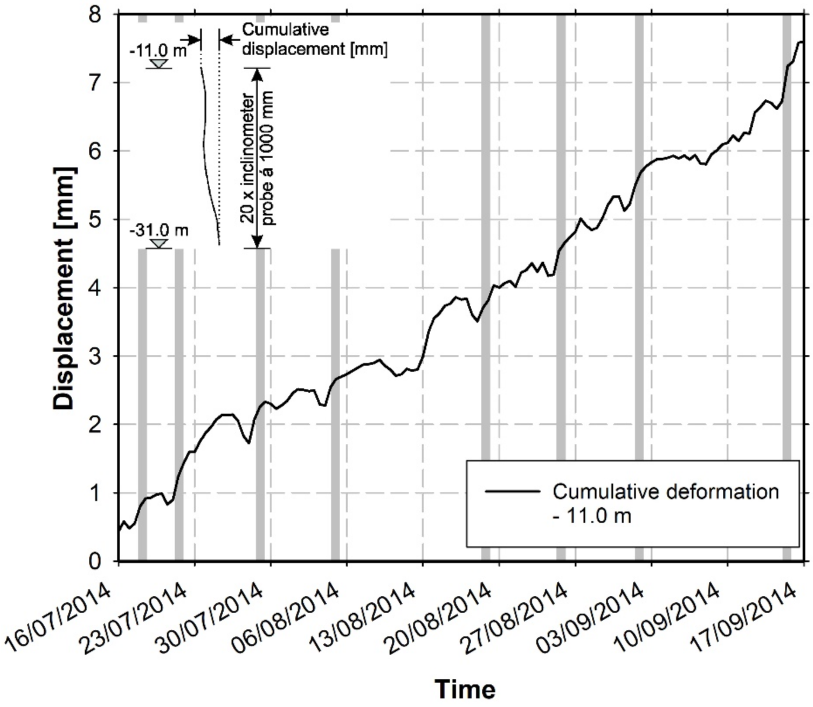

Fig. 75: Cumulative displacements in A-direction from -31.0 to -11.0 m below ground surface in inclinometer casing INC 1

The cumulative displacements of all inplace-inclinometer probes at a depth of 11 m below the ground level in borehole INC 1 is presented in Figure 75. Furthermore, days when there was a fast water level lowering after a long period of a high water level in the water storage basin are marked in the graph with a grey bar. In many cases, these marked days coincide with an increased displacement rate.

Based on the comparison in Figure 75, it can be concluded that a fast water level lowering after a long period of high water level leads to an acceleration of the slope movements at the slope toe. This result is in good agreement with the observations from the model test on quasi-saturated soils (chapter 2.6). The model test showed that the most critical situation, concerning the effective stresses and the shear resistance in the soil, is induced by a fast water level lowering after a high water level has been in place for a longer time period.

During a period with almost no water level changes in the storage basin (due to inspection works from September to October 2015), the deformations of the regular inclinometers INC 1 and INC 2 (inplace-inclinometer were not installed at this time) were measured in short intervals. The results are shown in Figure 76 together with the water level in the storage basin. From 2nd September 2015 to 5th October 2015 the water level did not change significantly. During this period, the rates of the head displacements of INC 1 and INC 2 decreased considerably. When the water level fluctuations started again (14th October 2015), the displacement rate also increased. Thus from this analysis of the deformation measurements and the water storage operation, a connection between the two can also be established. Reduced water level changes lead to smaller displacement rates in the area of the slope toe.

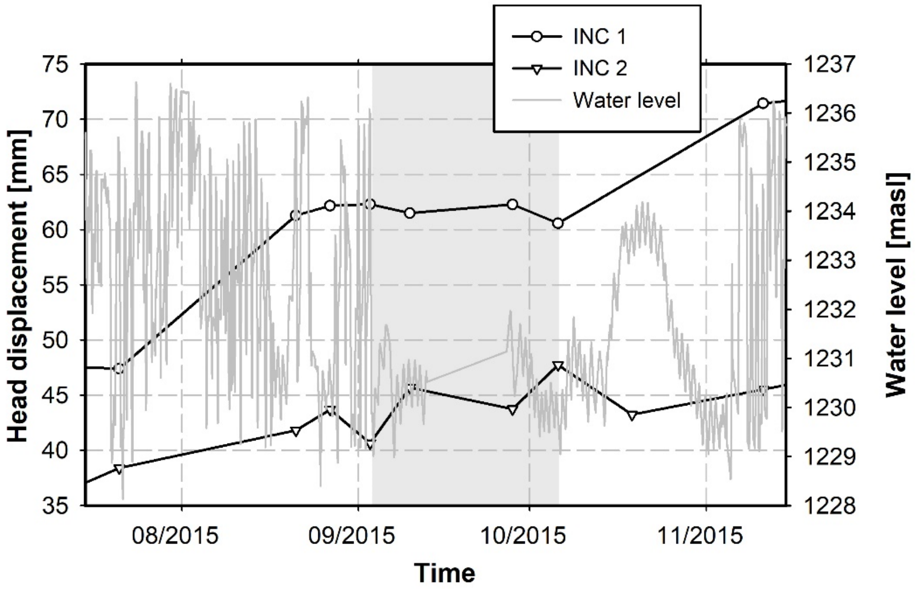

Fig. 76: Comparison of head displacements of inclinometers INC 1 and INC 2 with water level in the storage basin

Finally, some monitored slope displacements, geodetic measurement point E and head displacements of INC 1 at the slope toe, are also compared with the precipitation rate as shown in Figure 77. Generally, the precipitation is lower in the winter period and in the years 2014 and 2016 the displacement rate of point E also decreased slightly during the winter period. However, in the other years, the monitored displacements in point E showed no seasonal changes. In the case of inclinometer INC 1, no clear relationship between displacement rate and precipitation rate can be derived from the measurement data. During September and October 2015, a high precipitation rate was recorded. However, the inclinometer measurements showed no increased displacement rate but rather they showed a significant reduction of the displacement rate during this period due to the reduced storage operation as aforementioned. Therefore, it can be concluded that the precipitation has a very limited influence on the movement rates at the toe of the slow moving landslide. However, when considering the results of all geodetic measurements (e.g. point E), it is recognizable that the influence of the precipitation is higher in the middle part (point E) and the upper part of the slope than in the lower part of the slope.

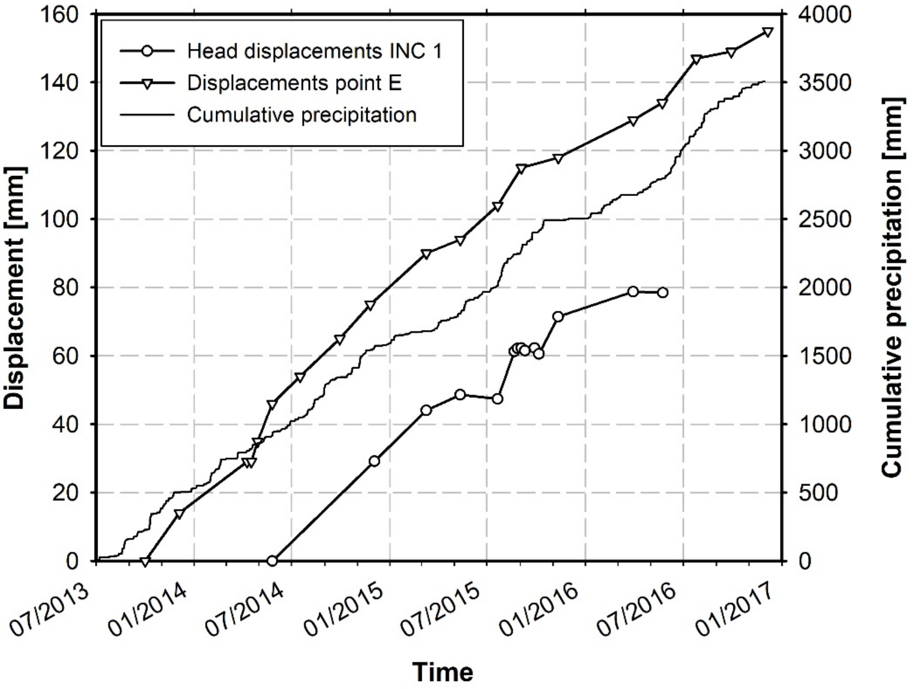

Fig. 77: Comparison of head displacements of inclinometer INC 1 and total displacements of geodetic measurement point E with precipitation

5.4.5 Summary of the in-situ measurements

In summary, the water level changes in the storage basin lead to excess pore water pressures in the subsoil at the slope toe. Furthermore, the measurements with the inplace-inclinometer indicated a clear relationship between the water level changes and the movement rates at the slope toe. Regarding precipitation, while the precipitation rate varies with the seasons, only small seasonal changes in the movement rate are apparent, and not consistently during the entire observation period. For the deformation measurements at the slope toe, no seasonal influences of precipitation were observed. Therefore, it can be assumed that precipitation has a negligible influence on the slope movement at the slope toe, whereas the influence appears to be larger in the middle part and the upper part of the slope.

6 Numerical modelling of a slow moving landslide

6.1 Introduction

This chapter describes the numerical modelling of the slow moving landslide, which is next to a water storage basin used for hydroelectric pump-storage operations, as presented in the case study throughout this thesis.

In chapter 5 the mechanisms of a slow moving landslide next to a water storage basin have been presented based on in-situ measurements. The comparison of various measurement quantities clearly showed that the movement behaviour of the slope is influenced by the storage operation and to a lesser extent by precipitation. In the course of this chapter, the behaviour and the mechanisms of the slow moving landslide are investigated with the aid of numerical analyses, which are based on the results of the presented preliminary studies and the in-situ measurements in order to answer the questions presented in chapter 5.1.

Before the results of the numerical analyses are presented, the challenges with regard to the modelling of the slow moving landslide and the water storage basin are discussed in chapter 6.2. A possible procedure for obtaining realistic initial conditions concerning the stress state, the creep behaviour and the hydraulic conditions is presented. Furthermore, a simple approach from the literature for modelling the infiltration at the ground surface due to precipitation and evaporation based on not very accurate measurement data is introduced. An overview over the constitutive models used for the numerical modelling and the applied material parameters are summarized.

Using a FE-model of the considered landslide and the adjacent water storage basin in Plaxis 2D 2016 (Brinkgreve et al. 2016), back-calculations of the measured pore water pressures with and without the quasi-saturated stage are performed in order to investigate the reasons for them. The findings from chapter 2 and chapter 3, in combination with the FEA, are used to discuss the mechanisms that lead to the excess pore water pressures present in this case study. Furthermore, using the back-calculations of the pore water pressures for different storage operations (fast or slow drawdowns and periods without storage operations), a realistic modelling of the measured pore water pressures can be obtained. Finally, the limitations of the FE-model are pointed out to complete the picture.

Subsequently, numerical back-calculations of the measured displacements and displacement rates are performed. The following factors, water level changes, environmental factors (precipitation and evaporation) and creep effects of the lacustrine fine sediments are considered in these back-calculations. By performing a systematic study, the influence of each individual factor on the total displacements is estimated. For these numerical studies, the Soft Soil Creep model (SSC) is used to model the lacustrine fine sediments. In addition, back-calculations of the movement behaviour using the HS model and the HSS model for the lacustrine fine sediments are performed for comparison purposes.

In the final part of this chapter, based on the knowledge of which factor has a major contribution to the total displacements, appropriate stabilization measures can be suggested.

6.2 Numerical model

6.2.1 Geometry and boundary conditions

The cross section presented in chapter 5.2 was used. The rock surface was modified slightly at the transition from lacustrine sediments to *Intact rock*, as the steep boundary in this area (shown in chapter 5.2) always led to failure in the FEA. As the location of the rock surface is not exactly known from the performed subsurface explorations, this modification of the rock surface seems reasonable.

The FE-model is presented in Figure 78 with a total length of 380 m and a total height of 256 m. The identification of the various soil layers is also shown in Figure 78. For the discretization, 5,287 6-noded elements are used. For selected simulations (pore water pressures and deformations), comparative calculations were also performed with 15-noded elements but no significant differences in results occurred. Therefore, for all calculations, only 6-noded elements are used to save calculation time.

The areas with expected high deformations (*Transition zone* and lacustrine sediments at slope toe) are more finely discretised. For the *Intact rock*, a very coarse discretization is used, as no results are extracted from this area. Generally, the *Intact rock* could be replaced by a displacement boundary condition (no displacements in vertical and horizontal direction) at the rock surface. However, this would complicate the step-by-step activation of the different soil layers according to the geological development of the valley. Therefore, the intact rock was modelled with a very stiff, linear-elastic material.

At the left and right boundary of the model, the displacements are fixed in horizontal direction. At the bottom of the model, no displacements are allowed in horizontal and vertical direction. Water inflow and outflow at the left, right and lower boundary of the model are prevented. Concerning the hydraulic boundary conditions at the ground surface, reference is made to chapters 6.2.3 and 6.2.4.

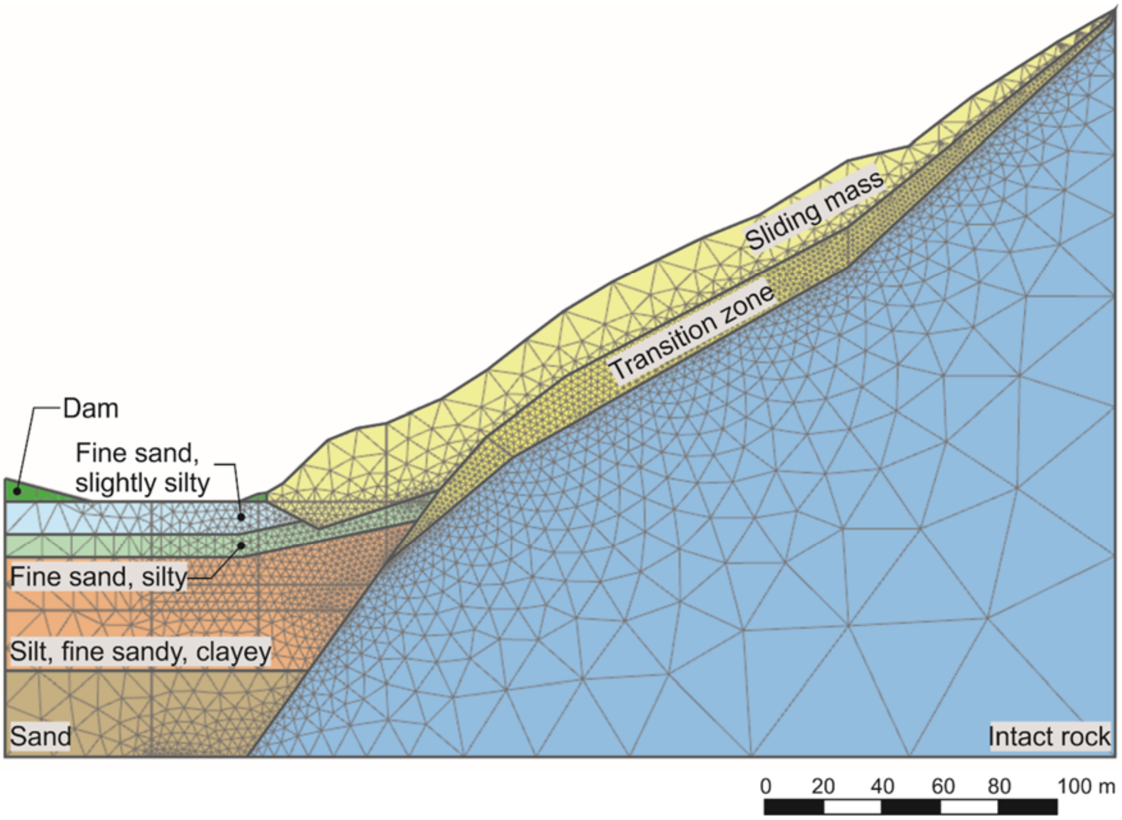

Fig. 78: FE-model for slow moving landslide and water storage basin (5,287 6-noded elements)

6.2.2 Material parameters

The results of the laboratory tests performed on the material from the lacustrine fine sediments and their derived material parameters have been presented in chapter 5.3. The laboratory tests were performed only on samples from the layer *Silt, fine sandy, clayey*. The determined parameters in chapter 5.3, therefore, are only valid for this layer. The above soil layer (*Fine sand, silty*) is slightly coarser and the amount of clay is lower. Therefore, the stiffness of this soil layer was increased by 25% and the soil permeability was increased by a factor of 20 as compared to the *Silt, fine sandy, clayey*. For these two soil layers representing the lacustrine fine sediments (*Fine sand, silty* and *Silt, fine sandy, clayey*), the Hardening Soil model (HS), the Hardening Soil Small model (HSS) and the Soft Soil Creep model (SSC) are applied. However, the majority of the numerical studies is performed with the SSC model, while the HS model and the HSS model are only used for comparison purposes. The material parameters are summarized in Table 11 and Table 12 for the HSS model and the SSC model, respectively. For the HS model the same parameters as for the HSS model are used but the parameters for small strain stiffness ($G_{0,ref}$ and $\gamma_{0.7}$) are neglected. Soil unit weight (γ_{unsat} and γ_{sat}), strength parameters (φ', c' and ψ') and soil permeability (k_x and k_y) are the same for all constitutive models.

The two soil layers *Fine sand, slightly silty* and *Sand* are modelled with the HSS model, and their material parameters, which have been chosen from experience, are presented in Table 13.

Tab. 11: Material parameters for lacustrine fine sediments: HS model and HSS model

Parameter	Unit	Fine sand, silty	Silt, fine sandy, clayey
Model	-	HS / HSS	HS / HSS
γ_{unsat}	kN/m³	19.0	19.0
γ_{sat}	kN/m³	20.0	20.0
$E_{50,ref}$	kPa	15,000	12,000
$E_{oed,ref}$	kPa	8,750	7,000
$E_{ur,ref}$	kPa	45,000	36,000
ν'_{ur}	-	0.2	0.2
p_{ref}	kPa	100	100
m	-	1.0	1.0
φ'	°	32.5	27.5
c'	kPa	2.0	3.0
ψ'	°	0.0	0.0
k_x / k_y	m/sec	$10^{-6} / 10^{-7}$	$5 \cdot 10^{-8} / 5 \cdot 10^{-9}$
$G_{0,ref} / \gamma_{0.7}$	kPa / -	$56{,}250 / 2 \cdot 10^{-4}$	$45{,}000 / 2 \cdot 10^{-4}$

Tab. 12: Material parameters for lacustrine fine sediments: SSC model

Parameter	Unit	Fine sand, silty	Silt, fine sandy, clayey
Model	-	SSC	SSC
λ^*	-	0.0104	0.013
κ^*	-	$3.84 \cdot 10^{-3}$	$4.8 \cdot 10^{-3}$
μ^*	-	$0.48 \cdot 10^{-3}$	$0.6 \cdot 10^{-3}$
ν'	-	0.15	0.15

Tab. 13: Material parameters for *Fine sand, slightly silty* and *Sand*

Parameter	**Unit**	**Fine sand, slightly silty**	**Sand**
Model	-	HSS	HSS
γ_{unsat}	kN/m³	19.0	19.0
γ_{sat}	kN/m³	20.0	20.0
$E_{50,ref}$	kPa	35,000	50,000
$E_{oed,ref}$	kPa	35,000	50,000
$E_{ur,ref}$	kPa	105,000	150,000
ν'_{ur}	-	0.2	0.2
p_{ref}	kPa	100	100
m	-	0.5	0.5
φ'	°	35.0	37.5
c'	kPa	2.0	1.0
ψ'	°	0.0	0.0
k_x / k_y	m/sec	$5\cdot10^{-6}$/ $5\cdot10^{-6}$	$5\cdot10^{-8}$ / $5\cdot10^{-9}$
$G_{0,ref}$ / $\gamma_{0.7}$	kPa / -	175,000 / 10^{-4}	375,000 / 10^{-4}

Tab. 14: Material parameters for *Sliding mass* and *Transition zone*

Parameter	**Unit**	**Sliding mass**	**Transition zone**
Model	-	Mohr-Coulomb	Mohr-Coulomb
γ_{unsat}	kN/m³	20.0	20.0
γ_{sat}	kN/m³	22.0	22.0
E_{oed}	kPa	200,000	200,000
ν'	-	0.3	0.3
φ'	°	40.0	33.0
c'	kPa	10.0	1.0
ψ'	°	0.0	0.0
k_x / k_y	m/sec	10^{-3} / 10^{-3}	10^{-3} / 10^{-3}

For the *Sliding mass* and the *Transition zone* a Mohr-Coulomb model is utilized. The material of these two soil layers is characterized as a sheared and weathered rock with many joints filled with gravel, sand and silt. A determination of soil parameters for this type of soil in the laboratory is difficult. Therefore, the strength parameters of these two layers, especially of the *Transition zone*, were determined by means of back-calculations in order to achieve a stress state for the slope, which is near the ultimate limit state. Stiffness parameters for these slope materials were estimated from engineering judgement. The soil permeability was assumed with a high value of $k = 10^{-3}$ m/sec according to the observations during the drilling works as described in chapter 5.3.1. A summary of the parameters for the slope materials (*Sliding mass* and *Transition zone*) is given in Table 14.

The performed analyses also incorporate rainfall infiltration into the slope, i.e. water flow under unsaturated conditions is modelled. Therefore, a characterization of the slope material under unsaturated conditions is necessary. The water retention curve (WRC) used for both relevant soil layers (*Sliding mass* and *Transition zone*) is based on the van Genuchten model (van Genuchten 1980). The applied WRC corresponds to a curve for a coarse top soil of the Hypres data set (Brinkgreve et al. 2016). Furthermore, the selected curve is similar to the water retention curves utilized by Pinyol et al. (2012) for a rock (siltstone, limestone) in their numerical study of a landslide and Alonso et al. (2005).The WRC and the corresponding van Genuchten parameters are shown in Figure 79. The used WRC is not based on laboratory tests, because they were not available, but estimated from the material characterization in the borehole logs.

6.2.3 Water level changes in storage basin

The water level changes in the storage basin due to the operation of the pumped-storage power plant are recorded continuously. In the FEA these water level changes are modelled by a transient phreatic level. For the back-calculation of the pore water pressures at the slope toe, detailed data sets, i.e. one value every two hours, are used. For the simulation of the displacements during a whole year, the position of the water level in the basin was updated every 8 hours. An analysis of the water level data showed that the 8 hour intervals are still sufficient to capture the fast water level changes. Figure 80 shows the water level definition for this case study in the FE software Plaxis 2D 2016 (Brinkgreve et al. 2016). Figure 81 to Figure 83 present the water level over time for the periods that are analysed in detail for the back-calculation of the pore water pressures at the slope toe. The modelled periods are indicated in the following by the abbreviations WL 1 (15/09/2014 – 21/09/2014), WL 2 (31/08/2014 – 06/09/2014) and WL 3 (03/09/2015 – 10/10/2015).

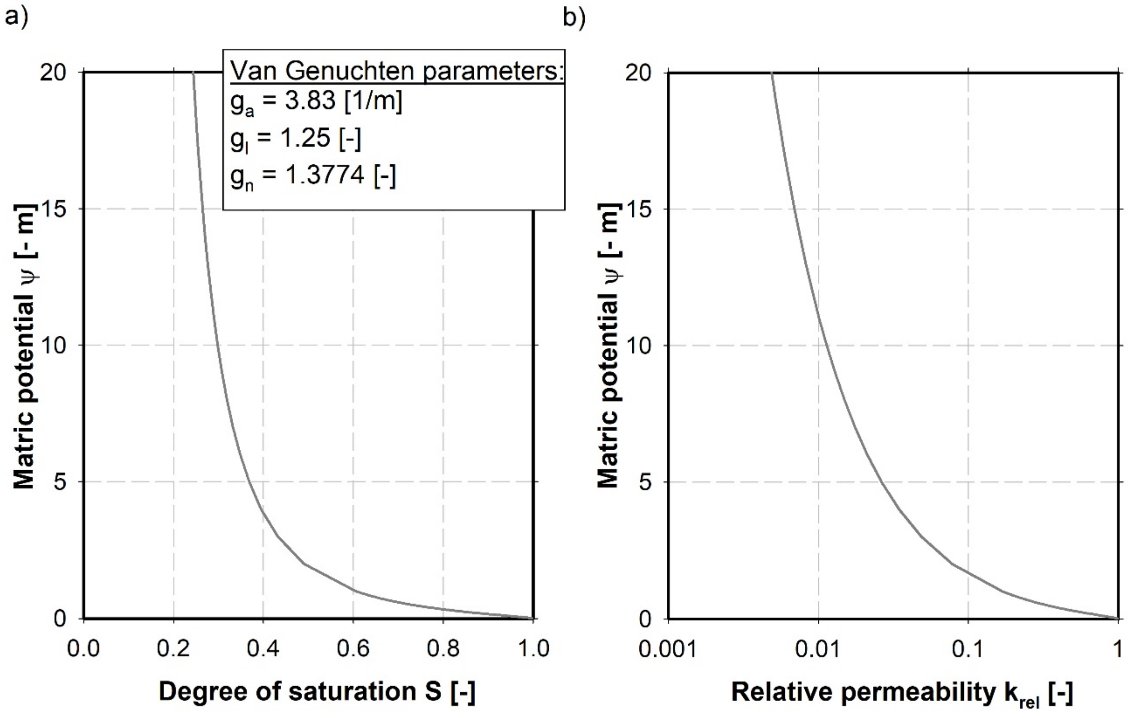

Fig. 79: Parameters for unsaturated conditions of *Sliding mass* and *Transition zone*: a) water retention curve and b) relative permeability

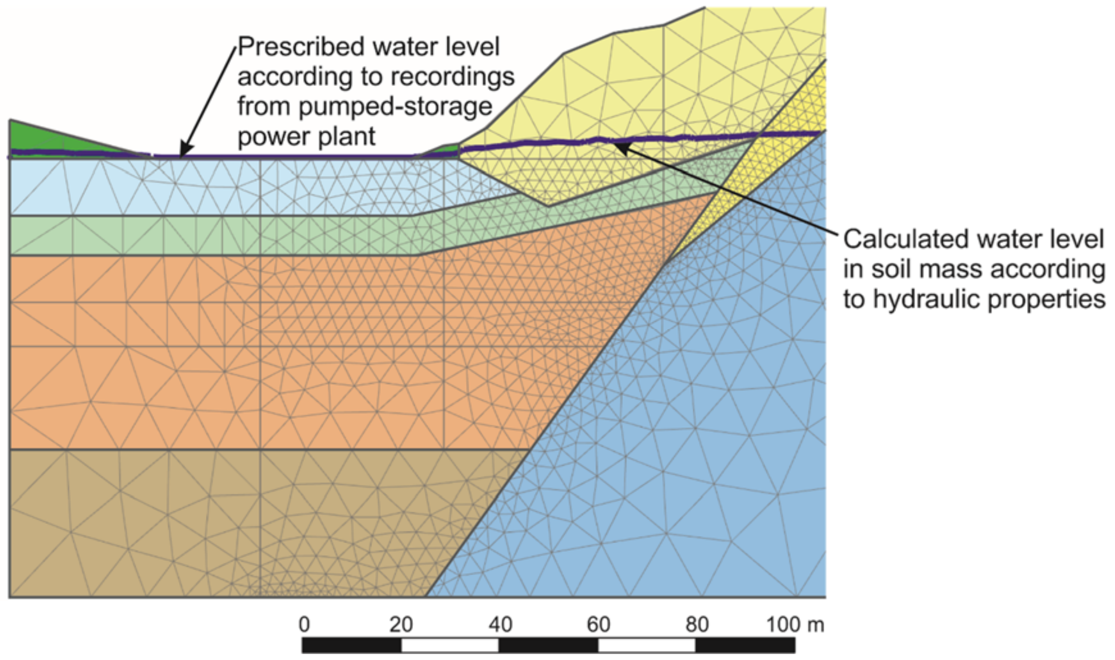

Fig. 80: Definition of water level in Plaxis 2D 2016

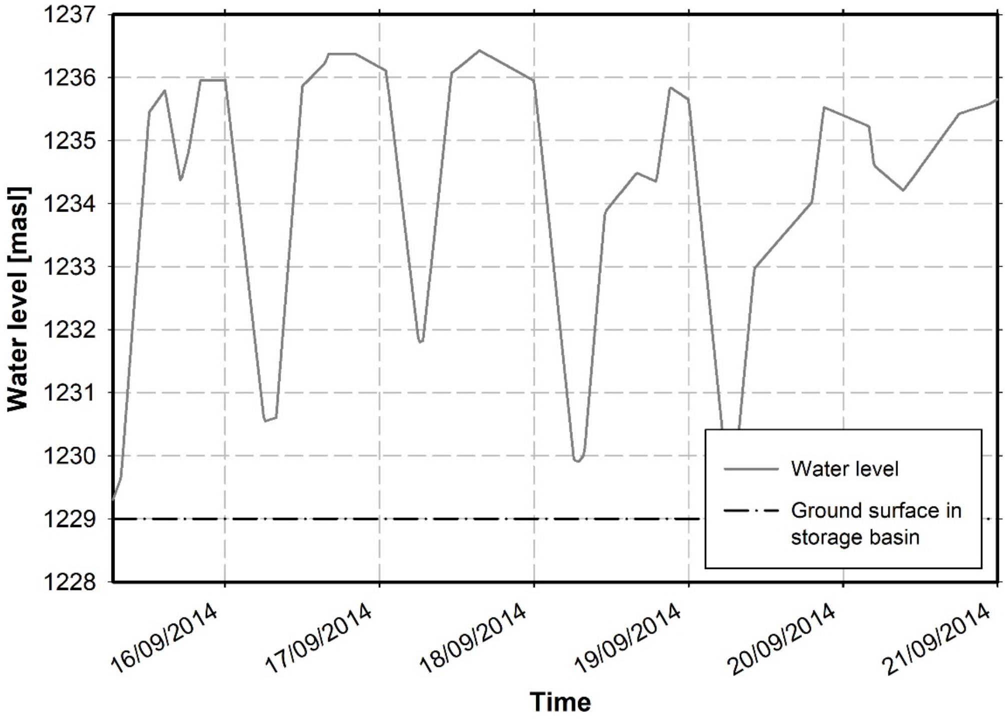

Fig. 81: Water level changes (WL 1) from 15/09/2014 until 21/09/2014 for back-calculation of pore water pressures at slope toe

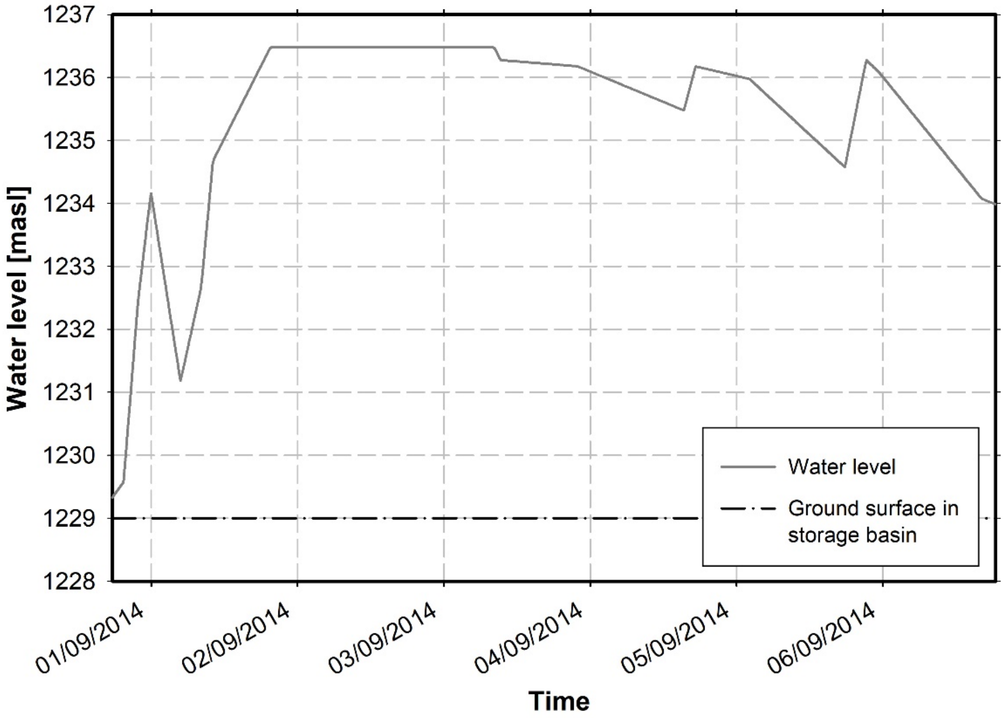

Fig. 82: Water level changes (WL 2) from 31/08/2014 until 06/09/2014 for back-calculation of pore water pressures at slope toe

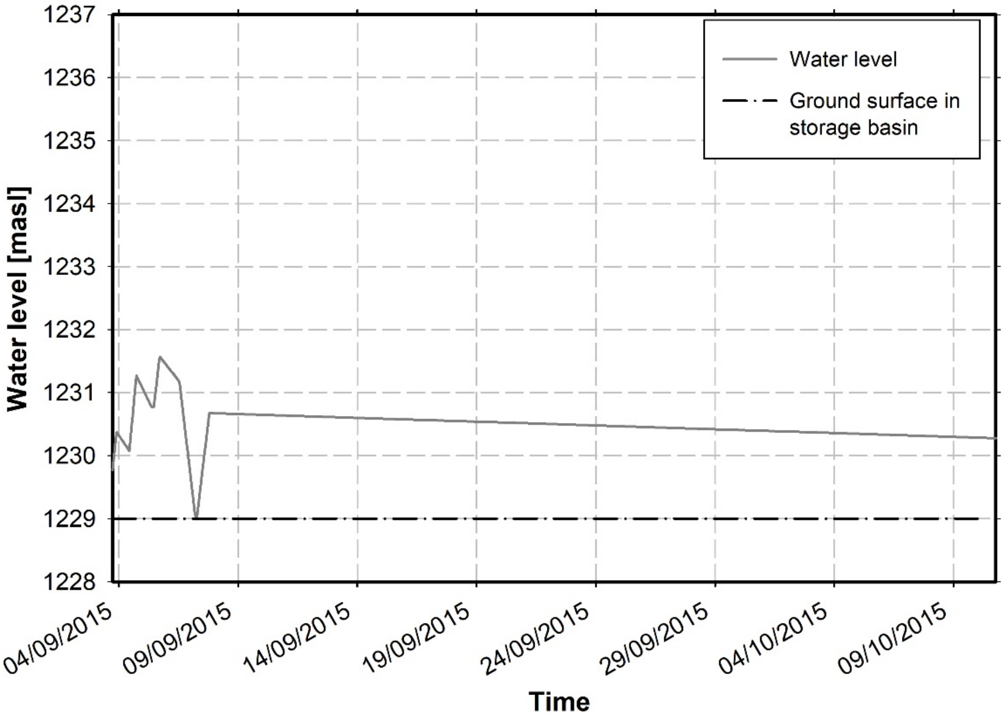

Fig. 83: Water level changes (WL 3) from 03/09/2015 until 10/10/2015 for back-calculation of pore water pressures at slope toe

6.2.4 Infiltration (precipitation and evaporation) on ground surface

Measurement data concerning the actual precipitation, evaporation and transpiration on site are very limited. Additionally to the daily precipitation, only monthly averages for the air temperature, the sunshine hours and the days per month with a snow cover are available. A detailed modelling of the infiltrating water at the top ground surface due to precipitation, evaporation and transpiration is, therefore, not possible. As only monthly averages are available for the majority of the data, the infiltration applied in the FE-model also only uses monthly averages.

In general, the infiltration at the ground surface is determined with the following equation (Fredlund et al. 2012).

$$\begin{aligned} &Net\ infiltration\ (I) = Precipitation\ (P) - \\ &Actual\ evaporation\ (AE) - Transpiration\ (T) - \\ &Runoff\ (R) \end{aligned} \tag{48}$$

The precipitation *P,* in Equation 48, is obtained from data recordings on site. Actual evaporation AE is determined from the potential evaporation under consideration of the acting suction in the subsoil. While environmental influences (sun, wind) extract water from the subsoil, the increasing suction holds the water in the subsoil (Fredlund et al. 2012). The potential evaporation describes the evaporation from an open water surface. Therefore, the actual evaporation can be significantly lower than the potential evaporation. For the determination of the potential evaporation *PE* (Equations 49 to 51), an empirical equation according to Thornthwaite (1948) is used (Fredlund et al. 2012). This equation results in a monthly average for the daily potential evaporation *PE*.

$$PE = 0.533 \cdot \left(\frac{L_d}{12}\right) \cdot \left(\frac{N}{30}\right) \cdot \left(\frac{10 \cdot T_a}{I}\right)^{a_t} \tag{49}$$

$$I = \sum_{month=1}^{12} \left({}^{T_a}/_5\right)^{1.514} \tag{50}$$

$$\begin{aligned} a_t = {} & (6.75 \cdot 10^{-7}) \cdot I^3 - (7.71 \cdot 10^{-5}) \cdot I^2 + \\ & +(1.79 \cdot 10^{-2}) \cdot I + 0.492 \end{aligned} \tag{51}$$

The potential evaporation *PE* according to Thornthwaite (1948) depends on the duration of daylight L_d, the number of days per month N, the mean monthly temperature T_a and correlation factors I and a_t.

For the determination of the actual evaporation, the FEA would require a coupling of the evaporation with the suction in the subsoil. This coupling mechanism is not provided in the utilized FE software and a manual adjustment of the actual evaporation during the FEA proved to be very difficult. Therefore, the influence of the suction on the evaporation is neglected in the following FEA. Furthermore, the influence of the transpiration as presented in Equation 48 is neglected. Fortunately, transpiration would decrease infiltration rates, while the influence of suction on the evaporation would increase infiltration rates, i.e. it is reasonable to assume that the combined effect can be neglected for the purpose of this study.

During periods with snow cover, almost no infiltration occurs. Therefore, the infiltration is set to zero during the months of January and February because for these two months, a snow cover was recorded during the entire month. However, their precipitation was considered in the infiltration of the two subsequent months (March and April) due to snow melting.

The runoff, as presented in Equation 48, is determined automatically during the FEA by defining a maximum water height that is allowed at the ground surface. In this case, water heights higher than the defined maximum (0.01 m) lead to a runoff. However, runoff does not occur in the performed analyses due to the high permeability of the slope material.

Figure 84 shows an overview of the precipitation, the potential evaporation and the resulting infiltration from August 2014 until September 2015, as used in the FEA. The majority of the following back-calculations were also performed for this period.

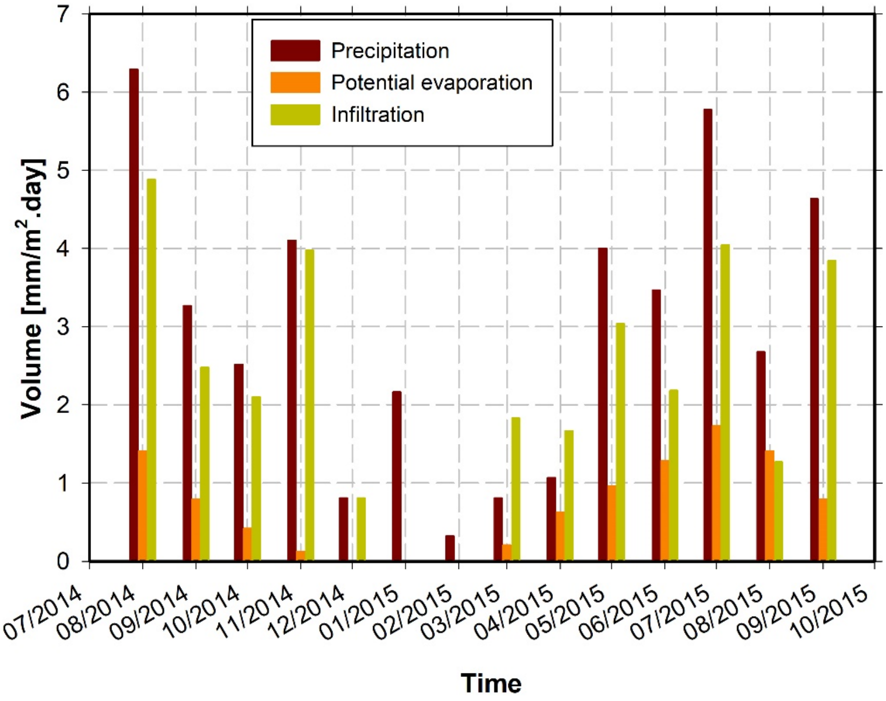

Fig. 84: Applied precipitation, potential evaporation and the resulting infiltration in the FEA

In summary, the environmental influences affecting this case study are modelled in a very simplified way, mainly due to lack of data. However, the modelling of these environmental influences is considered as sufficient for a quantitative estimation of their influence on the total displacements and for a qualitative discussion of the changes (stress state, saturation and flow) in the subsoil due to the infiltration.

6.2.5 Initial conditions

Defining the initial conditions for the following back-calculations of the pore water pressures and the slope deformations represented a challenging task. This applies particularly for the Soft Soil Creep model as the creep strain rate decreases with increasing creep strains, i.e. a decreasing creep rate with time. Therefore, a particular time is simulated before the events for the back-calculations at the present state are performed in order to achieve almost constant displacement rates with respect to the time scale of the maximum back-calculated period (up to one year). Other authors (e.g. Ronchetti et al. 2008, Schädler et al. 2014) also used a similar procedure for modelling a slow moving landslide. A possible alternative would be the definition of an appropriate OCR value for the relevant materials, resulting in the desired creep rate (Waterman & Broere 2017). However, this would lead to a constant OCR value for the entire soil layer, whereas the performed procedure (time for creep) leads to more realistic (inhomogeneous) OCR values, reflecting the actual load and consolidation conditions. This simulation of time for creep is performed along with the simplified simulation of the geological history. The detailed simulation procedure of the geological history is presented in Figure 85.

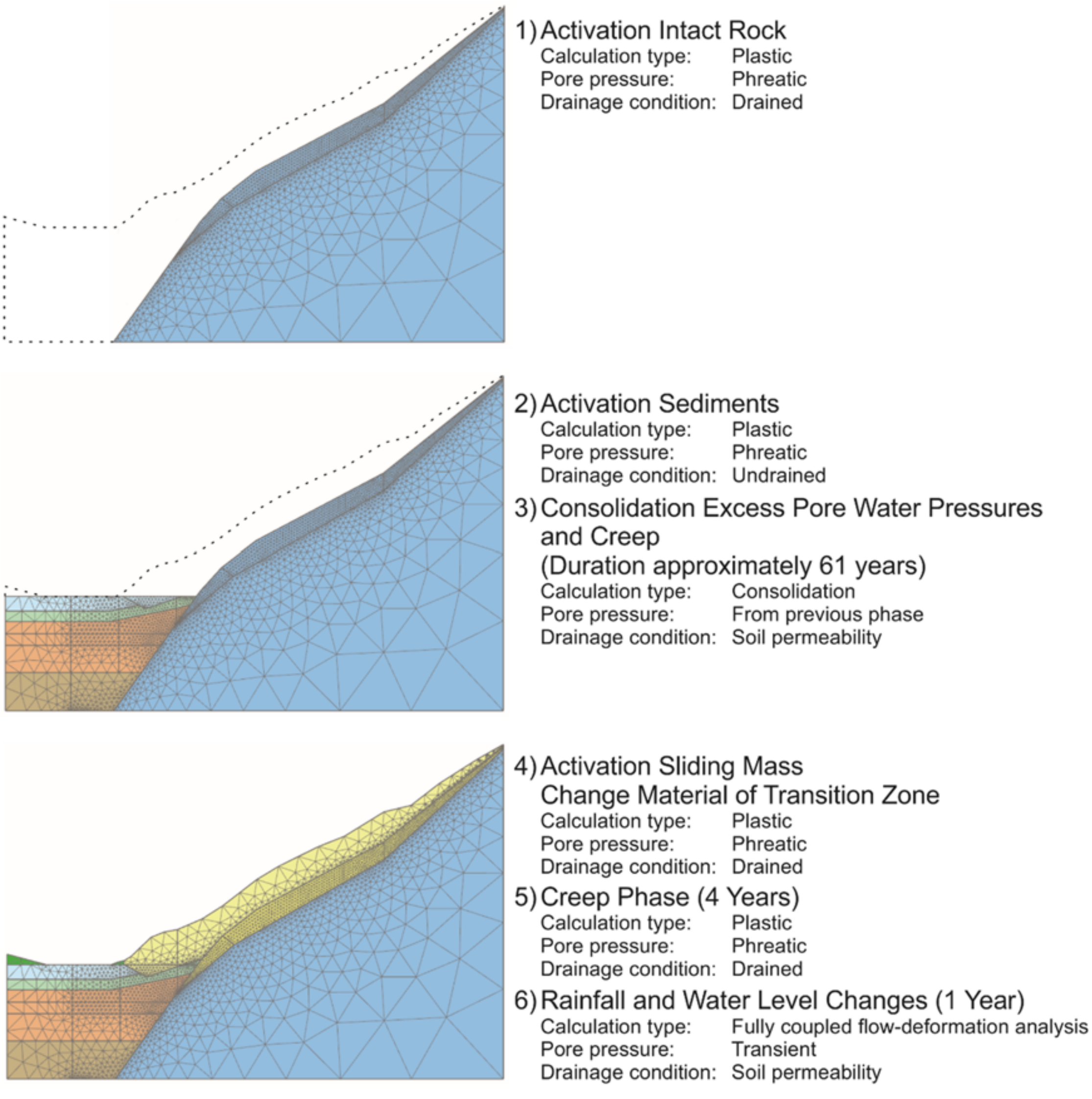

Fig. 85: Simplified simulation procedure of geological history

The simulation starts with the activation of the intact rock. Subsequently, the sediments beneath the water storage basin are activated under undrained conditions, which leads to high excess pore water pressures. This is followed by a phase of consolidation for the dissipation of the excess pore water pressures in the sediments. During the consolidation phase the lacustrine fine sediments are allowed to creep and the overconsolidation ratio is increased. This leads to almost constant creep strains, at least for the period of one year. Afterwards the transition zone and the sliding mass are activated and the material of the lacustrine fine sediments is left to undergo creep for a further five years. During the last year, the water level changes and the precipitation of a characteristic year are applied to achieve reasonable hydraulic conditions (saturation, suction and permeability) in the subsoil. Finally, this simulation should lead together with the simulation of the geological history to appropriate initial stress states. The activation of the sliding mass leads to significant stress changes at the slope toe. This results again in increased creep strain rates, which decay with time. Therefore, the additional creep phase (four + one years) is performed to achieve again an almost constant creep strain rate as described before.

Figure 86 shows the initial conditions for the isotropic overconsolidation ratio OCR of the lacustrine fine sediments and for the degree of saturation *S* in the slope material. The isotropic overconsolidation ratio is between 1.4 and 1.5 in the area of the slope toe. The plot of the saturation shows that no fully saturated zone occurs in the slope due to the assumed characteristic precipitation. The high permeability of the slope and the high slope angle lead to a water flow downslope instead of a water level increase in the slope. However, in the lower part and in the upper part of the slope, the degree of saturation is higher due to the water level in the water storage basin and the low depth of the *Intact rock*, respectively.

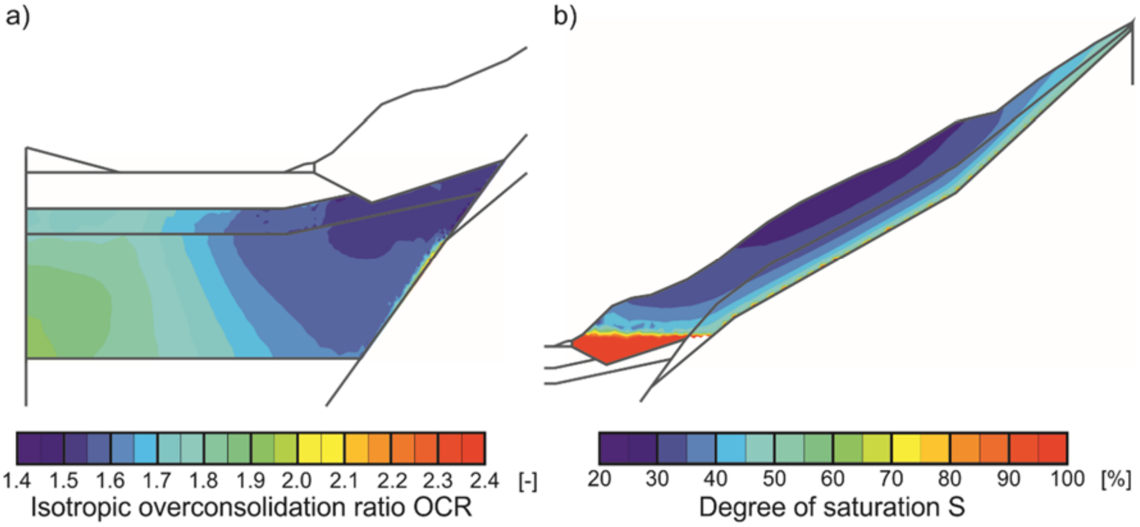

Fig. 86: Initial conditions: a) isotropic overconsolidation ratio of lacustrine fine sediments and b) degree of saturation in the slope

6.3 Back-calculations of pore water pressures at slope toe

Based on the comparison of various measurement quantities in chapter 5.4, an influence of the storage operation on the measured excess pore water pressures at the slope toe has been identified. As a reminder, fast water level changes with a large height of the water level change lead to high excess pore water pressures, whereas a constant water level in the storage basin leads to almost constant excess pore water pressures. The studies in chapter 2 showed that high excess pore water pressures might result from a quasi-saturated stage of the soil. However, as shown in chapter 3, excess pore water pressures may also develop under saturated conditions from fast water level changes in the area of a slope toe when the permeability of the subsoil is low enough. On the basis of the previous presented 2D-model of the water storage basin and the slow moving landslide the question regarding the actual reason of the excess pore water pressures should be answered. For this task, typical water level changes (as presented in chapter 6.2.3) are applied to the FE-model considering different stages of saturation (quasi-saturated and saturated). The results of the FEA are compared to the measurement data from the pore water pressure gauges, which is presented in the following. This comparison should help to establish whether the quasi-saturated stage is necessary for the back-calculation of the measured pore water pressures.

Figure 87 to Figure 89 show a comparison of the measured and the calculated excess pore water pressure for a fully saturated stage of the subsoil beneath the water storage basin, for three types of water level changes (WL 1, WL 2 and WL 3 as presented in chapter 6.2.3). According to these analyses, it seems that a back-calculation of the excess pore water pressures is possible without a quasi-saturated stage. Furthermore, the numerical results, using a saturated stage, show very good agreement with the measurements for all considered types of water level changes. Even for the long period with an almost constant water level (WL3), the deviation of the numerical results from the measurements is small. The constant excess pore water pressure during periods with almost no water level changes has already been discussed in chapter 5.4.2. In this context, the influence of any water level in the valley with a higher potential or an underconsolidated state of the lacustrine fine sediments has been identified as possible reasons for the constant excess pore water pressures. However, these factors are not considered in the FEA. Therefore, during a long period without water level changes, a dissipation of the excess pore water pressures with time would be expected from the results of the FEA. This is not the case, as shown in Figure 89 and therefore, surprising. A small dissipation of the excess pore water pressures until the 19th October 2015 is visible from the numerical results. However, afterwards the excess pore water pressures show an almost constant level, similar to the measurement results.

To discuss why there is a development of the excess pore water pressures in the FEA without using a quasi-saturated stage, contour lines of the groundwater head in the lacustrine fine sediments are presented in the following (Figure 90 and Figure 92) and the reasons for the constant excess pore water pressure during a period with no water level changes are discussed.

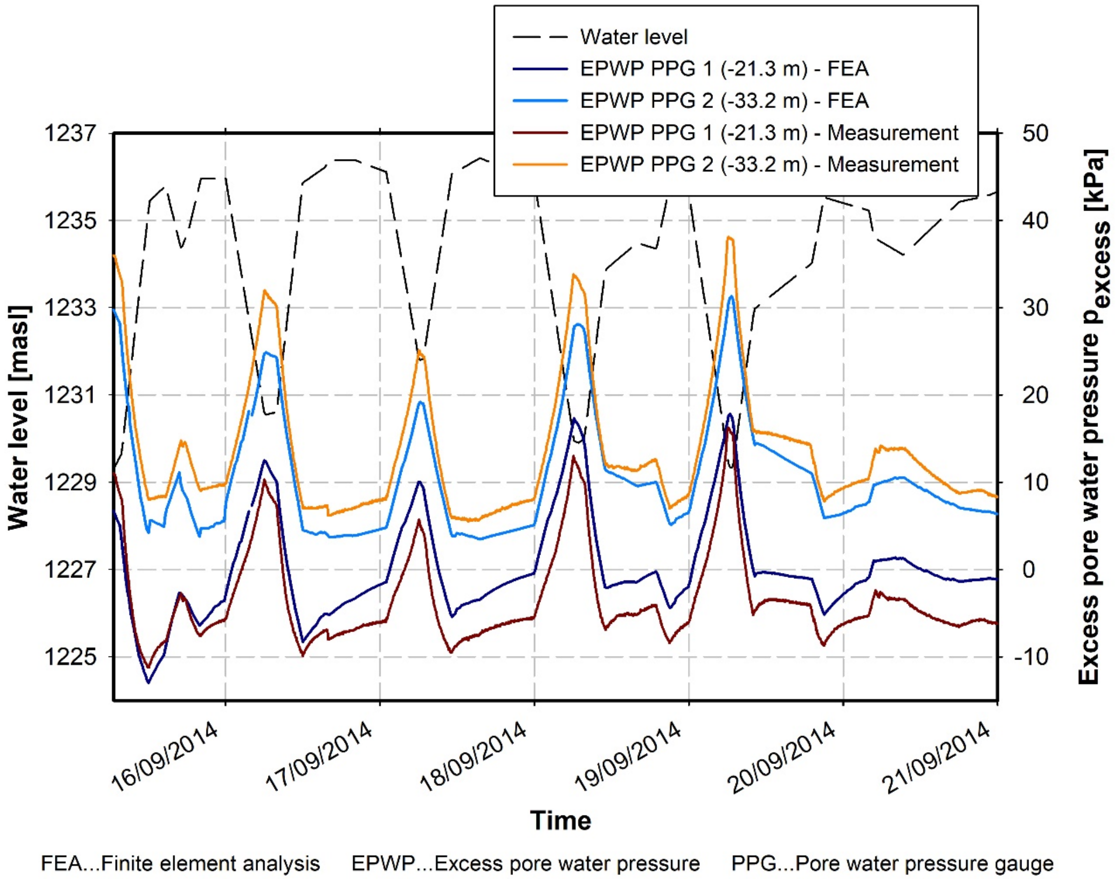

Fig. 87: Back-calculation of excess pore water pressures at slope toe for water level changes WL 1

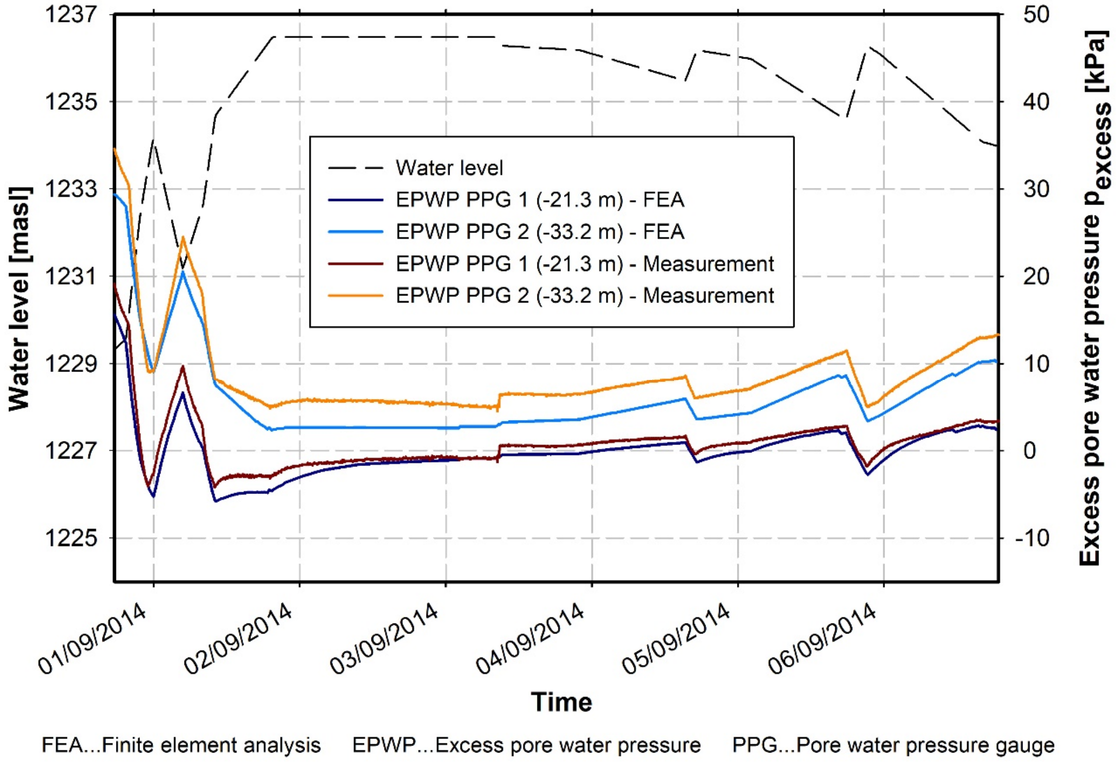

Fig. 88: Back-calculation of excess pore water pressures at slope toe for water level changes WL 2

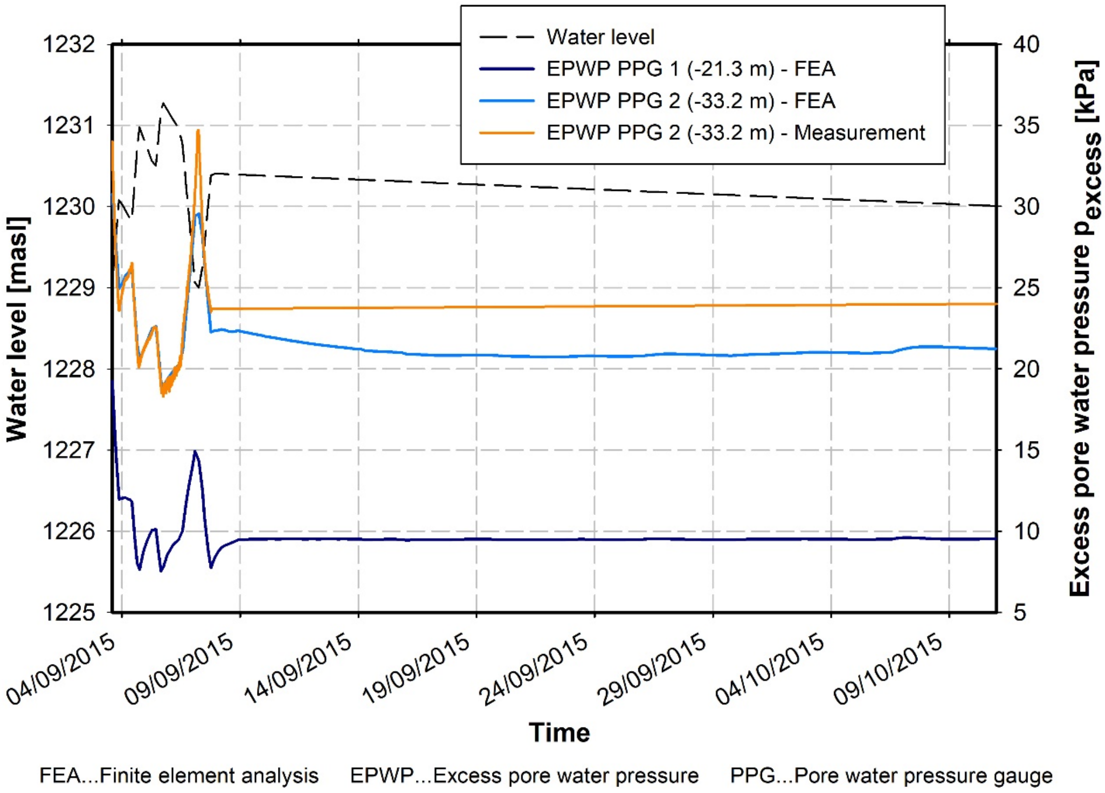

Fig. 89: Back-calculation of excess pore water pressures at slope toe for water level changes WL 3

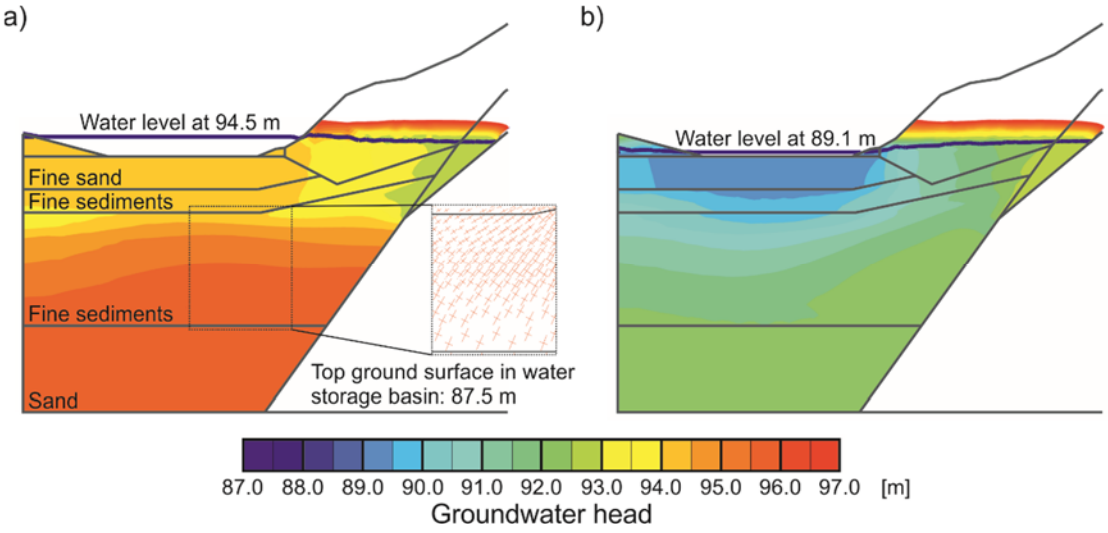

Fig. 90: Groundwater head after a) impoundment and b) drawdown (WL 1 – 16/09/2014)

Figure 90 shows the groundwater head after impoundment and drawdown during the water level changes WL 1 (plots are related to the 16/09/2014). The groundwater head corresponds to the hydraulic potential with respect to the reference level in the FE-model (y = 0.0 m). According to Figure 90, the water level in the rear part of the slope material at the slope toe is almost constant, irrespective of the water level changes in the water storage basin. At the front part of the slope toe, the water level in the slope material is higher or lower than the water level in the basin according to low water levels and high water levels, respectively. In the slope material, a hydrostatic pore water pressure distribution prevails (identifiable by the vertical equipotential lines). This is due to the high permeability of the slope material. Beneath the slope material, the equipotential lines are turning to the left. This behaviour indicates excess pore water pressures in the lacustrine fine sediments. The excess pore water pressures are mainly a result of the changing total stresses at the ground surface due to the water level changes as discussed in chapter 3. Furthermore, the higher water level in the slope material has a significant influence on the pore water pressures at the slope toe. In chapter 3, the development of excess pore water pressures in a low permeability subsoil due to the changing unit weight of the slope material has been presented. This changing unit weight requires the slope material to be highly permeable to ensure the water level in the slope is changing almost simultaneously with the open water level (see chapter 3.2.2). However, this is not the case for this slope. Although the permeability of the slope material is relatively high ($k = 10^{-3}$ m/sec), the water level in the slope material does not change with the open water level. Therefore, the effect of the changing unit weight of the slope material is secondary in this particular case. However, it should be noted that analyses using a very high permeability of the slope material and thus a water level in the slope that is changing simultaneously with the open water level, also showed similar excess pore water pressures. In this case, the effect of the changing unit weight is increased, but the influence of the higher (or lower) water level in the slope material is reduced, balancing each other’s effects.

The hydraulic potential in the upper fine sand layer is equal to the water level in the storage basin. This area is hardly influenced by the slope. Furthermore, the permeability of the fine sand is high, compared to the silt. With increasing depth, the mean excess pore water pressure is larger than zero. This is reflected by a hydraulic potential in the lower soil layers that is generally higher than the water level in the basin (see Figure 90). Even after the impoundment, this higher hydraulic potential can be recognized from the results of the FEA (see Figure 90 a). However, the magnitude of the excess pore water pressure, related to the water level in the basin, is smaller after the impoundment as shown in Figure 91. Calculations with the presented FE-model and artificial water level changes (sinusoidal water level oscillation) showed a continuous increase of excess pore water pressures over time until a certain constant mean excess pore water pressure is reached. Afterwards, the excess pore water pressures are fluctuating around a mean value (Augustin 2017). This behaviour indicates that the soil permeability is too low for the entire dissipation of the excess pore water pressures, generated by a water level lowering, during the phase of impoundment. A similar behaviour can be observed with the real water level changes. Furthermore, the influence of the slope is still present in the lower soil layers. This is indicated by the rotated principal stresses as shown in Figure 90 a. The increase of total stresses due to the slope movements also lead to increased hydraulic potentials in the lower layers.

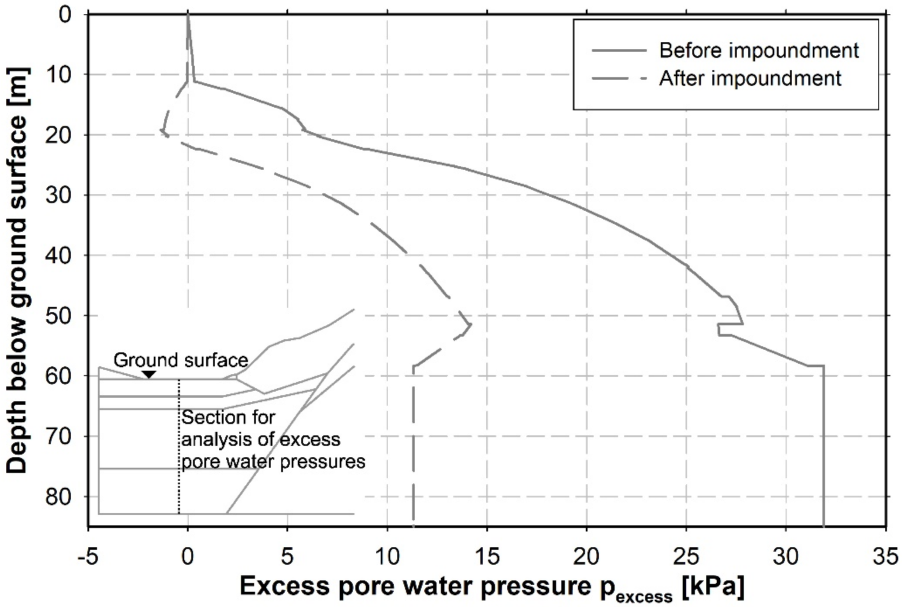

Fig. 91: Excess pore water pressure over depth for impoundment on the 16/09/2014

As mentioned before, a dissipation of excess pore water pressure with time in the case of a constant water level in the storage basin would be expected from the FEA. However, the numerical results show almost no dissipation during the analysed period of 35 days (see Figure 89). For this analysed period, Figure 92 a and Figure 92 b show the groundwater head at the beginning (09/09/2015) and at the end (09/10/2015) of the period with a constant water level. According to these plots, two effects lead to the constant excess pore water pressure in the FEA. Firstly, the very low soil permeability of the lower layer of the lacustrine fine sediments (*Silt, fine sandy, clayey*) prevents a fast dissipation of the deeper excess pore water pressures, i.e. the entire dissipation of the excess pore water pressures of the silt and below the silt is impossible within the analysed 35 days. This can be seen by comparing the groundwater head before (Figure 92 a), and after (Figure 92 b), the period with a constant water level. The groundwater head in the sand layer is almost the same in Figure 92 a and Figure 92 b. Secondly, especially for the area of the installed pore water pressure gauge PPG 2, the high water level in the *Transition zone* has a big influence on the dissipation of the excess pore water pressures. According to Figure 92 b, the water level in the slope is almost the same as in the storage basin after the analysed 35 days but it is higher in the *Transition zone*. This is due to the low permeability of the elevated layer of the lacustrine fine sediments sitting over the *Transition zone*, which prevents a fast lowering of the water level in the *Transition zone* as shown in Figure 92 b. The higher water level of the *Transition zone* also affects the numerical results in the area of the pore water pressure gauge PPG 2, which is indicated by the equipotential lines turning to the left. However, according to the previous discussion, the excess pore water pressures would dissipate in the FEA, if the analysed period were long enough.

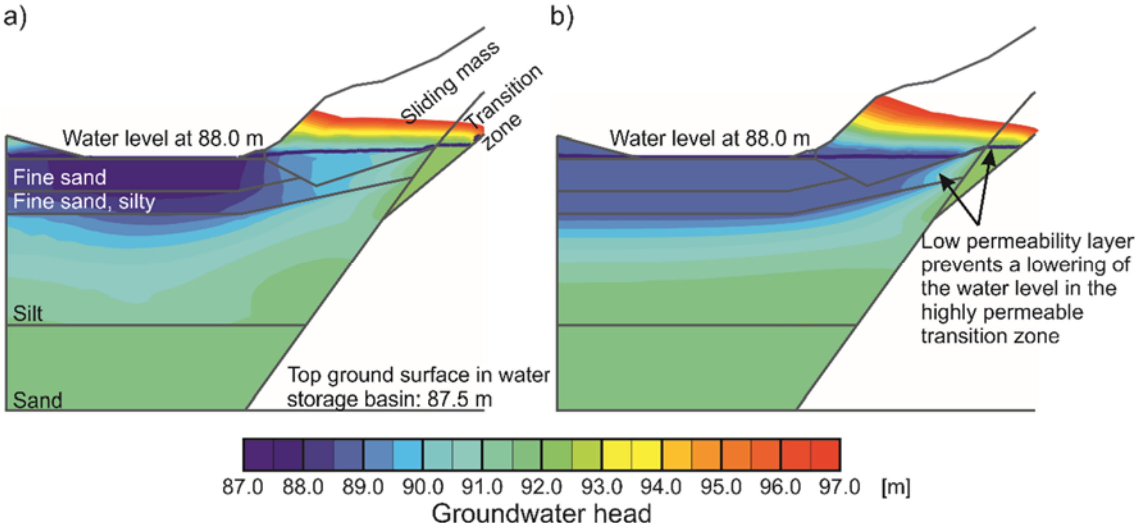

Fig. 92: Groundwater head during a period with constant water level on the a) 09/09/2015 (WL 3) and b) 09/10/2015 (WL 3)

Whether the previously identified effects, which lead to constant excess pore water pressure in the numerical analysis, are also the reason for the measurement results on site, cannot be assessed in the course of this thesis due to lack of data. It is not guaranteed that the layer of *Fine sand, silty* is rising in reality in the same way as modelled in the FE-model, as no subsurface explorations are available for this area. Furthermore, no information about the dissipation of the excess pore water pressures after 35 days is available from the in-situ measurements. Therefore, any dissipation during longer periods of a constant water level in the FEA cannot be confirmed by measurements.

The analyses presented so far, concerning the back-calculation of the excess pore water pressures, have been performed with a saturated stage for the soil layers beneath the water storage basin, i.e. quasi-saturation has been neglected, and the back-calculations of the pore water pressure worked very well. For comparison purposes, the excess pore water pressures generated due to the water level changes WL 1 are back-calculated assuming a quasi-saturated stage for the soil layers beneath the water storage basin. Two different water retention curves (WRC) for the quasi-saturated stage are considered and are presented in Figure 93. For this comparison, instead of the SSC model the HSS model was applied for the two layers *Fine sand, silty* and *Silt, fine sandy, clayey*. Consequently, the influence of the constitutive model on the calculated excess pore water pressures can be also evaluated, using the results for a fully saturated subsoil considering the SSC model (Figure 87) and the HSS model (Figure 94) for the lacustrine fine sediments.

For the reference degree of saturation, i.e. that degree of saturation at a pore water pressure equal to zero, two values are considered $S_{(pwater=0)} = 95\%$ and

$S_{(pwater=0)}$ = 98%. Henry's parameter, which determines the amount of air solved into water, is always assumed with h = 2%.

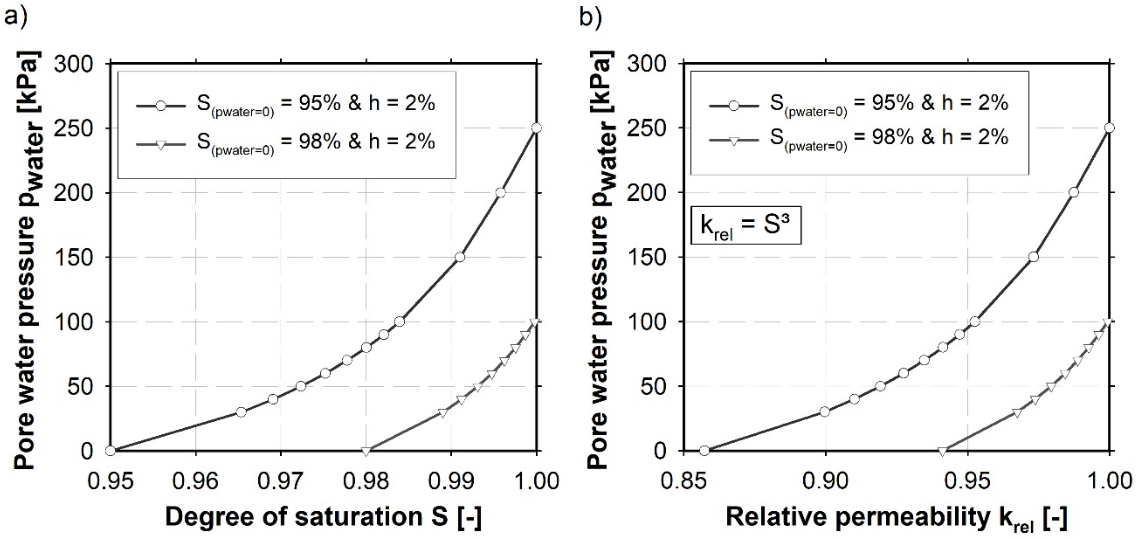

Fig. 93: a) Water retention curve and b) relative hydraulic permeability for soil layers beneath water storage basin considering a quasi-saturated stage

Depending on the reference degree of saturation, the influence of quasi-saturation is recognizable until the installation depths (21.3 m and 33.2 m) of both pore water pressure gauges (Figure 94). Assuming a reference degree of saturation $S_{(pwater=0)}$ = 95%, the excess pore water pressures in the areas of pore water pressure gauge PPG 1 as well as PPG 2 are changed, in comparison to the results for a fully saturated soil. A significant change is shown for PPG 1. The magnitude of the excess pore water pressures is up to 2.5 times higher than for a saturated stage ($S_{(pwater=0)}$ = 100%). This is contradictory to the measurement results, which are similar to the calculation results assuming a saturated stage (shown in Figure 87). Applying a reference degree of saturation $S_{(pwater=0)}$ = 98%, the results for a quasi-saturated stage are almost identical to the results assuming a saturated stage. The reason becomes apparent when taking a closer look at the WRC for $S_{(pwater=0)}$ = 98% in Figure 93 a. Assuming a hydrostatic pore water pressure distribution, the soil is fully saturated from a depth of 10 m downwards as full saturation is reached at 100 kPa according to the WRC in Figure 93 a. Therefore, the pore water pressures in the depth of the installed measurement devices (~21 m and ~33 m below TGS) are not influenced by the quasi-saturated stage. This comparison shows that a quasi-saturated stage may prevail in reality in the upper soil layers (10-15 m below ground surface), but probably not in deeper layers.

Comparing the calculated excess pore water pressures for the SSC model (Figure 87) and for the HSS model (Figure 94) under saturated conditions, shows that the results of both constitutive models are very similar for a fully saturated stage.

In summary, the back-calculation of the measured pore water pressures under the assumption of a saturated stage and using the hydraulic parameters presented in chapter 6.2.2 was very successful, even though the hydraulic boundary conditions are extremely variable (water level changes, precipitation, different permeabilities, unsaturated water flow). For the considered period without water level changes (35 days), the numerical results are similar to the measurements. However, due to lack of data some uncertainties remain whether the FE-model is able to reproduce the real hydraulic behaviour (pore water pressures) for a significantly longer period without water level changes. Based on the conclusions from this chapter, for the following back-calculations concerning the slope deformations, a saturated stage is assumed. However, the influence of the quasi-saturation with a high reference degree of saturation ($S_{(pwater=0)}$ = 98%) is studied for the determination of the safety factor of the slope.

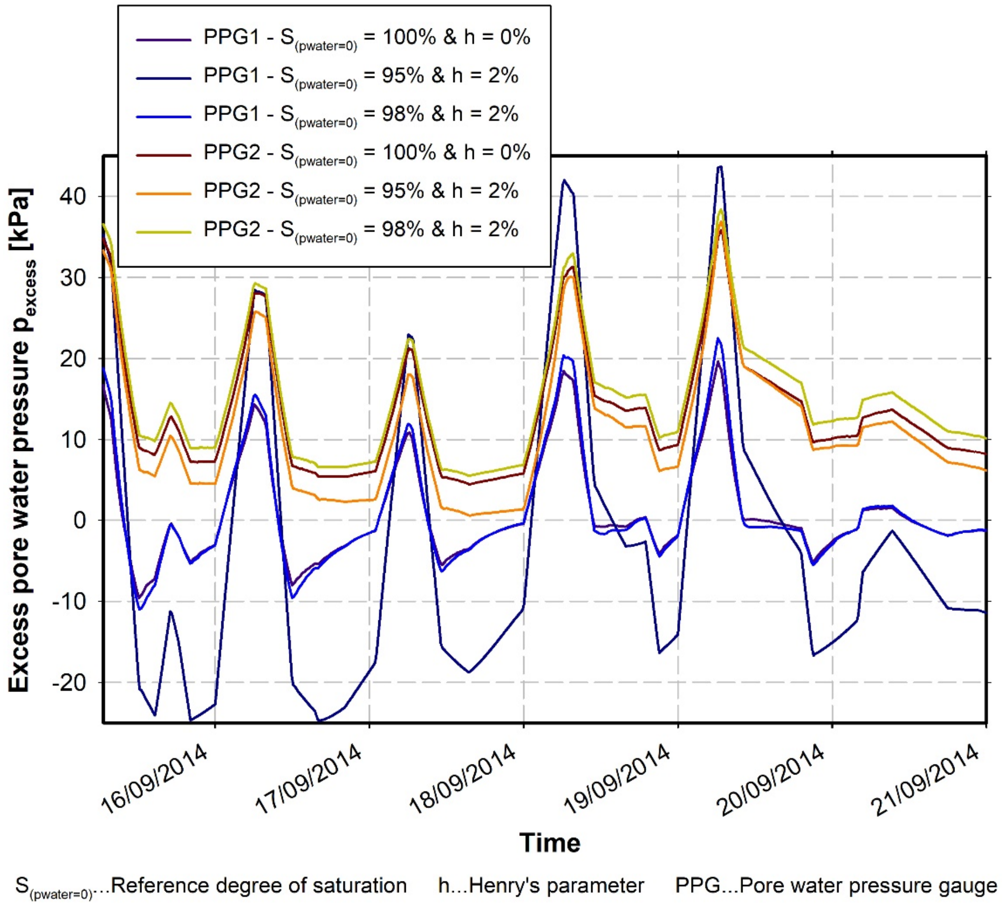

Fig. 94: Influence of quasi-saturation on excess pore water pressures due to water level changes WL1 (HSS model)

6.4 Back-calculations of slope deformation

In the present chapter, the quantitative contribution of individual influencing factors to the measured total slope deformations are estimated based on numerical back-calculations. The investigated influencing factors are the water level changes in the water storage basin, the environmental factors (precipitation and evaporation) and the creep effects of the lacustrine fine sediments. In addition, the results from back-calculations of the slope movements with the HS model and the HSS model are compared to the results from the SSC model (chapter 6.4.5).

6.4.1 Influencing factors for slope movements

To estimate the quantitative contribution of the aforementioned factors to the total displacements, the following procedure has been applied.

Starting from the numerical results for the simulation of a characteristic year (initial conditions) as described in chapter 6.2.5 and Figure 85, further calculation phases are performed to estimate the component of deformation due to each of the aforementioned factors, as illustrated in Figure 95.

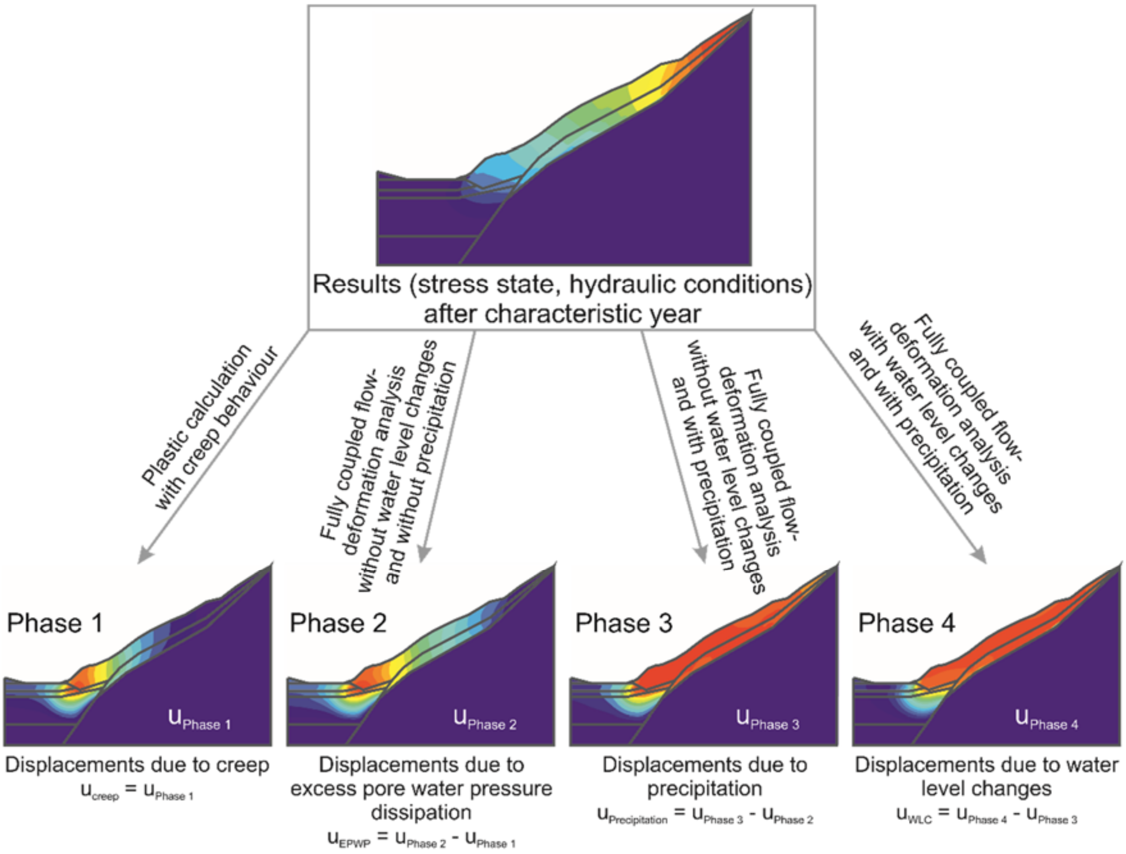

Fig. 95: Procedure to determine deformation component due to various influencing factors

In a first step, a plastic calculation (Phase 1) with steady state hydraulic conditions from the characteristic year is performed, i.e. a constant groundwater level is assumed and the infiltration rate at the ground surface is zero. The simulated time is one year. Under these assumptions, only the effect of creep in the lacustrine fine sediments at the slope toe is considered, i.e. the resulting slope deformations are only due to creep. The hydraulic conditions are those of the last iteration step (end of July 2014) from the simulated characteristic year. Therefore, the calculated creep displacements from this calculation phase are only valid for the assumed hydraulic conditions. Different hydraulic conditions would lead to slightly changed values for the calculated displacements. However, this selected hydraulic state reflects an average state with average excess pore water pressure beneath the water storage basin. Furthermore, it is not influenced from any fast water level lowering in the storage basin nor significant changes in the precipitation rate. Generally, in the subsequently performed fully coupled flow-deformation analyses (Phase 2-4), the hydraulic conditions (pore water pressure and water flow) change with time.

In the next step, a one year calculation phase (Phase 3) without water level changes, but with precipitation and evaporation, is modelled. The initial conditions concerning the hydraulic state are the same as for the previously described calculation phase (Phase 1), i.e. they correspond to the end of the calculation phase (July 2014) simulating a characteristic year. This calculation phase is performed as a fully coupled flow-deformation analysis. Consequently, the pore water pressures and the water flow change with time. However, the water level in the storage basin is constant and is located 5.8 m above the ground surface in the storage basin. Accordingly, the calculation results show the slope deformations due to creep and precipitation. The difference between the slope deformations from this calculation phase (Phase 3) and from the previously calculated phase (Phase 1), creep only deformations, provides the slope deformations due to the influence of the precipitation (and the evaporation) on the slope movements. However, during the numerical analysis of Phase 3 (one year without water level changes but with precipitation), a small dissipation of excess pore water pressures beneath the water storage basin occurs due to remaining excess pore water pressures from the water level changes in previous phases. This dissipation also leads to small deformations, which cannot be attributed to the effect of precipitation and do not occur in reality because during the back-calculated period, water level changes do occur in the storage basin. Therefore, another fully coupled flow-deformation analysis (Phase 2) is performed without water level changes and without precipitation to estimate this small part of slope deformations due to the excess pore water pressure dissipation. Unfortunately, the hydraulic conditions in the slope also change during this analysis (Phase 2). This leads to additional displacements, which cannot be eliminated. Consequently, the estimated deformation component due to the dissipation will be slightly too high. Regardless of the exact magnitude of the displacements determined in this calculation phase (Phase 2), the results should show that not all displacements calculated in the analysis (Phase 3) described before (without water level changes but with precipitation) are solely due to the precipitation. Furthermore, the results will show that the deformation component due to the dissipation of the excess pore water pressure is negligible. Figure 96 shows the groundwater head in the lacustrine sediments after the analysis of the characteristic year (initial conditions), after the fully coupled flow-deformation analysis without water level changes and without precipitation (Phase 2) and after the analysis that considers the precipitation (Phase 3). A change in the groundwater head between the characteristic year and the other two calculation phases is recognizable. However, a comparison of the results for the latter two analyses (without precipitation (Phase 2) and with precipitation (Phase 3)) shows that both lead to similar results for the groundwater head in the subsoil beneath the storage basin. Therefore, as stated earlier, it can be assumed that the analysis without precipitation (Phase 2) reproduces, with sufficient accuracy, the minor effect of the dissipation of the excess pore water pressures that occurs in the analysis with precipitation (Phase 3).

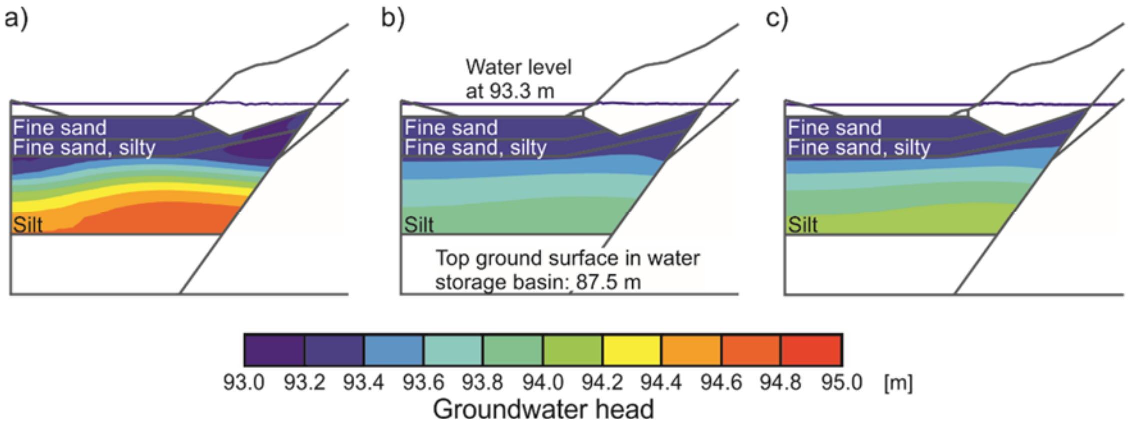

Fig. 96: Groundwater head after a) characteristic year, b) analysis without precipitation and c) analysis with precipitation

Finally, a one-year calculation phase (Phase 4), which considers all the factors together is performed, i.e. creep, water level changes and environmental factors are considered in the fully coupled flow-deformation analysis. It is assumed that the difference between the displacements calculated in this phase and the displacements from the phase considering exclusively precipitation and evaporation (Phase 3) represents the displacement component due to the water level changes. In the following, the isolated deformation results are presented.

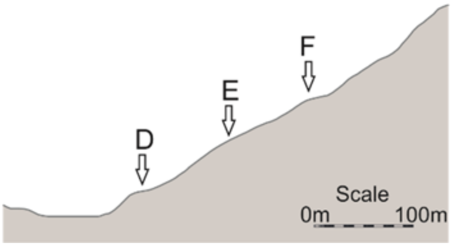

Fig. 97: Selected nodes for displacements (node D corresponds to INC 2)

In the following figures (Figure 98 to Figure 100), the numerically calculated displacements for one year of three selected nodes (shown in Figure 97) on the slope are presented for the four performed calculation phases just described. The difference in displacements between two time-displacement lines is the influence of each additionally considered factor, as indicated by the label of the curves. Furthermore, the measurement results of corresponding geodetic measurement points are plotted in the diagrams for comparison. The numerically applied infiltration rate (see chapter 6.2.4) is also shown in the figures.

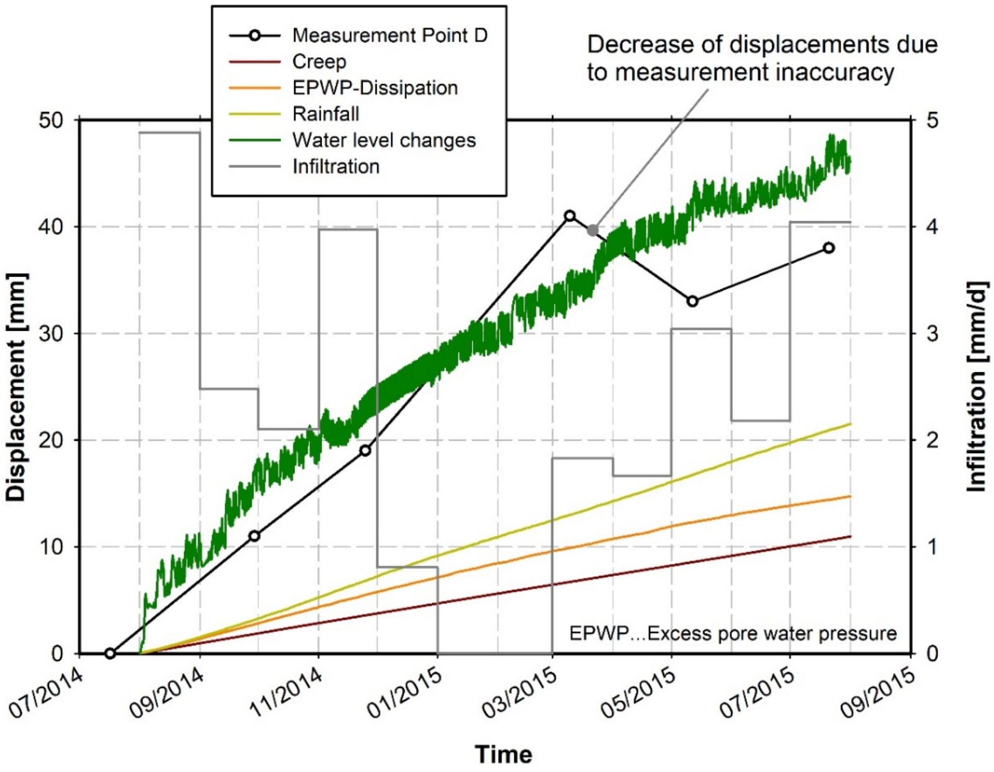

Fig. 98: Back-calculated displacements due to various influencing factors in node D

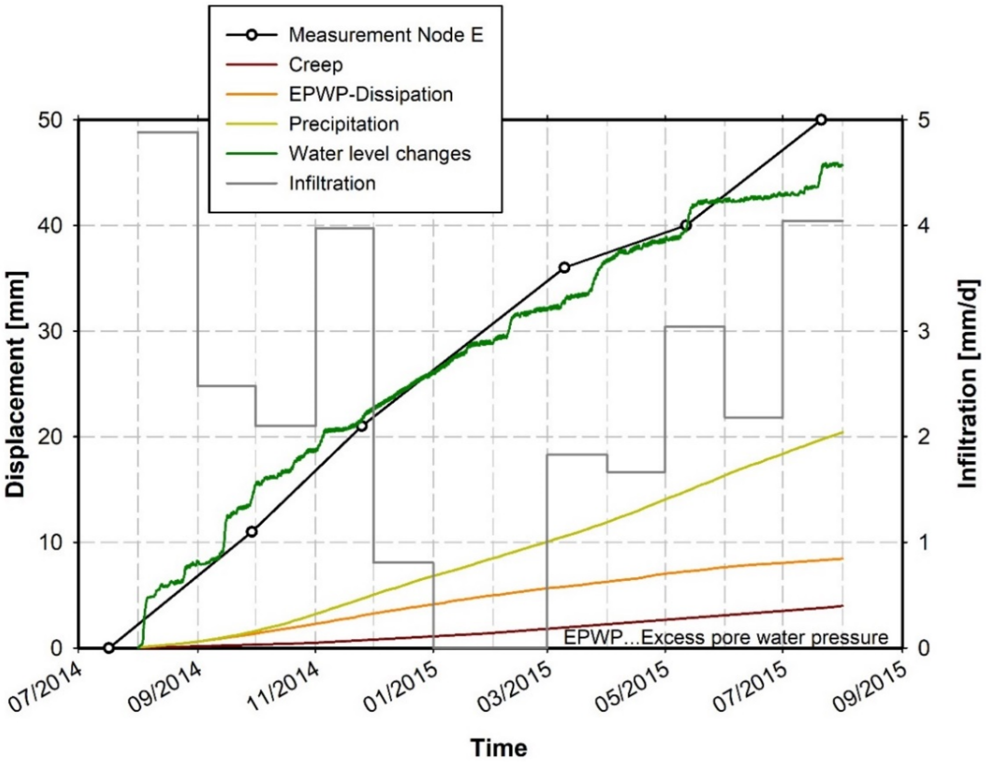

Fig. 99: Back-calculated displacements due to various influencing factors in node E

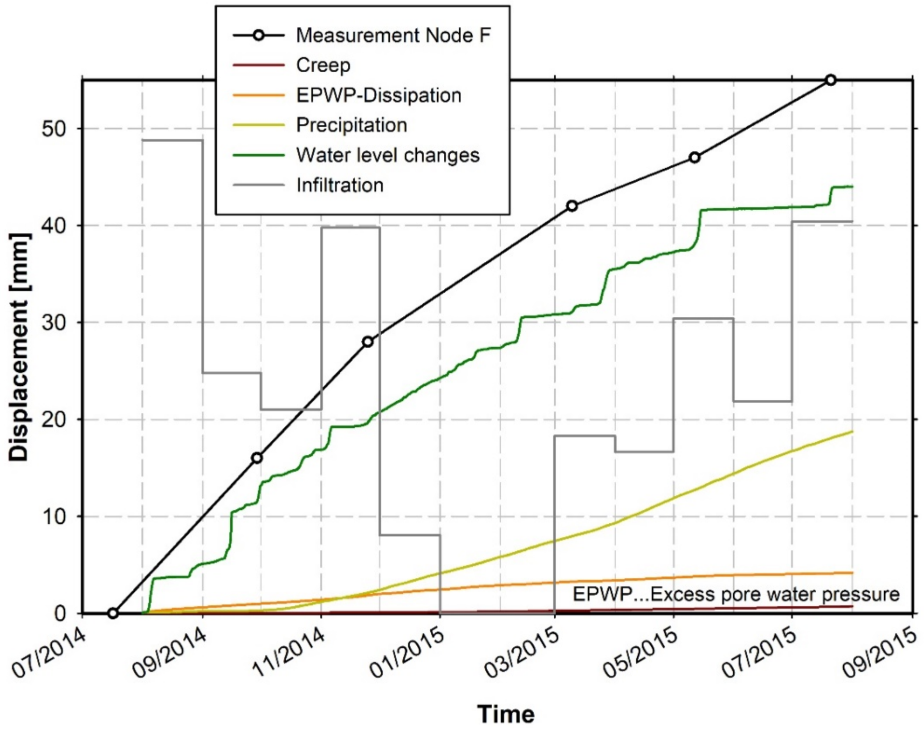

Fig. 100: Back-calculated displacements due to various influencing factors in node F

The results from the back-calculation of the slope deformations (Figure 98 to Figure 100) show that the calculated displacements (with the consideration of all influencing factors) and the measured displacements are in relatively good agreement. The highest geodetic measurement point (point F) shows slightly higher displacements than the numerical results for node F. This difference might be due to differences in the position of the sliding surface as the depth of the sliding surface influences the magnitude of the displacements at the ground surface. The position of the sliding surface is not known in the area of measurement point F and was assumed to be parallel to the ground surface for the numerical modelling. Therefore, the difference of the calculated displacements from the measurements might indicate a deeper position of the sliding surface than the one assumed in the FE-model. The good correlation between measurements and calculations confirms the validity of the FE-model with regard to both, the hydraulic behaviour (see chapter 6.3) and the mechanical behaviour. However, various sensitivity analyses have shown that other factors also influence the magnitude of the slope displacements. For example, the friction angle of the *Transition zone* has a high influence on the displacement magnitude.

The calculated displacements show a decreasing effect of the creep behaviour of the lacustrine fine sediments with an increasing distance up from the slope toe: the creep behaviour (brown line) leads to annual displacements of approximately 10 mm (brown line) in node D, whereas the displacements due to creep deformations in node F are negligible.

The displacements due to the dissipation of the excess pore water pressures are small (< 5mm / year) and negligible.

The effect of the environmental factors (precipitation and evaporation) on the displacements (difference between olive green and orange line) increases with distance up from the slope toe. In node D, precipitation and evaporation lead to 8 mm annual displacements. However, in node E and node F the displacements due to the environmental factors are approximately 15 mm.

The magnitude of the displacements resulting from the water level changes in the storage basin (difference between green and olive green line) is almost constant for the entire slope. The annual displacements due to the water level changes are approximately 25 mm.

In summary, the influence of the creep behaviour on the displacements is decreasing with the increasing distance up from the slope toe, whereas the influence of the precipitation is increasing. The influence of the water level changes is almost constant for the entire slope. An overview is presented in Figure 101. Comparing the different displacement magnitudes with regard to the influencing factors, the water level changes can be identified as the main reason for the displacements, but the precipitation and the creep behaviour also add to the displacements.

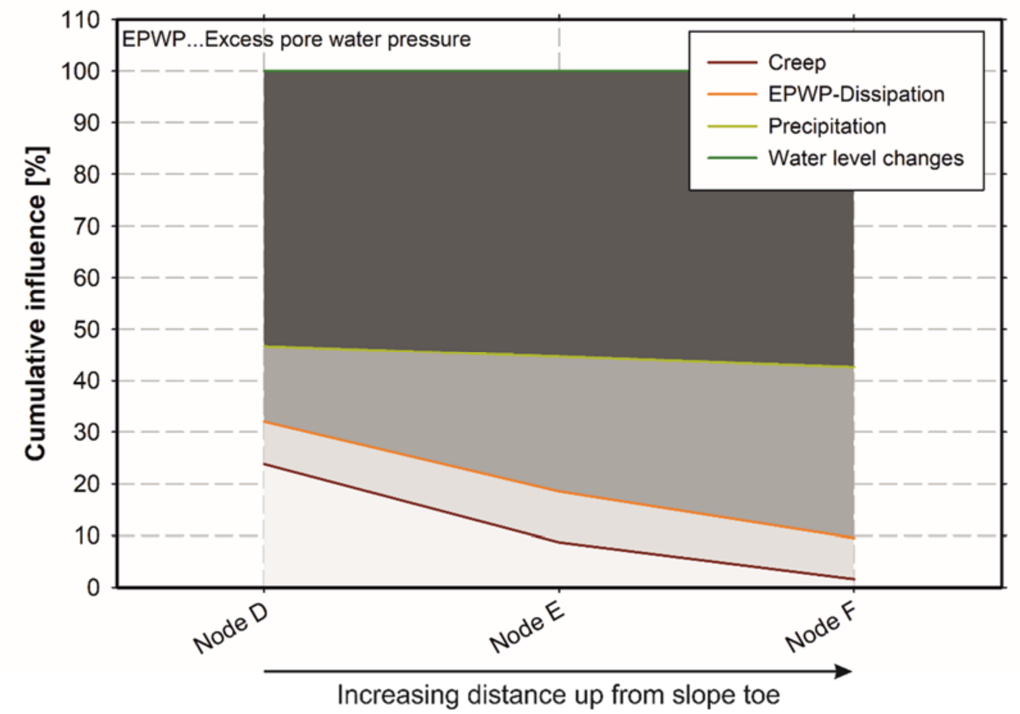

Fig. 101: Cumulative influence of influencing factors on the slope deformations

6.4.2 Further deformation results

In the preceding section, a series of calculations was used to quantify the influence of certain factors on the displacements in the slope, over a period of one year. In this section, some further deformation results, at the surface and at the depth, are examined, using the inclinometer measurements.

Firstly, at the slope surface, the deformation behaviour of the FE-model during a period with an almost constant water level is studied more closely. For this investigation, the already presented and discussed period from 09/09/2014 until 09/10/2014 (water level changes WL 3) is used. During this period, only small water level changes occurred in the water storage basin and the deformation of inclinometer INC 2 was measured at short time intervals.

Figure 102 shows a comparison of the numerical results and the head displacements of inclinometer INC 2 for the mentioned period. As can be seen from this comparison, the numerical behaviour (node D) is very similar to the real behaviour. Accordingly, the numerical analyses confirm the observations from the measurements, which suggested a fast decrease of the displacement rates after stopping the storage operation.

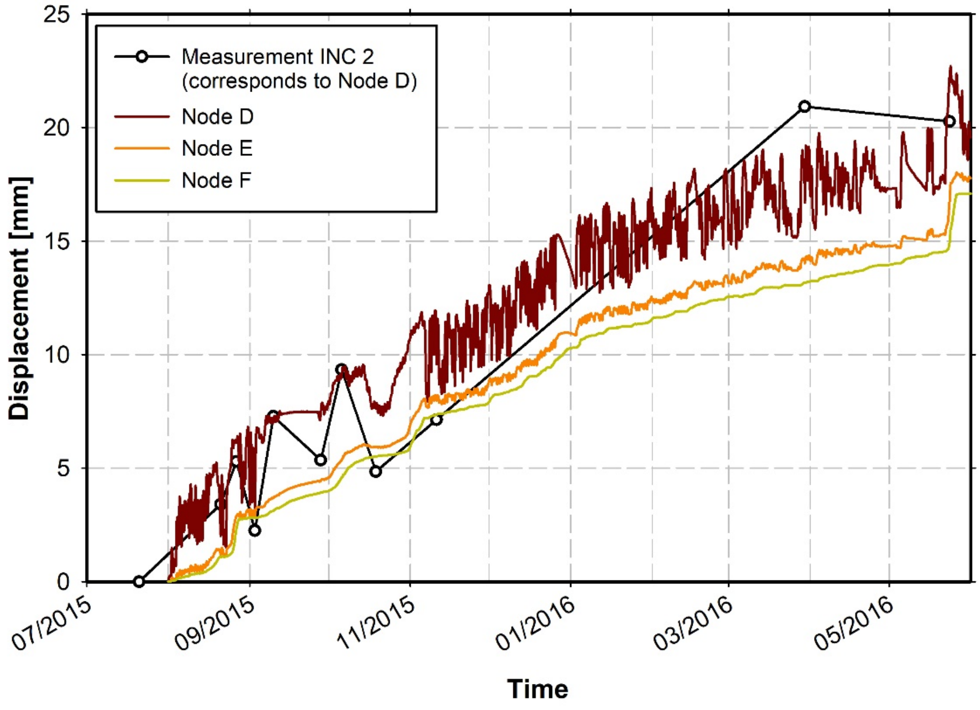

Fig. 102: Numerically calculated displacements during the period without water level changes in the water storage basin (WL 3)

In addition to the deformations at the ground surface of the slope, calculated displacements at depth are analysed at the position of the installed inclinometer INC 2. The results are compared to the resulting deformations from the inclinometer measurements in the period from August 2014 to July 2015, as shown in Figure 103.

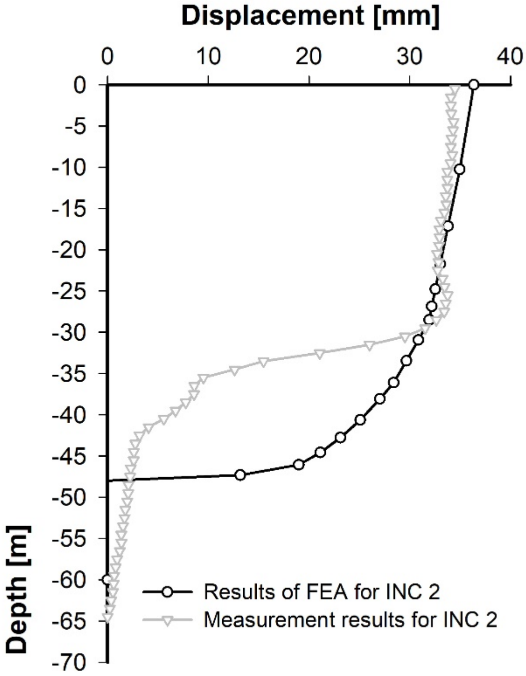

Fig. 103: Comparison of numerical results and measurement results for inclinometer INC 2 from August 2014 until July 2015

It can be seen from Figure 103 that the numerical calculations lead to almost the same head displacements as the measurements showed. Furthermore, the deformation behaviour from 0 m to 30 m beneath the ground surface in the FEA is nearly identical to the measured deformations. However, the position of the main sliding surface is different. In the FEA, the sliding surface occurs at the transition from *Intact rock* to *Transition zone*, whereas the measurements indicate the main sliding surface at the transition from *Sliding mass* to *Transition zone*. In the numerical analysis, the sliding surface in this area is prescribed by the position of the rock surface, which is similar to a boundary condition with fixed displacements. However, in reality, the position of the sliding surface is determined mainly by the occurrence of weak layers or sheared zones, leading to a numerical shortcoming as these soil layers cannot be modelled in detail in the FE-model. Therefore, it is obvious that an exact match of the measured and the calculated position of the sliding surfaces is hardly possible. However, as will be presented in chapter 6.5, the most critical sliding surface during a safety analysis is at almost the same depth as the main sliding surface identified in the measurements.

6.4.3 Reason for rapid increase of slope displacements

In this section, a possible reason for the rapid increase of calculated displacements demonstrated from time to time in selected nodes on the slope (Figure 98 to

Figure 100) are discussed. For example, such a jump in the time-displacement curves can be observed from 14/09/2014 until 16/09/2014, as shown in Figure 104. This rapid increase of the displacements correlates with a fast water level lowering after a longer period with high water levels. As already discussed in chapter 5.4.4, such storage operations often lead to increased displacement rates, at least at the slope toe. Figure 75 presents a comparison of aforementioned storage operations with the measured displacements from inclinometer INC 1. During the mentioned period (14/09/2014 – 16/09/2014), the measurements also showed an increased displacement rate. It can be mentioned that the measurements and the numerical results show also a good agreement in this case. In Figure 104 several time steps are highlighted. For these five time steps, selected numerical results will be presented in the following for a better understanding of the reasons for the jumps in the time-displacement curves.

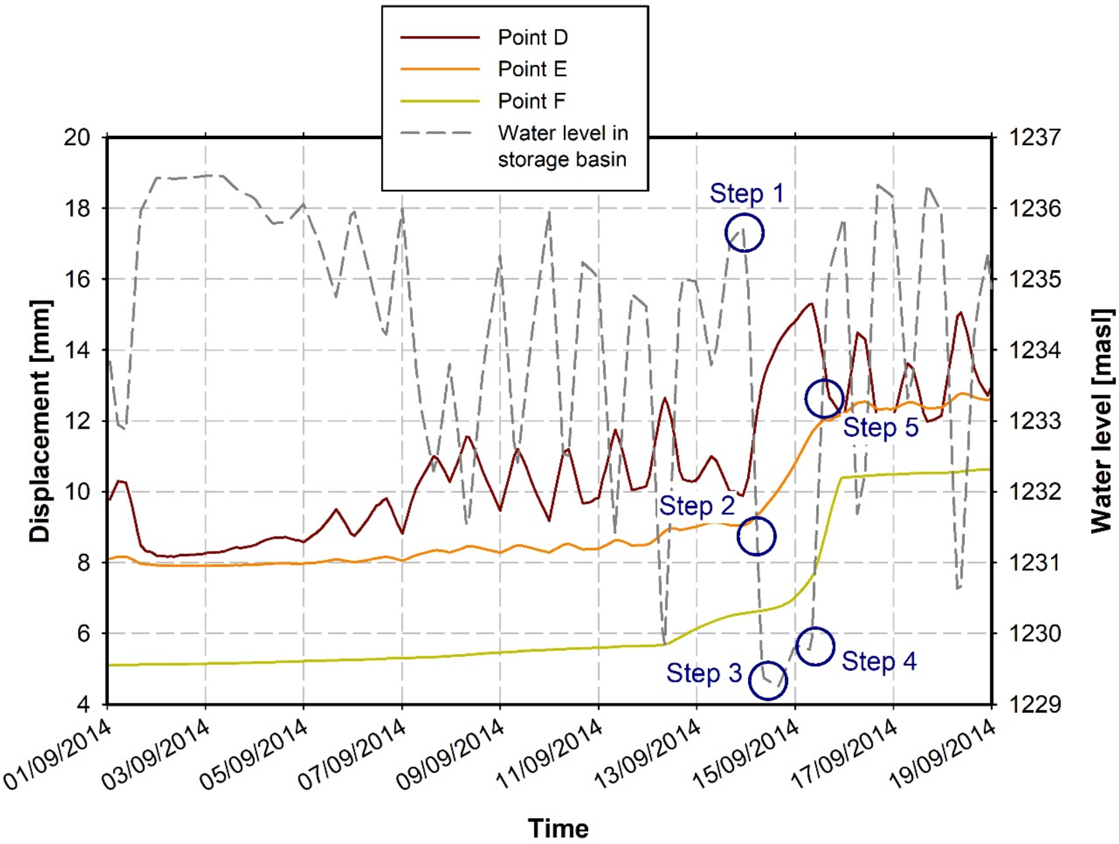

Fig. 104: Time-displacement curve from 01/09/2014 until 19/09/2014 with jump in calculated displacements

Figure 105 presents the groundwater head during the fast water level lowering. The magnitude of the excess pore water pressures is the difference between groundwater head in the subsoil and the corresponding water level. Before the fast water level lowering (Step 1) the groundwater head in the subsoil beneath the water storage basin is almost homogeneous, with a high potential between 94.0 m and 95.5 m (small excess pore water pressures) above the reference level in the FE-model. Beneath the slope toe, the groundwater head is slightly smaller. This generally high groundwater head in the subsoil is due to the mostly high water level in the water storage basin during the preceding weeks. During the fast drawdown (Step 2) positive excess pore water pressures occur. The magnitude of the excess pore water pressures is increasing with depth. Furthermore, relatively high excess pore water pressures also develop at the front part of the slope toe, marked as stress point SP 1 in Figure 105. This position is similar to the position where the maximum positive excess pore water pressures occurred in the preliminary study concerning a drawdown in a homogeneous slope. At the end of the drawdown (Step 3), the maximum excess pore water pressures with regard to the water level in the storage basin are approximately 40 kPa. This magnitude is at the upper limit of the observed range for the measured excess pore water pressures. After the drawdown, high excess pore water pressure develop in particular beneath the sliding mass (stress point SP 2) in addition to the lower soil layers. Neglecting the generally high excess pore water pressures in the deep soil layers, the position of the high excess pore water pressures moves during the drawdown from the front of the slope toe to the area beneath the slope toe, as shown in Figure 105.

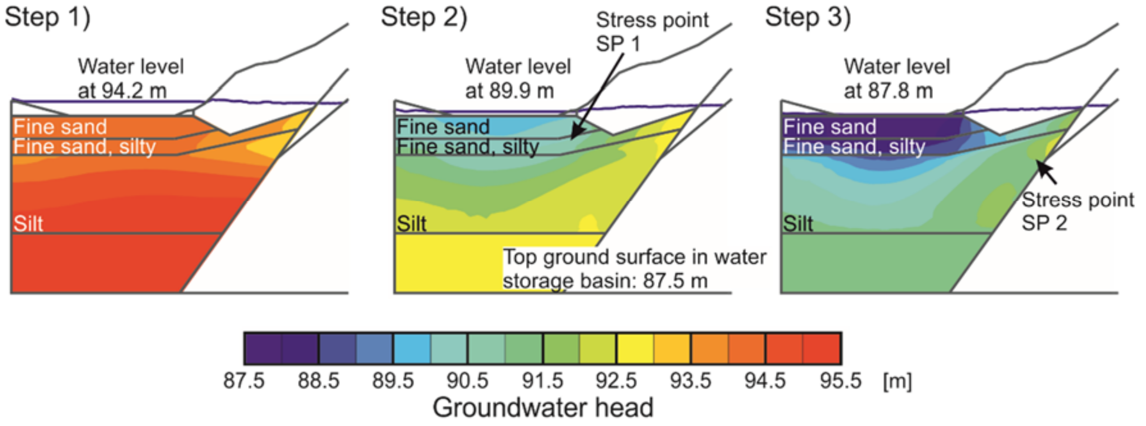

Fig. 105: Groundwater head during fast water level lowering (14/09/2014 – 16/09/2014)

In Figure 105, two stress points (SP 1 and SP 2) mark the areas where the high excess pore water pressures occur during the drawdown. The stress paths for these selected stress points are presented in Figure 106 and Figure 107, where it can be seen that both stress points reach a failure state. The same is true for all surrounding stress points in these areas. Stress point SP 1 is in a failure state for most of the time of the drawdown (from Step 2 to Step 4 as indicated in Figure 104), whereas stress point SP 2 reaches a failure state after the rapid drawdown (Step 4 as indicated in Figure 104).

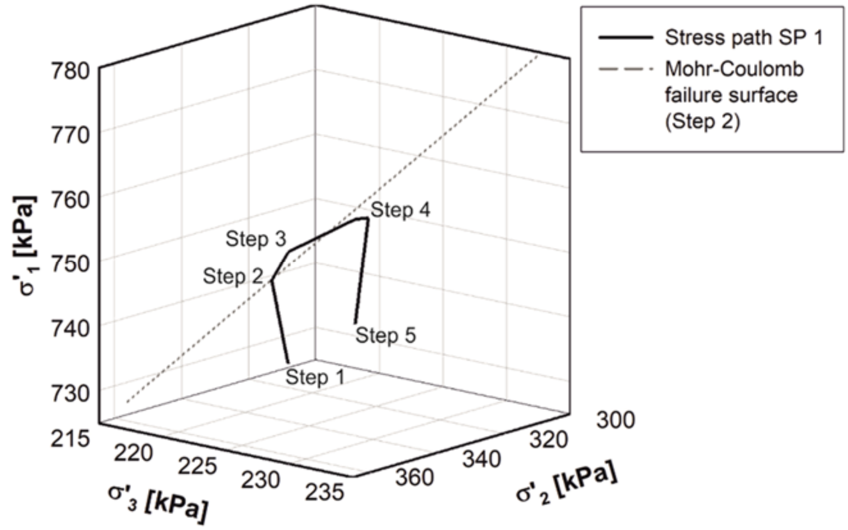

Fig. 106: Stress path SP 1 (marked in Figure 105) during fast water level lowering (14/09/2014 – 16/09/2014)

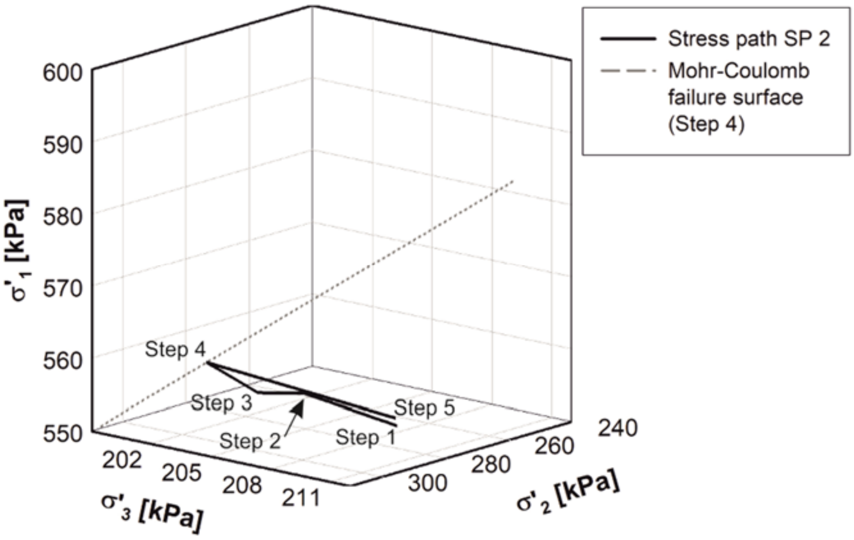

Fig. 107: Stress path SP 2 (marked in Figure 105) during fast water level lowering (14/09/2014 – 16/09/2014)

In the case of the SSC model, these failure states lead to instantaneous plastic strains. They result in a rapid increase of the deformations. Furthermore, the failure states lead to load redistribution in all relevant soil layers and therefore, additional plastic strains are produced. The deformations start at the front part of the slope and proceed beneath the sliding mass, according to the temporal development of the failure states, shown in Figure 108.

Because of the fast water level lowering, the OCR of the lacustrine fine sediments in the area of the slope toe decreases (Step 3). This leads to an increased strain rate. During the subsequent water level increase, the OCR increases again (Step 5). The temporal development of the isotropic OCR is shown in Figure 109.

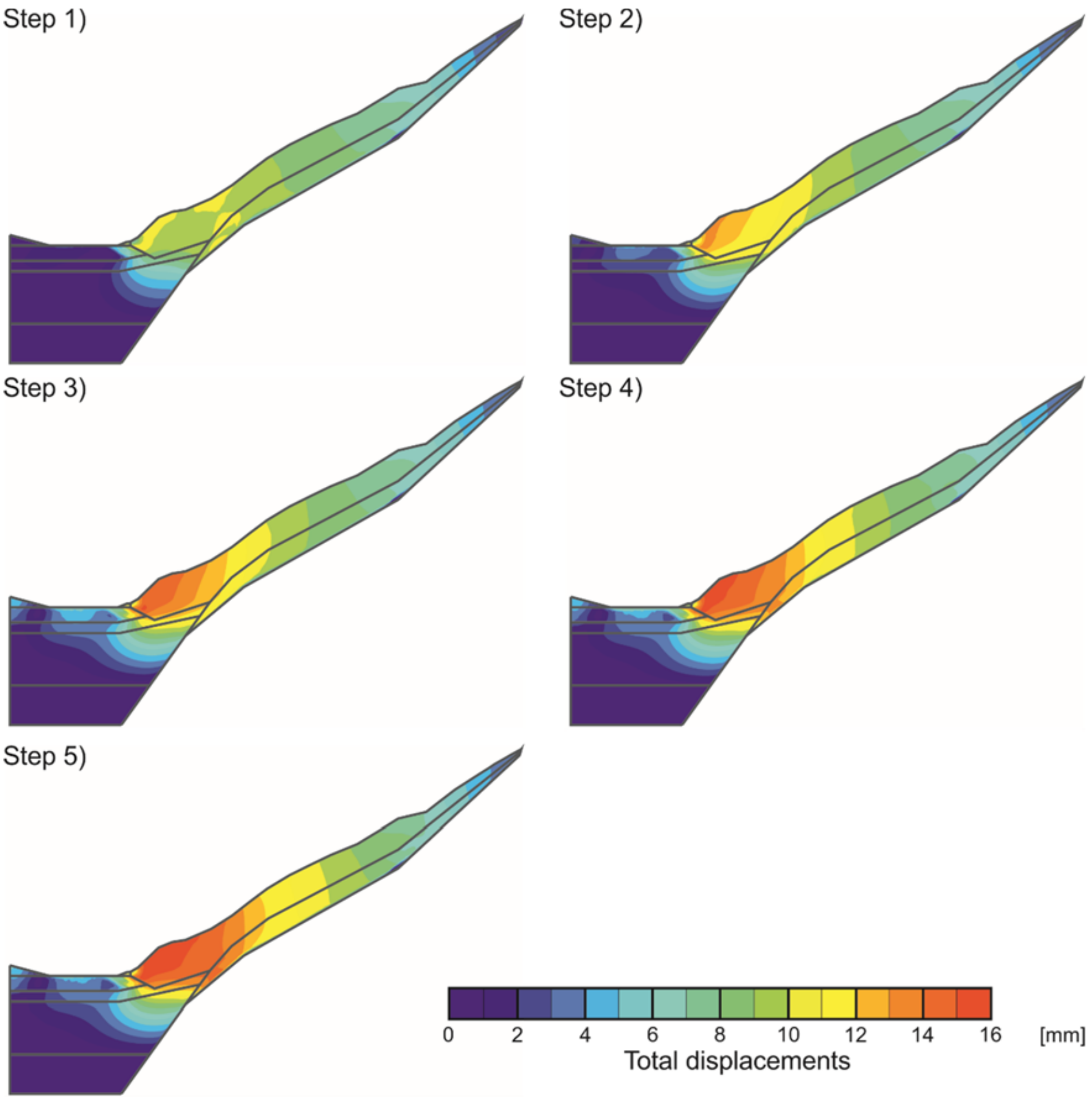

Fig. 108: Temporal development of total displacements during fast water level lowering (14/09/2014 – 16/09/2014)

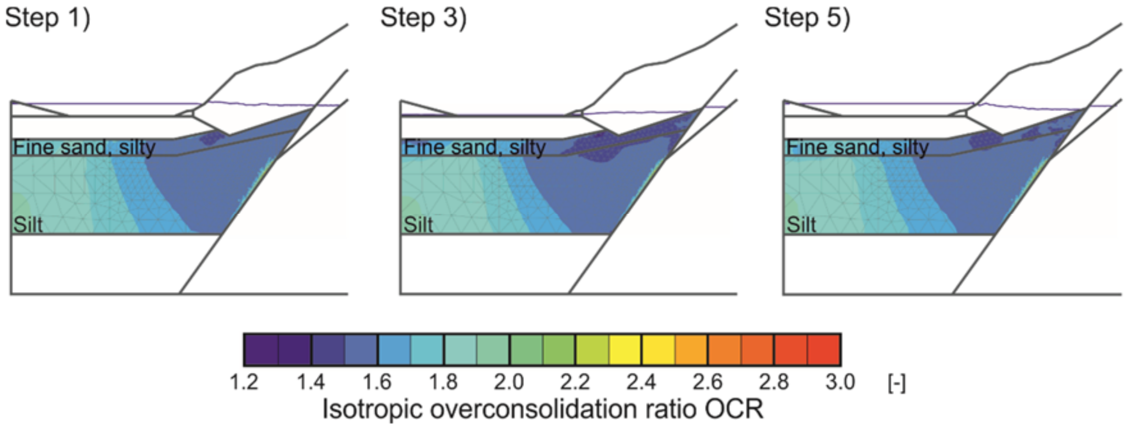

Fig. 109: Temporal development of isotropic OCR in lacustrine fine sediments during fast water level lowering (14/09/2014 – 16/09/2014)

6.4.4 Influence of precipitation on displacement rate

In the previous chapter 6.4.3, the influence of the water level changes on the slope deformations has been discussed based on the observed jumps in the time-displacement curves. In the following, the hydraulic and mechanical mechanisms, which develop in the slope due to the changing precipitation and evaporation rates (infiltration rate) are discussed.

Figure 110 shows the calculated displacements in node E due to precipitation, using the SSC model for the lacustrine fine sediments at the slope toe. A closer look reveals that the precipitation leads to different displacement rates. During the period with no infiltration (time ~150-210 days, labelled with Step 1), the displacement rate is lower. This period corresponds to months without precipitation and evaporation. After a certain time with infiltration (time ~210-250 days, labelled as Step 2) the displacement rate increases and the time-displacement curve becomes steeper. After a long time with infiltration (~100 days later, labelled as Step 3), the displacement rate again reduces slightly.

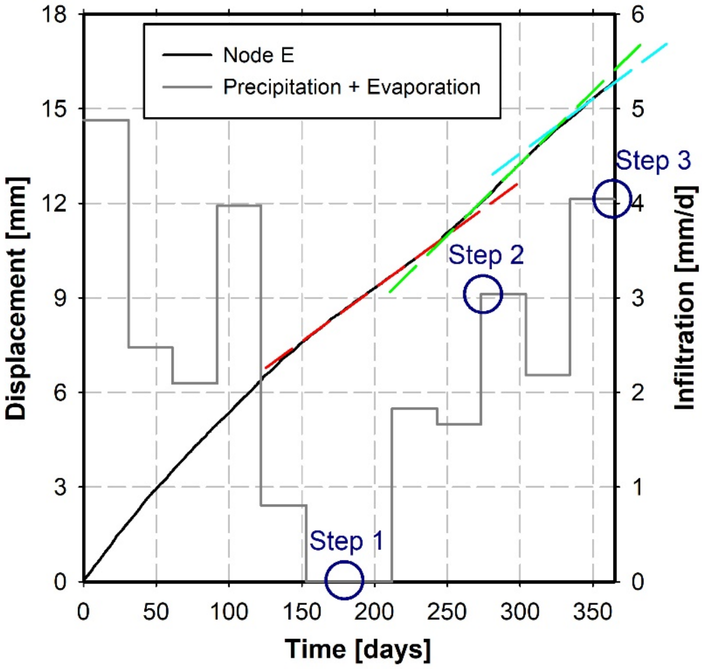

Fig. 110: Displacements in node E due to precipitation and evaporation (infiltration) with different displacement rates

A lower displacement rate in the case of low infiltration and an increase of the displacement rate in the case of heavy rainfalls is commonly known from measurements and numerical studies. However, the decrease in the displacement rate after a long time with infiltrating water at the ground surface (time ~325-365 days in Figure 110) may be unexpected. A possible reason for this behaviour is discussed in the following, on the basis of Figure 111, which shows different numerical results for the time steps marked in Figure 110.

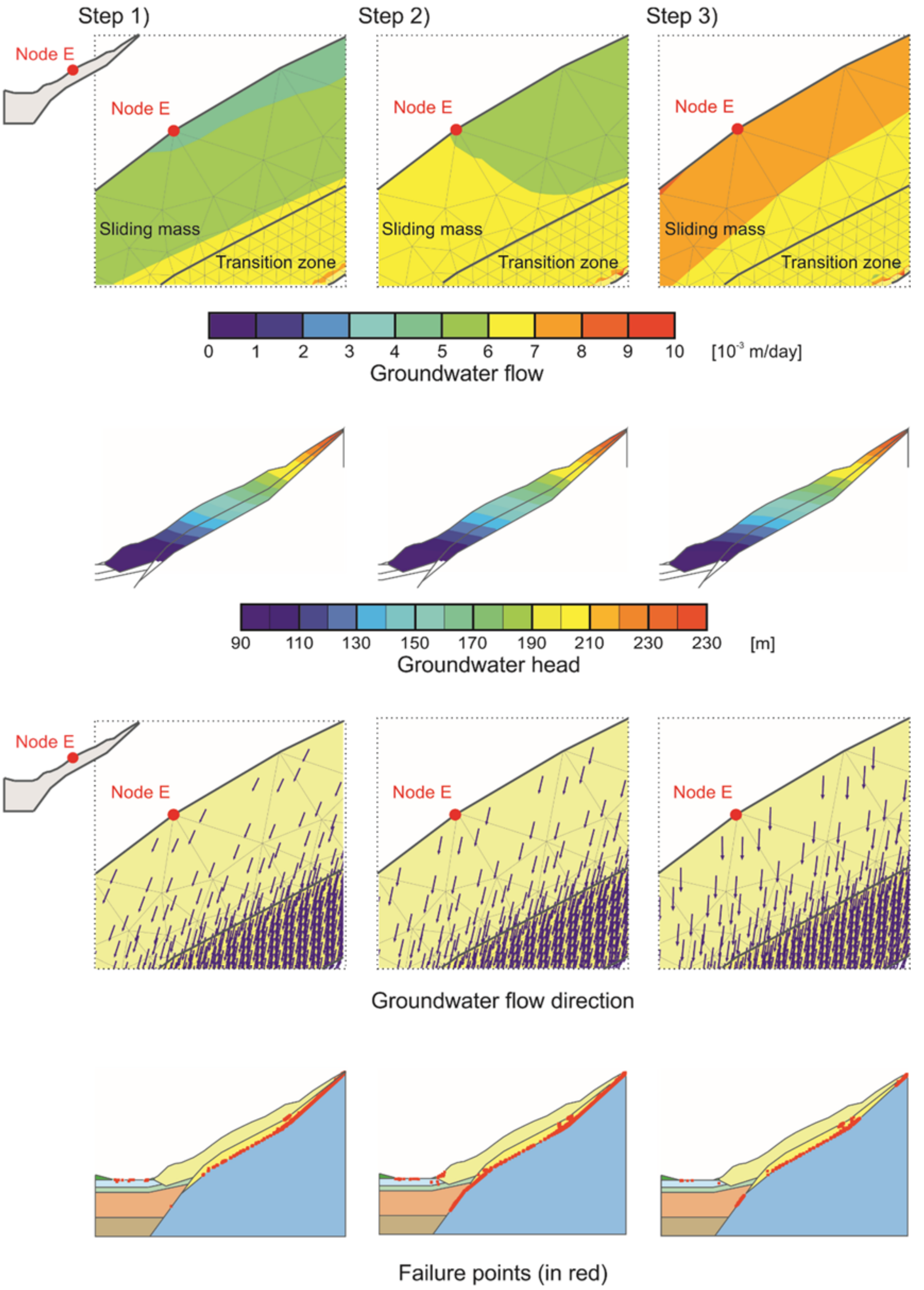

Fig. 111: Influence of precipitation and evaporation on hydraulic and mechanical conditions in the slope

The first row of Figure 111 shows the groundwater flow, which is increasing from Step 1 to Step 3 (shown in Figure 110) due to the applied infiltration and the increasing permeability. The permeability increases, as the degree of saturation increases. This relationship is represented by the hydraulic input parameters concerning the unsaturated flow (see chapter 6.2.2). The corresponding groundwater head is shown in the second row of Figure 111. Starting from steep equipotential lines during the period without infiltration (Step 1), the equipotential lines become flatter (recognizable in Step 2 and Step 3) because of the infiltrating water. The increased degree of saturation reduces the prevailing suction in the slope and the equipotential lines, therefore, turn towards horizontal. The increasing ground water flow and the decreasing suction would suggest increased displacement rates. However, the changing inclination of the equipotential lines presented in the second row of Figure 111 also leads to a change in the flow direction, which is presented in the third row of Figure 111. The flatter equipotential lines result in a flow direction, which, at the end of the presented time period (Step 3), is almost vertical. Consequently, the destabilizing force due to water flow is decreasing. Finally, this effect can also be observed in the fourth row of Figure 111, which shows the number of stress points that have reached failure, as indicated by the red dots. Due to the decreased destabilizing effect of the water flow, the shear stresses on the sliding surface are decreased and a fewer stress points that have reached failure can be observed. Furthermore, the stresses acting on the soil layers beneath the storage basin are also reduced, which leads to less plastic strains and a decreased strain rate in the soil layers modelled with the SSC model. In conclusion, these effects result in a decreased displacement rate for the slope.

This section has demonstrated some interesting effects of precipitation on the slope behaviour in case of a highly permeable slope. However, a few points should be mentioned. To begin with, measurement results, which could potentially confirm the changes in displacement rates presented in Figure 110, are not available because of sparse (long time intervals between) geodetic measurements. Furthermore, the effect of the water level changes in the basin cannot be eliminated in reality and therefore, the effect of water infiltration on the ground surface will always be superimposed by the effect of the water level changes. In addition, it has to be mentioned that a very simple Mohr-Coulomb model is used for the slope material. Therefore, the special characteristics of unsaturated soils such as swelling, collapse, suction dependent stiffness, hysteresis during drying-wetting cycle are not considered.

6.4.5 Slope deformations using alternative constitutive models

In chapter 6.4.1, the influence of various factors on the slope deformations has been investigated by using the SSC model for the lacustrine fine sediments (*Fine sand, silty* and *Silt, fine sandy, clayey*).

For comparison purposes, the same analyses (considering all influencing factors) as performed in chapter 6.4.1 have been performed using the HS model and the HSS model. Based on these comparative analyses, it can be checked whether a time-dependent model such as the SSC model is actually necessary to back-calculate the measured displacements.

Figure 112 presents the total displacements of the node F on the slope as calculated with the HS model, the HSS model and the SSC model. As can be seen from this graph, the different constitutive models lead to significantly different displacements. The same behaviour can be observed for the two other investigated nodes (D and E).

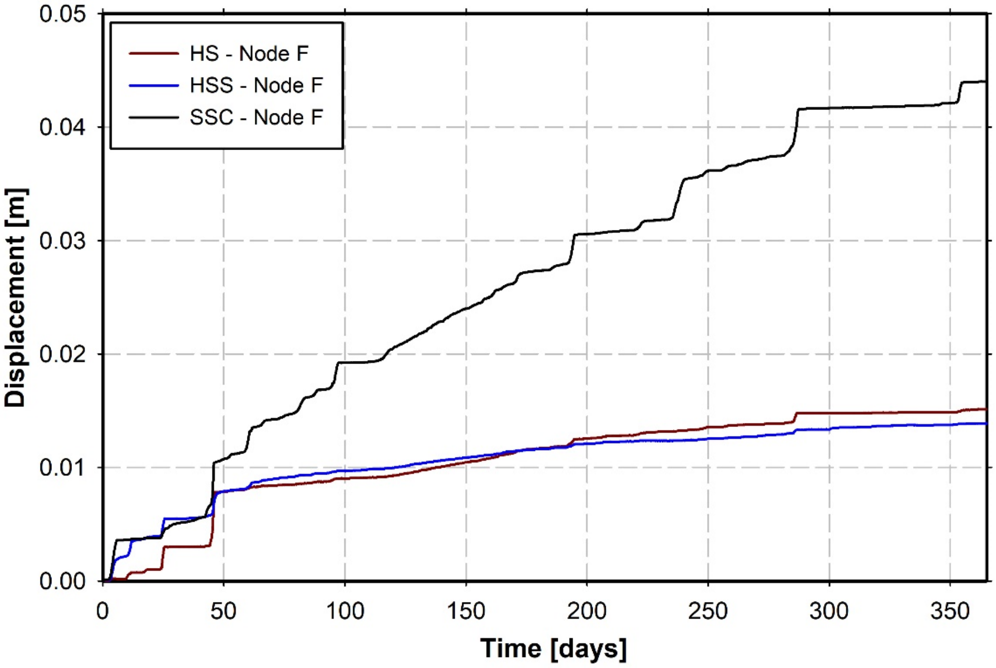

Fig. 112: Total displacements in node F for different constitutive models (HS model, HSS model and SSC model)

Both models (HS model and HSS model) lead to increasing slope deformations in the first 50 days. Afterwards, the increase of the displacements is small. The first increase of the displacements (~0-50 days) is due to stress redistributions and accompanying plastic strains in several stress points. However, the jumps in the displacement curves due to a very fast water level lowering are recognizable to a certain extent in the results of all constitutive models.

With the HS model and the HSS model for the lacustrine fine sediments, the influence of the precipitation and the evaporation on the slope deformations is very small. A similar behaviour as described in chapter 6.4.4 could not be observed with the HS model and the HSS model.

In summary, the presented results show that a back-calculation of the measured slope deformations with the HS model and the HSS model would be impossible.

6.5 Determination of the factor of safety for the slow moving landslide

The previously described numerical studies confirmed the assumptions made on the basis of the measurement data analysis, namely a connection between the storage operation and the slope deformations. Furthermore, the effect of other influencing factors on the slope deformations has been studied. As a usual practice, the effect of an external influence on a slope stability is evaluated by comparing the factors of safety (FoS) for the slope, with and without the influence. Thus, the FoS of the investigated landslide is presented for selected states that represent different excess pore water pressure situations to show the influence of the storage operation on the slope stability (FoS). The FoS has been calculated for following dates:

- 14/09/2014 before the jump in the time-displacement curves discussed in chapter 6.4.3 – named as ‘Before jump in time-displacement curve’
- 17/09/2014 for a high water level (~1236.5 masl) and low excess pore water pressures (compare water level changes WL 1 in Figure 81) – named as ‘Low EPWP’
- 19/09/2014 for a low water level (~1229.0 masl) and high excess pore water pressures (compare water level changes WL 1 in Figure 81) – named as ‘High EPWP’
- 09/10/2015 after a long period with no water level changes (water level at ~1230.0 masl) and mean excess pore water pressures (compare water level changes WL 3 in Figure 83) – named as ‘After period without water level changes’

The factor of safety is numerically determined according to Equation (52).

$$FoS = \frac{tan\varphi'_{input}}{tan\varphi'_{reduced}} = \frac{c'_{input}}{c'_{reduced}} \tag{52}$$

In the following, the factors of safety are determined with a drained safety analysis, as this type of safety analysis lead to much smaller oscillations during the calculation of the FoS. The absolute values of the calculated factors of safety are irrelevant; the focus is put on the change of the FoS due to different excess pore water pressure conditions. Figure 113 shows the FoS for the previously described states. The maximum difference between the calculated FoS is 3 percentage points. The highest FoS corresponds to a period with very small slope deformations (after a period without water level changes). The lowest FoS corresponds to a period with increased slope deformations (jump in slope-displacement curve). This shows that even a small change in the factor of safety can already result in a significant change in the displacement rate.

A similar relationship between FoS and displacement rate has been observed for other slow moving landslides (e.g. Lippomann 1988, Marte & Ausweger 2014).

Figure 113 shows that the storage operation and the resulting excess pore water pressures influence the slope stability. Storage operations, which lead to significantly high excess pore water pressures, should, therefore, be avoided.

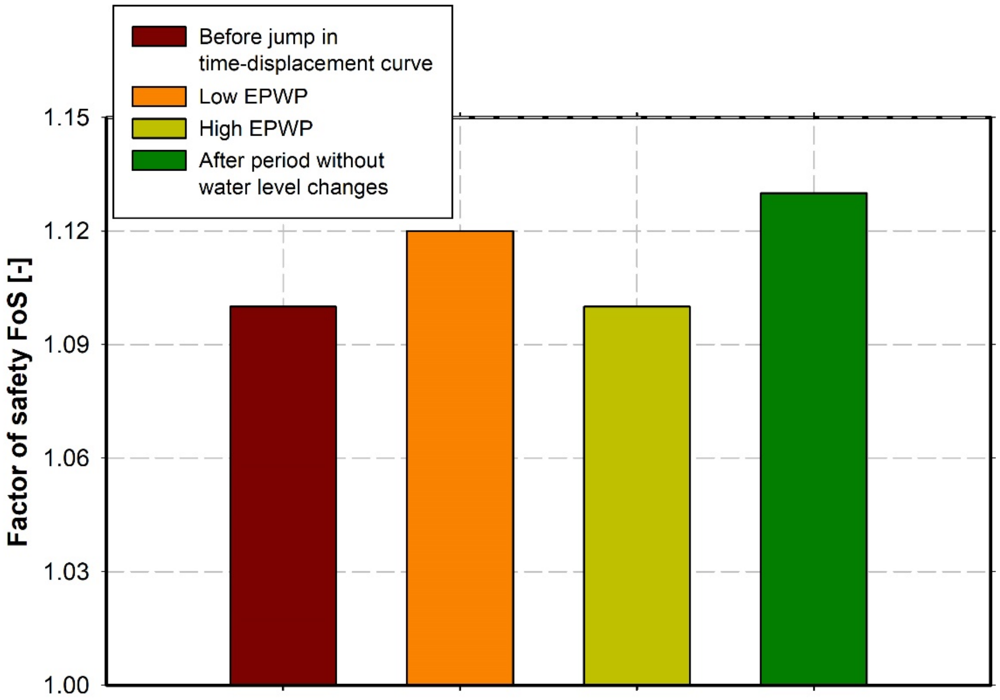

Fig. 113: Factor of safety for different excess pore water pressure conditions

In a further step, a comparison of the failure mechanism from the safety analysis, at the position of the installed inclinometers, to the qualitative measurement results is made in Figure 114 and shows a good agreement, i.e. the critical sliding surface in the FEA is almost at the same depth as the main sliding surfaces in the inclinometer measurements. The absolute value of the deformations cannot be compared, as the deformations calculated in the safety analyses have no physical meaning.

6.6 Possible remediation measures

The water level changes at the slope toe and the resulting excess pore water pressures have been identified as the main reason for the slope movements based on in-situ measurements and numerical investigations. However, the numerical studies showed that other factors (creep and environmental factors) also influence the slope movements.

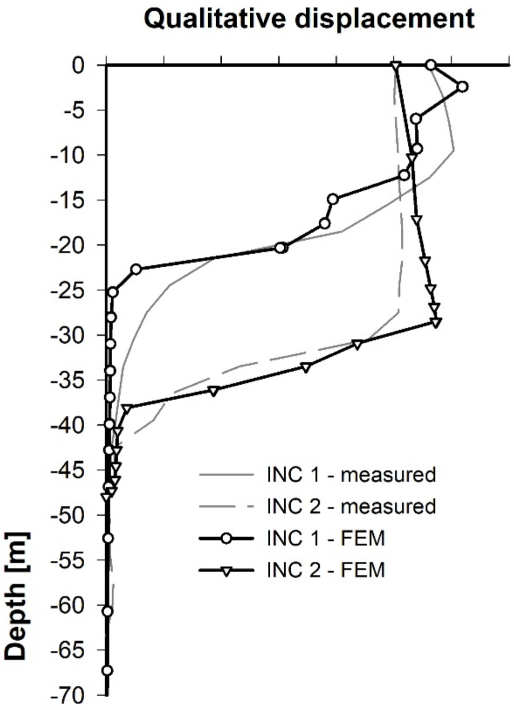

Fig. 114: Comparison of deformations from inclinometer measurements (INC 1 and INC 2) and qualitative deformations from safety analyses before jump in time-displacement curves

Based on this better understanding of the mechanical and hydraulic mechanisms, it seems reasonable to find a remediation measure to compensate the negative effect of the water level changes in the storage basin, namely the excess pore water pressures at the slope toe. For a complete elimination of the effect of the water level changes, the best option would be the ending of the storage operation. However, this is not feasible due to economic reasons. It is, therefore, particularly important to know that in the context of increased slope movements, a fast water level lowering in the water storage basin is unfavourable. This has been shown by all investigations (preliminary studies, model test, comparison of in-situ measurements and numerical studies). Another possible measure to reduce the measured excess pore water pressures might be by installing gravel columns or vacuum drains at the slope toe.

In the case of gravel columns, problems might occur with regard to the contact erosion between the gravel columns and the surrounding fine-grained soil (Augustin 2017). Furthermore, an installation of the gravel columns is only possible in a very limited area, as it is not possible to operate with heavy machines in the water storage basin and on the slope. Therefore, the gravel columns can only be installed at the berm at the slope toe. In this case, the area that can be influenced by the gravel columns, seems to be too small to obtain a significant change in the excess pore water pressures at the slope toe and furthermore, in the movement rate of the landslide.

Vacuum drains would have a significant influence on the pore water pressures at the slope toe. However, the permanent operation of vacuum drains in alpine regions might be problematic due to environmental influences (e.g. frost).

An alternative remediation measure would be the installation of pre-stressed anchors as an additional support for the slow moving landslide. Due to the local conditions, installation in the area of inclinometer INC 2 would be preferable. However, in this case, the reduction of the displacement rates at the slope toe (below the installed anchors) would be smaller than above the installed anchors and would have to be accepted.

7 Conclusions and further research

7.1 Conclusions

During geotechnical investigations concerning a slow moving landslide next to a water storage basin, questions regarding the influencing factors on the slope deformations were raised. An evaluation of the quantitative contribution of various factors, especially of the water level changes in the storage basin of the pumped-storage power plant, on the total displacements, based only on in-situ measurements was impossible. Furthermore, measurement results such as the measured excess pore water pressures at the slope toe could not be explained without further in-depth examinations. These open questions presented throughout the thesis have formed the basis for this thesis, which presents a possible solution to overcome the challenges linked to investigations concerning slow moving landslides by combining in-situ measurements and numerical analyses.

In order to study the mechanisms and triggers of the slow moving landslide, the required theoretical background has been established in the first part of this thesis.

After an introduction to quasi-saturated soils, the significant influence of the saturation stage on the hydraulic properties of the soil has been shown. While the compressibility of the pore water increases due to small air bubbles in the pore water, the permeability decreases. The increased pore water compressibility has been derived in a theoretical context based on Boyle’s law for ideal gases and Henry’s low concerning the solubility of air into water. In this context, a relationship between the pore water pressure and the degree of saturation has been derived, which can be used, subsequently, for the definition of the water retention curve in the quasi-saturated stage. The behaviour of quasi-saturated soils can be modelled in the context of linear poroelasticity (consolidation theory) by applying a decreased bulk modulus for the pore water. However, an easier method for the correct modelling of quasi-saturated soils (including a pore water pressure dependent degree of saturation) is provided by the theory of unsaturated soil mechanics, which incorporates a relationship between pore water pressure and degree of saturation. Thus, a direct consideration of the water retention curve for quasi-saturated soils in the framework of unsaturated soil mechanics is possible, especially as the utilized FE software PLAXIS 2D provides a simple feature to input user-defined water retention curves. For the calculations in this thesis, which incorporate a quasi-saturated stage of the soil, a modified water retention curve has therefore been considered. Experimental model tests and numerical back-calculations of the model tests have been performed to investigate the influence of fluctuating water levels above a soil column on the pore water pressure development in a quasi-saturated soil. The test results have shown that significant excess pore water pressures are produced in a quasi-saturated soil due to water level changes above the ground surface. This is also true for one-dimensional conditions, under which no excess pore water pressures would develop, if a saturated stage was assumed. Based on the numerical back-calculations of the model tests, the theoretically derived relationship between pore water pressure, degree of saturation and pore water compressibility has been verified.

Numerical studies on the soil behaviour during rapid drawdowns have shown that excess pore water pressures might develop in the area of slopes due to fast water level changes. The magnitude of the excess pore water pressures is significantly influenced by the ratio between the drawdown rate and the soil permeability. Furthermore, the compressibility of the pore water is an important factor for the excess pore water pressures. A changed pore water compressibility results from a quasi-saturated stage. Consequently, the excess pore water pressures, which are produced due to a rapid drawdown, increase in case of quasi-saturation.

Based on the preliminary studies concerning quasi-saturated soils and rapid drawdowns, it has been shown that both mechanisms could lead to the measured excess pore water pressures at the slope toe of the slow moving landslide.

A simple numerical study on a biaxial test with a recurring loading and partial drainage conditions has been performed in order to study the behaviour of the SSC model under the aforementioned conditions. The results of this study have shown that the SSC model leads to increasing displacements with time. However, the increase of displacements per loading cycle is decreasing with time according to the formulation of the SSC model.

Based on the in-situ measurement results from the site of the landslide and the storage basin, the following relationships have been derived.

- The excess pore water pressures at the slope toe are linked to the water level changes in the water storage basin. The magnitude of the produced excess pore water pressures depend on the velocity and the height of the water level change.
- The displacement rate of the slope movements correlate with the storage operation. While fast and high water level changes lead to increased displacement rates, a period with no water level changes lead to a significant decrease in the displacement rates.
- A clear correlation between precipitation rate and displacement rate could not be detected for the lower part of the slope. However, for the middle and upper part of the slope, the precipitation has some influence on the displacement rate.

An estimation of the quantitative influence of the different factors (water level changes, precipitation and evaporation and creep behaviour) on the displacements based on the measurement results has been impossible. Therefore, and for a better understanding of the different mechanisms that lead to the slope deformations, comprehensive numerical back-calculations have been performed.

The FE-model of the slow moving landslide and the adjacent storage basin incorporates the water level changes in the basin, the precipitation and evaporation (in a simplified manner) and the creep behaviour of the lacustrine fine sediments. After establishing appropriate initial conditions concerning the stress state, the hydraulic conditions and the creep behaviour, measured pore water pressures and slope deformations have been back-calculated. Based on these back-calculations, it can be concluded that a quasi-saturated stage of the subsoil is not necessarily required to back-calculate the excess pore water pressures. The changing total stress on the slope surface due to water level changes, in combination with a water level in the slope material that is different to the open water level lead to excess pore water pressures at the slope toe. These effects have also been discussed comprehensively in the course of a preliminary study concerning rapid drawdowns. All considered types of water level changes have been successfully back-calculated. Furthermore, the water level changes have been confirmed as the reason for the excess pore water pressures.

The back-calculation of the slope displacements worked well by applying the SSC model for the lacustrine fine sediments at the slope toe. However, it has to be mentioned that the magnitude of the slope deformations in the FE-model depends on many factors (e.g. friction angle of slope material). Furthermore, appropriate assumptions concerning the initial conditions (overconsolidation ratio OCR) of the creep model (SSC model) have to be made to obtain the correct strain rate. An appropriate OCR for the back-calculation of the slope deformations has been established by simulating a specific period in which the relevant soil material is allowed to creep. Nevertheless, the back-calculations have shown very clearly that the water level changes in the storage basin are the main reason for the slope movements. However, the creep behaviour of the lacustrine fine sediments at the slope toe and the precipitation lead to additional deformations. The influence of the creep behaviour decreases in the middle and upper part of the slope, whereas the influence of the precipitation increases in this area. Furthermore, it has been shown that the jumps in the time-displacement curves from the FEA correlate with measured increased displacement rates. In most cases, these high displacement rates in the measurements correspond to a fast water level lowering after a long period with high water levels. Such storage operations lead to instantaneous displacements at the slope toe in the FEA due to local failures at the slope toe, which lead finally to jumps in the time-displacement curves. Based on further calculations, the influence of the precipitation on the displacement rates has been discussed. It has been possible to show that a long period with precipitation does not necessarily result in continuously increasing displacement rates because the flow direction rotates. However, this can only be true in the case of a highly permeable and steep slope, where no water level increase occurs in the slope.

Finally, the influence of the storage operation on the factor of safety of the slope has been discussed. As it has been shown, the factor of safety varies by just 3%

due to the changing water levels, although the differences in the displacement rates are significantly higher.

Important information for the energy company that operates the pumped-storage power plant has been obtained from the studies in this thesis. Throughout the thesis a fast water level lowering after a long period with high water levels has been identified as the most critical storage operation for the slow moving landslide. This outcome has resulted in a detailed catalogue of measures that should be taken in the case of a negative trend in the continuous in-situ observations (however, this was not part of this thesis). Moreover, the presented findings from this thesis are a good basis for a subsequent efficient design of possible remediation measures to reduce the risk of the slow moving landslide to the surroundings. On top of that, this thesis contributes to a better understanding of the mechanisms of slow moving landslides next to water storage basins. Furthermore, this thesis shows that geotechnical investigations concerning slow moving landslides based solely on measurements or numerical analyses are not practical. Instead, a combination of both methods has many advantages and leads to an improved understanding of the mechanisms of the landslide.

7.2 Further research

The investigations in this thesis are strongly influenced by the considered case study. However, there are open issues, particularly concerning the theoretical background. Therefore, it is recommended that further research in the context of slow moving landslides focus especially on the following tasks:

- Examination of the influence of the type of safety analysis after a fully coupled flow-deformation analysis on the calculated factor of safety.
- Determination of a water retention curve for the considered slope material and investigation of its influence on the slope deformations.
- Application of a high order constitutive model for unsaturated soils (e.g. Barcelona Basic model) for the slope material.
- Further investigations concerning appropriate constitutive models for slow moving landslides. Especially, a time dependent constitutive model, which also incorporates a non-local formulation for strain softening.
- Definition of crucial measurement quantities for a better modelling of the environmental factors in order to install the required measurement technique beforehand.
- In general, investigations of the influence of quasi-saturated stage in other boundary value problems (e.g. dewatering, dynamic loading).

8 Bibliography

Alonso, E.E.; Olivella, S.; Pinyol, N.M. (2005)
A review of Beliche Dam. Géotechnique, Vol. 55, No. 4, 267-285.

Augustin, M.M. (2017)
Influence of gravel columns on development of pore pressures beneath water storage basin. MSc Thesis, Graz University of Technology. Austria.

Benz, T. (2007)
Small-Strain Stiffness of Soils and its Numerical Consequences. Ph.D. Thesis, Universität Stuttgart, Mitteilungen des Institutes für Geotechnik, Heft 55. Germany.

Benz, T. (2012)
Viscoplasticity – Possible creep formulations – Soft Soil Creep in 3D. Proc. CREEP School 1 – Creep in Soft Soils September 10-11, 2012, CREEP (ed), Trondheim, Norway, 31-46.

Berilgen, M.M. (2007)
Investigation of stability of slopes under drawdown conditions. Computers and Geotechnics, Vol. 34, No. 7, 81-91.

Bicalho, K.V. (1999)
Modeling water flow in an unsaturated compacted soil. Ph.D. Thesis, University of Colorado. USA.

Bicalho, K.V.; Znidarcic, D.; Ko, H.-Y. (2000)
Air Entrapment Effects on Hydraulic Properties. Proc. Geo-Denver 2000, Denver, USA, 517-528.

Bicalho, K.V.; Znidarcic, D.; Ko, H.-Y. (2005)
An experimental evaluation of unsaturated hydraulic conductivity functions for a quasi-saturated compacted soil. Proc. International symposium on advanced experimental unsaturated soil mechanics, Tarantino, Romero & Cui (eds.), Trento, Italy, 325-329.

Biot, M.A., (1941)
General Theory of Three-Dimensional Consolidation. Journal of Applied Physics, Vol. 12, No. 2, 155-164.

Bjerrum, L. (1967)
Engineering geology of Norwegian Normally-Consolidated Marine Clays as Related to Settlements of Buildings. Seventh Rankine Lecture. Géotechnique, Vol. 17, No. 2, 81-118.

Black, D.K.; Lee, K.L. (1973)
Saturating Laboratory Samples by Back Pressure. Journal of the Soil Mechanics and Foundations Devision, Vol. 99, No. 1, 75-93.

Blaickner, M. (2017)
Slope stability under consideration of groundwater fluctuations. MSc Thesis, Graz University of Technology. Austria.

Boutonnier, L. (2007)
Comportement hydromécanique des sols fins proches de la saturation cas des ouvrages en terre: coefficient B, déformations instantanées et différées, retrait / gonflement. Ph.D. Thesis, Institut National Polytechnique de Grenoble. France.

Boutonnier, L. (2010)
Coefficient B, Consolidation and Swelling in Fine Soils Near Saturation in Engineering Practice. Mechanics of Unsaturated Geomaterials, L. Laloui (ed), 327-352. London & Hoboken: ISTE Ltd and John Wiley & Sons.

Brinkgreve, R.B.J.; Kumarswamy, S.; Swolfs, W.M. (2016)
PLAXIS 2D 2016 – User Manual. Delft: Plaxis bv.

Butterfield, R. (1979)
A natural compression law for soils (an advance on e-log p'). Géotechnique, Vol. 29, No. 4, 469-480.

Daghighi, D. (2016)
Permeability of layered soils. MSc Thesis, Graz University of Technology. Austria.

Dorsey, N.E. (1940)
Properties of Ordinary Water-Substances. New York: Reinhold.

Engl, D.A. (2013)
The Creep Equilibrium Analysis Method (CrEAM). Ph.D. Thesis, Graz University of Technology. Austria.

Ewers, J. (2016)
Porenströmung als Auslöser für Erosion?. BAWMitteilungen, Vol. 99, 45-58.

Faybishenko, B.A. (1995)
Hydraulic Behavior of Quasi-Saturated Soils in the Presence of Entrapped Air: Laboratory Experiments. Water Resources Research, Vol. 31, No. 10, 2421-2435.

Fredlund, D.G. (1976)
Density and compressibility characteristics of air–water mixtures. Canadian Geotechnical Journal, Vol. 13, No. 4, 386-396.

Fredlund, D.G.; Rahardjo, H.; Fredlund, M.D. (2012)
Unsaturated Soil Mechanics in Engineering Practice. New Jersey: John Wiley & Sons.

Galavi, V. (2010)
Groundwater flow, fully coupled flow deformation and undrained analyses in PLAXIS 2D and 3D. PLAXIS internal report, 290 pages.

Garlanger, J.E. (1972)
The consolidation of soils exhibiting creep under constant effective stress. Géotechnique, Vol. 22, No. 1, 71-78.

Hardin, B.O.; Black, W.L. (1969)
Closure to vibration modulus of normally consolidated clays. ASCE Journal of Soil Mechanics and Foundation Division, Vol. 95, No. 6, 1531-1537.

Havel, F. (2004)
Creep in soft soils. Ph.D. Thesis, Norwegian University of Science and Technology. Norway.

Head, K.H.; Epps, R.J. (2011)
Manual of Soil Laboratory Testing Volume II: Permeability, Shear Strength and Compressibility Tests, 3rd edition. Scotland: Whittles Publishing.

Hendry, M.T.; Macciotta, R.; Martin, C.D.; Reich, B. (2015)
Effect of Thompson River elevation on velocity and instability of Ripley Slide. Canadian Geotechnical Journal, Vol. 52, No. 3, 257-267.

Hofmann, R.; Sausgruber, J.T. (2017)
Creep behaviour and remediation concept for a deep-seated landslide, Navistal, Tyrol, Austria. Geomechanics and Tunneling, Vol. 10, No. 1, 59-73.

Jagau, H. (1990)
Verhalten unvorbelasteter tonig-schluffiger Böden unter zyklischen Einwirkungen. Ph.D. Thesis, Universität Fredericiana in Karlsruhe, Veröffentlichungen des Institutes für Bodenmechanik und Felsmechanik, Heft 118. Germany.

Kim, T.C.; Novak, M. (1981)
Dynamic properties of some cohesive soils of Ontario. Canadian Geotechnical Journal, Vol. 18, No. 3, 371-389.

Köhler, H.-J. (2000)
Einfluss von Gasblasen auf die Mechanik des Bodens unter Wasser. Proc. 2. Kolloquium Bauen in Boden und Fels, Ostfildern, Germany, 705-772.

Köhler, H.-J.; Montenegro, H. (2005)
Investigations regarding soils below phreatic surface as unsaturated porous media. Proc. International Conference „From Experimental Evidence towards Numerical Modeling of Unsaturated Soils“, September 18-19, 2003, Schanz (ed), Weimar, Germany, 139-157.

Lai, B.T.; Fabbri, A.; Wong, H.; Branque, D. (2015)
Poroelastic behaviour of fine compacted soils in the unsaturated to saturated transition zone. Computers and Geotechnics, Vol. 69, 627-640.

Li, X.L.; Collin, F.; Radu, J.-P.; Bolle, A.; Charlier, R. (2001)
Experimental and numerical studies on the mechanical behaviour of two quasi saturated fine soils. Proc. 15th international Conference on Soil Mechanics and Foundation Engineering, Istanbul, Turkey, 597-600.

Likitlersuang, S.; Teachavorasinskun, S.; Surarak, C.; Oh, E.; Balasubramaniam, A. (2013)
Small strain stiffness and stiffness degradation curve of Bangkok Clays. Soils and Foundations, Vol. 53, No. 4, 498-509.

Marinas, M.; Roy, J.W.; Smith, J.E. (2013)
Changes in Entrapped Gas Content and Hydraulic Conductivity with Pressure. Groundwater, Vol. 51, No. 1, 41-50

Marte, R.; Ausweger, G.M. (2014)
Modellierung des Verhaltens von Kriechhängen. Der Bauingenieur, Vol. 89, No. 2, 79-88.

Montenegro, H.; Köhler, H.-J.; Holfelder, T. (2005)
Inspection of excess pressure propagation in the zone of gas entrapment below the capillary fringe. Proc. International Conference „From Experimental Evidence towards Numerical Modelling of Unsaturated Soils“, September 18-19, 2003, Schanz (ed),Weimar, Germany, 159-172.

Montenegro, H.; Stelzer, O.; Odenwald, B. (2015)
Parameterstudie zum Einfluss von Gasbläschen im Grundwasser auf Porenwasserdruck und effektive Spannung bei Auflast- oder Wasserspiegeländerungen. BAWMitteilungen, Vol. 98, 69-80.

Montenegro, H. (2016)
Infiltrationsdynamik in Erdbauwerken (BAW-Nr. A39520310047). Karlsruhe: Bundesanstalt für Wasserbau, Abteilung Geotechnik, Referat Grundwasser.

Nitzsche, K. (2016)
Displacement patterns in slopes during excavation process. Ph.D. Thesis, Technische Universität Dresden, Mitteilungen des Institutes für Geotechnik, Heft 21. Germany.

Peck, A.J. (1969)
Entrapment, stability, and persistence of air bubbles in soil water. Australian Journal of Soil Research, Vol. 7, 79-90.

Pestana, J.M.; Salvati, L.A. (2006)
Small-Strain Behavior of Granular Soils. I: Model for Cemented and Uncemented Sands and Gravels. Journal of Geotechnical and Geoenvironmental Engineering, Vol. 132, No. 8, 1071-1081.

Pinyol, N.M.; Alonso, E.E.; Olivella, S. (2008)
Rapid drawdown in slopes and embankments. Water Resources Research, Vol. 44, No. 5, 1-22.

Pinyol, N.M.; Alonso, E.E.; Corominas, J.; Moya, J. (2012)
Canelles landslide: modelling rapid drawdown and fast potential sliding. Landslides, Vol. 9, No. 1, 33-51.

Puzrin, A.M.; Sterba, I. (2006)
Inverse long-term stability analysis of a constrained landslide. Géotechnique, Vol. 56, No. 7, 483-489.

Puzrin, A.M.; Schmid A. (2012)
Evolution of stabilised creeping landslides. Géotechnique, Vol. 62, No. 6, 491-501.

Richards, L.A. (1931)
Capillary conduction of liquids through porous mediums. Journal of Applied Physics, Vol. 1, 318-333.

Ronchetti, F.; Schädler, W.; Meier, J.; Borgatti, L.; Corsini, A.; Schanz, T. (2008)
Deformation modelling of the Valoria earth slide – earth flow. Poster EGU General Assembly 2008, Vienna, Austria.

Sakaguchi, A.; Nishimura, T.; Kato, M. (2005)
The Effect of Entrapped Air on the Quasi-Saturated Soil Hydraulic Conductivity and Comparison with the Unsaturated Hydraulic Conductivity. Vadose Zone Journal, Vol. 4, No. 1, 139-144.

Schädler, W.; Borgatti, L.; Corsini, A.; Meier, J.; Ronchetti, F.; Schanz, T. (2015)
Geomechanical assessment of the Corvara earthflow through numerical modelling and inverse analysis. Landslides, Vol. 12, No. 3, 495-510.

Schädler, W. (2010)
Slope movements of the earthflow type – engineering-geological investigation, geotechnical assessment and modelling of source areas on the basis of case studies from the Alps and Apennines. Ph.D. Thesis, Friedrich-Alexander-Universität Erlangen-Nürnberg. Germany.

Schanz, T. (1998)
Zur Modellierung des mechanischen Verhaltens von Reibungsmaterialien. Habilitation, Universität Stuttgart, Mitteilungen des Institutes für Geotechnik, Heft 45. Germany.

Schanz, T.; Vermeer, P.A.; Bonnier, P.G. (1999)
The Hardening-Soil model: Formulation and verification. Proc. International Symposium Beyond 2000 in Computational Geotechnics, Brinkgreve (ed.), Amsterdam, The Netherlands, 281-290.

Scherzinger, T. (1991)
Materialverhalten von Seetonen – Ergebnisse von Laboruntersuchungen und ihre Bedeutung für das Bauen in weichem Baugrund. Ph.D. Thesis, Universität Fredericiana in Karlsruhe, Veröffentlichungen des Institutes für Bodenmechanik und Felsmechanik, Heft 122. Germany.

Schuurman, I.E. (1966)
The compressibility of an air/water mixture and a theoretical relation between the air and water pressures. Géotechnique, Vol. 16, No. 4, 269-281.

Schwager, M.V. (2013)
Development, analysis and applications of an ‘inclinodeformeter’ device for earth pressure measurements. Ph.D. Thesis, ETH Zurich. Swiss.

Schweiger, H.F.; Breymann, H. (2005)
FE-analysis of five deep excavations in lacustrine clay and comparison with in-situ measurements. Proc. 5th International Symposium Geotechnical Aspects of Underground Construction in Soft Ground, Bakker, Bezuijen, Broere & Kwast (eds.), Leiden, The Netherlands, 887-892.

Skempton, A.W. (1954)
The Pore-Pressure Coefficients A and B. Géotechnique, Vol. 4, No. 4, 143-147.

Song, E.-X. (1990)
Elasto-plastic consolidation under steady and cyclic loads. Ph.D. Thesis, Delft University of Technology. The Netherlands.

Stelzer, O.; Montenegro, H.; Odenwald, B. (2014)
Consolidation analyses considering gas entrapment below the phreatic surface. Proc. Numerical Methods in Geotechnical Engineering 2014, Hicks, Brinkgreve & Rohe (eds.), Delft, The Netherlands, 1037-1042.

Stelzer, O. (2016)
Zur Berücksichtigung der Kopplung von Grundwasserströmungen und Bodenverformung bei der numerischen Berechnung der Porenwasserdruckverteilung. BAWMitteilungen, Vol. 99, 17-33.

Tarantino, A. (2010)
Basic Concepts in the Mechanics and Hydraulics of Unsaturated Geomaterials. Mechanics of Unsaturated Geomaterials, L. Laloui (ed), 3-28. London & Hoboken: ISTE Ltd and John Wiley & Sons.

Terzaghi, K. (1925)
Erdbaumechanik auf bodenphysikalischer Grundlage. Leipzig: F. Deuticke.

Thornthwaite, C.W. (1948)
An Approach toward a Rational Classification of Climate. Geographical Review, Vol. 38, No. 1, 55-94.

Tschuchnigg, F. (2013)
3D Finite Element Modelling of Deep Foundations Employing an Embedded Pile Formulation. Ph.D. Thesis, Graz University of Technology, Gruppe Geotechnik Graz, Heft 50. Austria.

Van Genuchten, M.T. (1980)
A Closed-form Equation for Predicting the Hydraulic Conductivity of Unsaturated Soils. Soil Science Society of America Journal, Vol. 44, No. 5, 892-898.

Vaughan, P.R. (2003)
Observations on the behaviour of clay fill containing occluded air bubbles. Géotechnique, Vol. 53, No. 2, 265-272.

Vermeer, P.A.; Neher, H.P. (1999)
A soft soil model that accounts for creep. Proc. International Symposium Beyond 2000 in Computational Geotechnics, Brinkgreve (ed.), Amsterdam, The Netherlands, 249-262.

Vermeer, P.A.; Leoni, M. (2005)
Creep in Soft Soils. Presentation 5th International Workshop of Young Doctors in Geomechanics, Paris, France.

Verruijt, A. (2015)
Theory and Problems of Poroelasticity. Delft: Delft University of Technology.

Wang, H.F. (2000)
Theory of Linear Poroelasticity—with Applications to Geomechanics and Hydrogeology. New Jersey: Princeton University Press.

Waterman, D.; Broere, W. (2017)
Practical application of the soft soil creep model. https://www.plaxis.com (13/11/2017).

Wheeler, S.J. (1986)
The stress-strain behaviour of soils containing gas bubbles. Ph.D. Thesis, University of Oxford. United Kingdom.

Widmoser, B. (2016)
Experimentelle und numerische Untersuchungen zur Porenwasserdruckveränderung bei Wasserspiegelschwankungen über der Geländeoberkante im „quasi-gesättigten“ Boden. MSc Thesis, Graz University of Technology. Austria.